

**Electrochemistry and magnetism
of lithium doped
transition metal oxides**

Dissertation

zur Erlangung des akademischen Grades

Doctor rerum naturalium

(Dr. rer. nat.)

vorgelegt

der Fakultät Mathematik und Naturwissenschaften
der Technischen Universität Dresden

von

Andreia Ioana Popa
aus Bacau, Rumänien

July 2009

Gutachter: Prof. Dr. Bernd Büchner
Gutachter: Prof. Dr. Hans-Henning Klauß
Gutachter: Prof. Dr. Alexander Revcolevschi

Tag der mündlichen Prüfung: 16.12.2009

Contents

| | | |
|----------|---|------------|
| 1 | Introduction | 1 |
| 2 | Electrochemical aspects in transition metal oxides compounds | 5 |
| 2.1 | Lithium ion batteries | 5 |
| 2.1.1 | Electrochemical cell | 5 |
| 2.1.2 | Classification of batteries | 10 |
| 2.2 | Electrode materials used in lithium ion batteries | 11 |
| 2.3 | Effects of electrochemical treatment on physical properties | 19 |
| 2.4 | Conclusion | 24 |
| 3 | Experimental methods and techniques | 25 |
| 3.1 | Electrochemical synthesis and methods | 25 |
| 3.1.1 | Electrochemical setup | 25 |
| 3.1.2 | Electrochemical techniques | 28 |
| 3.2 | Magnetization measurements | 36 |
| 4 | Electrochemically doped Vanadium Oxide Nanotubes | 39 |
| 4.1 | Oxide nanostructures | 39 |
| 4.2 | Properties of electrochemically doped compounds | 48 |
| 4.2.1 | Electrochemical characterization and synthesis | 48 |
| 4.2.2 | Magnetic properties of $\text{Li}_x\text{VO}_x\text{-NT}$ | 73 |
| 4.3 | Conclusion | 89 |
| 5 | Electrochemically doped $\text{Sr}_2\text{CuO}_2\text{Br}_2$ | 91 |
| 5.1 | Cuprate Superconductors | 91 |
| 5.2 | Properties of electrochemically doped $\text{Li}_x\text{Sr}_2\text{CuO}_2\text{Br}_2$ | 95 |
| 5.2.1 | Electrochemical characterization and synthesis | 95 |
| 5.2.2 | Magnetic properties of $\text{Li}_x\text{Sr}_2\text{CuO}_2\text{Br}_2$ | 99 |
| 5.3 | Conclusion | 107 |
| 6 | Electrochemically doped MnO_2 nanostructures | 109 |
| 6.1 | Manganese oxide compounds | 109 |

Contents

| | | |
|----------|--|------------|
| 6.2 | Properties of electrochemically doped MnO ₂ nanostructures | 114 |
| 6.2.1 | Electrochemical characterization and synthesis | 114 |
| 6.2.2 | Magnetic properties of Li _x MnO ₂ nanostructures | 121 |
| 6.3 | Conclusion | 136 |
| 7 | Conclusions | 139 |
| | Bibliography | 143 |
| | List of Figures | 159 |

1 Introduction

After much development in the past years, energy conversion devices, e.g. batteries, are showing high performance by using materials with sophisticated structures. Because of their intensive use, lithium batteries are the subject of many studies all over the world, from both a technological and a fundamental research point of view. In this field, the preparation method, the structure and the particle size of the electrode materials, as well as their physical properties play a very important role to steadily improve the performance of energy storage devices.

Most of the current lithium batteries are based on transition metal oxides. For example, one can find layered rock-salt LiCoO_2 , LiMn_2O_4 and $\text{Li}(\text{Ni},\text{Mn},\text{Co})\text{O}_2$ as cathode materials. This family of materials has been investigated in order to, e.g. establish the intercalation process and Li diffusion mechanism, that limits the performance of these materials for applications [1–4]. From a fundamental research point of view, electrochemistry, i.e. the chemistry that governs the reactions in a battery, offers the possibility to adjust the charge carrier density in a “gentle” way. Classically, charge carrier density can be optimized by tuning solid state reactions or oxygen stoichiometry by a thermal treatment in a controlled oxygen atmosphere. One disadvantage of these techniques is the high temperature necessary for solid state synthesis. With electrochemical methods, the charge carrier density can be modified and controlled by the (de)intercalation (extraction or insertion) of small ions, e.g. lithium, in the structure at room temperature. This intercalation process has the potential to not severely affect the host structure, and to modify the oxidation state of the transition metal ion in a transition metal oxide compound. This process takes place at room temperature, i.e. at low temperature compared to those used for conventional solid state synthesis. Therefore, metastable oxidation states which can not be obtained by conventional approaches are reachable with electrochemical methods.

The main goal of the present work is to take advantage of electrochemistry as a technique to modify transition metal oxidation states by lithium doping and to study the effects on their magnetic properties. The physical properties of transition metal

1 Introduction

oxides are strongly influenced by the relation between the electronic, magnetic, and orbital degrees of freedom of the transition metal ion electrons. Therefore, e.g., different electronic configurations of the d shell electrons lead to different physical properties, like e.g. metallic, superconducting or insulating character of the host system. Electrochemical methods make it possible to insert and extract electrons and thereby alter the electronic configuration of the transition metal ion. This gives the possibility to investigate the electronic phase diagrams of conventionally prepared compounds, as a function of composition.

The approach of modifying materials with electrochemical methods to prepare novel materials has been successfully employed in the past. For example, lithium can be extracted electrochemically from LiVP_2O_7 to obtain a completely new phase with a different crystallographic structure, i.e. VP_2O_7 [5]. The physical properties of Li_xCoO_2 are strongly influenced by the Co oxidation state and Li-vacancy interactions [6]. This kind of dependence is also found in Li_xNiO_2 [7], Li_xTiS_2 [8], and $\text{Li}_x\text{Mn}_2\text{O}_4$ [9]. The interplay between spin and charge in doped frustrated spin magnet Na_xCoO_2 results in a novel ordering phenomena. The Na content in $\text{Na}_x\text{CoO}_2 \cdot y\text{H}_2\text{O}$ can be electrochemically modified to 0.3, then, for $y = 1.3$, the system shows superconductivity with a transition temperature of $T_c = 5 \text{ K}$ [10].

In order to improve the performance of lithium batteries based on transition metal oxides, the lithium diffusion mechanisms and the process of extraction/insertion of electrons can be investigated by electrochemical methods. Another way to improve the performance of lithium batteries is downscaling the particle size of the electrode materials to the nanometer scale. There are many advantages that these materials provide: shorter Li diffusion lengths, high surface area, and increased durability of the battery. The shorter path lengths for electronic transport permits the usage of materials with lower electronic conductivity than bulk materials. Although intensively studied, there are many remaining issues to be resolved such as e.g. minimizing electrode/electrolyte reactions due to the high surface area and low volumetric energy densities (amount of electrical energy stored per unit volume). Many efforts have been concentrated in order to synthesize these new “nano materials” for high performance energy storage devices. Among these materials, Si-C nanocomposites, $\text{Li}_{4+x}\text{Ti}_5\text{O}_{12}$, and Ti-O_2 are few examples of a large family of materials [11, 12]. MO nanoparticles with $M = \text{Co}, \text{Ni}, \text{Fe}$ or Cu show very good electrochemical properties [13]. Over the last years materials with olivine structure, especially LiFePO_4 [14, 15] and LiMnPO_4 [16, 17] have been intensively developed as very promising candidates for positive electrode materials in long-life batteries required to power, for example electric cars. Different forms of manganese oxides [18–

20], V_2O_5 [21] or Vanadium oxide nanotubes [22, 23] have been studied as well as possible cathode materials for lithium batteries.

In this work, the interplay of electrochemical and magnetic methods has been successfully accomplished. Electrochemistry has been used instead of solid state chemistry to control the valence of the transition metal ion and to study the change in magnetic properties of different compounds. In the work at hand, electrochemistry together with magnetometry and solid state spectroscopy (ESR, NMR, μ SR *) have been exploited. These different methods have been combined to study compounds which are valuable for both technological application as cathode materials and basic research. By applying an electrical voltage, lithium is inserted in the crystal structure of the transition metal compound and therefore the valence state of the transition metal ion is modified. In a transition metal compound, as those studied in this work, doping affects the number of electrons in the $3d$ shell. As mentioned at the beginning of this introduction, this number of $3d$ electrons determines the magnetic state of the compound. The modification of the magnetic properties of the studied compounds has been analyzed by the techniques mentioned above. Magnetometry is sensitive to magnetic phase transitions and changes of the effective magnetic moments of the transition metal ion. Complementary information can be gained by employing local probe techniques, like ESR, NMR, and μ SR, especially sensitive to crystal electric field splittings, spin states, magnetic interactions and spin dynamics. Particularly, μ SR can be used to detect the homogeneity of magnetic and superconducting phases.

This work is structured as follows: Chapters 2 and 3 describe the electrochemical cell and its components (anode, cathode, electrolyte). The discharge/charge process of lithium batteries, as well as the electrochemical setup and techniques used in this work are explained in details. Chapter 4 contains the study of electrochemically doped Vanadium oxide nanotubes (VOx-NT). After a brief review of different VOx structure and synthesize methods, the electrochemical performance of VOx-NT is analyzed. Here, the results of electrochemical doping of Li_xVO_x -NT and its effect on the magnetic properties will be presented. In chapter 5 the magnetic and superconducting properties of electrochemically doped $Sr_2CuO_2Br_2$ will be discussed. In chapter 6 the studies of α - MnO_2 nanostructures are presented. Its electrochemical performance and magnetic properties after lithium doping will be discussed. Finally, the results are summarized in the last chapter.

*ESR: Electron Spin Resonance, NMR: Nuclear Magnetic Resonance, μ SR: Muon Spin Relaxation

This page intentionally contains only this sentence.

2 Electrochemical aspects in transition metal oxides compounds

2.1 Lithium ion batteries

The aim of the present work is to study the effects of electrochemical doping on the physical properties of different transition metal oxide compounds. These compounds were used as cathode materials in an electrochemical setup that will be described in detail later in this work. The applied setup is similar to the one used for studies of materials for lithium-ion batteries. In the work at hand, electrochemistry represented a synthesis method for obtaining materials which are not easily, or not at all prepared with classical non-electrochemical methods. Some of the studied materials could have advantages for being used as electrode materials in lithium-ion battery technology. However, this is not the subject of this thesis.

In this chapter, basics of an electrochemical cell, like shape or components, as well as explanations about how discharging and charging of a battery develops are present. Different battery technologies will be mentioned as well. Electrode materials already used in lithium batteries are mentioned. The advantages and disadvantages of using nanoscaled electrode materials in lithium battery technology is debated. In the end of this chapter, the possibility of inducing novel properties by using electrochemical methods will be shortly reviewed.

2.1.1 Electrochemical cell

For clarity, a description of lithium batteries basics and the processes they are based on will follow. A battery can be illustrated as a chemical device used for storing electricity. The electricity can not be easily stored in a direct way. Therefore, historically the need appeared to find a way to indirectly store electricity. As an example of indirect electricity storage is given by pumped-hydro schemes that convert electrical energy into potential energy or night storage heaters that convert electrical

2 Electrochemical aspects in transition metal oxides compounds

energy into thermal energy [24]. Batteries do not store electricity directly, but rather transform chemical energy into electric energy. They have the advantage of being available in a wide range of shape and sizes, as exemplified in Fig. 2.1, they are able to deliver instantaneous electric power, and they are available as “one-time” use or multiple-cycle batteries.

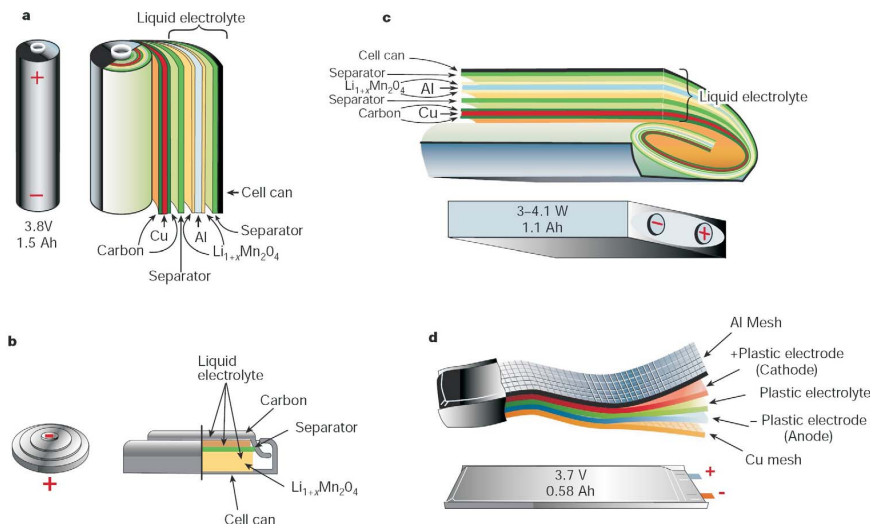


Figure 2.1: Different shapes and design components of lithium batteries: a - cylindrical; b - coin; c - prismatic; d - thin and flat- see below text for details. Taken from [25].

As stated before, the batteries convert chemical energy into electrical energy. This is performed through redox reactions. A redox reaction is the transfer of electrons between two species, therefore reduction or oxidation of species involved in the reaction. A battery consists of one or more electrochemical cells. An example of a standard electrochemical cell is shown in Fig. 2.2. It contains a positive and a negative electrode placed in a recipient with electrolyte. In a battery, these cells may be connected in parallel or in series, depending on the voltage and capacity that they should provide [25].

Each component of an electrochemical cell will be briefly discussed.

The anode

The anode is also called the negative electrode. It is the electrode that releases electrons to the external circuit when a voltage is applied between the two electrodes of the cell. During the electrochemical reaction the oxidation occurs here, thus the anode material is oxidized and its valency increases (also called the oxidizing electrode). When choosing an anode material one has to take into account: material

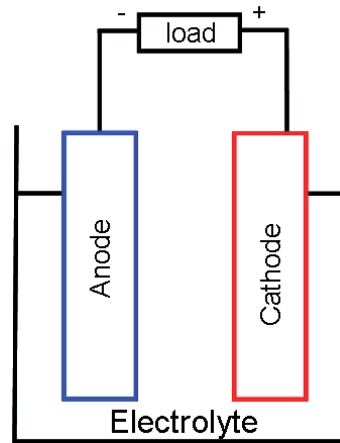


Figure 2.2: Classical electrochemical cell during discharge, when the positive electrode is the cathode and the negative electrode is the anode.

efficiency as reducing agent, high coulombic output (Ah/g), stability as well as easy and cheap fabrication. In commercial lithium-ion batteries, graphite-Li metal is used as anode material.

The cathode

The cathode, or the positive electrode is the electrode that accepts electrons from the external circuit. During the electrochemical reaction it is reduced, thus the valency decreases. The reduction occurs at this electrode and that is why it is also called the reduction electrode. The cathode has to be an efficient oxidizing agent, has to be stable when it is in contact with the electrolyte and it should have a high working voltage. Typical cathode material, commercially used is represented by the layered oxides LiMO_2 where M may be Co or Ni.

Fig. 2.3 illustrates an overview of possible positive and negative electrode materials that are already, or might be in the future, used in Li-based cells. The variety of the working potential of several materials versus Li^+ can be deduce from this picture as well.

The electrolyte

Electrolytes are formed when a salt is placed into a solvent. The electrolyte is an ionic conductor, that means it is able to conduct ions between two electrodes inside of a cell. The electrolyte itself is an electronic insulator [24]. If the electrolyte would be an electronic conductor this would cause an internal short circuit in the cell

2 Electrochemical aspects in transition metal oxides compounds

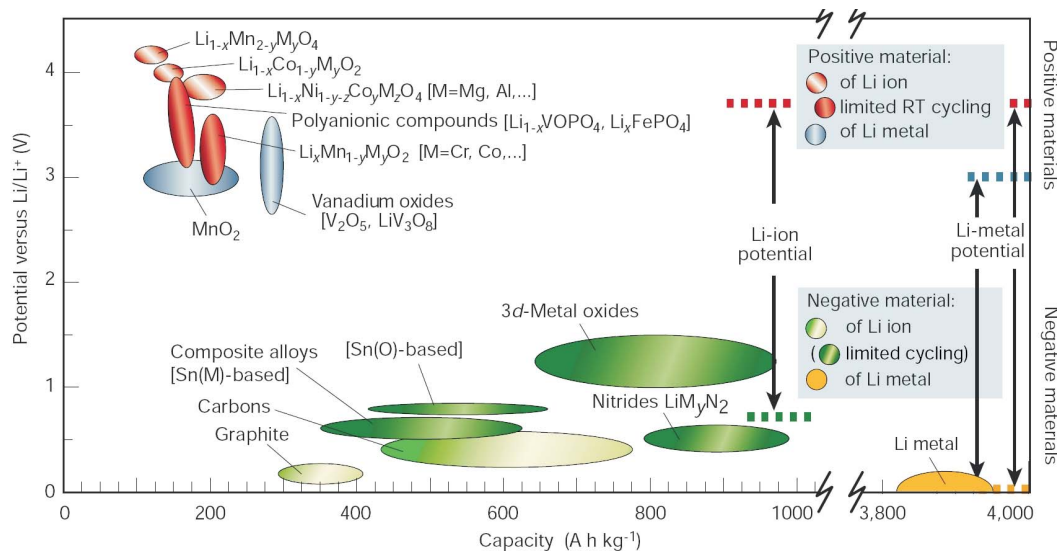


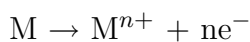
Figure 2.3: Voltage versus capacity for positive and negative electrode materials, currently or possibly used in the lithium batteries technologies [25].

and/or self discharge. The electrolyte has to be non-reactive with the electrode materials, and it should not be dependent on changes in temperature. Low cost it is another advantage.

Inside the cell the anode and the cathode are immersed in the electrolyte but they are electronically isolated. In a practical cell the two electrodes are separated by a separator soaked in electrolyte, in order to maintain the desired ionic conductivity. The separator is usually porous and insulating. Its role is to completely separate the two electrodes in order to avoid short circuits. The shape of a battery can vary from a cylindrical shape to button, flat or prismatic as shown in Fig. 2.1. The cells are well sealed in order to prevent leakage and drying-out.

A description of the discharge and charge process in a battery will be presented in the following part of this chapter. The discharge process is shown in Fig. 2.4. When applying an external voltage between the two electrodes, as a result of a chemical reaction, electrons coming from the negative electrode (anode) flow through the external circuit to the positive electrode (cathode) and they will be accepted in the cathode material. In this way, during a discharging process the anode is oxidized and the cathode material is reduced.

Chemically we can write the discharge process as follows: For the negative electrode where the anodic reaction takes place and where the oxidation occurs a loss of electrons results:



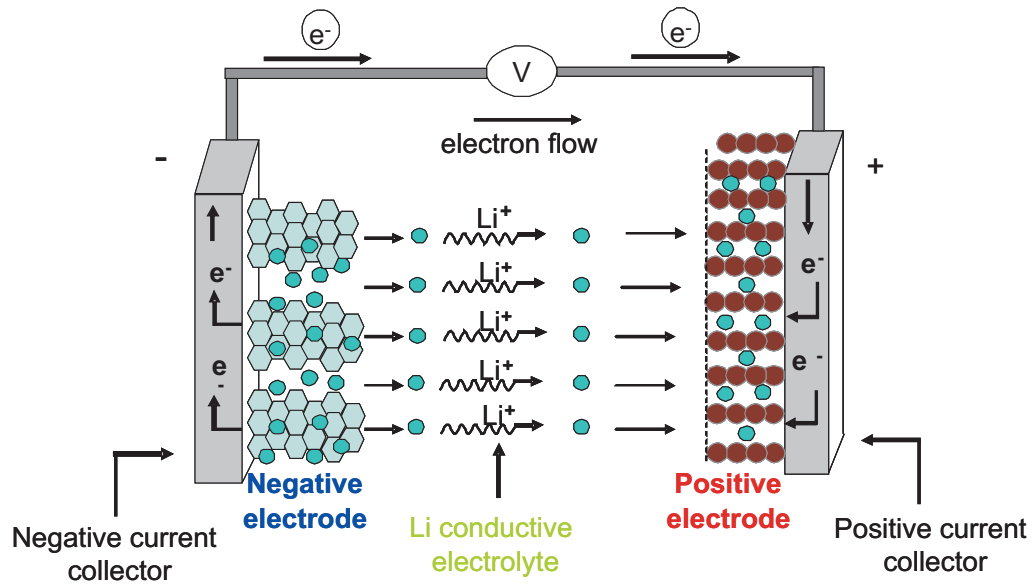
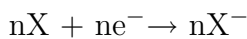
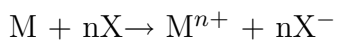


Figure 2.4: Operation of a electrochemical cell, here is described the discharge mode.

For the positive electrode, where the cathodic reaction takes place and where the reduction occurs a gain of electrons results:



The overall reaction for the discharge process can be written as:



During the discharging process of a battery the negative ions, the anions, move toward the negative electrode (the anode). The positive ions, the cations, move toward the positive electrode (the cathode).

The charging process of a battery is shown in Fig. 2.5. During this process the flow of negative and positive ions is reversed compared to the discharge process. While an external voltage is applied between the two electrodes during the charging process, the reaction at the negative electrode is a reduction reaction while an oxidizing reaction takes place at the positive electrode. During charging (recharging) a battery the anode becomes the positive electrode and the cathode becomes the negative electrode. Because this is confusing when thinking in terms of electrolysis, where the anode is always the negative electrode and the cathode is always the positive one, for clarity one should refer to these electrodes as negative and positive electrodes.

Chemically we can describe the charging process as following: the cathodic reaction at the positive electrode causes a reduction of the metal ions and a consumption of electrons:

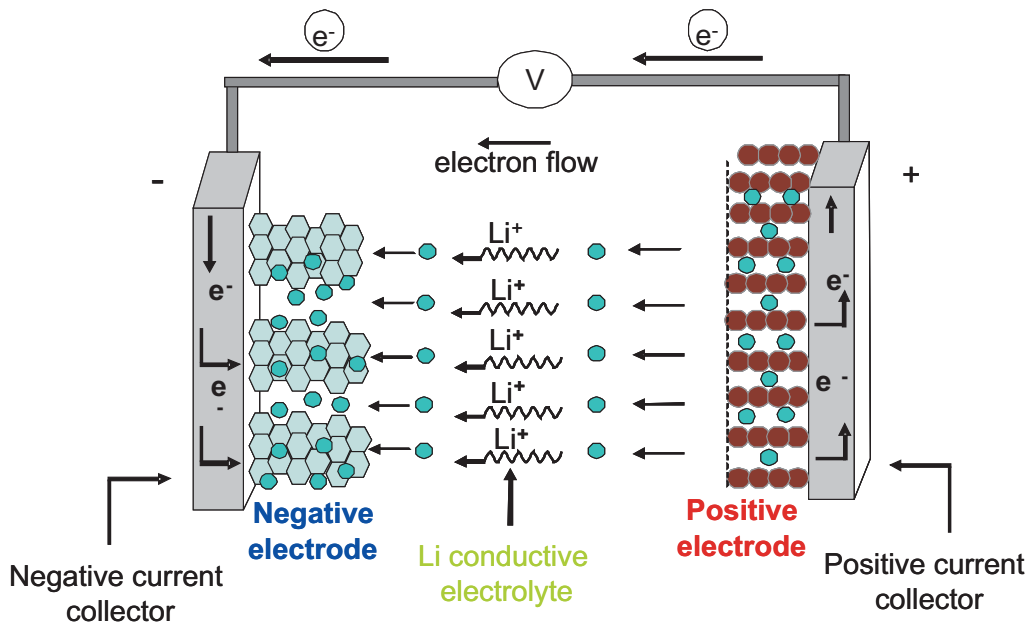
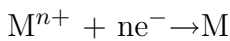
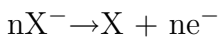


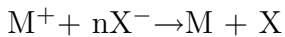
Figure 2.5: Operation of a electrochemical cell, here is described the charge mode.



The anodic reaction takes place at the positive electrode resulting in an oxidation and an excess of electrons:



The overall reaction for the charge process can be written as:



In this first part, components of a battery and processes, i.e. discharging and charging of a commercial battery, were described. The goal of this thesis was not explicitly to study in detail the electrochemical behavior of different potential electrode materials, therefore no further aspects and processes that might take place during cycling an electrochemical cell will be described.

2.1.2 Classification of batteries

Batteries can be divided in two categories: primary, non-rechargeable batteries and secondary, rechargeable batteries. Once the primary batteries are discharged they remain discharged and they can not be used anymore. They are typically used in portable electronics and electric devices. They have the advantage of good shelf life (period of time that a battery can be used without major deteriorations), high

energy density (amount of electrical energy stored per unit of volume) and simplicity of use. They can have different shape but are mostly found in cylindrical and flat shapes.

Primary lithium cells can have voltages of 3.4 V or higher. When comparing the alkaline cells with lithium cells, the latter have a higher energy density but a lower rate capability given by lower conductivity of the non aqueous electrolyte. Lithium primary batteries use both solid and liquid cathodes. From the first group we can mention CF_x , MnO_2 , FeS_2 or CuS . MnO_2 and CF_x cells. These are used for low-rate applications. They can offer $\geq 80\%$ of their theoretical capacity after 10 years of storage.

Secondary, rechargeable batteries can be divided in two categories: the energy storage devices and the batteries discharged when used in applications and then recharged before the next usage.

Alkaline secondary batteries use aqueous solution electrolytes, such as KOH or NaOH, which give them a big advantage from the electrode material/electrolyte interaction point of view. These electrolytes are less reactive than the acidic electrolytes. A representative of an alkaline secondary battery worth mentioning is the NiCd battery available in many shapes and sizes, with very long shelf life, excellent low-temperature and high-rate capabilities.

A lithium ion battery shows a higher energy density and lighter weight. Portable electronic devices mostly use this type of battery. A typical commercial lithium ion battery can be described by a carbon/graphite anode, organic electrolyte and a LiCoO_2 as anode. The lithium ion battery market is growing more and more, with new cathode and anode materials capable of doubling the current lithium battery performances in the next years.

A summary of different battery technologies is presented in Fig. 2.6, both for primary and secondary batteries. The electrical energy per unit of weight, $\text{W}\cdot\text{h}/\text{kg}$ or per unit of volume, $\text{W}\cdot\text{h}/\text{l}$ delivered by a battery depends on the cell voltage and capacity ($\text{A}\cdot\text{h}/\text{kg}$). Both these parameters depends on the material chemistry. From all battery systems presented above, those with lithium represent a big percentage of worldwide sales of portable batteries.

2.2 Electrode materials used in lithium ion batteries

High performance of renewable energy technologies is achieved by using devices with sophisticated structures. Most of the limitations of these technologies result

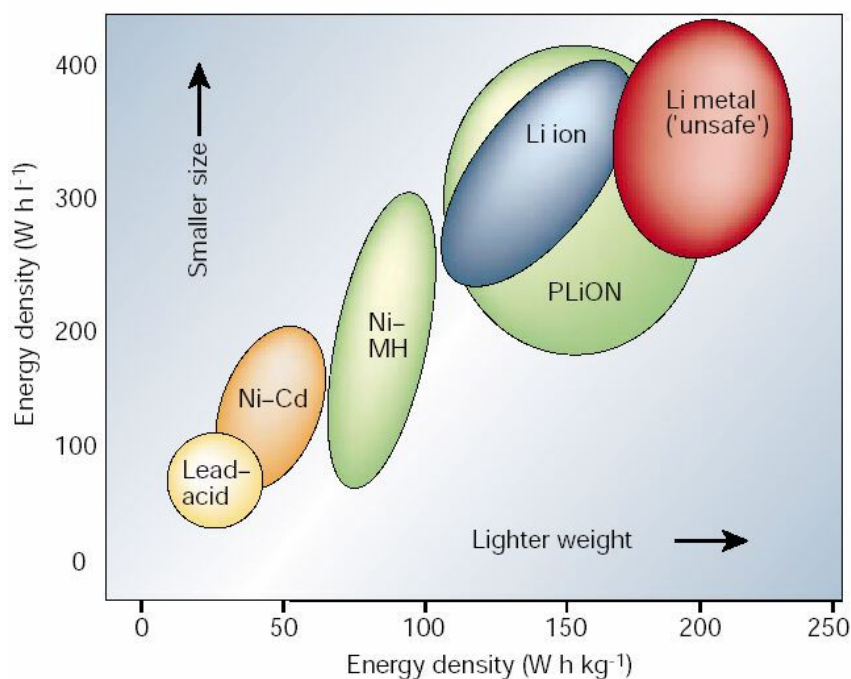


Figure 2.6: Comparison of volumetric and gravimetric energy density for main types of batteries, from Ref [25].

from the properties of the employed materials - for example, photovoltaic cells have limited energy conversion efficiency due to poor charge carrier mobilities in organic polymer and semiconductors; poor charge and mass transport properties decrease the energy and power density (the power density of a battery indicates the electrical power per unit of volume) of portable electric power sources [26]. The solutions to these issues are special compounds, tuned by molecular or atomic engineering. Material properties improved in this way, yielding more efficient energy conversion and energy storage devices.

One approach lies in nanoscience. Nanostructured materials lie at the heart of fundamental advances in efficient energy storage and conversion, where surface processes and transport kinetics play determining roles. Limitations of lithium batteries are caused by the slow solid-state diffusion of Li^+ ions within the electrode material. Nanostructured materials mitigate the problem of slow diffusion because the distance that Li^+ ions must diffuse in the solid state is limited to the radius of the nanoparticle. Therefore, these kinds of materials improve the intercalation/deintercalation kinetics of the electrode material due to the short diffusion distances and high surface areas that they provide. This field of research is becoming more important every day. At present, different nanostructures are easily synthesized [27–29]. For example, carbon nanotubes [30], metallic nanowires [31–33] and

nanotubes based on various transition metal oxides, e.g. TiO_2 [34], Co_3O_4 [35], VO_x -NT [36] are being intensively studied for their ability to host “guest” atoms. This incorporation or doping with guest atoms can change the materials properties such as ferroelectricity, ferromagnetism or magnetoresistivity [37]. Nanomaterials have a wide application range such as logic circuits, magneto-electronic devices, magnetic data storage devices, medical therapeutics and biotechnological application, lithium batteries and much more.

In this section, some materials already used as electrode materials in lithium batteries will be described. From a fundamental point of view they represent a big interest, because they can change their properties when studied under electrochemical conditions. For clarity we can divide these compounds into two categories: compounds with close-packed lattice and compounds with more open structures, for example nanostructures.

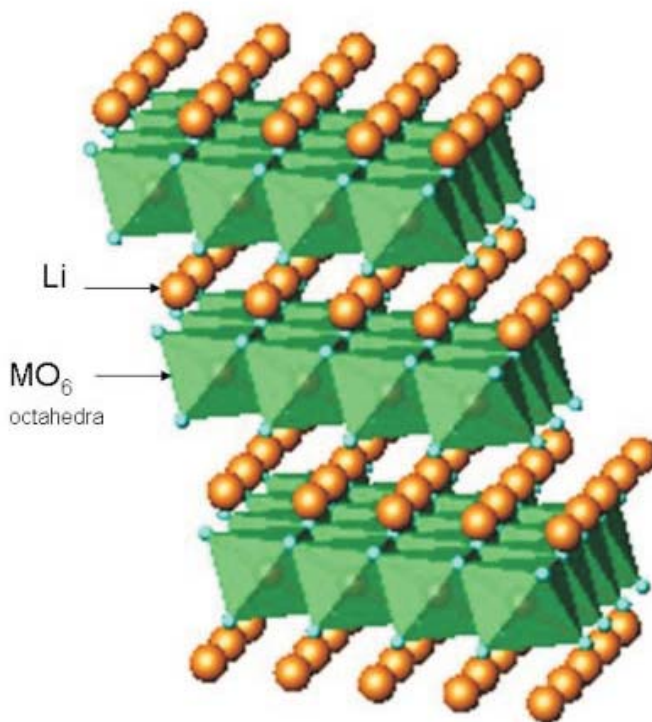


Figure 2.7: The LiMO_2 structure, where M is a transition metal ion, e.g. Co or Ni. The MO_6 octahedra layers are separated by sheets of Li. Lithium occupies octahedral sites between the oxygen atoms of neighboring cobalt oxide layers.

The first group refers to compounds with alternating anionic (e.g. lithium) and cationic (e.g. transition metal oxide layers) sheets. Lithium ions can intercalate in

2 Electrochemical aspects in transition metal oxides compounds

the remaining empty layers of the structure [38]. In this group compounds such as LiTiS_2 , LiCoO_2 , $\text{LiNi}_{1-x}\text{Co}_x\text{O}_2$ or $\text{LiNi}_x\text{Mn}_x\text{Co}_{1-2x}\text{O}_2$ can be mentioned. An example of the crystallographic structure of LiMO_2 compound is shown in Fig. 2.7. However, compounds which do not have Li in the structure can be found. These compounds can incorporate the alkaline metal ion into empty layers of their structure by electrochemical intercalation. An advantage of these materials, from the lithium battery point of view is that they can provide high energy densities (180 Wh/kg for LiCoO_2 , or 170 Wh/kg for $\text{Li}(\text{NiCoMn})\text{O}_2$).

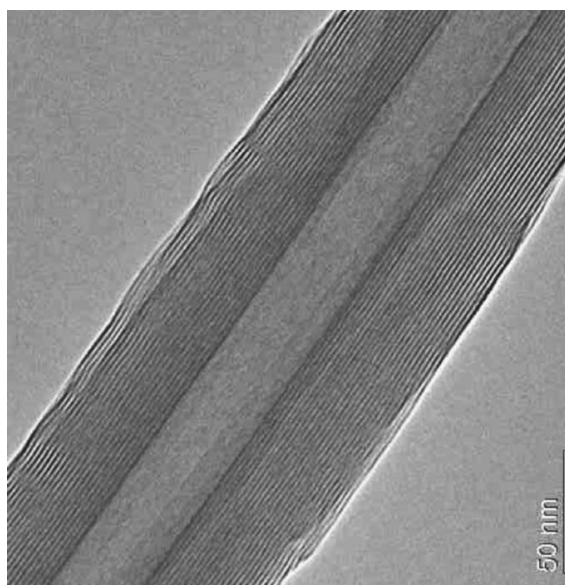


Figure 2.8: TEM picture of Vanadium Oxide Nanotubes. More details about the structure will be described in Chapter 4.

Vanadium oxide nanotubes [39], manganese oxides [19] with their tunneled structure: α -, β - and γ - MnO_2 and transition metal phosphates, e.g. nanoscaled olivine LiFePO_4 [14] can be given as examples of the group of more open structures. Within these materials the lithium-ion intercalation is easier to achieve due to their nanostructured morphologies. These offer big surface areas, small charge and ion diffusion distances and the possibility to easily change the structure volume during electrochemical treatment. In Fig. 2.8 a TEM picture of a Vanadium oxide nanostructure with its nanotube shape is shown [28]. Further details will be presented in Chapter 4 which is explicitly dedicated to this compound.

In present times, layered LiCoO_2 , LiNiO_2 and spinel LiMn_2O_4 are commonly used in rechargeable lithium batteries [25]. Removal (deintercalation) and addition (intercalation) of atoms (Li for example) can be done without strong structural changes of the host material [40].

LiCoO_2 is intensively used for commercial lithium batteries due to its high potential exceeding 3.6 V vs Li. This potential is three times higher than the working potential of alkaline systems, and thus offers high gravimetric energy densities of around 150 W·h/kg. The layered structure gives structural stability where the cation ordering is conserved after several Li intercalation/deintercalation processes [41]. Therefore, good electrochemical stability after a large number of cycles at room temperature without significant loss of efficiency is another advantage of this material.

In 1980 Goodenough and coworkers showed the reversible deintercalation of lithium in LiCoO_2 thus making it a possible cathode material [42]. The system crystallizes in the rhombohedral system $R\bar{3}m$. The structure is an ordered rock salt type with an ABCABC stacking of O and Co planes, with Li cations ordered in alternated octahedral sites of (111) planes. Co^{3+} ions occupy octahedral sites and form strong bondings with neighboring oxygen atoms producing Co-O-Co sheets. Li^+ layers are in between these CoO_2 sheets, forming a sandwich like configuration. The valency of M in LiMO_2 compounds (M=transition metal) compensates for the charge on the intercalated lithium.

In LiCoO_2 it is only possible to reversibly cycle 0.5 Li/Co before oxygen is lost from the oxide layers, or before the electrolyte is oxidized and the Li^+ ions are replaced by H^+ ions [43]. Structural changes might be influenced either by low reaction rates given by phase changes, or by poor stability when having low Li contents. It has been reported that the conductivity of Li_xCoO_2 changes with composition, behaving like metal when $x = 0.6$ and like a typical semiconductor when $x = 1.1$. The doping level $x = 1.1$ represents the typical lithium composition in commercial cells. For this doping level the conductivity changes by two orders of magnitude [44], and for $x = 1$ it changes by four orders of magnitude [40] at ambient temperatures, compared to relatively small conductivity of 10^{-3} S/cm for $x = 0$ [45].

The intercalation process in the ternary transition metal compounds LiMO_2 results in a non stoichiometric compound. This means that during the process the average oxidation state of the M ion is changed and causes changes in the electronic structure. Modification of the lattice structure influences the intercalation/deintercalation of lithium.

2 Electrochemical aspects in transition metal oxides compounds

Although Li_xCoO_2 is easily synthesized by solid state or wet chemical methods, and even though it has good electrochemical properties, the compound is highly toxic and expensive to produce due to the limited availability of cobalt. Therefore, the usage of this compound in creating small cells for computers, cell phones or cameras is limited.

The Li_xCoO_2 patent [46] did not introduce only this compound, but all layered transition-metal oxides with similar structures, where the transition metal oxide can be from vanadium to nickel. Moreover, mixtures of transition metals, e.g. $\text{LiCo}_{1-y}\text{Ni}_y\text{O}_2$ are also described.

Li_xNiO_2 is similar to Li_xCoO_2 from a structural point of view. The preparation of the first compound is a bit more difficult to achieve due to the extra nickel ion on the lithium sites. Therefore, a deviation from the normal stoichiometry is given by $\text{Li}_{1-y}\text{Ni}_{1+y}\text{O}_2$. The extra nickel reduces the Li diffusion coefficient by pinning the NiO_2 layers together [47]. As a consequence, this compound was not studied as much as Li_xCoO_2 for use it as an electrode in lithium battery technologies.

Another possible electrode material used in lithium batteries is LiMn_2O_4 developed by Bellcore laboratories [48, 49]. It has $\approx 10\%$ less capacity than Li_xCoO_2 , but it has the advantage of being less toxic and much easier to be synthesized, due to rich material sources [25]. In $\text{Li}_x\text{Mn}_2\text{O}_4$ the intercalation/deintercalation process can take place for Li values x between 0 and 2. For x between one and two, the compound has two different phases, cubic in bulk and tetragonal at the surface [26]. These examples described above were part of possible electrode material with a close-packed structure. As said before, the second group of materials used as electrodes for lithium batteries are those with more open structures, i.e. nanotubes or layered materials with particle sizes in the nm range. A large part of this thesis deals with the study of Vanadium oxide nanotubes and MnO_2 nanostructures. Therefore, details especially of these two compounds will be described in Chapter 4 for Vanadium Oxide Nanotubes and Chapter 6 for MnO_2 nanostructures.

The following will be a description of nanostructured electrode materials used for lithium batteries. The advantages and disadvantages of using nanometer size particles instead of micrometer ones will be discussed. In nanoscale materials where particles have nanosize length, the process for the intercalation/deintercalation of Li ions is a surface reaction. In these materials, during the electrochemical process, the lithium ions are not restricted in their movement within the electrode, or this restriction is much smaller than in materials with micrometer size particles.

Is it well known that rechargeable lithium batteries represent the dominant power sources for electronics due to their high energy density. These batteries can store

two to three times the energy per unit weight and volume compared to conventional rechargeable batteries [12]. Although batteries with micrometer-sized particle electrodes give a high energy density they might be low-power devices, and that means they have a slow charge/discharge rate. Lithium diffusivity in the solid state ($\approx 10^{-8} \text{ cm}^2 \text{ s}^{-1}$) limits the rate of the intercalation/deintercalation process, and implicitly the charge/discharge rate. Therefore, efforts were made to synthesize lithium intercalation hosts which would provide higher rates. Materials with small dimension represent a great help in achieving this goal.

In the following, the advantages and disadvantages of nanomaterials will be presented [12]. Possible advantages are represented by:

- possibility of new reactions that were not achieved using micrometer sized materials

Once the idea of “nano” appeared, materials which were considered electrochemically inactive were synthesized with nanosized particles that improved the electrochemical performance. One example is the nanosized transition metal oxide electrode, MO, where M can be either Co, Ni, Cu, or Fe. These materials have high recharging current rates, 700 mAh/g electrochemical capacity and 100% capacity preservation for approximately 100 charge/discharge cycles [13]. The high Li storage capacity of these materials has been explained by an interfacial storage mechanism [50, 51].

Another example is represented by the higher capacity and cycling stability for 3 nm SnO₂ particles than for the 4 or 8 nm diameter particles of the same material [52]. The Sn nanoparticles are better isolated in the LiO₂ matrix, therefore 3 nm SnO₂ particles show less aggregation of Sn particles into large clusters.

- increasing the lithium intercalation/deintercalation rate

Testing the electrochemical properties of the nanomaterials yielded better properties than compared with their bulk correspondents. The improved electrochemical properties were higher specific storage capacity, high current for charge/discharge cycles and cycle stability. These appear due to the short distances for lithium-ion transport within the particle, and due to the high contact area between the electrode and the electrolyte. When replacing micrometer size particles with nanometer size particles, the time needed for the intercalation decreases with the square of the particle size [11].

In bulk materials the Li ion diffusion coefficient is small and therefore the storage capacities are small as well, especially if high currents rates for cycling at room

2 Electrochemical aspects in transition metal oxides compounds

temperature are used. For example, TiO_2 bulk material can retain a small amount of lithium ion at room temperature [53, 54]. For nanoscaled TiO_2 with particles size of ≈ 15 nm a full loading of lithium ion in Li_xTiO_2 with $x > 1$ was observed [55, 56].

- larger electrode/electrolyte contact area

When the surface area is high, the contact between the electrolyte and the electrode is high, and therefore, a high lithium-ion flux across the interface is achieved. This improves the charge/discharge current rates. Large surface areas can reduce the specific current density of the nanomaterial. This can stabilize the nanoelectrode and conserve a high capacity at high charging/discharging current densities [57]. For example, CoO could have 85% of its total capacity at C/2 rates. C/2 represents the current needed to charge or discharge one lithium in two hours [13].

- short path lengths

Nanoelectrodes can provide short path lengths for both lithium and electron transport. Commercial batteries use micrometer size electrodes with high surface area. This is not practical for lithium ion diffusion, and for high charge/discharge rates because of the long path for lithium ion transport and low contact area between the electrode and the electrolyte [58]. Therefore, using nanoelectrodes high power and high energy density can be obtained, by providing short path length for Li and electron transport.

In order to obtain a short path length for electron transport, efforts were made to synthesis active electrode materials, such as V_2O_5 [59], TiO_2 [60] or MnO_2 [61] directly on acetylene carbon black. Carbon black is usually mixed with the electrode material in order to obtain better conductivity, and hence, as a result, higher rate performances.

- stable cycle performance

Besides the advantages presented before, nanoelectrodes also have good cycle stability [55, 57]. Expanding or contracting the volume structure during cycling, together with lithium insertion/extraction or lithium alloying/de-alloying decreases battery capacity. For example, Si is not suitable for lithium batteries despite having a big theoretical capacity of ≈ 4200 mAh/g due to the drastic volume change during cycling in $\text{Li}_{4.4}\text{Si}$ [62]. Nanoelectrodes can solve this problem by maintaining the electrode integrity during cycling, and thus obtaining a stable cycle performance.

Besides the advantages of using nanoelectrodes, these materials present disadvantages as well, when using them as electrode materials in lithium batteries.

- Synthesis of these nano sized materials can be more complicated than that of the bulk materials. The nano size is not easily controllable during preparation.
- The advantage mentioned earlier of high electrolyte/electrode surface area in the nanoelectrodes has the disadvantage of giving more possibility to have side reactions with the electrolyte, thus the internal particle contact is more difficult to achieve.
- Nanopowders have less density than the same material in micrometer size, and the volumetric energy density decreases.

As a conclusion of this subsection it should be stated that, synthesizing and studying nanometer size materials represents a big hope in improving lithium battery technology although present batteries are mostly working with micrometer sized electrode materials. The next generation of lithium batteries will probably have higher energy and higher power than the current batteries due to functionality based on nanostructured materials as electrodes and electrolytes.

2.3 Effects of electrochemical treatment on physical properties

This thesis focuses on the idea of studying magnetic properties of electrochemically doped transition metal oxides. Nanostructured vanadium oxides and manganese oxides, as well as other layered compounds were studied after lithium insertion using electrochemical methods.

The goal using electrochemistry as a technique to synthesize materials was to obtain materials with transition metal ions in high or mixed oxidation states, which were not easy to prepare using conventional solid state chemistry. The physical properties of transition metal oxides depends on the relation between the electronic, magnetic and orbital degrees of freedom of the electrons coming from the transition metal ion. Therefore, the electronic configuration of the d shell gives the metallic, superconducting or insulating character of the system. The interplay of local magnetic moments and charge carriers plays an important role in the variety of properties that systems with transition metal ions can present. In this way, it is very important to control the charge carrier concentration by powering the oxidation state of the transition metal ion. By applying an electrical voltage as it was described in section 2.1, Li can be inserted or extracted resulting in a decreased or increased valency of

2 Electrochemical aspects in transition metal oxides compounds

the transition metal ion from the system under study. Using this technique we can synthesize mixed valency compounds, a non-integer valency value for the transition metal ion, or a high valency.

Modifying the oxidation state by electrochemical doping gives the possibility to investigate phase diagrams of already chemically doped compounds. Compounds with unusual oxidation states or structural conditions, which were not chemically obtained can be investigated as well.

To underline the importance of using this technique an overview of compounds which were synthesized by electrochemistry for the first time and showed interesting physical properties is given below. Different properties that a compound may exhibit once Li is inserted or extracted from the structure will be also presented.

For example, in the case of LiVP_2O_7 , V^{3+} can be oxidized in V^{4+} by electrochemical extraction of lithium at 4.2 V versus Li^+/Li . The compound is part of the AMP_2O_7 family with A being a monovalent cation and M a transition metal [63]. The compound has high ionic conductivity which made it an possible positive electrode in lithium batteries [64].

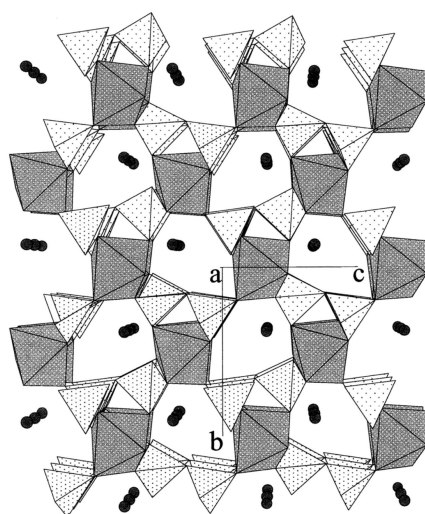


Figure 2.9: The LiVP_2O_7 structure. The $[\text{P}_2\text{O}_7]$ groups are shown in white, the VO_6 octahedra in gray and the lithium is drawn in black [5].

LiVP_2O_7 is isostructural to LiFeP_2O_7 [65] and both materials crystallize in the $\text{P}2_1$ group [66]. In Fig. 2.9 the crystal structure of LiVP_2O_7 , formed by $[\text{P}_2\text{O}_7]$ groups and VO_6 octahedra is presented. The $[\text{P}_2\text{O}_7]$ groups and the VO_6 octahedra define tunnels (see Fig. 2.10) from/into which Li can be reversibly extracted/reinserted.

One electron can be electrochemically extracted from LiVP_2O_7 by a two-phase process. At the end of the oxidation, Li is completely extracted and the resulting

compound VP_2O_7 has a different structure than the starting compound, upon Li deintercalation [5]. The structure is similar to the starting compound but with small differences due to the oxidation of vanadium from V^{3+} to V^{4+} and absence of lithium from the structure. In this structure each VO_6 octahedra is connected with five $[\text{P}_2\text{O}_7]$ groups.

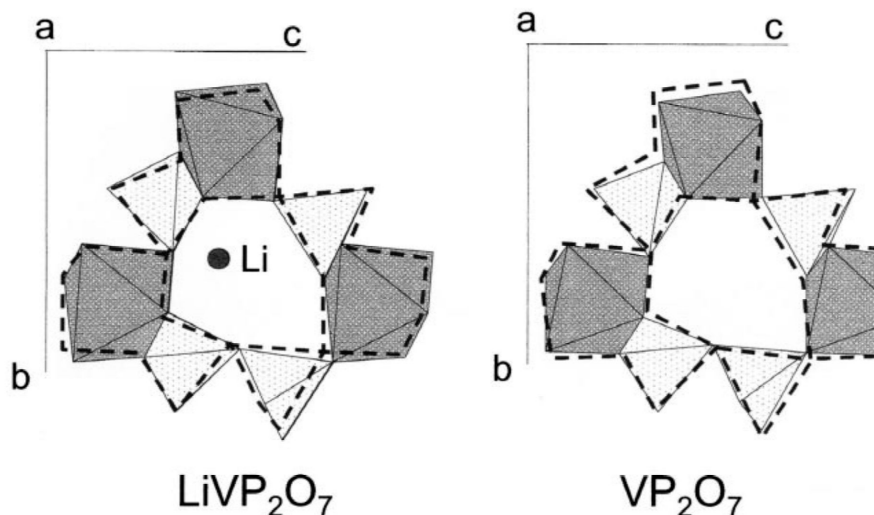


Figure 2.10: Tunnels in LiVP_2O_7 and VP_2O_7 . In both figures the dashed lines represent the tunnel shape of the other structure in order to observe the structure distortion [5].

The lithium ions are small. In the case of LiVP_2O_7 is located at the tunnel borders with an asymmetrical coordination of 6 oxygen atoms. After lithium removal these tunnels are enlarged due to electrostatic repulsion between neighboring oxygen atoms as can be seen from Fig. 2.10. This together with the vanadium oxidation (which shortens the V-O distances) explains the distorted cell of VP_2O_7 compared to that from the starting compound LiVP_2O_7 .

In this way, a new transition metal oxide, the vanadium diphosphate was electrochemically obtained after oxidation of LiVP_2O_7 . The insertion/deinsertion is reversible. After the oxidation of LiVP_2O_7 the new VP_2O_7 is obtained and after recharging, with lithium reinsertion, the initial compound is re obtained.

The LiCoO_2 system was introduced earlier in section 2.2. Changes in the initial compound result in configurational Li-vacancy interactions, variations of the number of electrons or changes in the stability of the oxygen packing [6].

Upon Li removal through different mechanisms phase transitions are created in layered LiCoO_2 . At the beginning Li it is arbitrarily removed and the remaining Li can experience an ordering transition, if enough vacancies are formed. This kind

2 Electrochemical aspects in transition metal oxides compounds

of ordering transition, also called configurational transition, was observed in other intercalation compounds such as Li_xNiO_2 [7], Li_xTiS_2 [8] or $\text{Li}_x\text{Mn}_2\text{O}_4$ [9].

In Li_xCoO_2 (as well as in other compounds), Li is ionized to Li^+ and most of its electron valence is transferred to the O-Co host. Therefore, removing Li electrochemically from the host material led to phase transitions through the formation of electronic holes. LiCoO_2 is insulating or semi-conducting, and becomes metallic when Li is removed. The host material is modified by supporting the crystal field splitting of one cation coordination over another resulting in a change of the band filling. When Li is totally removed, LiCoO_2 changes from the ionic CdCl_2 stacking to a covalent Co-O arrangement [67].

It has been shown in [68] and [69] that the metallic behavior obtained after the first Li extraction does not completely vanish upon Li insertion back into the system. Here it was observed that Li-rich phases have a semiconductor behavior and the more deintercalated phases are metallic.

In Li_xCoO_2 with $0.9 \leq x \leq 1$ the electronic conductivity increases with Li deintercalation [70]. In Fig. 2.11 the variation of the logarithm of the electrical conductivity versus the reciprocal temperature of Li_xCoO_2 with $0.55 \leq x \leq 1$ is shown [71]. For $0.94 \leq x \leq 1$ the electronic conductivity is thermally activated. This activation energy decreases with Li deintercalation, and it varies with temperature. For $0.5 \leq x \leq 0.74$ the plots are almost flat indicating metallic or pseudometallic behavior. For $x = 0.55$ and $x = 0.70$ true metallic behavior is found between 175 K and 300 K.

Ménétrier et al. have presented ^7Li NMR studies on Li_xCoO_2 with $0.94 \leq x \leq 1$, and they suggest the existence of Co^{4+} ions in the Co^{3+} configuration of the starting material. Electronic properties and ^7Li NMR studies show a localized character of Co^{4+} ions down to $x = 0.94$ upon Li deintercalation. At this x value a second phase with delocalized-electron type behavior appears. The NMR investigation shows a drastic change in the electronic interactions of Li depicted by a loss of observability of Li^+ surrounding localized Co^{4+} and by shifting of the Knight shift for Li in the metallic phase compound.

Further examples of advantages given by the synthesis using electrochemical methods include systems containing some other alkali metal ion than Li, for example $\text{Na}_x\text{CoO}_2 \cdot y\text{H}_2\text{O}$. The structure contains CoO_2 layers which are separated by a thick insulating layer of Na^+ ions and water molecules. It is very interesting to be able to control the Na content. Theoretically, for $x = 0$ the compound is a Mott insulator on a triangular lattice with $S = 1/2$. The compound having $x = 0.3$ and $y = 1.3$

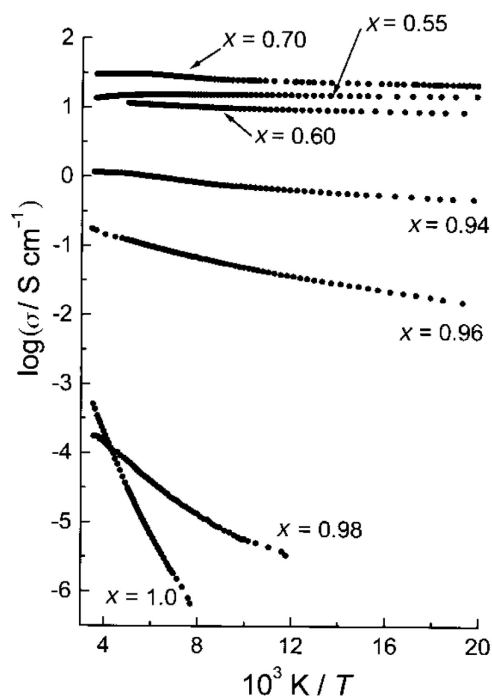


Figure 2.11: Electrical conductivity versus reciprocal temperature for Li_xCoO_2 with $0.55 \leq x \leq 1$, on a logarithmic representation [71].

has been discovered to show superconductivity with a T_C of 5 K [10]. After the high- T_C cuprates this is the second superconducting material obtained from doping a Mott insulator.

Chou et al. [72] succeeded in electrochemically synthesizing $\text{Na}_{0.3}\text{CoO}_2 \cdot 1.3\text{H}_2\text{O}$ by extracting Na from single crystals Na_xCoO_2 . The single crystals were initially grown using the floating-zone technique. The susceptibility data recorded on this compound show a superconducting transition around 4 K and together with specific heat measurements, the data show that the system may be viewed as a Fermi liquid with strong mass enhancement due to correlations. The resistivity measurements show that the sample is a good metal with large anisotropy between the resistivity measured in c direction and the one measured in ab direction.

Here, electrochemistry joined the floating-zone technique to produce high quality single crystal of the hydrated $\text{Na}_x\text{CoO}_2 \cdot y\text{H}_2\text{O}$ which show superconductivity below 4 K, previously obtained only by chemical deintercalation methods [10].

In the end, it is important to consider that spin and charge degrees of freedom or the orbital degree of freedom can play a very important role in the physics of doped transition metal oxides. Systems with frustrated orbital lattices are good candidates for materials with unusual quantum effects, very interesting for both basic research as well as for possible applications.

2.4 Conclusion

Basics of an electrochemical cell, as well as the role of its three main components (anode, cathode, electrolyte) have been described in this chapter. The discharging and charging process in a electrochemical cell used for lithium batteries have been described. Details about materials already in use for lithium battery, like Li_xCoO_2 were given in this chapter. The importance of downscaling the size of the electrode material possibly used in lithium battery has been described by advantages and disadvantages of this process. Among advantages given by nanosized material, increasing of Li intercalation/deintercalation rate due to shorter diffusion distances or larger electrode/electrolyte contact area improving the charge/discharge rates can be mentioned.

Electrochemistry is a novel technique, a powerful tool which yields the possibility to vary the oxidation state of transition metal ions and therefore inducing structural deformations which change the electronic properties as it has been shown in examples earlier in this chapter. Of course, all these changes might influence the cation's insertion/extraction processes. By studying physical properties of materials doped with the help of electrochemistry it may result a better understanding of the processes of cation exchange in very deep detail. This would improve the functionality of alkali-ion batteries.

3 Experimental methods and techniques

In this chapter, both the electrochemical and magnetic methods used in this thesis will be introduced. With the help of electrochemistry, doped materials were synthesized which afterwards have been studied using magnetic methods in order to investigate potential changes of their magnetic properties. The setup used for electrochemical testing will be introduced as well.

3.1 Electrochemical synthesis and methods

To begin with, a description of the electrochemical setup used and the methods applied to the materials studied in this work will follow. For an initial characterization of the compound behavior, Cyclic Voltammetry (CV) was performed. Afterwards, in order to obtain the lithium doped compound, galvanostatic or potentiostatic techniques were employed. In most of the cases, the materials were mixed with Carbon Black (supplied by Timcal Ltd, Bodio, Switzerland), an amorphous carbon which improves the electronic conductivity, therefore improving the electrochemical performances of the materials.

3.1.1 Electrochemical setup

Before describing the methods, the setup used in the electrochemical experiments will be introduced. For all the experiments, the materials were placed in a two-electrode Swagelok type cell consisting of commercially available parts, as shown in Fig. 3.1.

Mounting of the cell was always done in an argon-filled dry box. In electrochemical experiments, lithium metal was used as the negative electrode, and the studied material as the positive one. The electrolyte, provided by Ferro Corporation (Ohio,

3 Experimental methods and techniques

USA) was one molar (1M) solution of LiFP_6 salt (Lithium Hexafluorophosphate) in an ethylene carbonate (EC)/ dimethyl carbonate (DMC) mixture 1:1 in weight. In order to avoid short circuits between the two electrodes of the cell, they were separated by a porous and insulating material. In this case, the separator is represented by two sheets of Whatman GF/D borosilicate glass fiber, soaked in electrolyte in order to maintain good ionic conductivity.

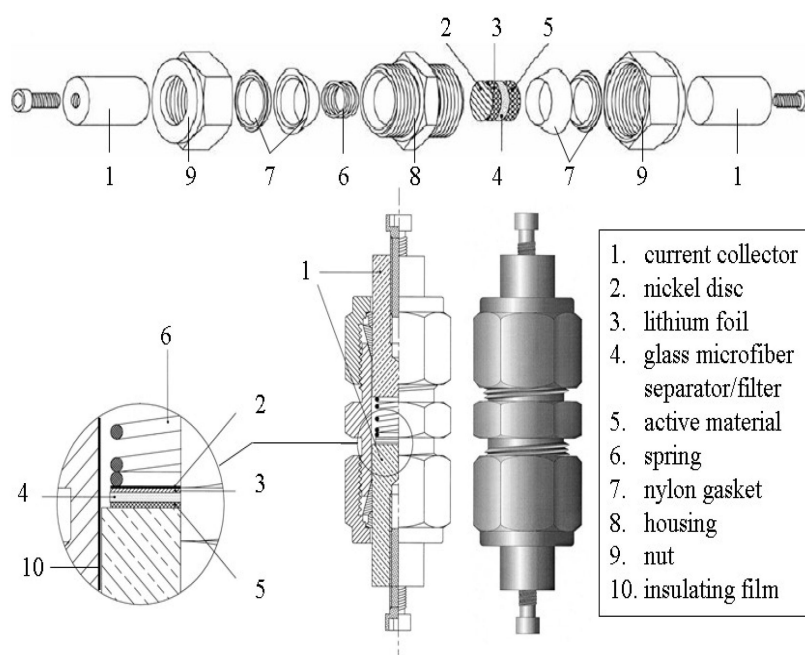


Figure 3.1: Sketches of the Swagelok-type cell used for electrochemical testings. Adapted from [73].

Two sizes of Swagelok cell were available for the experiments. A small one with approximately 1 cm diameter was used for general testing and synthesis of material in quantities of about 30 mg. For larger amounts of powder (400 mg), the second cell with a diameter of approximately 2 cm was used.

Generally speaking, in a three electrode electrochemical experiment, when the goal is to observe, measure, or control the potential of an electrode (working electrode-WE) it is necessary to use a reference electrode (RE). This electrode maintains a potential that remains practically unchanged during the course of the experiment. The potential of the WE is measured or/and expressed relative to the RE. The RE has an invariant, well known electrode potential and a very high inner resistance so that no significant current passes through this electrode. The third electrode required for electrochemical experiments, is the counter electrode (CE). It is the one

that represents the source of electrons that will be exchanged in the electrochemical process.

It was mentioned earlier that the cell used for this work is a two-electrode cell. In the discharge mode the two electrodes are used as follows: the negative one is represented by the lithium metal (the counter electrode) and the positive electrode is represented by the active material (the working electrode). In this work, the RE is not used, because the main focus is on electrochemical synthesis and therefore, the exact reproduction of the positive electrode is not necessary. This is a common practice in studies of electrode materials for lithium ion batteries, see e.g. Ref. [13, 14, 25]. Once the cell is mounted, the next step is to connect it to a potentiostat. The potentiostat is attached to a computer, for controlling the experiments, data acquisition, and evaluation of the results. A schematic view of how the potentiostat and the cell are connected is presented in Fig. 3.2.

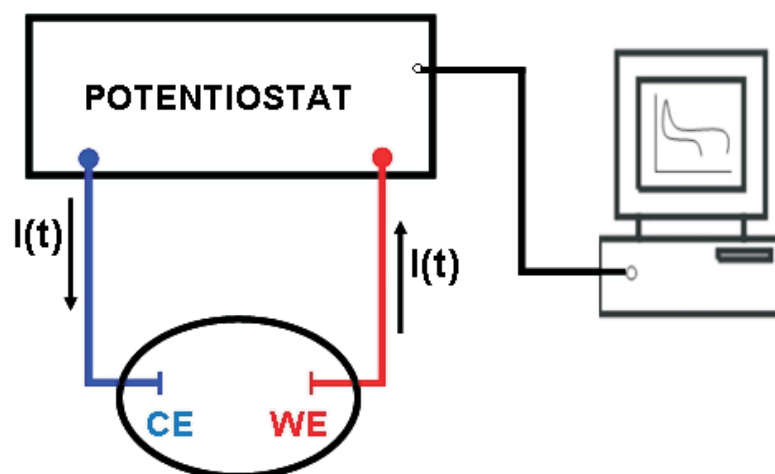


Figure 3.2: Setup of the electrochemical experiment (**CE**: Counter Electrode, **WE**: Working Electrode).

A potentiostat is a power supply containing both a voltmeter and an amperometer. It controls the voltage over a wide range of currents, as well as controlling the current over a wide range of potentials. In other words, a potentiostat is a controlling and measuring device. When a three electrode cell is connected to the potentiostat, the device keeps the WE at a constant potential with respect to the RE. The potentiostat contains an electric circuit that controls the voltage across the cell. This is done by passing a current through a resistor to the CE using a current follower (operational amplifier) [74].

The potentiostat controls the potential difference between the WE and RE by passing a current between WE and CE.

3 Experimental methods and techniques

In this work, a VMP multichannel controller with separate potentiostatic and galvanostatic channels delivered by Princeton Applied Research (Illingen, Germany) was used. For this potentiostat the current can be varied from 1 nA up to 400 nA with 760 pA resolution, it has a programmable voltage resolution varying from $300\mu V$ to $5\mu V$ and a $20\mu s$ acquisition time. This makes this potentiostat a very powerful tool for electrochemical experiments. The cell used in these experiments is a two electrode cell in which the RE is connected to the WE.

3.1.2 Electrochemical techniques

In this section the methods used for electrochemical testings and synthesizing will be introduced. It was previously mentioned that these methods are represented by galvanostatic methods i.e. the Galvanostatic Intermittent Titration Technique (GITT) [76] as well as potentiostatic methods, i.e. the Cyclic voltammetry (CV) and the Potentiostatic Intermittent Titration Technique (PITT) [76]. For the galvanostatic methods the current is controlled and then potential is monitored. In the potentiostatic case the voltage is adjusted and the current response is measured.

When studying possible electrode materials the relation between the voltage and the Li composition plays a crucial role by giving information about the equilibrium phase diagram of the compound. When looking at a diagram where the voltage is plotted versus the Li composition in the material, one can learn about mono-phase or two-phase domains. If the dependence of the voltage versus the composition is continuous, a solid-solution single phase domain exists. If the dependence presents a plateau then this indicates a two-phase domain [77]. For an easier view of these information that can be derived from a galvanostatic measurement, Fig. 3.3 is presented. The dashed lines highlight the region where the biphasic domain exists due to the plateau in the voltage versus composition dependence plot. The rest of the graph, with continuous dependence of the voltage as a function of the composition, represents mono-phasic domains.

Information regarding electrochemical stability, kinetics and reversible or irreversible reactions as well as thermodynamic parameters which can determine the nature of a discharged cathode are also important, when the appropriateness of a compound as electrode material is analysed [79].

In order to determine the relation/dependence of the voltage and lithium composition one can either use techniques which control the current, or those controlling the voltage in an electrochemical cell i.e. GITT or PITT, respectively. GITT is more

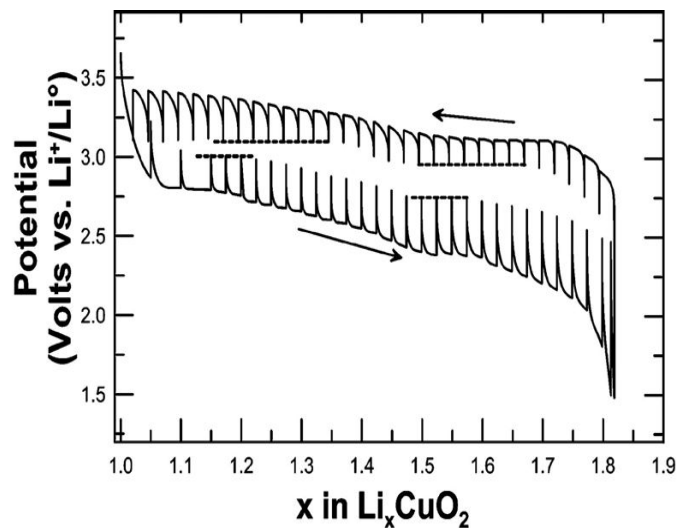


Figure 3.3: GITT experiment: representation of monophasic and biphasic domains. The biphasic domains are indicated by the dashed lines. In the rest of the representation, a continuous dependence of the voltage as a function of the composition is an indication of the mono-phasic regions. The arrows indicate whether the compound is discharged (\rightarrow), or charged (\leftarrow) [78].

frequently used for studying the behavior of the compound over a large number of cycles, so it requires more time to be performed. PITT is mainly used for basic studies of the intercalation processes taking place in a possible electrode material.

Galvanostatic Intermittent Titration Technique

During a GITT experiment, using the galvanostatic mode of the electrochemical interface, a constant current can be applied for a given time, and successive charge increments can therefore be performed. The current is applied stepwise, and in between the steps when the current is equal to zero the system is in open circuit mode in order to determine the corresponding equilibrium potential for each current step. This equilibrium potential can be reached very slowly or not at all in the time chosen for the experiment, therefore this may be designated as a quasi-equilibrium potential. Information about this parameter can be drawn in most of the cases anyway, but they can be uncertain [78].

By applying this galvanostatic technique, the evolution of the voltage over time or over the lithium composition can be obtained. This kind of plot can yield information on whether single phase domain or a two phase domain of the intercalation process is present during charging or discharging of a compound. This is shown in Fig. 3.4.

3 Experimental methods and techniques

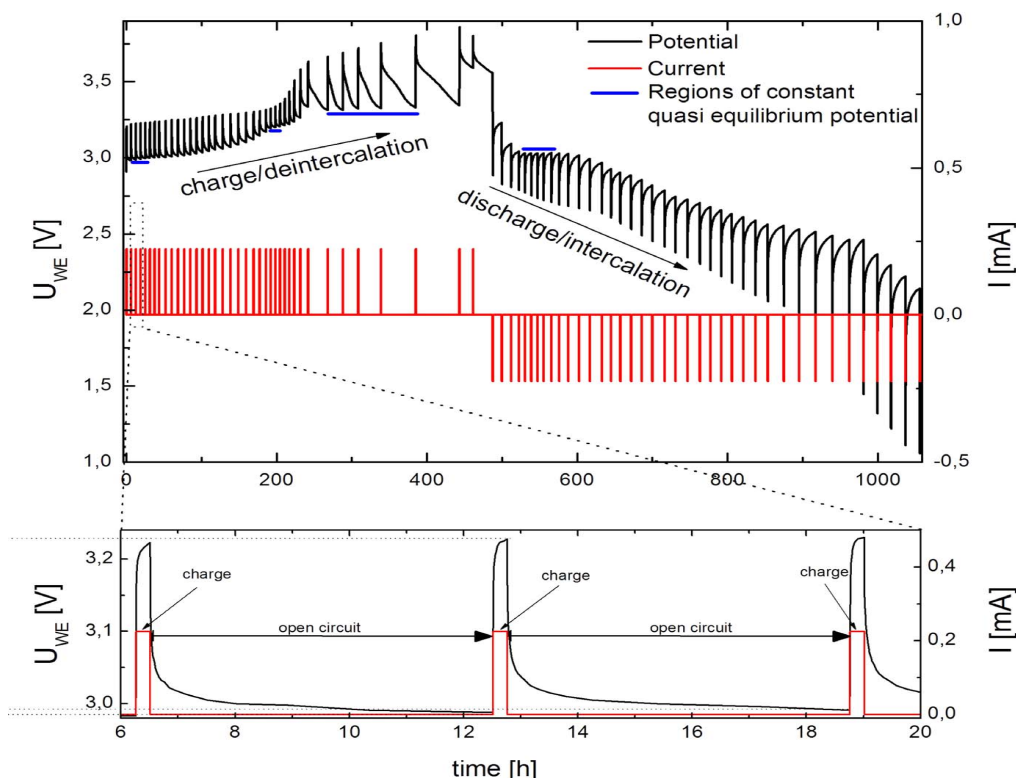


Figure 3.4: Typical GITT experiment on Li_2CuO_2 : in the upper part of the graph the evolution of the voltage from the WE and the *a priori* established current (here $I=0.2$ mA) versus time is represented. In the lower part of the graph a closer representation of the stepwise applied current and the voltage evolution after the current is turned to zero is shown. From Ref. [80].

Galvanostatic techniques are mostly used for studying the behavior of a possible electrode material upon a large number of cycles (repetitive charging/discharging). This is done using a cycle rate established prior to the experiment within a voltage range. The cycling rate is usually expressed as C/t where t is time, in hours, in which one lithium per formula unit can be extracted/inserted from/into the material

GITT is intensively used for determination of the differential(incremental) intercalation capacitance and the chemical diffusion coefficient of lithium ions in various materials [81–86]. In literature, it was found that GITT does a better job of eliminating the parasitic contributions of the background currents to the total measured response than PITT [87].

Potentiostatic Intermittent Titration Technique

During a PITT experiment, a voltage equal to the initial equilibrium voltage of the cell is applied using a potentiostat. The voltage is applied stepwise and changed

by a fixed amount to a value (higher or lower) close to the initial voltage. In this time the current I is registered for a given time, or until it reaches a I_{min} . When $I=I_{min}$ then the voltage is stepped again, and this continues until a V_{min} or a V_{max} is reached. After this limit is reached the direction of the process is reversed. A representation of this kind of process is illustrated in Fig. 3.5.

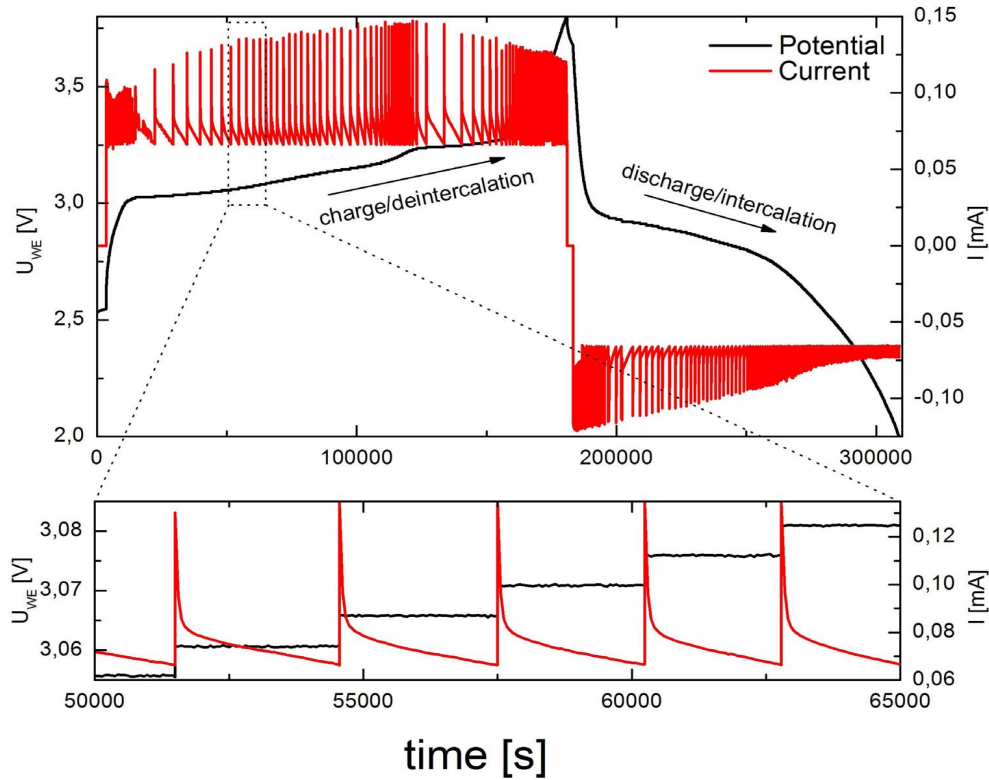


Figure 3.5: Typical PITT experiment on Li_2CuO_2 : the relation between the WE voltage versus time is plotted. The voltage was increased by 5 mV increments each time the current was dropped below $C/50$. From Ref. [80].

The result of this experiment is a voltage cycle between V_{min} and V_{max} . The time needed for this kind of experiment is much less than that needed for GITT experiments. At each voltage step the current I has a larger value. At the end of the step $I=I_{min}$ which is usually fixed to 1/100 of its initial value [79]. Under these conditions a full cycle needs $\approx 1/10$ of the time needed to perform a full cycle in galvanostatic conditions. In the case of PITT a full cycle experiment is performed in order to test the cell reversibility, to verify hysteresis and irreversible contributions to the total charge exchanged during the process [79].

Information related to the differential capacity can be obtained when performing this kind of experiments. The curve in Fig. 3.6 was obtained from direct current data of a potentiostatic experiment, by differentiating the discharge/charge curve formed

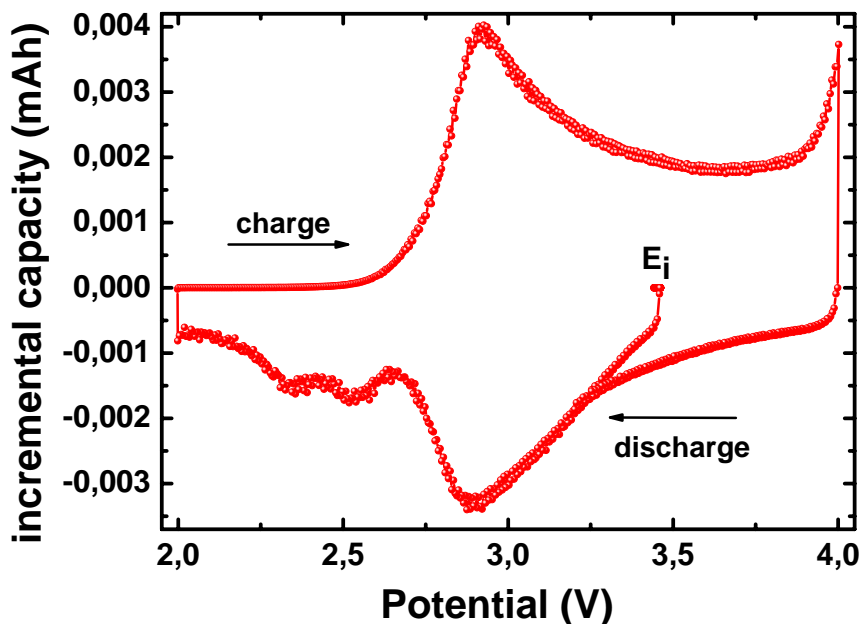


Figure 3.6: The incremental capacity from a potentiostatic experiment. The voltage values at which the capacity has maximum values can be seen. Each of these maximum values is a trace of a reaction in the cell/active material at the potential at which the maximum is measured. E_i represents the starting potential.

by the relation between the voltage V versus charge Q . Nevertheless, the same kind of interpretation can be extracted from galvanostatic experiments as well, but the time needed in this case is again much longer. From this last kind of experiment one can not gain precise resolution of the derivative curve, as one can obtain using potentiostatic experiments. PITT is favorable when small diffusivity values in electrodes or electrolyte are expected [88]. Apart from kinetic or thermodynamic information that can be extracted from an electrode material using these galvanostatic and/or potentiostatic techniques, they can be used as synthesizing methods as well. This is mainly how these techniques were used in this work. When used for this purpose the charge or discharge cycle or a sequence of charges or discharges can be stopped when the desired composition of the active material is reached [7, 67, 70, 71].

Cyclic Voltammetry

The third technique that is used for studying the behavior of possible electrode materials is the Cyclic Voltammetry. This technique is a potentiodynamic method where the potential of the WE is controlled using a triangular waveform.

A CV experiment scans the WE potential linearly using a triangular potential waveform. During the time the voltage is swept, the potentiostat measures the resulting current developed from the redox reactions taking place in the system. The voltage is scanned between two opposite limits. By scanning the potential between these limits, reproducible I-V curves are obtained. This reproducibility depends on various parameters such as electrolyte purity, identity of the electrode material, choice of the two limiting voltages and the rate chosen for changing the voltage (the scan rate).

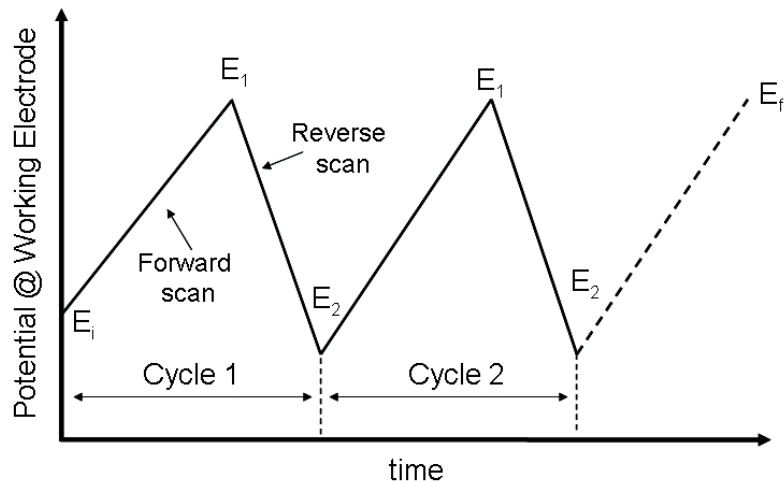


Figure 3.7: Sketch of a Cyclic Voltammogram experiment.

Fig. 3.7 shows the potential versus time in a CV experiment. E_i is the initial voltage of the cell which during the experiment is swept between the two opposite limits E_1 and E_2 using a fixed rate. After the first cycle, once the E_2 limit is reached, the voltage scan is reversed and the voltage is swept back to E_1 . This can go further for as many cycles as desired for testing the electrochemical behavior of the system.

A CV curve is shown in Fig. 3.8. At the beginning of the experiment there is no current flowing through the system. Once the system is swept with the scan rate ν a current starts to flow and reaches a peak at a specific voltage for a specific redox reaction and electron transfer takes place. Afterwards, the current drops to zero if no other reaction takes place.

During the first half cycle (forward scan) when going from E_i to E_1 some species are oxidized/reduced and in the second part of the cycle (reversed scan) the same species are reduced/oxidized depending on the state the system had at the beginning of the cycle (oxidized or reduced). The oxidation/reduction peaks in a CV are caused by the diffusion layer formed near to the electrode surface. If one considers that at the initial state of one system is oxidized, then one can say that the systems has only

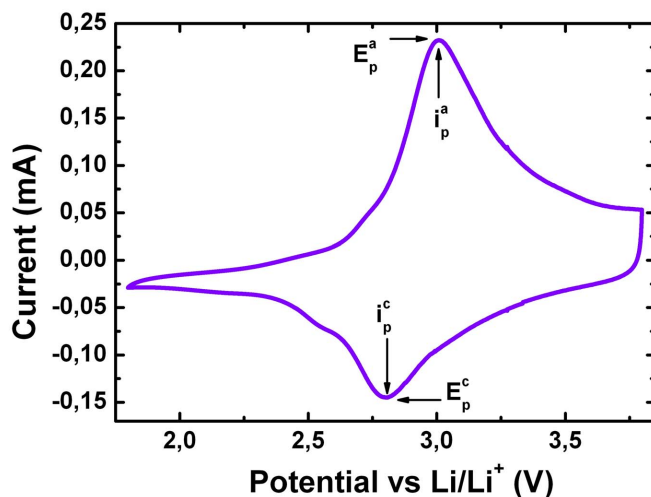


Figure 3.8: I-V curve obtained from a CV experiment: E_p^a represents the voltage where the anodic peak current i_p^a is found; E_p^c represents the voltage where the cathodic peak current i_p^c is found.

oxidized species O . These O species will be reduced during a cyclic voltammogram to the reduced species R . Once a potential is applied, the surface concentration of O decreases toward zero and a concentration gradient is established near the surface. This region where the oxidized species concentration decreases is known as the diffusion layer, with a thickness δ . In the beginning, the concentration gradient is steep, therefore δ is small. This thickness increases with time and the concentration gradient decreases. Here it should be mentioned that the current that flows in this kind of experiment is proportional with the square root of time needed for the experiment to run (Cottrell equation [89]).

In experiments where the potential is being swept, such as in the case of CV experiments, the current peaks show the continuous change of concentration gradient with time, therefore, the increase in the peak current in such experiment corresponds to diffusion control achievement. The current drop, beyond the peak, has a $t^{-1/2}$ dependence and it is independent of the applied potential. That is the reason why the reversal current has the same shape as the forward one.

CV is the most widely used technique for obtaining information about electrochemical reactions that take place on an electrode material when it is cycled. It is a fast technique, and it can provide information about thermodynamics and redox reactions as well as the kinetics of processes.

In order to inspect the reversibility of a system there are a few things that can be checked using the results of a Cyclic Voltammogram. A significant parameter is that the current must be directly proportional to the concentration (in mol/cm³), and it should increase with the square root of the scan rate (Randles-Sevcik equation [90]). In this case, the kinetics of the reaction is controlled by the diffusion of species from the bulk solution to the electrode surface. Then, the reverse-to-forward peak current ratio i_p^a/i_p^c is equal to 1 in the case of a reversible process. This ratio can be strongly affected by chemical reactions coupled to the redox process. The formal potential of the redox process (the standard electrode potential) for a reversible couple is centered between E_p^a and E_p^c :

$$E^\circ = \frac{E_p^a + E_p^c}{2}$$

For a reversible couple the separation between the peak potentials is represented by:

$$\Delta E_p = E_p^a - E_p^c = \frac{59}{n} \text{ mV}$$

where n is the number of electrons, and 59 mV represent the so called Nernstian slope, equal to the change of the equilibrium electrode potential when the concentration of the species involved in the electrode reaction changes by a factor of ten.

For multi electron transfer in reversible processes, a CV has different distinct peaks if E° is successively higher and well separated for each electron transfer. For irreversible processes, where electron exchange is slow, the peaks are reduced in size and widely separated. Irreversible systems are characterized by a shift of the peak potential E_p as a function of the scan rate. The peak potential E_p and the half peak potential $E_{p/2}$ differ by $48\alpha n$ mV where α is the transfer coefficient. The voltammogram is more drawn-out as αn decreases[90]. The peak current in irreversible processes is lower in height than in reversible systems.

Cyclic voltammetry is very important for obtaining information about chemical reactions that might interfere before or after a redox process [91]. The appearance of a chemical reaction affects the surface concentration of the electroactive species. Therefore, due to the mixture between the chemical reactions and redox processes, changes in the shape or peak positions in a CV are found. If the redox process is followed by a chemical reaction and if the chemical reaction is very fast, the reduced species are converted in the chemical reaction and no reverse peak will be seen in

the CV. For slow chemical reactions preceding the electron transfer, the ratio i_p^a/i_p^c is larger than unity. This ratio is closer to 1 with decreasing the scan rate values. The reverse peak is not affected by the coupled reaction, but the forward one is not proportional to the square root of the scan rate.

Although not the main aim of this work, all three techniques (GITT, PITT and CV) can be nicely used together in order to obtain basic and very detailed information about processes that take place in potential electrode materials. They help obtaining information about the kinetics and thermodynamics of active materials for possible application in lithium ion batteries. In this work, CV was used to characterize the electrochemical behavior of different materials that might be applied as cathodes in lithium batteries. GITT and PITT were used as synthesis methods in order to obtain compounds with different levels of lithium doping. For some of the compounds this doping may have been obtained with other methods than electrochemical ones (i.e. chemical reactions), but for others the synthesis with electrochemical methods is new and has advantages as described in section 2.3.

3.2 Magnetization measurements

After studying the electrochemical behavior of possible electrode materials, electrochemical techniques for synthesizing intermediate lithium doped compounds were used. After these compounds were obtained the goal was to study differences in the physical properties, magnetic properties in this case, of materials with different amounts of intercalated lithium. The interest was in the static susceptibility as a function of temperature and variations in magnetization obtained by changing the applied magnetic field.

In order to study the magnetic properties of both undoped and doped compounds, a Magnetic Properties Measurement System (MPMS) by Quantum Design (Darmstadt, Germany) based on a SQUID (Superconducting Quantum Interference Device) was used. The temperature dependence of the magnetization when applying different magnetic fields (2 Oe-50 kOe) were measured between 2 K and 350 K. The field dependence of the magnetization for different temperature ranging from 2 K to 300 K was studied as well. For some samples the magnetic response after applying a very small magnetic field (2 – 20 Oe) was studied. For this purpose the MPMS has a “low field” option that gives the possibility of minimizing the remnant field in the SQUID and therefore a more precise value of the applied magnetic field is obtained.

In Chapter 4 of this work, investigations of the influence of Li-doping on the local magnetic properties of the samples were done by using nuclear magnetic and electron

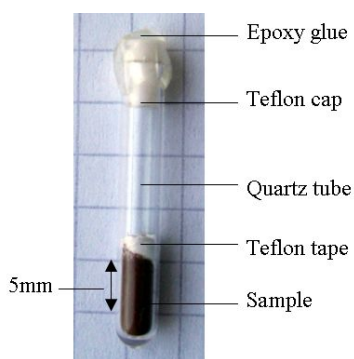


Figure 3.9: Sealed quartz tube used for magnetic measurements.

spin resonance experiments (NMR and ESR). NMR measurements were performed by E. Vavilova, Zavoisky Physical-Technical Institute of RAS, Kazan, Russia. The data were recorded in IFW-Dresden, on a Tecmag pulse solid-state NMR spectrometer in a temperature range 4.2 K to 300 K. The NMR spectra were acquired by a point-by-point magnetic field sweeping. Dynamic magnetic properties of powder samples were studied by Y. Arango, IFW-Dresden, using a conventional X-band ESR spectrometer ($f = 9.5$ GHz) in a field range of 0 – 9 000 G. Zero field (ZF) Muon Spin Relaxation (μ^+ SR) measurements were performed by H-H. Klauss and coworkers in Paul Scherrer Institut in Villingen, Switzerland.

All the samples characterized with all three techniques mentioned above were kept and measured in an airtight sealed quartz tube to avoid exposure to humidity. The sample holder and the quartz tube is shown in Fig. 3.9. Preparing and mounting the samples was always performed in an Argon atmosphere inside of an Argon box.

This page intentionally contains only this sentence.

4 Electrochemically doped Vanadium Oxide Nanotubes

4.1 Oxide nanostructures

Among nanostructured materials those with tubular morphology are of large interest due to size-induced properties and complex nanoscale architecture. The use of nanoparticles represents a big advantage when is envisaged about downscaling conventional technology by at least one order of magnitude. Vanadium oxide can be found in many forms and can have many and very different chemical or physical properties, depending on the oxidation state of the vanadium ions. A short review of the synthesis methods and corresponding morphologies of the VO_x-NT is presented in the beginning of this chapter. VO_x can be synthesized in a nanotubular shape if organic spacer molecules which help the VO_x layers to retain the nanotube shape, are used. These spacer molecules play a very important role in the nanotube properties as it will be shown later on. The VO_x-NT structure is similar to that of BaV₇O₁₆nH₂O with $n = 4.4$, as it was also proved by work of Liu et al. [28]. Taking the advantage of electrochemical methods, low-spin vanadium oxide have been doped with lithium. The electrochemical properties of different vanadium batches will be described in this chapter. Differences between the electrochemical behavior of several batches will be discussed. The discharge specific capacity evolution of VO_x-NT over cycling will be investigated. Different concentration of lithium in Li_{*x*}VO_x-NT have been achieved using electrochemical methods, and the effect of doping onto the magnetic properties will be analyzed. Different techniques will be applied in order to understand the effect of doping in the magnetic properties of Li_{0.1}VO_x-NT. A systematic dependence of a nonlinear response of the magnetization in small applied fields will be verified. These results will bring new insights into the magnetic properties of nanoscaled transition metal oxide.

In section 2.2 the importance of using materials with nano size particles was described. These nanomaterials are being studied extensively due to the possible

chemical and physical properties that they exhibit. Interestingly, properties of the nanomaterials are often different than their bulk counterparts due to particles re-sizing. The fine structures of nanomaterials show a wide range of interesting phenomena such as low-dimensional magnetism, induced magnetism in noble metals, electron interference patterns, oscillatory magnetic coupling and “giant” magnetoresistance [92]. For instance, reading heads for hard discs contain nanosized magnetic multilayers [93]. A magnetic grain size of ≈ 10 nm was found to be a good compromise in recording media devices [94].

Iijima was studying an arc-discharge evaporation method for producing the C₆₀ carbon molecule in the shape of a soccer ball. With this method and with the help of high-resolution electron micrographs, he discovered in 1991 nanometer-size needle-like tubes of carbon now known as “nanotubes” [95]. He observed the spontaneous formation of the nanotubes on top of the electrode surface of the light arc under catalytic participation of metals of the iron group. Generally, these cylindrical nanostructures can be considered as rolled up layers of graphite with half spherical or polyhedral graphite domes at their ends [96]. These carbon nanotubes have virtually unlimited applications, for example: as gas detectors, field emitters, tips for scanning-probe microscopy, or as quantum wires or electrochemical devices etc. [97]. The diameter of nanotubes plays an important role in defining the material’s properties, for example it can influence the insulating, semiconducting or metallic behavior of the compound [98–100]. At that time it was suggested that from other compounds with a layered structure similar to the graphite one could be able to form nanotubes or fullerene-like structures [97]. The pioneer discovery of Carbon Nanotubes (CNT) by Iijima together with the interesting physical and chemical properties of this novel material encouraged scientists for research on nanotubes formed by other layered materials, like TiO₂, Co₃O₄, VO_x-NT, ZnO, MoO₃, ZrO₂, In₂O₃, Ga₂O₃ [101]. Boron nitride BN, ZrSe, SnS₂ or MoS₂ are other examples of nanomaterials [102].

Among these nanostructures, tubular materials play an important role due to different contact regions that they possess, relevant for the interaction of the nanosized material with its environment. As shown in Fig. 4.1 the important parts are the inner and outer diameter of the tube, the ending of the tube and the structured tube walls. In the following, a more detailed review about previous work on Vanadium Oxide compounds is given. The main focus will be on both the synthesis and structure of this compound. More details about electronic and magnetic properties will be given in the last section of this Chapter.

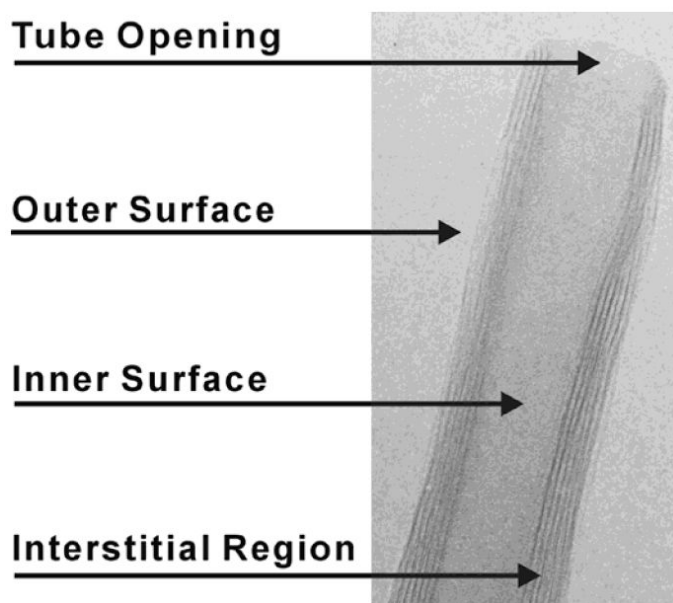


Figure 4.1: TEM image of one VO_x-NT illustrating the nanotube topology [103].

Synthesis methods and corresponding morphologies

Vanadium Oxide represents an important role in catalysis, electrochemistry or ceramics, therefore it was of big interest to synthesize nanostructured materials out of this compound. A tubular VO_x shape was obtained for the first time by Ajayan et al. using carbon nanotubes as a template [104]. The preparation of these oxide nanotubes was done by annealing a mixture of partially oxidized carbon nanotubes and V₂O₅ powder. The CNT were externally coated with layered V₂O₅ structure.

This work was followed by that of Spahr et al. by direct chemical synthesis of V alkoxide precursors. Together with neutral surfactant molecules, i.e. primary aliphatic amines, they succeeded in obtaining a novel tubular redox-active form of VO_x [105]. Structure directing agents were used in order to help the oxide layers during the synthesis to form the nanotube-like morphology. These agents are organic molecules with one non polar part and hence giving them a hydrophobic end, a hydrocarbon chain, and a polar part resulting in a hydrophilic end [106]. Spahr and coworkers started with hydrolysis of a solution of vanadium triisopropoxide in hexadecylamine gave. After aging, it turned into a lamellar structured composite of surfactant and hydrolyzed VO_x. This was followed by a treatment in hydrothermal conditions and the result were isolated and star like grown together nanotubes with a composition of VO_{2.40}(C₁₆H₃₃NH₂)_{0.34}. The obtained material shows a paramagnetic behavior and has a semi metallic conductivity probably due to mixed valent vanadium centers. It is known that vanadium can have different oxidation states,

4 Electrochemically doped Vanadium Oxide Nanotubes

e.g. 3^+ , 4^+ , 5^+ . More interestingly, it can be found in a mixed oxidation state, for example $V^{4.4+}$ [28]. These nanotubes have a cylindrical, open-ended shape, diameters between 15-100 nm, and tunnel openings between 5-50 nm.

Krumeich et al. obtained VO_x-NT using a sol-gel method followed by a hydrothermal treatment. They started with vanadium alkoxide precursors and primary amines $C_nH_{2n+1}NH_2$ with $4 \leq n \leq 22$. Instead of the primary amine also α , ω -diamines $H_2N[CH_2]_nNH_2$ with $14 \leq n \leq 20$ were used. Using X-ray diffraction experiments, and Transmission Electron Microscopy (TEM) it was suggested that the tubes are up to $15\mu m$ long, with outer diameter of 15-150 nm and inner diameter of 5 nm to 50 nm. The tube walls have 2 to 30 VO_x layers with amines or diamines intercalated between the layers [103]. In this case, the structure of the VO_x layers does not depend on the amine that was chosen as structure-directing template. A double arrangement of amine molecules between the VO_x layers with their headgroup pointing towards the layer is most likely present as depicted in Fig. 4.2 [107].

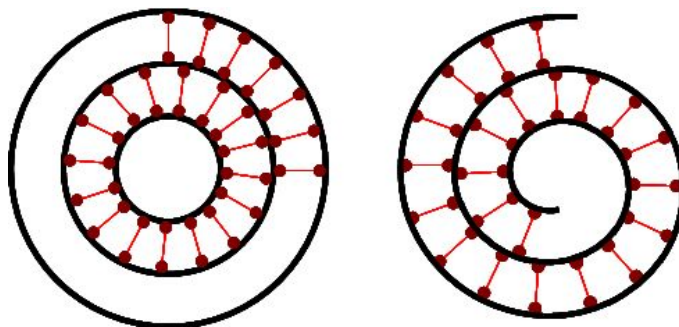


Figure 4.2: Concentric scrolls and serpentine like structure are possible morphologies for VO_x-NT.

Most of the tubes have open ends, although occasionally tubes closed by a set of parallel layers perpendicular to the tube can be found. Closed tubes by a pointed cap of conically deformed layers are possible as well. This effect is not dependent on the template used. The template might influence the morphology of the nanotubes. For example: if monoamines are chosen then the nanotubes have wide openings. They are rather “thin”, with 2 to 10 layers of VO_x. On the other hand, if diamines are used, the nanotubes are “thicker”, with smaller inner diameters and more than 10 VO_x layers. Depending on the used template, the distance between the VO_x layers differs. The longer the amines or diamines, the larger the distance between the layers (it may vary between 1.7 nm-13.8 nm).

Muhr et al. studied VO_x-NT with $[C_nH_{2n+1}NH_2]_{1.9}V_7O_{17}$ formula, using monoamines with $n = 12 - 18$ as templates. According to their X-ray photoelectron spectroscopy (XPS) studies the amine molecules are protonated. The positive

charge is compensated by negatively charged VO_x layers. Therefore the oxidation state of the V is affected by the organic spacer molecule. It was suggested that the chemical composition is related to BaV₇O₁₆*x* H₂O, although the two compounds have different VO_x substructure. BaV₇O₁₆*x*H₂O has 45% of V⁴⁺. The mean oxidation state of this compound is 4.6. For VO_x-NT the procentage is 71% while the mean oxidation state is 4.3. These tubes were found to have semiconducting behavior with a resistivity of 600 Ωcm at room temperature [103]. Bieri et al. synthesized for the first time VO_x-NT with aromatic amines (phenylpropylamine) as templates, using the same steps during synthesis as mentioned before. The VO_x-NT presented above were produced using primary amines. The resulted nanotubes have similar shapes and sizes as the previous VO_x-NT [108]. It was mentioned earlier that most of the tubes have serpentine like morphology, with single or double layer scrolls which gives the high structural flexibility of the material. With the help of standard TEM preparation procedures for cross section studies, it was revealed that besides scroll like layers tubes built up by concentric closed cylinders are also possible. This is rarely found (less than 1%) and mostly when the tube has six or less VO_x layers [109]. Interestingly, more or less disordered mixture of both morphology is possible.

VO_x-NT Structure

All these VO_x-NT exhibit the same structure of BaV₇O₁₆*n*H₂O with *n* = 4.4. The barium vanadium oxide bronzes have V₇O₁₆ layers stacked along the [001] unit cell direction with Ba²⁺ ions and H₂O molecules located between the layers [110].

As shown in Fig. 4.3 the VO_x layers contain three different V atom positions: V(1), V(2) and V(3). The first two are coordinated by six oxygen atoms, and forming distorted octahedra. The third one has tetrahedral coordination, with four oxygen atoms. In Fig. 4.4 the side view and plan view of the structure is illustrated. Clearly, the V(2)O₆ octahedra share edges on both sides with two units of V(1)O₆ octahedra. Each one of these V(1)O₆ share an edge with another V(1)O₆, thus the result are zig-zag chains. The chains are interconnected into single layers by sharing one oxygen atom. The layers are stacked along the [001] direction. They form double layers of octahedrally coordinated (V(1), V(2))O₆ units having tetrahedrally coordinated V(3)O₄ unit in between. The octahedrons have typical distortions to VO_x compounds. It was suggested that V(3) exhibits 3⁺ valency, while V(1) and V(2) have either 4⁺ or 5⁺ valency, with a preference to 5⁺ for V(1) when the symmetry is lower [110]. Ba cations can be found in two different interlayer positions, both

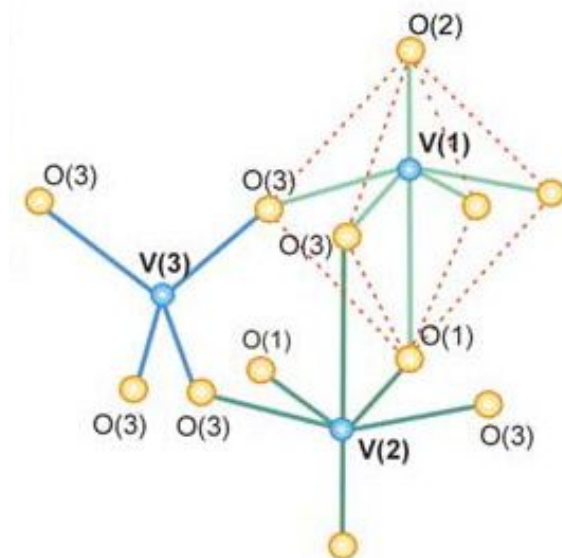


Figure 4.3: BaV₇O₁₆ structure, with exemplification of the three possible vanadium atom positions [39].

coordinated by vanadyl oxygen atoms from the layers above and below, and by interlayer water molecules.

VO_x-NT with amines as template have a special flexibility, different from other nanotube systems [97]. The amines embedded in between crystalline VO_x layers can easily be exchanged by various metal cations: alkaline, alkaline-earth or transition metals. It was shown that the tubular morphology of the nanotube is preserved after the partial exchange of the amines [111]. The parameter influenced by this exchange is the distance between the VO_x layers. For example in C_n-VO_x-NT with α -monoamines, C_nH_{2n+1}NH₂ ($4 \leq n \leq 22$) the template was successfully exchanged with alkaline Na⁺. The VO_x interlayer distances decreased from 2.8 nm to 1.1 nm. K⁺ is possible to be intercalated as well. Diluted RbCl or CsCl solutions lead to the destruction of the tubular morphology. The tubular structure is unaffected by LiCl solution, and the interlayer distance is not affected. It is possible to intercalate alkaline-earth metals (Mg²⁺, Ca²⁺) cations while preserving the tubular morphology. Treatments with SrCl₂ affects the structure. Solutions of BaCl₂, RbCl₂, CsCl destroys the structure completely. Transition metal cations (Fe²⁺, Co²⁺, Ni²⁺ or Cu²⁺) can easily be exchanged. The tube morphology is preserved relatively well. Pb²⁺ was not intercalated, and the tubes were destroyed. During the intercalation of these metal cations and together with interlayer distance modifications, the oxidation state of V is not modified [111].

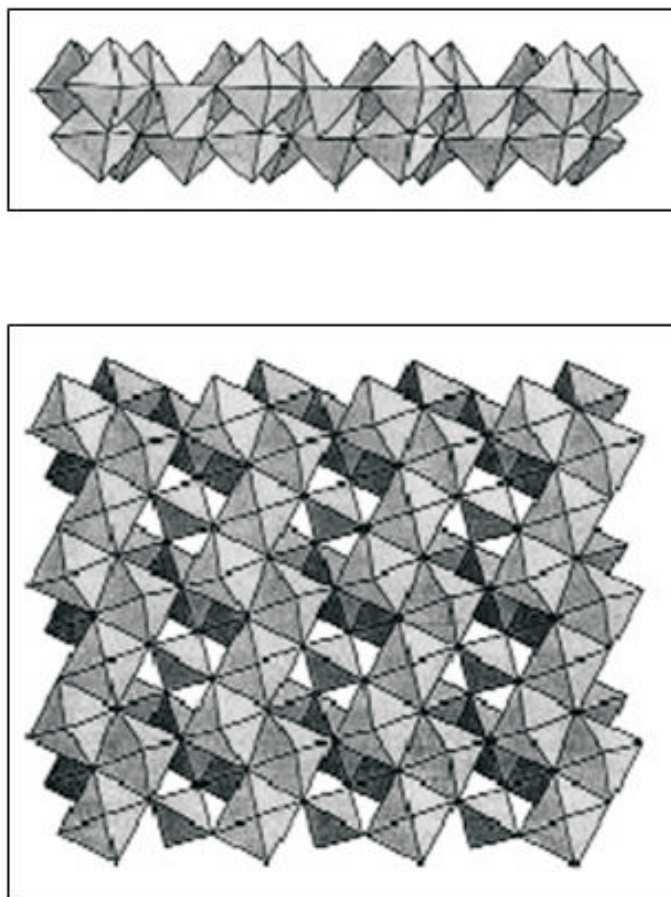


Figure 4.4: Side and plan view of $\text{BaV}_7\text{O}_{16}$ structure [39].

If the layered structure of VO_x and the various possibilities for guest intercalation is considered, one can obtain a good material for electrochemical insertion of lithium. Indeed, $\text{VO}_x\text{-NT}$ with and without templates ($\text{C}_{16}\text{H}_{33}\text{NH}_2$) are found to be redox-active and, therefore, can electrochemically insert Li by a reversible process [22]. Vanadium oxide alkylammonium nanotubes, $\text{NT-V}_2\text{O}_{5+\sigma}[\text{C}_{12}\text{H}_{25}\text{NH}_3]$ were synthesized, and Mn was inserted into the structure (exchanged with the amines). The result was $\text{Mn}_{0.1}\text{VO}_{2.5+\sigma}n\text{H}_2\text{O}$ [112]. These nanotubes are electrochemically active in Li cells and they react with Li in a reversible way. Another way to improve the functionality of VO_x was given by Pilai et al., who for the first time synthesized $\text{VO}_x\text{-NT}$ with addition of ammonia during the hydrolysis step of the synthesis. Their tubes had larger diameters (200 nm). Interestingly, the tube walls have two different alternating interlayer distances. The amines give the larger interlayer distances while NH_4^+ ions are located in the more narrow layers [113]. These layers are stiffer than the ones containing the amines.

Electronic properties of VO_x-NT

Electronic properties of VO_x-NT studied in this work have been characterized in [28], using photoemission and electron energy-loss spectroscopy (EELS). The nanotubular structure as well the mixed valency have been certified. The electron diffraction pattern was obtained using an EELS spectrometer, by reducing the energy loss to zero. For VO_x-NT the pattern can be divided in two parts. One for momentum transfer q lower than 1 \AA^{-1} , which gives information about the inter-layer distances between the VO_x layers. These distances depend on the length of the template used in the synthesis of the nanotubes. For VO_x-NT, a distance between the VO_x layers of 26.1 \AA was established. The second part of the electron diffraction concerns the q higher than 1 \AA^{-1} region. This gives information about the structure of the VO_x layers which form the nanotube walls. From this region it was established that there are well defined structural units forming the nanotubes walls in a repetitive manner. As mentioned before, the structure of VO_x-NT is similar with that of BaV₇O₁₆*n*H₂O with $n = 4.4$, result shown also by this electron diffraction experiment [28]. The diffraction peaks in high q region were identified as a contribution from a two-dimensional quasitragonal cell, in which a and b axes lie in VO_x-plane ($a=b$) while, the c axis is perpendicular to this one, and it is determined by the organic spacer molecule.

The color of the studied material was black, which it is known as being a sign of mixed V oxidation state as found for example also in V₆O₁₃. Li et al. used core-level photoemission (XPS), through information given by the V $2p$ and O $1s$ spectra in order to analyze the valency of the VO_x-NT. The V $2p$ spectrum presents two peaks in the excitation spectra due to spin-orbit splitting, resulting from excitation from V $2p$ core states to unoccupied $3d$ states (L_3 , excitation from $2p_{3/2}$ to $3d$, and L_3 , from $2p_{1/2}$ to $3d$). The O spectra has one peak at 530 eV with a shoulder in higher energy related to absorbed oxygen and/or water in the sample surface. The ratio V $2p_{3/2}$ to O $1s$, VO_{2.5} stoichiometry was established. The 516.46 eV and 524.07 eV maximum of VO_x-NT and the previously mentioned one from the O, are compared with positions of the maximum in V₂O₅ and V₆O₁₃. Assuming that the binding energy sifts linearly with increasing of the ionicity from V⁴⁺ to V⁵⁺, the resulting valency for the VO_x-NT is 4.4.

Influence of lithium doping on electronic properties of these VO_x-NT has been performed [138]. The *in situ* lithium doping was done under UHV conditions, by short evaporation periods of Li, from below onto the sample, using a commercial Li-getter, and simultaneously annealing to 100 °C. The effect of doping was controlled by observation of changes into the electron diffraction patterns at regular intervals.

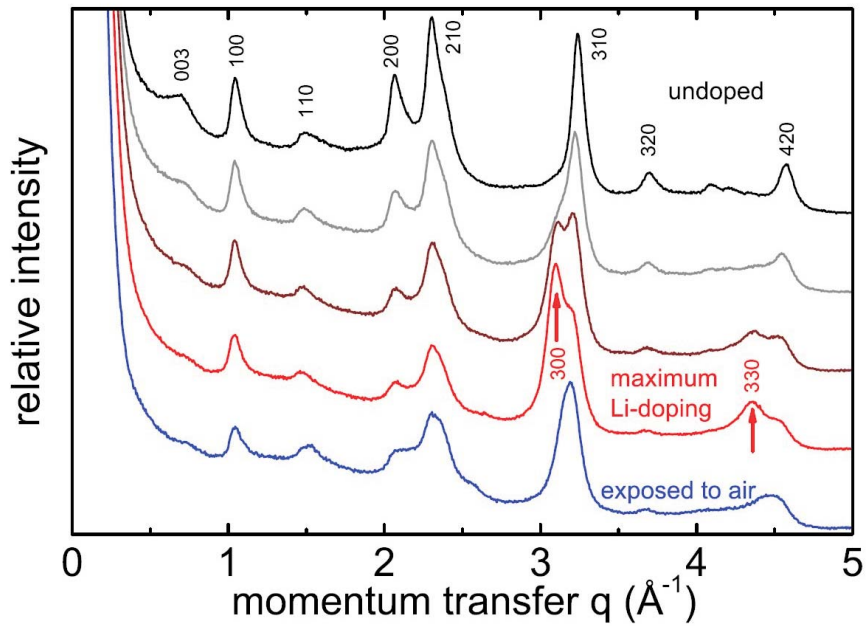


Figure 4.5: Changes in the electronic diffraction pattern of VO_x-NT upon doping with lithium. For clarity, the curves are shifted vertically with increasing Li-content from top to bottom, taken from Ref. [138].

Fig. 4.5 illustrates the diffraction patterns for undoped and doped VO_x-NT, as well as the highest doped sample after air exposure, the blue curve. Upon doping, significant changes in these patterns occur. Two new peaks at 3.1 \AA^{-1} and 4.35 \AA^{-1} appear and increase gradually with increasing the doping level. The appearance of these peak in the high q region suggest that the VO_x layers are affected by doping. Except the appearance of these two peak, no drastic changes are seen, suggesting that the structure of the VO_x-NT is stable upon doping. When the sample with the maximum doping level is exposed to air, the features present in the doped sample disappear, indicating that after air exposure the Li reacts with oxygen and/or water and the characteristics of the undoped sample are partly restored.

Core level excitation spectra (L edges) for undoped and doped VO_x-NT were also performed by Hellmann et al. [138]. The doped sample presents an energy shift of the L-edge, with 0.7 eV lower than the undoped compound. The L₃ edge becomes sharper compared to the undoped, and the L₂ edge becomes broader and smaller in intensity. Also a new feature appears between the L₃ and L₂ edges. By doping, the oxidation state of the V ions decreases as a consequence of a higher occupation of the 3d shells. This results in a downshift of the excitation energy with increasing the occupation of the 3d levels due to an additional screening of the 2p core hole. By comparing these results with similar results on V₂O₅ (V⁵⁺), VO₂ (V⁴⁺) and V₂O₃ (V³⁺), one finds that by doping the oxidation state was reduced to even V³⁺. A

charge transfer of approximately 1.4 electrons has been estimated, with 15 %-20 % uncertainty. After air exposure of the highest doped sample, the effect of doping vanishes, as it was observed in electron diffraction patterns as well.

These spectroscopic experiments have shown that the structure of the VO_x-NT studied in this work, is stable upon doping. A reversible Li insertion can be obtained, resulting in modification of the vanadium ions oxidation state. As shown, the structure is sensitive to air exposure, regaining the features present in the undoped compound.

4.2 Properties of electrochemically doped compounds

The importance of different contact regions that nanotubes have was mentioned earlier in this work: the inner and outer wall surfaces as well as the tube ending. Especially for the insertion processes (controlled by diffusion in electroactive material), nanotubes with large inner and outer diameters have tremendously improved properties. It is believed that this occurs due to shorter diffusion paths in the solid and a higher surface/bulk ratio which gives faster heterogeneous kinetics [22]. The nanotube shape can provide electrolyte filled channels that facilitate the ion transport to the insertion sites.

4.2.1 Electrochemical characterization and synthesis

Vanadium oxide nanotubes studied here were synthesized using the hydrothermal procedure described in [107] and [39]. A solution of vanadium (V⁵⁺) triisopropoxide [VO(iOPr)₃] and a primary amine (CH₃-(CH₂)₁₁-NH₂) in a molar ratio of 2 : 1 in absolute ethanol (3 ml per g of [VO(iOPr)₃]) was stirred under nitrogen atmosphere for 1 h. This resulted in a light-yellow solution of alcoxide-amine adduct. This was hydrolyzed with water (5 ml per g of [VO(iOPr)₃]) while stirring. The adduct was continually stirred and aged at room temperature for ≈4 days, turning dark orange. The hydrothermal reaction of this composite in an autoclave at 180 °C for 8 days yielded a “black” powder which was then washed with ethanol and hexane and dried at 85 °C in vacuum for ≈30 h. This material was characterized using Scanning Electron Microscopy (SEM) and TEM. In Fig. 4.6, TEM and SEM images are presented. The tubular morphology can be clearly seen in the mentioned figures. The tubes have inner diameters between 20 nm and 30 nm while the outer diameters

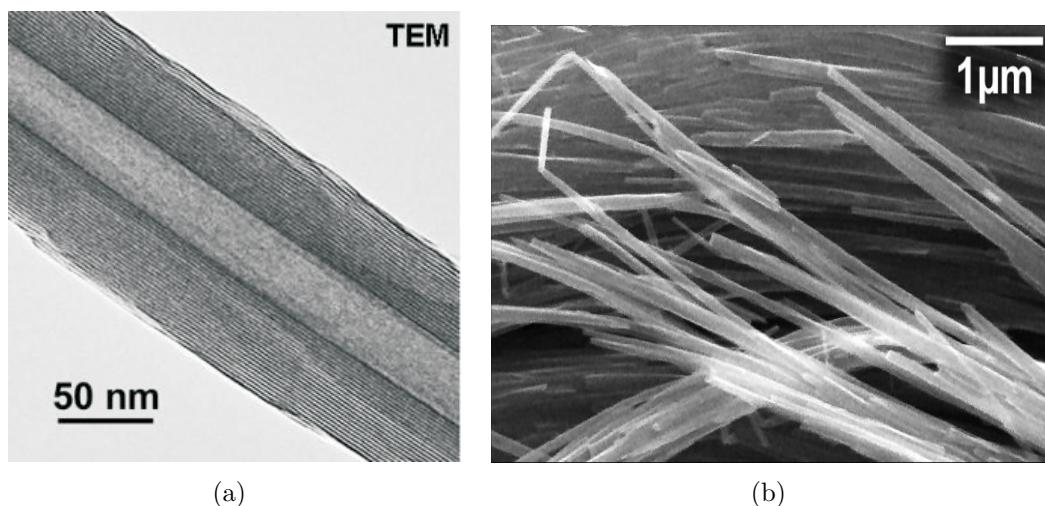


Figure 4.6: Nanotube morphology of Vanadium Oxide Nanotubes : a) Transmission electron microscopy b) Scanning electron microscopy.

range from 50 nm to 100 nm. The walls consist of several vanadium oxide layers with organic molecules embedded in between, helping them to form a sandwich structure and thus stabilize during the nanotube formation.

Cyclic voltammetry

Electrochemical experiments on different batches of VO_x-NT were performed. Initially, cyclic voltammograms were performed in order to investigate VO_x-NT as cathode material in Li batteries, followed by galvanostatic or potentiostatic experiments. All the experiments were performed in a two-electrode Swagelok like cell. In some of the samples, 5 to 10wt% of Carbon SP were added for better electronic conductivity of the material. Approximately 10 to 20 mg of this mixture were used for each experiment. After testing the material, potentiostatic experiments were performed in order to obtain the final lithium intercalated compounds used for magnetic investigations. In some of the cases, VO_x-NT together with the Carbon SP were mixed with PVDF binder (Polyvinylidene fluoride-(CH₂CF₂)_n-) 5 to 10wt% and then pressed into pellets. Each pellet was 8 mm in diameter and ≈1 mm in thickness. In this case, the pellets were used as cathode material for charge/discharging investigations.

The cyclic voltammograms for the first cycle for VO_x-NT, batch number 5 are shown in Fig. 4.7. Here, VO_x-NT were mixed with 10% Carbon SP. The starting potential was around 3.2 V. From this value, the potential was linearly scanned between 1.8 V and 3.5 V using different scan rates. First, the cell was discharged (going from 3.2 V

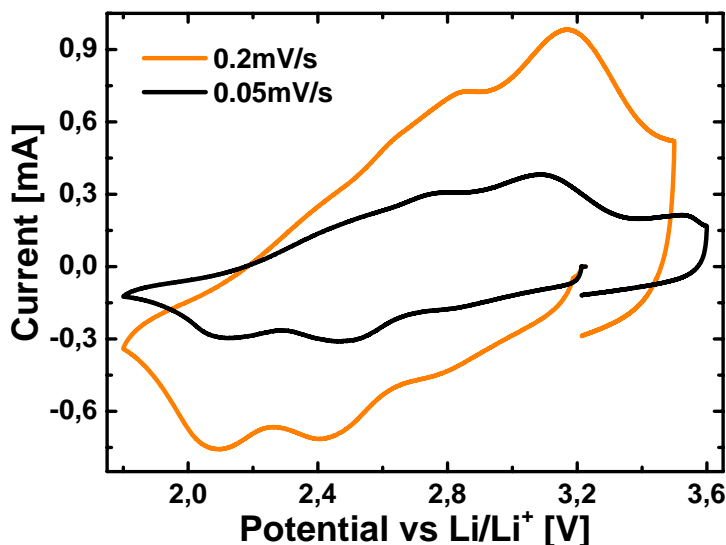


Figure 4.7: Cyclic voltammogram for the first cycle for VO_x-NT#5 with two different scan rates.

to 1.8 V) with scan rates of 0.2 mV/s and 0.05 mV/s, respectively. As the cell started to be discharged, thus Li intercalation occurred, two reduction peaks indicating two different electron transfer are encountered at 2.42 V and 2.09 V. During the cell charging two peaks at 2.83 V and 3.17 V are found. From this picture one can say that the discharged species in the cathodic sweep were reversibly charged during the anodic sweep, or, in other words that the electron transfer process is reversible in this case. At 2.73 V, the cathodic scan presents a shoulder, which is probably coupled to the anodic peak at 2.64 V. No further CV on this material was possible due to lack of material.

In Fig. 4.8 the first CV for VO_x-NT batch#12 is shown. Three different sweeping rates were used, i.e. 0.01 mV/s, 0.02 mV/s and 0.05 mV/s. Here, the curves were obtained from pure material without any additives. The difference between the three curves is the current intensity, which is higher with increasing the sweeping rate as expected. A very broad feature between approximately 2 V and 2.8 V is visible for all three scan rates used. This feature might be assigned to possible reduction peak during discharging the material. For 0.02 mV/s scan rate a possible oxidation reaction occurs around 3.6 V. The electrochemical behavior of this material was not as expected from the literature. In order to improve the electrochemical properties of the material, this was mixed with 10% Carbon SP. The result for the first cycle is presented in Fig. 4.9, where two CV with 0.02 mV/s and 0.05 mV/s were performed.

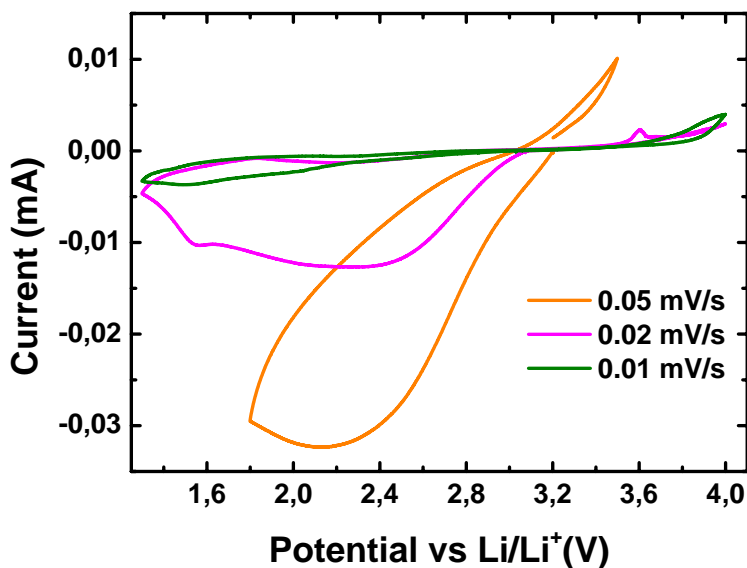


Figure 4.8: Cyclic voltammograms for the first cycle for VO_x-NT#12 without any additives using three different sweeping rates.

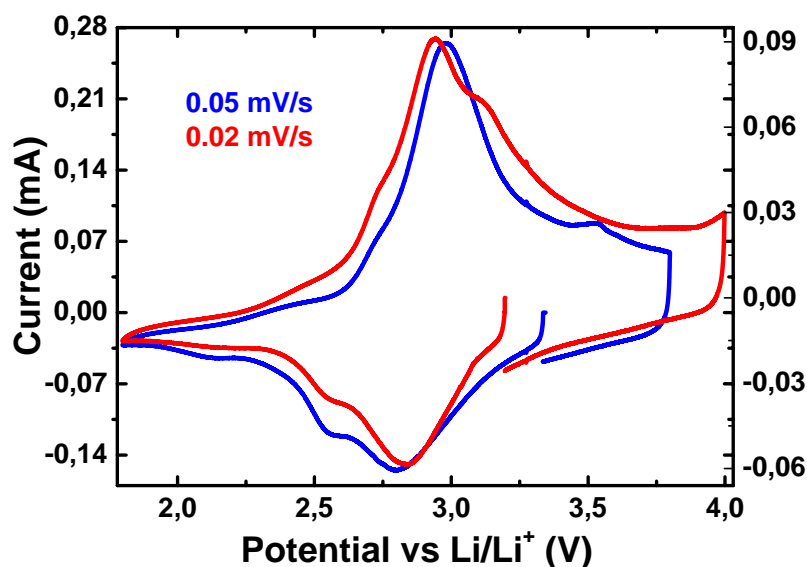


Figure 4.9: Cyclic voltammograms for the first cycle for VO_x-NT#12 with different scan rate: 0.05 mV/s (blue) and 0.02 mV/s (red).

Both experiments were made on the same cell. The first one was done with 0.05 mV/s, the blue curve. The cell was cycled between 1.8 V and 3.8 V, and four consecutive sweeps were performed. The starting potential was around 3.3 V. The experiment started with the discharging of the cell. After four cycles with this sweep-

ing rate were finished, the CV with 0.02 mV/s was started, the red curve. In this case the material was cycled between 1.8 V and 4 V. Once the discharging had started, electron transfer due to reducing of the V^{5+} to V^{4+} , seen in the form of a very pronounced reduction peak is present around 2.8 V. For the CV with 0.02 mV/s the reduction peak shifted slightly to more positive values. A quasi reversible electron transfer is present for both experiments. This can be assumed from the position of the oxidation peak, at potential slightly higher than the one where the reduction pair peak is present.

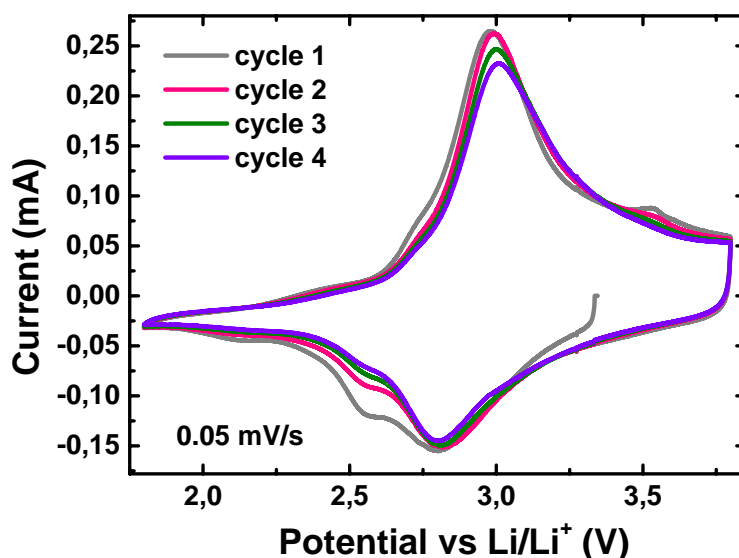


Figure 4.10: Cyclic voltammograms for VO_x-NT#12 using a scan rate of 0.05 mV/s.

In Fig. 4.10 CVs for four cycles with 0.05 mV/s are shown. The main electron transfer during discharging is situated at 2.8 V and during the cycling it is positioned nearly at the same place with slightly differences in the current peak intensity. For the first cycle, the current peak intensity i_p^a amounts to 0.018 mA and for the fourth one it is 0.027 mA. The reduction peak has a shoulder at 2.56 V, most probably connected to the oxidation one at ≈ 2.7 V. With cycling, this peak loses intensity, almost vanishing in the fourth sweep. In this CV experiment, the anodic peak is situated at 2.98 V and over cycling its position is shifted by only 0.018 V, settling at 3 V in the fourth cycle. The current peak intensity decreases with cycling: from $i_p^c=0.066$ mA in the first sweep to 0.045 mA in the last one. CVs on VO_x-NT#12 with scan rate of 0.05 mV/s show reversible intercalation of the lithium into the structure. Discharge and charge capacity values taken from this experiment are not high enough for this material, i.e. ≈ 100 mAh/g (the theoretical value lies around

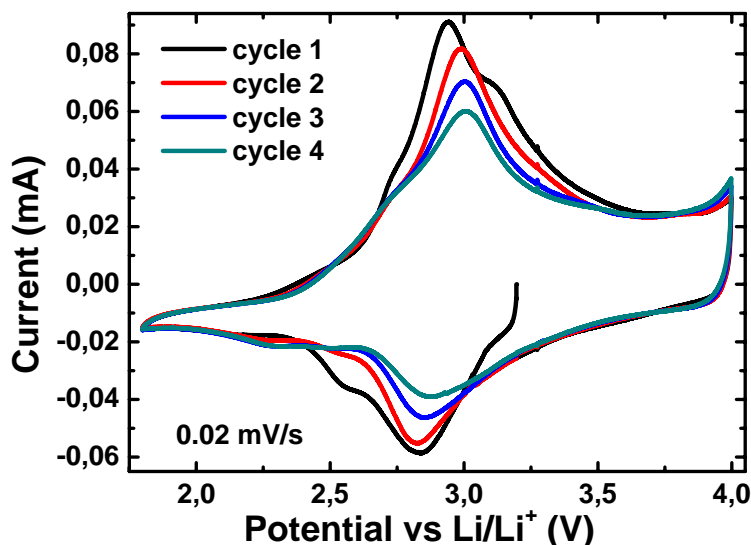


Figure 4.11: Cyclic voltammograms for VO_x-NT#12 using a scan rate of 0.02 mV/s.

370 mAh/g). In Fig. 4.11 four CVs with scan rate of 0.02 mV/s are illustrated. It is worth remembering that this experiment was performed after the one with a scan rate of 0.05 mV/s. Therefore, the starting potential of this experiment it is a bit lower. This shift is probably due to slight aging of the material during the first cycling. The starting potential was 3.2 V. The reduction peak is situated at 2.83 V, and it changes to 2.88 V in the last cycle. The current peak intensities for these four cycles decrease from $i_p^a=0.0089$ mA in the first cycle to $i_p^a=0.0035$ mA in the last one. These intensities are much lower, as expected, than the ones obtained in previous experiments with a scan rate of 0.05 mV/s. In cyclic voltammetry, charge transfer influences the experiment by shifting the peak potential and reducing the current peak value. The electron transfer during charging is situated at 2.94 V in the first cycle and at 3 V in the fourth cycle. The current peak intensities in this case are decreasing from $i_p^c=0.024$ mA in the first sweep to $i_p^c=0.011$ mA in the last one. As shown by Fig. 4.11 compared to Fig. 4.10, the experiment performed with a scan rate of 0.02 mV/s has the peak positions and current peak intensities over cycling varying much more than for the experiment performed with 0.05 mV/s. This might appear from structural deformations during cycling, or aging of the material. The modifications occurring in the anodic peak can be due to a resistance of the reduced VO_x layers to re-adopt their original structure. It is known that for repeated cycling it is normal to obtain broader peaks due to aging effect and loss of crystallinity that VO_x-NT experience [23].

4 Electrochemically doped Vanadium Oxide Nanotubes

It was shown above for VO_x-NT batch#5 that the electrochemical behavior of VO_x-NT without carbon is not as expected from known results on similar compounds. On the next batches which were under study, no CV on material without any carbon additive was done. Therefore, all the experiments shown further on will be on VO_x-NT with 5 – 10% added Carbon SP.

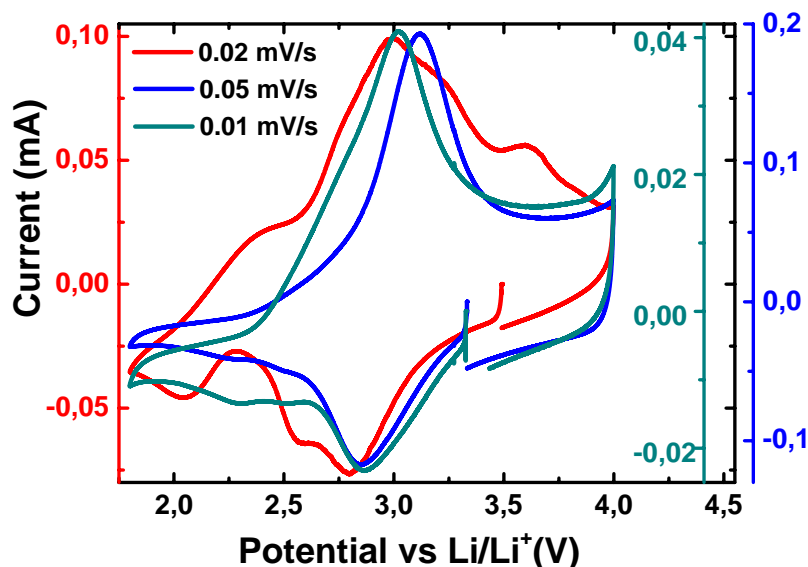


Figure 4.12: Cyclic voltammograms for the first cycle for VO_x-NT#13 with scan rates of 0.02 mV/s (red), 0.05 mV/s (blue) and 0.01 mV/s (green).

In Fig. 4.12, the first cycle using scan rates of 0.02 mV/s, 0.05 mV/s and 0.01 mV/s are shown. The experiments were done in this order: first the one with a scan rate of 0.02 mV/s, then the one with 0.05 mV/s and finally using a scan rate of 0.01 mV/s. These experiments were all performed in the same electrochemical cell. The starting potential was 3.49 V for a scan rate of 0.02 mV/s and it was a bit smaller, around 3.3 V, for the other two scan rates used. Using the first two sweeping rates, four cycles were performed. For a scan rate of 0.01 mV/s, only a single cycle was done. All experiments were cycled between 1.8 V and 4 V, and for each case, the discharge was the first cycling mode. Generally speaking all three curves present a very pronounced reduction peak connected with one anodic peak.

Fig. 4.13 shows the first scan completed on this material, using a scan rate of 0.02 mV/s. The starting potential value is very close to the one obtained from the first cycling on VO_x-NT#12. This shows that the material behavior is quite stable over the mounting procedure. The reduction peak in this CV shifts slightly to more positive values over cycling: from 2.8 V in the first cycle to 2.82 V in the

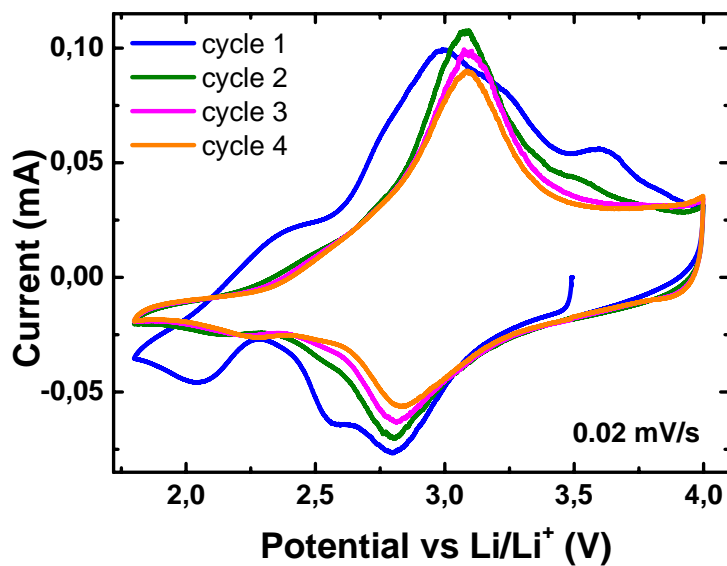


Figure 4.13: Cyclic voltammograms for VOx-NT#13 performed with a scan rates of 0.02 mV/s.

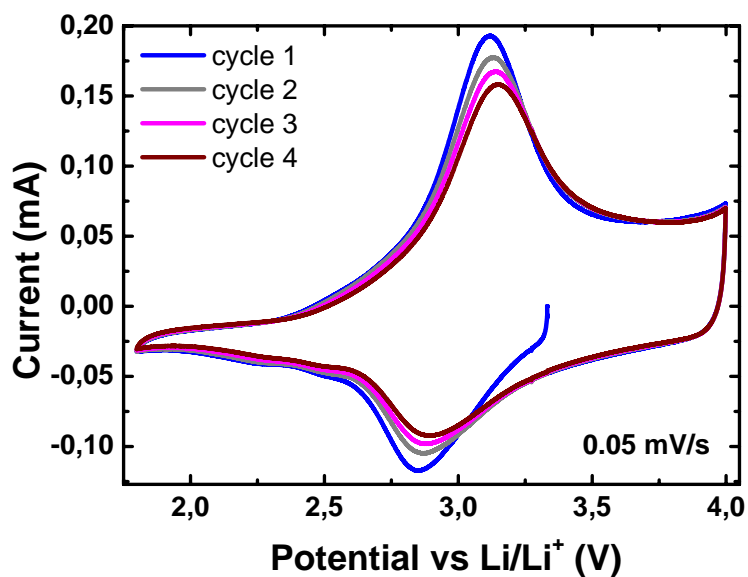


Figure 4.14: Cyclic voltammograms for VOx-NT#13 performed with a scan rates of 0.05 mV/s.

forth cycle. The current peak intensity decreases with cycling, from $i_p^a=0.010$ mA in the first cycle to $i_p^a=0.0084$ mA in the forth one. In the first cycle of this scan the shape of the CV is slightly different than in the next ones. The reduction peak has a pronounced shoulder at 2.57 V. In the second cycle this shoulder disappears. The

peak from 2.06 V in the cathodic scan may be due to reduction of V^{4+} to V^{3+} . It is known that this reduction appears at voltages equal or mostly lower than 2 V [118]. Both the reduction and the oxidation peaks are broader in the first cycle than in the next three. This can be explained by structural rearrangements after the first cycle. Shifting of the peak in the second cycle compared to the first ones suggest that irreversible phase transformations occurred during the Li insertion process. In the following cycles neither substantial changes in the peak potential nor in the curve shape are present. This indicates the reversibility of the electrochemical insertion/extraction process. The anodic peak of this experiment is situated at 2.99 V in the first cycle and it shifts to 3.08 V in the fourth one. The current peak intensity is 0.01 mA in the first cycle, then it increases in the second cycle to 0.022 mA. In the fourth one, it has a value of 0.017 mA. This might be another sign that the process in the first cycle is a bit different than the one in the following cycles. The reverse-to-forward peak ratio, for the first cycle is equal to one, a sign of a reversible redox process. This ratio deviates from this value in the following cycles.

In Fig. 4.14 a CV performed after the previous experiment is shown. The scan rate used was 0.05 mV/s. The starting potential was 3.3 V. The electron transfer during discharging experiment shifts slightly over cycling, from 2.84 V in the first cycle to 2.88 V in the fourth cycle. The current peak intensity decreases with cycling, from $i_p^a=0.015$ mA in the first cycle to $i_p^a=0.0077$ mA in the fourth one. The peak shapes in both cathodic and anodic sweeps are very similar over cycling, meaning that the structure is rather stabilized during this procedure. For the anodic sweep, the peak position changes from 3.11 V to 3.14 V in the fourth cycle. The current peak intensity decreases over cycling, from 0.036 mA to 0.022 mA. The CV with a scan rate of 0.01 mV/s was performed for only one cycle, see Fig. 4.12. The shape of this CV is more similar to the one scanned with 0.02 mV/s. The experiment with 0.05 mV/s suggest a more ordered structure compared with the experiment performed with the lower scan rate, 0.02 mV/s. This might be influenced by the speed of the experiment. Chemical reactions between different species present in the electrochemical cell, or possible impurities might evolve under a slow rate of scanning the potential in a cyclic voltammogram experiment. Therefore, when using a high scan rate in such experiment, one can avoid influences of these unwanted reactions. The result might be a smoother behavior of an electrode material upon cycling. For the last cycle performed with scan rate of 0.05 mV/s, the reduction peak position is at 2.86 V and the anodic one at 3.01 V.

The discharge and charge capacities taken from this experiment are as follows. For the curve obtained with a scan rate of 0.02 mV/s in the first cycle the discharge capacity is 145 mAh/g. This value is slightly lower than other similar experiments

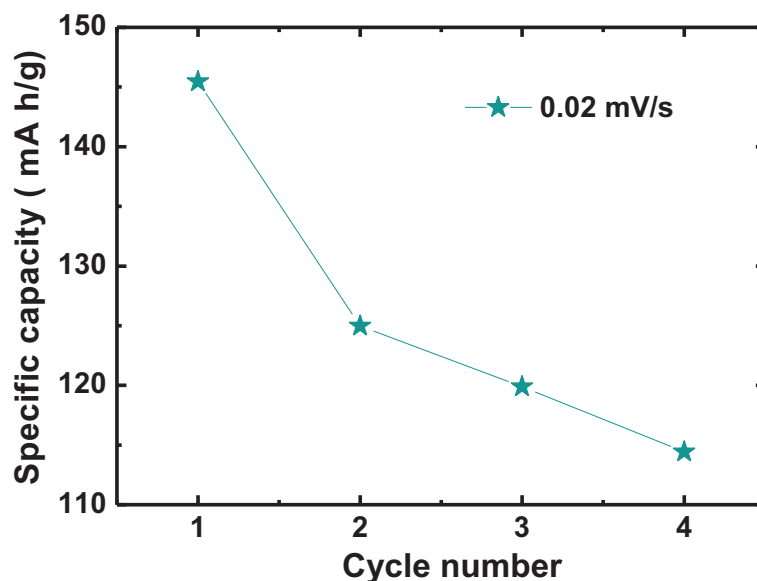


Figure 4.15: Discharge specific capacities values taken from cyclic voltammograms experiments on VO_x-NT#13 with scan rate of 0.02 mV/s.

found in the literature, as it will be discussed later on. Over the four cycles, this value decreases to 114 mAh/g, indicating loss of electroactivity. For the curves obtained with a scan rate of 0.05 mV/s this value decreases to almost half the value as shown in Fig. 4.15.

In Fig. 4.16 CV experiments on VO_x-NT#14 are shown. The starting potential was 3.2 V. The shape of the CV is similar to the other batches only that both the reduction and oxidation peaks are found at lower potential values. The reduction peak for the first cycle is situated at 2.56 V and for the last one at 2.82 V. The oxidation peak is at 2.96 V in the first sweep and moves to 3 V for the next 3 cycles. The discharge capacity for the first cycle is 123 mAh/g and increases to 153 mAh/g in the next one.

The next material that was studied was VO_x-NT#18. Three different scan rates were performed on the same cell. First, a scan rate of 0.02 mV/s was used, for four cycles, then a scan rate of 0.05 mV/s for the same number of cycles and then only one cycle with a scan rate of 0.01 mV/s. The results are shown in Fig. 4.17.

The starting potential is 3.4 V for the first experiment and stays nearly the same for the next experiments. Four cycles were performed for the scan rates of 0.02 mV/s and 0.05 mV/s. All experiments were cycled between 1.8 V and 4 V, and for each

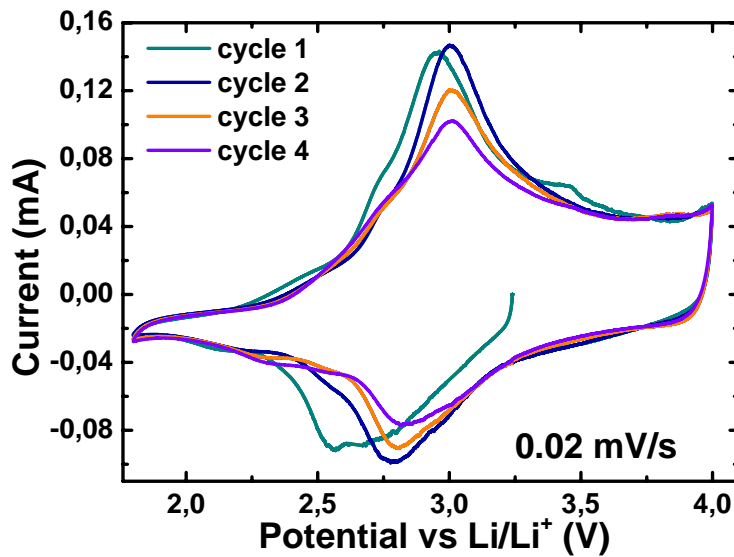


Figure 4.16: Cyclic voltammograms for VOx-NT#14 with scan rate of 0.02 mV/s.

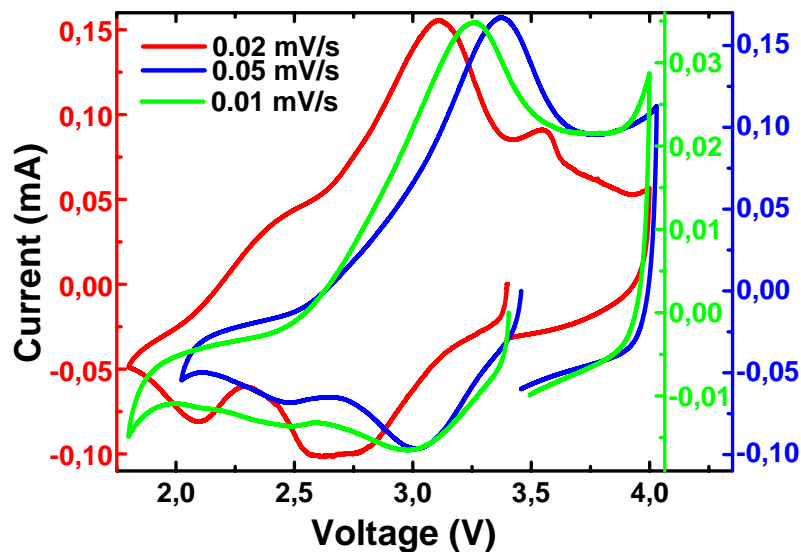


Figure 4.17: Cyclic voltammograms for VOx-NT#18 with scan rates of 0.02 mV/s (red), 0.05 mV/s (blue) and 0.01 mV/s (light green).

case, the discharge was the first cycling mode. All experiments show the pronounced reduction and oxidation peak as found in the other VOx-NT batches, the only difference is that the peaks are broader than in the other cases. This might be a sign of a more disordered structure in this particular batch.

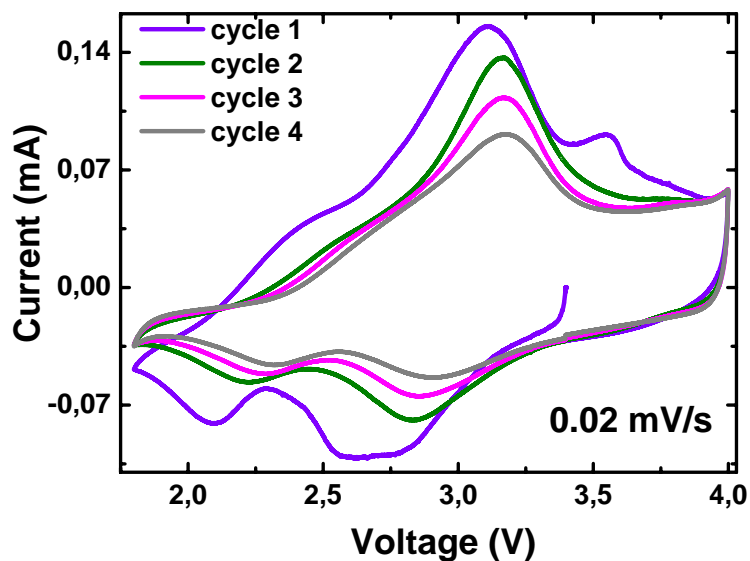


Figure 4.18: Cyclic voltammograms for VOx-NT#18 performed with a scan rate of 0.02 mV/s.

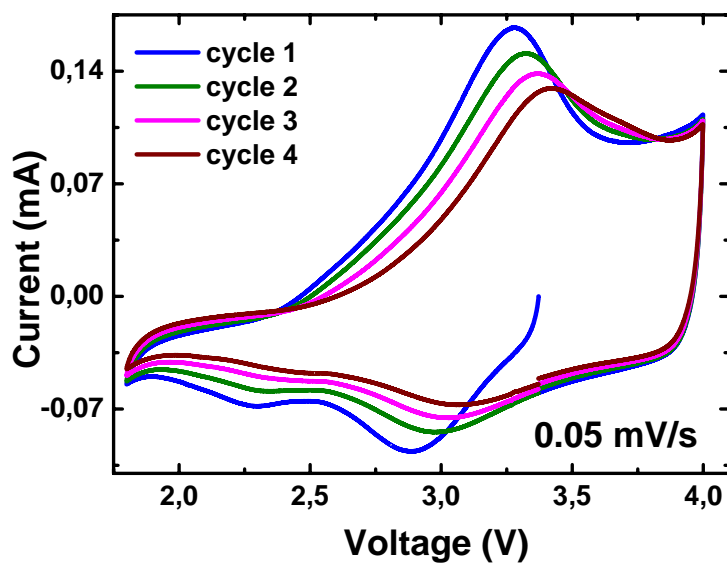


Figure 4.19: Cyclic voltammograms for VOx-NT#18 performed with a scan rate of 0.05 mV/s.

In CV performed with a scan rate of 0.02 mV/s, the electron transfer where V^{5+} reduces to V^{4+} it is at 2.62 V as shown in Fig. 4.18. During cycling it shifts to 2.9 V. This reduction peak in the first cycle is very broad, nearly showing like a plateau. It might also be that this peak is a combination of the reduction peak with a shoulder

4 Electrochemically doped Vanadium Oxide Nanotubes

as in Fig. 4.13, another sign of a disordered structure. A broader cathodic peak than the anodic one may indicate that Li insertion and extraction are governed by different mechanisms. In the next cycle this peak already becomes narrower, and it loses intensity. The current peak intensity decreases with cycling, from $i_p^a=0.003$ mA in the first cycle to $i_p^a=0.002$ mA in the fourth one. Here, as in the case of VOx-NT#13, a structural rearrangement takes place, starting with the second cycle. The anodic peak is at 3.1 V in the first cycle and it slightly shifts to 3.17 V in the last cycle. In this region the peaks are more narrow than in the reduction part. Fig. 4.19 shows the result from the second experiment on this material. The shape is the same as the last three cycles of the CV performed with a scan rate of 0.02 mV/s. The difference is that the peak positions are found at slightly higher potential values. For the first cycle, the reduction peak is at 2.88 V and it is found at 3.07 V in the last cycle. The current peak intensity is smaller than the previous experiment. The anodic peak is found at 3.27 V in the first cycle and it reaches 3.3 V in the fourth one. The peak positions for both reduction and oxidation in the case of the last experiment, with 0.01 mV/s are nearly the same as in the previous one. color

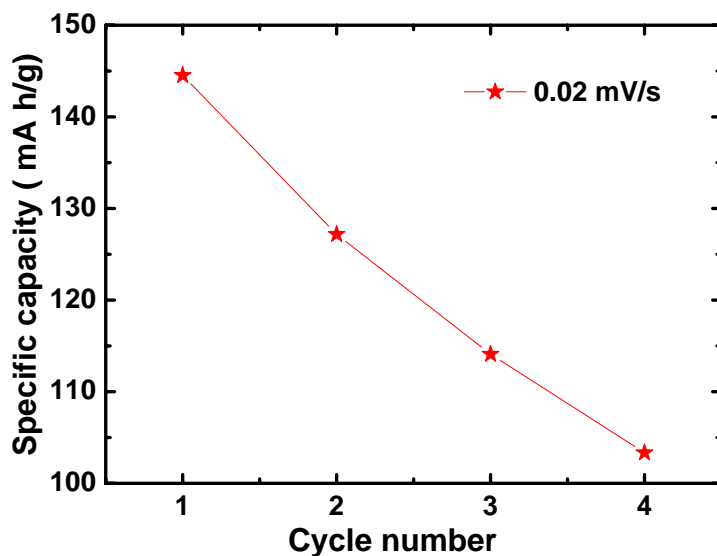


Figure 4.20: Discharge specific capacities values taken from cyclic voltammograms experiments on VOx-NT#18 with a scan rate of 0.02 mV/s.

The discharge and charge capacities informations taken from this experiment are shown in Fig. 4.20. Initially, a 145 mAh/g discharge capacity was obtained. This value continuously decreases with time.

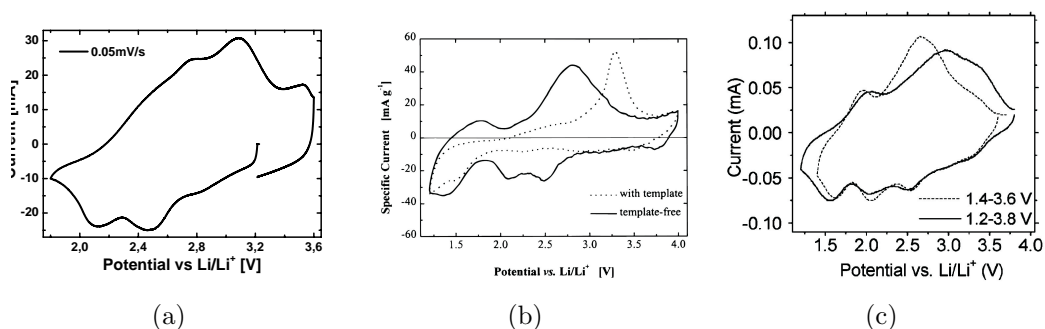


Figure 4.21: a) Cyclic voltammogram using a scan rate of 0.05 mV/s for: a) VO_x-NT batch#5; b) Template VO_x-NT (dashed line) and template free VO_x-NT (solid line) [22]; c) Ca-exchanged VO_x-NT [23].

In this work, results obtained from VO_x-NT#5 are clearly different than those from the other studied batches. By searching similarities in literature one can find that VO_x-NT#5 it is comparable to experiments taken on template free VO_x-NT [22]. The electrochemical studies performed on template and template free VO_x-NT are illustrated in Fig. 4.21(b). These nanotubes studied by Spahr and coworkers are formed from vanadium oxide triisopropoxide and hexadecylamine. The synthesis was a direct process via a modified sol-gel reaction. The result was VO_{2.45}(TEMP)_{0.34} with C₁₆H₃₃NH₂. Reduction peak for VO_{2.45}(TEMP)_{0.34} is found at potentials slightly higher than 1.5 V corresponding to electron transfer process. The corresponding oxidation peak appears at 3.3 V. The specific charge for Li insertion in this case was about 120 mAh/g and remained rather constant for the first 5 cycles. After 10 cycles it decreased to less than 100 mAh/g.

The templates were removed from these nanotubes by keeping them in a saturated solution of NaCl in ethanol. Both types of nanotubes contained several concentric shells. For the templated nanotubes, the shells had between 2.8 nm and 3 nm thickness. The template free nanotubes showed much smaller diameters of 0.86 nm, but the structure still looked ordered. Electrochemically speaking, these nanotubes behave very much different than those with templates in between the layers. Two reduction peaks are found at around 2 V and 2.5 V, with a corresponding broad oxidation peak at 2.7 V, indicating a quite reversible Li⁺ insertion process. The specific charge for Li insertion was 180 mAh/g in the first cycle. Clearly, the two kinds of nanotubes behave differently. This indicates that the amines play an important role in the electrochemical properties of this compound, by contributing to the a partial passivation of the nanotubes. As shown in Fig. 4.21(c) the CV of VO_x-NT batch#5 it is also comparable to Ca-exchanged VO_x-NT [23]. In this exchanged VO_x-NT, V₂O₅ was used instead of vanadium triisopropoxide as a precursor for the synthesis.

4 Electrochemically doped Vanadium Oxide Nanotubes

Several cathodic and anodic peaks were found, depending on the cut off potentials (the chosen limits for the potential to be swept). In VO_x-NT batch#5 the specific capacity for Li insertion for a first cycle was 140 mAh/g when the current was swept with a scan rate of 0.05 mV/s. This value is higher than the one for templated VO_x-NT and smaller than the one of template free nanotubes. Not enough potentiostatic experiments were performed on this batch, so no data about specific capacity over cycling behavior can be given.

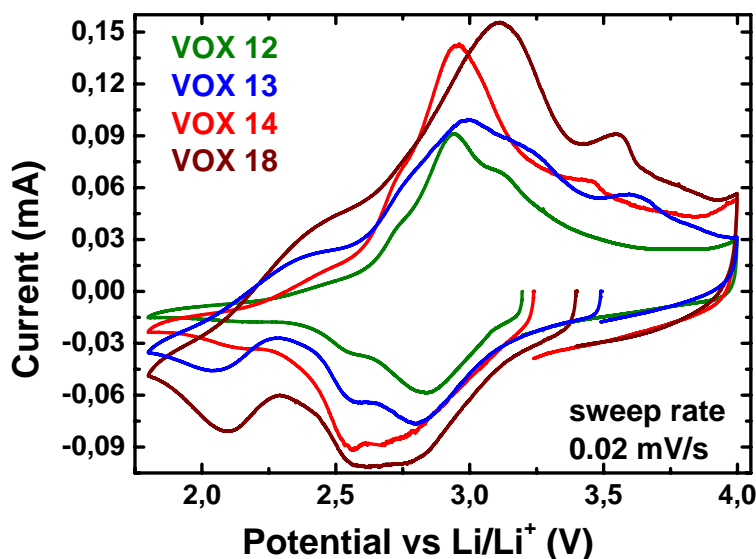


Figure 4.22: Cyclic voltammogram for the first cycle, performed with a scan rate of 0.02 mV/s, for all VO_x-NT batches.

In Fig. 4.22 a resume of the CV experiments on VO_x-NT batches presented above is illustrated. Generally speaking they have reduction/oxidation pair peaks in the same region, but with particular differences for each batch.

Sun et al. studied the relationship between the nanoscale structure and electrochemical performances of nanoscale scrolls of Vanadium Oxide [115]. The nanorolls are synthesized using a ligand-assisted templating method. The dodecylamine template was exchanged with Na⁺ through an ion-exchange process. The electrochemical properties of both VO_x-NT with and without template have been studied. They studied well-ordered vanadium oxide nanorolls as well as defect-rich ones. The differences between the two kinds of nanorolls lies in a different ratio of vanadium triisopropoxide-dodecylamine and water during the hydrothermal step of the synthesis. They have shown that these defect-rich nanorolls have a higher capacity than the well ordered compound. This was related to V⁴⁺/V⁵⁺ ratio, the cracks in the

wall and to residual organic surfactant in the nanorolls during cycling. Based on XPS analysis, Sun and coworkers suggested that the compound with lower electrochemical properties, the well ordered nanorolls, have 45% V^{4+} (V^{4+} to V^{5+} ratio is $\approx 1 : 1.2$). In the defect rich ones this ratio is $\approx 1 : 3.2$, with only 24% V^{4+} . It is known that the V^{4+} to V^{5+} ratio governs the formation of the nanorolls. During the hydrothermal step, the hexagonally ordered structure must transform into a lamellar structure. This happens when V^{5+} reduces to V^{4+} during this step. In this way, the inorganic charge density increases and the compound is dragged towards a lower curvature structure. During this hydrothermal step the thermal motion of the surfactant tails increases, giving rise to the same lamellar structure. These effects were previously observed in hexagonal-to-lamellar phase transitions in surfactant templated silica based materials [117]. Obtaining the well ordered or cracked nanorolls depends on the amount of the surfactant in the process. Higher amounts will give stronger hydrophobic interactions thus ordered material. Insufficient surfactant electrostatically associated with VO_x layers would give a lower vanadia hydrophobicity. This would inhibit the rolling up process, and the vanadia layers would be held together less strongly and less ordered, giving rise to cracked material. Sun et al. established under the same experimental conditions, discharge capacity of approximately 240 mAh/g for the well ordered VO_x nanorolls and much higher value of 340 mAh/g for the defect rich compound. These information given above suggest the influence that amines and vanadium oxidation state might reveal in electrochemical properties of this material.

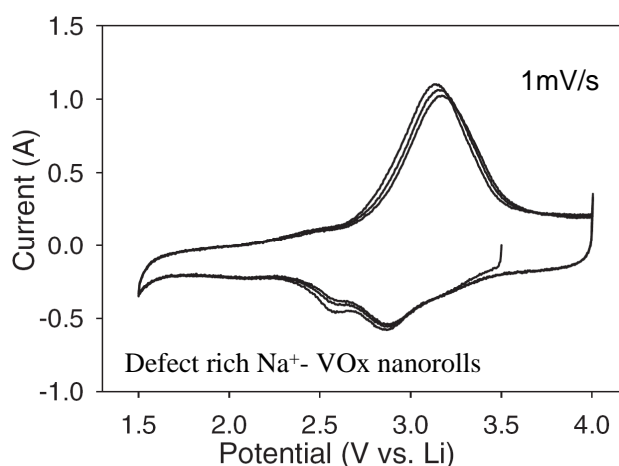


Figure 4.23: Cyclic voltammogram with a scan rate of 1 mV/s for Na⁺-exchanged VO_x-nanorolls [115].

Similarities with defect-rich Na^+ -exchanged VO_x -nanorolls [115] (see Fig. 4.23) were found for all the VO_x -NT batches except batch#5. These defect-rich nanorolls experience a reduction peak at 2.8 V with a shoulder at ≈ 2.6 V, as it was also found in VO_x prepared via sol-gel method [116]. The reduction peak is reversible, underlined by the same position maintained upon cycling. The anodic peak slightly shifts to more positive values. Generally speaking, it is clear that the VO_x -NT (except VO_x -NT#5) synthesized in this work behave like those which have cracks in the nanotube walls. As it was shown earlier, the hydrothermal step of the synthesis is very important for the final obtained compound. Except the main electron transfer exhibited at potential values between 2.5 V and 2.8 V during discharging, and between 3 V and 3.3 V during charging, in the CV illustrated in Fig. 4.22, other small features can be visible. These features might appear from either a different amount of surfactant in the nanotubes or a different ratio between V^{4+} and V^{5+} ions. V^{3+} ion can be present in the VO_x -NT only if the experiments are performed at potential lower than 2 V [118]. VO_x #14 and #18 clearly look more disordered than the other two batches, as it can be seen from much broader peak they present upon Li intercalation/deintercalation. Anyway, they all behave rather like disordered nanorolls than crystalline layered phases.

When looking at experiments presenting several CV's we see that in most of the cases, over cycling some changes appear. This might be due to amorphization or other structural changes of the material over cycling. This effect is also seen in decreasing of the discharge capacities over cycling, when the material loses electroactivity. This is shown in Fig. 4.24(a). Before going into details of discharge capacities behavior over cycling, informations about this characteristic of materials studied as possible application for lithium batteries will be given. Electrochemical studies of vanadium oxide nanotubes showed good properties of this compound when for example, through an ion-exchange process amines were exchanged with Mn^+ . $\text{Mn}_{0.1}\text{VO}_{2.5+\sigma}n\text{H}_2\text{O}$ can be reversibly intercalated/deintercalated with Li giving a specific capacity of 140 mAh/g [112]. Mo doped tubes have an initial specific capacity of 200 mAh/g that drops to half after 50 cycles [119]. Sun and coworkers studied well ordered and defect rich nanorolls, finding higher electrochemical properties for the latter ones [115]. Na^+ , Ca^+ and K^+ were successfully embedded in between VO_x layers produced from a vanadium triisopropoxide precursor. All of these have showed good electrochemical properties, with averaged specific capacities around 150 mAh/g over 100 cycles [114]. The theoretical capacity for these exchanged nanotubes is around 370 mAh/g if all vanadium is reduced to V^{3+} . This is unlikely, because totally reduction of V^{5+} to V^{3+} will bring strong structural deformations (collapsing) of the VO_x -NT structure. A specific capacity of 148 mAh/g

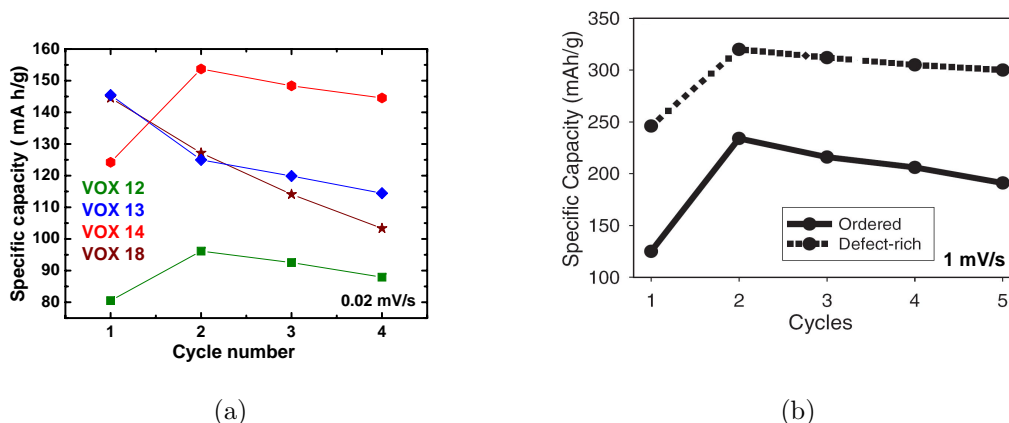


Figure 4.24: Specific capacities for: a) VO_x-NT; b) Ordered (solid line) and defect-rich (dashed line) vanadium oxide nanorolls [115].

to 310 mAh/g has been found for crystalline V₂O₅, depending on the rate of insertion/extraction [120, 121], compared to the theoretical value of 148 mAh/g [122].

For VO_x-NT#13 and #18 the first value of the specific discharge capacity was around 145 mAh/g. This value decreases in both cases over cycling, but a bit slower for VO_x-NT#13 than for #18. For the other two batches, #14 and #12, the values for the specific capacity are lower, 120 mAh/g and 90 mAh/g, respectively. These values could actually be higher, if the experiment would be performed on fresh electrode material. Anyway, instead of decreasing continuously as in the other two batches, the second cycle has a maximum specific capacity and then starts to decrease upon cycling. This kind of behavior was found in both ordered and defect-rich Na⁺-exchanged VO_x-nanorolls [115] (see Fig. 4.24). The theoretical capacity for one inserted Li is 140 mAh/g, 276 mAh/g for two inserted Li. Sun and coworkers found high capacity values of around 250-300 mAh/g for defect rich VO_x nanorolls. These values depend on the time spent for the ion-exchange process in order to obtain the Na⁺-exchanged VO_x-nanorolls. A short exchange time (10 minutes) would leave more residual amine molecules that would block the Li ions access to sites on the VO_x layers. A long exchange time (3 hours) leaves fewer amines, thus these materials have the highest capacity value for the first cycle. During Li deintercalation, due to small amount of surfactant molecules between the VO_x layers, some of the Li would remain in the structure. This lowers the reversible capacity for Li and decreases the number of available sites for lithium ions to occupy.

In Fig. 4.24(b) it is shown that not only amines play an important role in the electrochemical properties of a material but also the atomic and nanometer-scale structure have an effect on the specific capacity of these nanorolls. The defect-rich

ones always have superior specific capacities over the well ordered material. The specific capacity over cycling decreases less in the case of the defect rich nanorolls.

Therefore, it is probable that the results shown in Fig. 4.24(a) are due to the surfactant content influencing the electrochemical performance of our material. This surfactant can reduce the available surface area for redox reactions and can also form aggregates that would block the Li ions access to sites in the VO_x layers. These effects can be smaller if the nanotubes have cracks in the walls. This atomic-scale disorder would give a higher accessibility for Li ions and thus an increased specific capacity would appear.

Potentiostatic measurements

For potentiostatic measurements the same two-electrode setup was used. The potential was maintained constant until the current reached a previously established limit (C/t rate). After this current limit was reached the potential was decreased (for discharge) or increased (for charge) with 5 mV steps. The cells were mostly cycled between 2 V and 4 V. In Fig. 4.25, the voltage of the cell versus the amount of x in $\text{Li}_x\text{VO}_x\text{-NT}$ is shown. The cut off potentials were 2 V and 3.5 V, and the cell was cycled with $C/100$ (one complete discharge in 100 h). Around potential values of 2.8 V, 2.6 V and 2.4 V there is a sign of slight change in the curve slope. If this graph shows very clear plateaus in the potential range, then this is a sign of discrete phase formation during cycling. In Fig. 4.26, the derivative for the discharge and charge of the cell as a function of the applied potential is shown. If we compare this figure with Fig. 4.13 one can see that for the peak positions there are no drastic changes. In the first cycle there is a big peak around 2.1 V which might be a sign of formation of V^{3+} . This peak vanishes with cycling. In the second cycle the shoulder from ≈ 2.5 V vanishes as well. This was also found in the Fig. 4.13.

Fig. 4.27 illustrates the first three, the tenth and the fifteenth discharge-charge cycle of the VO_x-NT#13 electrode. The region where different slopes of the potential versus x in Fig. 4.25 might exist, correspond to a level of Li intercalation where only a single phase exists. This kind of behavior was also described for Li intercalation in nanostructures of orthorombic V_2O_5 [123]. Experiments performed on VO_x-NT#13 studied in this work, presented in Fig. 4.27, are compared with similar results on Ca-exchanged VO_x-NT, Fig. 4.28. In both experiments, VO_x-NT#13 and Ca-exchanged VO_x-NT, there are no distinct plateaus which would indicate the formation of different phases.

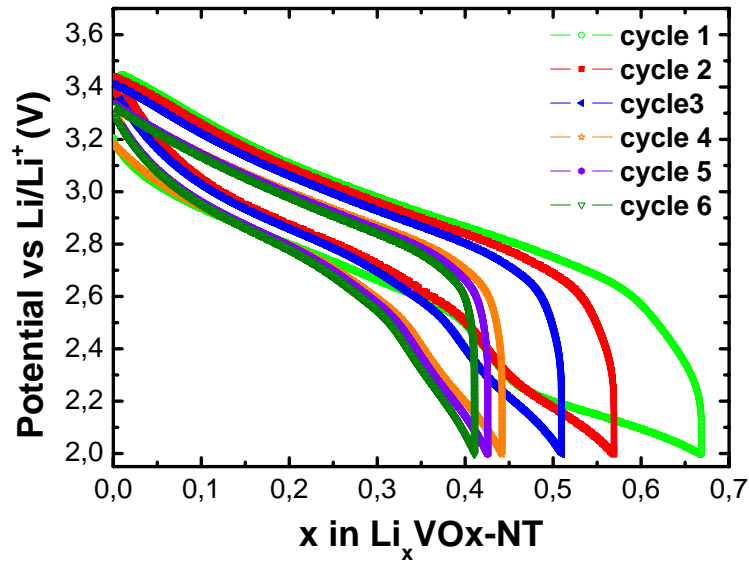


Figure 4.25: Voltage versus x in $\text{Li}_x\text{VO}_x\text{-NT}$ obtained from potentiostatic experiment on $\text{VO}_x\text{-NT}\#13$ with C/100 rate ($I=0.027\text{ mA}$).

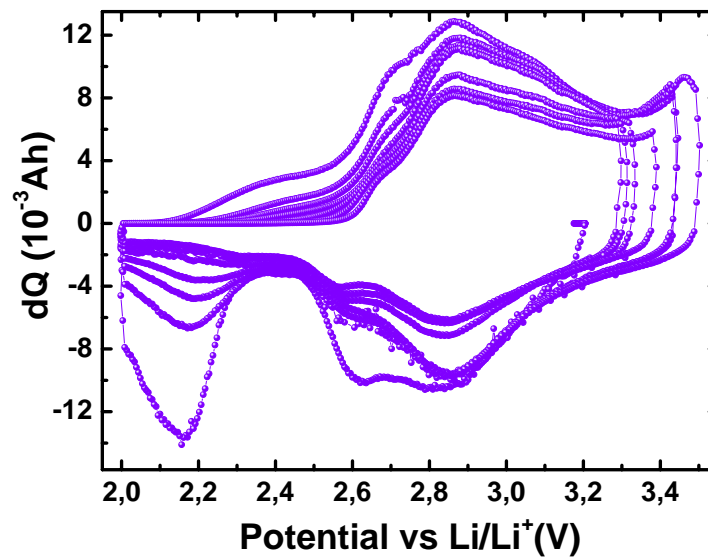


Figure 4.26: Incremental capacity versus cell potential obtained from potentiostatic experiment on $\text{VO}_x\text{-NT}\#13$ with C/100 rate ($I=0.027\text{ mA}$).

For the first discharge cycle in Fig.4.27, the specific capacity was found to be 130 mAh/g which corresponds to 0.66 Li intercalated into the structure. The second discharge cycle is slightly different than the first one possibly indicating an irreversible phase transformation of $\text{Li}_x\text{VO}_x\text{-NT}$ in the first cycle. The discharge

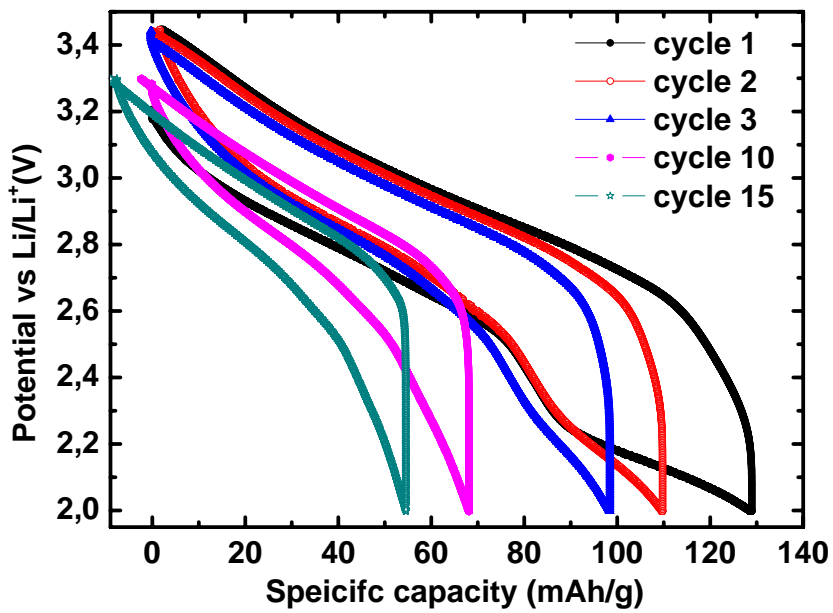


Figure 4.27: Electrode discharge/charge curves for VO_x-NT#13 for 1st, 2nd, 3rd, 10th and 15th cycle, recorded at $C/100$.

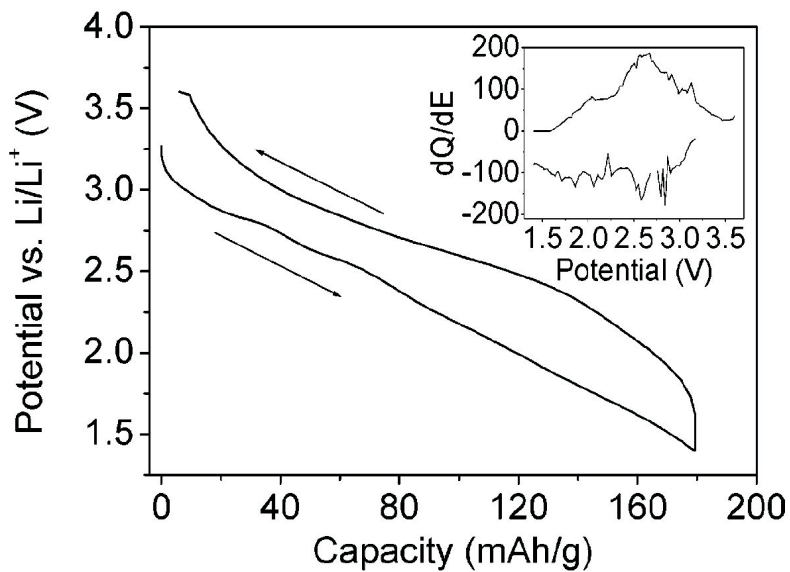


Figure 4.28: Electrode discharge/charge curve for Ca-exchanged VO_x-NT. The inset shows the derivative dQ/dE of the galvanostatic curves recorded at $C/7$. Results from Ref. [23].

capacity for the second cycle decreases to 110 mAh/g corresponding to 0.57 Li. In the third cycle this capacity reaches 97 mAh/g. For the following cycles the capacity is continuously decreasing until cycle 9 and then it maintains a constant

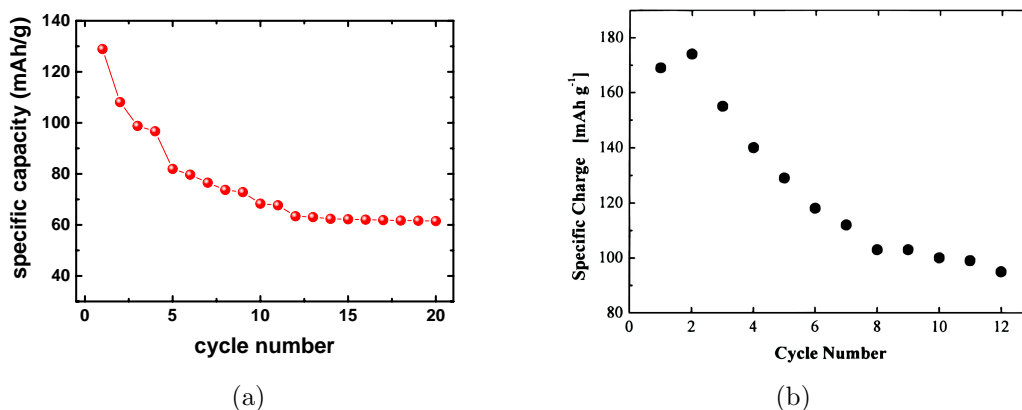


Figure 4.29: Variation of discharge capacities versus cycle number for a) VOx-NT#13 electrode; b) template free VOx-NT taken from Ref. [22].

value until cycle 20. Probably in the last cycles (9 – 20) the lithium intercalation/deintercalation process is reversible. The electrochemical behavior remains the same from cycle 4 till the end of cycling. These differences between the cycles show that the electrochemical properties are altered. Fig. 4.29(a) summarizes the decreasing of the capacity over cycling which is most likely due to destructive side reactions and/or phase transformations during the intercalation process. This indicates that the electrode cycle life would still need to be improved in this case, if the material is studied as a possible cathode material for Li battery technologies.

When comparing these results with literature (Fig. 4.29) a slightly higher initial discharge capacity value has been found for the results from Ref. [22]. The cycling dependence of the specific capacity is comparable. These results were obtained from template free VOx-NT and they are taken from potentiodynamic experiments performed at a scan rate of 0.05 mV/s. In the case of the template free VOx-NT the higher initial specific capacity value can be due to amines poverty in between the VOx-NT layers that diminish the Li intercalation/deintercalation process.

Experiments performed on VOx-NT#13 studied in this work, presented in Fig. 4.29(a) might be compared to Fig. 4.30, which displays results of a potentiostatic experiment on ion-exchanged VOx-NT [114]. The figures clearly differ, in the way that if in the case of VOx-NT#13 the discharge capacity decreases in time, for data of Nordlinder et al. they increase for the first 20 cycles. The authors assumed that insertion of Li⁺ ions into the nanotubes is diffusion limited. Therefore, the diffusion of Li ions further into the tubular material leads to an increase of capacity. Another explanation might be that the nanotubes contain cations that might be electrochemically active, therefore participating in discharge/charge of the material.

4 Electrochemically doped Vanadium Oxide Nanotubes

The last possibility is that in this first 20 cycles there is a continuous material modification. The fact that VO_x-NT with embedded amines instead of metal cations have lower electrochemical properties is known [118]. This might be due to less space for Li ions to be intercalated or deintercalated in the VO_x-NT containing amines between the layers. The amines are bulkier than the metal cations. Differences between Fig. 4.29(a) and Fig. 4.30 might also come from using different electrolyte. In the case of VO_x-NT#13 LiPF₆ was used, instead of LiBF₄ for metal cations exchanged VO_x-NT. Different electrolytes on the same material can give slightly different results [36]. Different C rates influence electrochemical performances as well [123]. An increased discharge rate reduces the degree of Li insertion, which decreases the discharge capacity of the electrode. These above information might be explanations for differences in between VO_x-NT#13 and Ca-exchanged VO_x-NT.

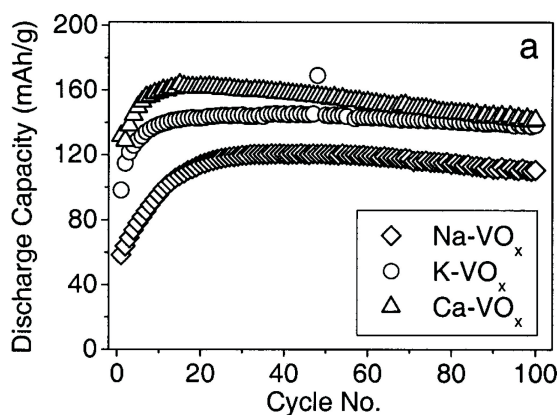


Figure 4.30: Discharge capacities for the ion-exchanged VO_x-NT, cycled with C/5 rate, results from Ref. [114].

Potentiostatic experiments were also performed on the VO_x-NT#12, which has a specific discharge capacity of ≈ 130 mAh/g in the first cycle. This value is preserved for the second cycle as well. For the third one the specific capacity increases to ≈ 140 mAh/g (see Fig. 4.31).

For VO_x-NT#18 potentiostatic experiment after CV was completed. For this reason, due to aging of the material the specific capacity values are small, without drastic changes over cycling. The incremental capacity versus the applied potential and the CV experiments performed on this batch look similar. The peaks are broader than for the other batches, underlying that this particular batch has specific structural deformations, different than the other studied VO_x-NT.

Potentiostatic experiment illustrated in Fig. 4.27 reveal a difference between the first three and following cycles of the experiment. Most of the cyclic voltammograms performed on all VO_x-NT show a difference between the first and following cycles in

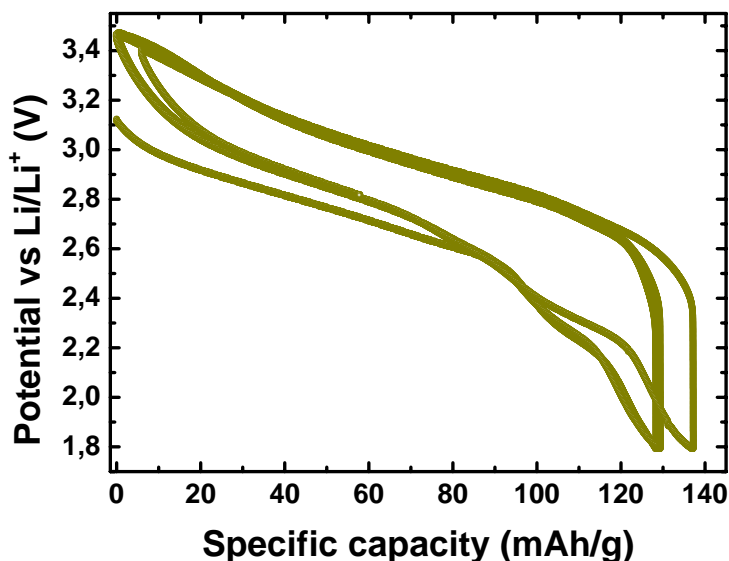


Figure 4.31: Potential versus specific capacity for VO_x-NT#12. Result of a potentiostatic experiment performed with a rate of $C/200$.

this kind of experiment. One can think that these differences appear from different intercalation process governing the beginning of an experiment, and its following cycles. For example, at the beginning of an experiment, Li⁺ ions are inserted in a quite disordered way between the VO_x layers. This might cause the interlayer distance to decrease. In a presumably second step of the intercalation process, Li⁺ ions diffuse to find a favorable site in the interlayer spaces of the structure, affecting the VO_x structure. This process for Li intercalation was also suggested for Ca-exchanged VO_x-NT studied by Nordlinder et al. [114].

In the case of all VO_x-NT electrodes studied here, a rather symmetric behavior of CVs as well as the potentiostatic studies implies that the discharge and charge of this material does not involve drastically structural rearrangements. There are still many things that might explain the differences between the behavior of all these batches. Slight contaminations of the electrolyte, composition of the electrode or assembling of the cell, that might give small differences for the experiments, can not be exclude. Firstly, not all samples were synthesized at the same time. VO_x-NT#5 looks similar to well ordered VO_x-NT. It also behaves different than the other VO_x-NT studied here. This particular batch was one of the first synthesized and used in this work. As the batch number increases the preparation time is later. This, and the fact that some of the samples were not kept secured from moisture might have influenced the electrochemical properties. It is known that the water content in this material might influence its electrochemical behavior [124]. Because

the water might hold some interlayer spaces of the structure, the number of spaces available for lithium intercalation/deintercalation might decrease. This, of course, leads to lower discharge/charge rates. The water content might also influence the ratio between V^{5+} and V^{4+} . Electrochemically cycling might be influenced by different amount of organic amines between the layers as well as the wall structure or size of the nanotubes. Different amounts of amines can induce cracks in the tube walls. More rigid amine chains might reduce the available surface area for redox reactions [115]. They can also form aggregates which might block the accessibility of Li ions. Different sizes of the nanotubes can give different Li diffusion distances. Short distances give high surface area, a very good property for material studied for Li ion battery technology [123]. A higher surface area lowers Li^+ insertion rate density in the intercalation process. This postpones the decreasing of the capacity. In other words, vanadium oxide nanotubes represent an extremely complex system. The electrochemical behavior of this compound can be affected by many parameters. The size of the nanotubes, together with the distances between the VOx layers affected by the number of amines or the water content which modifies the oxidation state of the V ions are some of the parameters influencing the performances as a cathode material of VOx-NT. The results presented in this subsection are satisfactory, comparable with similar results from the literature. Although the existence of the amines in this VOx-NT is sure, the specific capacity values are comparable to ones obtained on template free VOx-NT, indicating that the amines do not block completely the Li intercalation/deintercalation process.

Electrochemical synthesis

The previous described electrochemical studies on VOx-NT batches helped the understanding of the electrochemical properties of this material. From the cyclic voltammetry and potentiostatic studies presented above, it can be suggested that in order to obtain interesting samples for magnetization studies, the potential region around 2.9 V is the region where the main redox reaction takes place. Here, electron transfer takes place in which the nonmagnetic V^{5+} reduces to magnetic V^{4+} . In this way, the magnetic sites in the VOx-NT structure would increase, and therefore the paramagnetic signal of the VOx-NT would modify to a ferromagnet or superparamagnet as it will be described in the next section of this chapter.

For the materials that were studied from a magnetization point of view, either galvanostatic or potentiostatic techniques were applied in order to obtain the desired doping level. In the case of the galvanostatic technique, a constant current correlated with C/100 rate was applied. A condition for the potential not to drop lower than

2 V was fixed. In the case of VO_x-NT batch#5, four doping levels were prepared. The current was kept constant until $x = 0.05, 0.1, 0.15$ and 0.6 in Li_{*x*}VO_x-NT was reached. In the case of the first three samples, the potential reached 2.97 V, 2.79 V and 2.67 V respectively. For $x = 0.6$, this value was 2 V, the value for the limited potential condition.

For VO_x-NT batch#13, five different doping levels were synthesized. These were $x = 0.05, 0.1, 0.155, 0.2$ and 0.4 in Li_{*x*}VO_x-NT. These compounds were obtained under potentiostatic conditions. The potential was swept, starting from the initial potential value of around 3.4 V in all cases. Then this potential was decreased by 5 mV each time the current was lower than $C/200$. At the end of the Li intercalation the potential was between 3.1 V and 2.9 V. All the redox reactions in these regions where most probably from V⁵⁺ reducing to V⁴⁺, proved proved also by an increase of the magnetization values. After these doping levels were achieved, the powder was recovered from the Swagelok cell, washed with DMC using a centrifuge and dried for approximately one hour. Then these powders were kept in quartz tubes as it was shown in Chapter 3.

4.2.2 Magnetic properties of Li_{*x*}VO_x-NT

Magnetic properties of vanadium oxide

There are approximately 60 ways of combining V and O in order to obtain vanadium oxide materials with interesting physical properties and more important very useful applications. This wide variety of properties is given by the mixed valency that vanadium can have, and the possibility of changing the stoichiometry in the material. Further on, magnetic aspects in some vanadium oxides will be reviewed. VO₂ experiences a significant, thermally induced reversible metallic-to-insulating phase transition around 67 °C which influences optical, electrical and magnetic properties of the material [125, 126]. If VO₂ nanorods are heated to 800 °C in a reducing atmosphere it is transformed to V₂O₃ nanorods. At room temperature, V₂O₃ is described by a rhombohedral paramagnetic metal, while after cooling down below the transition temperature of 166 K it converts to a monoclinic antiferromagnetic insulator [127]. Santulli and coworkers established for V₂O₃ nanorods that the magnetic susceptibility above the transition temperature has AFM character, and it is governed by paramagnetic V moments. Below this temperature the interior of the nanoparticle is AFM while the spins on the surface are paramagnetic. At very low temperatures, there is an increase of the magnetic susceptibility due to the effect

of surface spins [126]. By doping VO_2 with Cr, the system exhibits new insulating phases at low temperatures suggesting that its physics is very close to the Mott-Hubbard insulator in which V atoms behave as spin-1/2 Heisenberg chains [128–130]. On the other hand, the VO_2 nanorods present different physical properties than the bulk counterpart. An interesting room temperature mixed phase of an insulating monoclinic and tetragonal structure, and a broad low-temperature magnetic transition strongly related to the displacement of V atoms were reported [131].

Vanadium oxide bronze, $\beta\text{-NaV}_6\text{O}_{15}$ has an AFM ordered ground state, while $\beta\text{-CaV}_6\text{O}_{15}$ is non magnetic. This difference was related to the density of V^{4+} ions. It is also known that the mixed valency material $\text{A}_x\text{V}_2\text{O}_5$ with A alkali or alkaline earth and metals have magnetic and electric properties depending on the x concentration of the cations [132]. Kondo et al. reported for the first time a transformation from localized moment magnetism to heavy Fermi liquid behavior in the case of metallic LiV_2O_4 with normal spinel-structure, containing equivalent V ions in slightly distorted octahedral coordination by oxygen [133]. The compound has an ideal tetrahedral arrangement of the $3d$ electrons, thus making it a heavy-fermion candidate in frustrated magnets [134].

V_3O_7 and V_6O_{14} with different organic materials between the layers are formed by one dimensional zig-zag chains of edge-sharing VO_5 pyramids. These systems exhibit spin-gap behavior explained by a simple model of isolated spin dimers of V^{4+} . High values of excitation-energy Δ or the exchange coupling energies J arise from the kinetic exchange mechanism between the $3d_{xy}$ electrons of V^{4+} ions in the middle of the edge-sharing VO_5 pyramids where oxygens are on the same side of the basal planes [135].

Magnetic properties of undoped and lithium doped $\text{VO}_x\text{-NT}$ ($\text{VO}_x\text{-NT}\#5$)

The magnetic properties of the $\text{VO}_x\text{-NT}$ that will be discussed here have been analyzed in detail elsewhere [136, 137]. Vanadium ions have mixed valency in this material as mentioned before, with an average valence count of $\sim +4.4$ (i.e. $x \approx 2.2$) [28, 138] obtained from EELS studies. Approximately 60 % of magnetic V^{4+} ($3d^1, S = 1/2$) and 40 % of nonmagnetic V^{5+} ($3d^0, S = 0$) sites are present in the VO_x layers. The magnetic sites were attributed to either individual spins, strongly gapped antiferromagnetic dimers or trimers [136]. Doping of $\text{VO}_x\text{-NTs}$ with either holes (iodine) or electrons (lithium) yields to a nonlinear and hysteretic magnetization response to applied magnetic fields suggesting the occurrence of ferromagnetism that persists even above room temperature [39]. This represents a very interesting result for a small spin 1/2, exhibiting novel functionalities in nanostructured oxides.

The temperature dependence of the magnetic susceptibility of the undoped VO_x-NT was measured between 2 K and 500 K but only the results up to 370 K will be analyzed due to material deterioration in high temperatures. The field dependence of the magnetization was measured at low temperatures between -5 T and 5 T. The temperature dependence of the magnetic susceptibility can be described by a Curie-like behavior at temperatures lower than 100 K. Above this temperature a strong deviation persists. As described earlier in this chapter, the VO_x-NT layers contain three different V sites, V(1) and V(2) in the zig-zag chains, octahedrally coordinated by the O and V(3), tetrahedrally coordinated and positioned in between the zig-zag chains. The V(3) it is attributed to magnetic V⁴⁺ while the V(1) and V(2) could be either V⁴⁺ or V⁵⁺ [136]. The spins in the octahedral sites, in the zig-zag chains are strongly antiferromagnetically correlated. When analyzing the data from the temperature dependence of the magnetic susceptibility, Vavilova and coworkers established that the antiferromagnetism at temperatures higher than 100 K can be described in terms of the noninteracting AFM dimers model. On the other hand, the low temperature magnetic response is governed by free spins as well as longer chain fragments, i.e. trimers. The vanadium ions coupled in dimers exhibit a spin gap of order of 700 K. The ratio between V⁴⁺ and V⁵⁺ was suggested by EELS experiments (60%: 40%) [28]. This ratio has been proved also by magnetization and ⁵¹V-NMR [136]. The Curie-Weiss fit ($\chi = \frac{C}{T - \Theta} + \chi_0$ [139]) for temperature ranges from 2 K to approximately 100 K gave a very small Θ of -4 K. χ_0 should have a small value, and it represents a temperature independent contribution to the magnetic susceptibility of the Van-Vleck paramagnetism of the V ions. In the undoped VO_x-NT, $\chi_0 = 7 \cdot 10^{-5}$ emu/mole is found.

Fig. 4.32 illustrates measurements of the temperature dependence of the magnetic susceptibility for both undoped and doped VO_x-NT performed in an applied field of 1 T. There is a clear difference between the undoped compound, with the lowest magnetic response and the set of 0.05, 0.1, 0.15, and 0.6. Moreover, the Li_{0.1}VO_x-NT has a much higher magnetic response than the materials with other doping levels. By doping the VO_x-NT system with lithium, one expects that some of the non-magnetic V⁵⁺ ions will be reduced to the magnetic ones, i.e. V⁴⁺. One might speculate that some of the V⁴⁺ could be reduced further to V³⁺. This situation is however unlikely due to low potential window needed for this reaction to take place which has to be lower than the one used in the present electrochemical synthesis. The magnetic moment at lower temperatures increases gradually with increasing the doping level in the Li_{*x*}VO_x-NT. In the Li_{0.1}VO_x-NT the magnetic response at low temperatures is roughly seven times higher than in the other lithium doped compounds. For all doping levels, the Curie Weiss fit was performed. For Li_{0.1}VO_x-

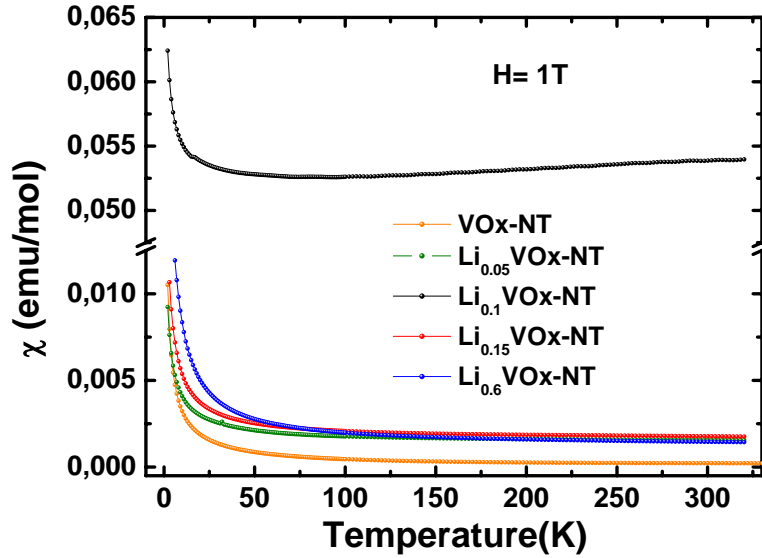


Figure 4.32: Temperature dependence of the magnetic susceptibility for $\text{Li}_x\text{VOx-NT}$ measured in 1 T applied field. The studied doping levels were $x = 0, 0.05, 0.1, 0.15,$ and 0.6 .

NT this fit was performed in the temperature range of 2 K up to approximately 100 K. For the other doping levels the fit was performed for the entire temperature regime without significant changes in the fittings parameters. The results are shown in Table. 4.1.

| $\text{Li}_x\text{VOx-NT}$ | C (emu · K/mol · Oe) | θ (K) | χ_0 (emu/mole) | p_{eff} ($\mu_B/\text{f.u.}$) |
|----------------------------|------------------------|--------------|---------------------|--|
| $x = 0.05$ | 0.0332 | -2.36 | 0.0014 | 0.51 |
| $x = 0.1$ | 0.0338 | -1.29 | 0.052 | 0.52 |
| $x = 0.15$ | 0.044 | -1.96 | 0.0016 | 0.59 |
| $x = 0.6$ | 0.088 | -2.32 | 0.0011 | 0.83 |

Table 4.1: Results of fitting the Curie-Weiss law to the magnetic susceptibility of $\text{Li}_x\text{VOx-NT}$ with $x = 0.05, 0.1, 0.15$ and 0.6 .

As these results show, the Curie constant C , the Curie-Weiss temperature θ or χ_0 do not strongly change with doping. Again, $\text{Li}_{0.1}\text{VOx-NT}$ makes a discordant note, in the way that for this doping level the value of χ_0 is much higher than in the other doping levels. The only parameter that does change for $x \neq 1$ is the effective magnetic moment p_{eff} of the V spins. The effective moment gradually increases with doping, as indicated by the Table. 4.1 from $0.51\mu_B$ for $x = 0.05$ to $0.83\mu_B$ for the highest doping level $x = 0.6$. In fact, this is the expected qualitative result, that, by doping, more magnetic moments are created. For the high temperature regime of $\text{Li}_{0.1}\text{VOx-NT}$, one could think to follow the same data interpretation as for the

undoped VOx-NT in the same temperature regime, as described by Vavilova et al. By fitting this data with a model of strongly interacting AFM dimers, the obtained results were unreasonable. Although in the undoped compound, there is a clear evidence for these strong AFM dimers in temperature above 100 K, it seems like, by doping this effect vanishes.

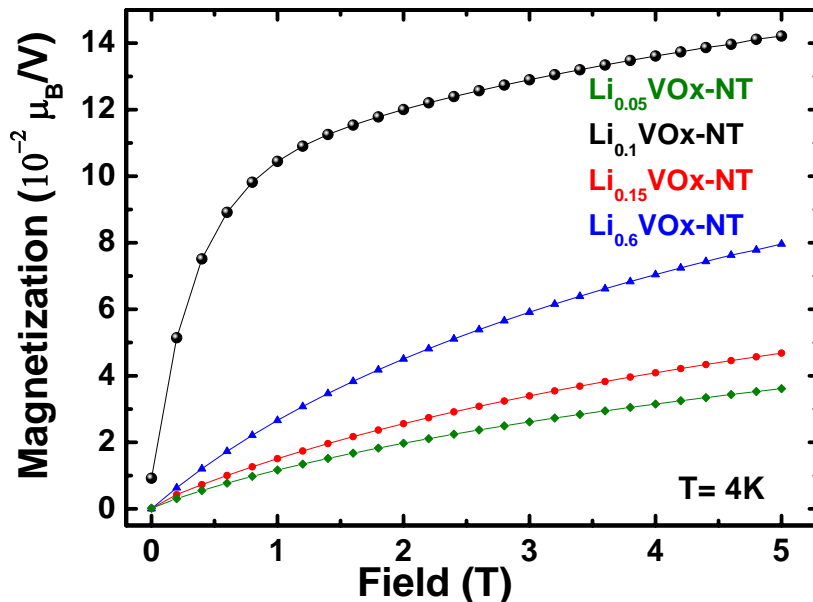


Figure 4.33: Field dependence in the magnetization of $\text{Li}_x\text{VOx-NT}$ measured at 4.2 K for $x = 0, 0.05, 0.1, 0.15,$ and 0.6 .

Fig. 4.33 shows the field dependence of the magnetization measured at 4.2 K for undoped and all the doped VOx-NT. Clearly, the $x = 0.1$ strongly differs from the magnetic response at other Li contents, as also described by the temperature dependence of the susceptibility. In order to analyze this field dependence of the magnetization, the data can be fit by a model. The magnetic response at low temperatures can be described by a linear contribution together with a nonlinear contribution. The equation for this model is the following: $M(H) = \chi_{lin}H + N_B N_A \mu_B B_s(x)$. The first part represents the linear and the second the nonlinear contribution to the magnetization results shown in Fig. 4.33. N_B represents the number of quasifree spins involved in this description. χ_{lin} is the linear contribution to the $M(H)$ curve. B_s represents the Brillouin function with $x = H + \lambda M$, where λ represents the mean-field parameter. The nonlinearity comes from spin alignment with the applied magnetic field in this (low) temperature regime. Important for this work was the evolution of the linear contribution to the field dependence of the magnetization and the number

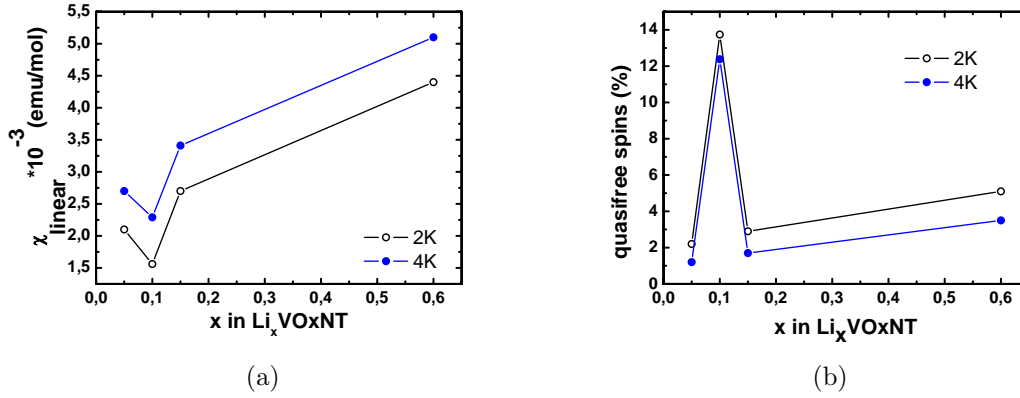


Figure 4.34: Results of the Brillouin fit at low temperatures, for $\text{Li}_x\text{VO}_x\text{NT}$: the evolution over doping of: a) linear contribution to $M(H)$ and b) number of quasifree spins.

of the quasifree spins. The results are shown in Fig. 4.34. The linear contribution gradually increases with the doping level. In the case of the measurement performed at 4 K, χ_{lin} increases from 2.7 emu/mol for $\text{Li}_{0.05}\text{VO}_x\text{NT}$ to 5.1 emu/mol for $\text{Li}_{0.6}\text{VO}_x\text{NT}$. The number of quasifree spins increase as well, from 1.2% for the lowest doping level, to 3.5% for the highest doping level. The $\text{Li}_{0.1}\text{VO}_x\text{NT}$ will be discussed and analyzed in details later on.

Fig. 4.35 illustrates the field dependence of the magnetization measured at 300 K for undoped and $\text{Li}_x\text{VO}_x\text{NT}$. Except the very strong magnetic response for 10% doping level that will be discussed later on, an increasing of the number of magnetic sites with doping is visible. As the inset shows, for $\text{Li}_{0.15}\text{VO}_x\text{NT}$ an interesting feature can be seen in applied fields lower than 0.5 T. As it will be shown in the last part of this chapter, this kind of behavior was also found for a different studied VO_xNT batches. More details will be given there, where the field dependence of the magnetization has been measured in smaller steps

From the temperature dependence and field dependence of the magnetic response of $\text{Li}_x\text{VO}_x\text{NT}$, one can clearly see that the magnetic response increases with lithium doping (electrons). This was proved by gradually increasing of the effective magnetic moment obtained from the Curie fit. The strong antiferromagnetism given by interactions within dimers, found in the undoped case, is not evident in the doped vanadium oxide nanotubes.

In order to obtain insights into the origin of the unusually strong magnetism found in $\text{Li}_{0.1}\text{VO}_x\text{NT}$, a complex experimental study with three different local spin probe techniques, namely, electron spin resonance (ESR), nuclear magnetic resonance (NMR) and muon spin relaxation/rotation (μSR) spectroscopies were performed.

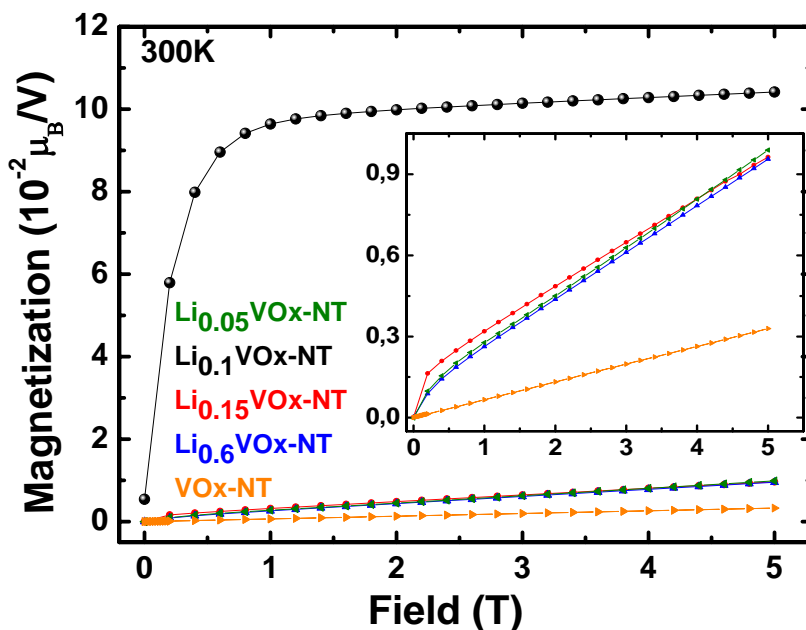


Figure 4.35: Field dependence of the $\text{Li}_x\text{VO}_x\text{-NT}$ magnetization measured at 300 K for $x = 0, 0.05, 0.1, 0.15,$ and 0.6 .

$\text{Li}_{0.1}\text{VO}_x\text{-NT}$ For a particular concentration of the Li-dopant a large magnetization M which can be easily saturated even at room temperature by a magnetic field $\mu_0 H$ of about 1 T is present in the sample. μSR and NMR measurements give evidence for a bulk nature of the effect. NMR data suggest that the magnetization is not uniform throughout the sample and that strongly magnetic regions are formed around the intercalated Li sites. ESR experiments reveal a sharp signal that bears essential features of a superparamagnetic resonance. Li intercalation appears to affect the charge disproportionation and hence the spin states and magnetic interactions in the rolled-up VO_x layers. It appears that for particular doping levels, nanosized interacting spin clusters that behave similar to superparamagnetic nanoparticles are formed.

The field dependence of the $\text{Li}_{0.1}\text{VO}_x\text{-NT}$ measured at $T=300\text{ K}, 50\text{ K}, 2\text{ K}$ together with the undoped $\text{VO}_x\text{-NT}$ measured at $T=300\text{ K}$ are shown in Fig. 4.36. The main result of the magnetization study is the observation of a non-linear behavior for the doping level $x = 0.1$. At 300 K, the $M(H)$ curve practically saturates in a field of $\sim 1\text{ T}$ at a value of $\sim 0.1\mu_B$ per V site with a small subsequent linear increase at higher fields. The data at 50 K and 2 K in Fig. 4.36 illustrate that at low T this saturation is superimposed by a stronger linear contribution to the magnetic response. In the inset of Fig. 4.36 a part of the field dependence of the magnetization measured at

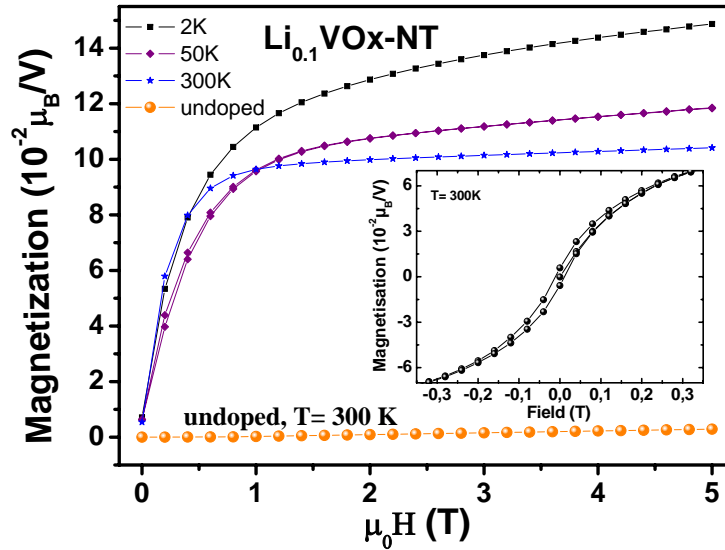


Figure 4.36: Field dependence of the magnetization of $\text{Li}_{0.1}\text{VO}_x\text{-NT}$ ($T=300\text{ K}$, 50 K , 2 K and $x = 0$ ($T=300\text{ K}$)). The inset shows part of the $M(H)$ loop, at $T=300\text{ K}$, for $x = 0.1$.

$T=300\text{ K}$ is shown. A small hysteresis can be seen with the coercivity $2H_c \sim 23\text{ mT}$. Further insight into the magnetic properties is provided by zero field (ZF) μSR data. Selected ZF- μSR spectra obtained on $\text{Li}_x\text{VO}_x\text{-NT}$ with $x = 0$ and $x = 0.1$, i.e. for the pristine and the magnetic materials, are shown in Fig. 4.37. For $x = 0$, both at 300 K and at 20 K the data show only a small decrease of the asymmetry signal $A(t)$ at short times. This clearly implies the absence of magnetic order in this temperature range. On a longer time scale of μs , there is a decrease due to the slow relaxation which we attribute to nuclear and fast fluctuating electronic magnetic moments.

The most important result of the ZF- μSR study on $\text{Li}_{0.1}\text{VO}_x\text{-NT}$ is the observation of a significant and rapid loss of asymmetry at early times. As displayed in Fig. 4.37(b), most of the relaxation occurs already during the dead time of the spectrometer ($\approx 5\text{ ns}$). The full asymmetry scale was defined by a subsequent measurement of a nonmagnetic compound. Such a rapid relaxation clearly indicates that a significant fraction of the muons experiences a local quasi-static magnetic field. The absence of an oscillating signal proves a broad static magnetic field distribution within the compound. Assuming for a quantitative analysis that a fraction of a muons experiences both the nuclear and the a electronic static magnetic field, the data are described by $A(t) = (1 - a) \cdot e^{-0.5(\sigma_{nuc}t)^2} + a \cdot (2/3e^{-\lambda_T t} + 1/3e^{-\lambda_L t})$. Here σ_{nuc} and $\lambda_{T,L}$ are muon relaxation rates due to interaction with nuclear and

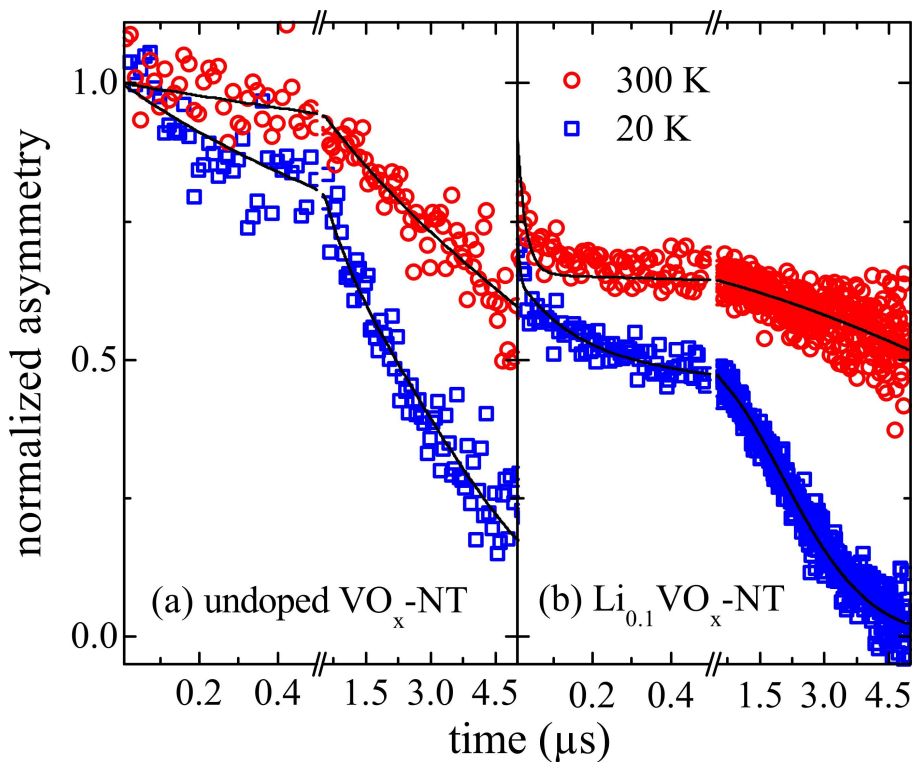


Figure 4.37: Selected ZF- μ SR spectra at 300 K and 20 K of $\text{Li}_x\text{VO}_x\text{-NT}$ with (a) $x = 0$ and (b) $x = 0.1$. The solid lines denote the evaluation of the data with a function as described in the text. Note the change of the timescale at $0.5\mu\text{s}$.

electron spins, respectively [140]. This analysis implies that $\sim 2/3$ of the muons in $\text{Li}_{0.1}\text{VO}_x\text{-NT}$ experience a static magnetic field originating from a magnetic ordered volume fraction at or in the vicinity of the muon stopping site(s). (Due to the electrochemical doping process, $\sim 17\%$ of the sample mass is paramagnetic carbon which contributes only to the slowly relaxing signal). The μ SR data hence unambiguously proof the bulk character of the magnetism found in the static magnetization.

NMR studies on ^{51}V and ^7Li shed further light on the effect of Li doping on the local magnetic properties. The ^{51}V NMR data in Fig. 4.38 a) reveal a gradual increase of the relative intensity of the low-field fast-relaxing shoulder of the ^{51}V signal at $\sim 9.16\text{ T}$ upon doping. Since this part of the spectrum is associated with the response of the magnetic ions' nuclei, shifted due to hyperfine interaction from the central slow-relaxing nonmagnetic V^{5+} peak at $\sim 9.16\text{ T}$ [136], its growth indicates an increasing fraction of magnetic vanadium ions upon Li intercalation and confirms that the doping process affects the whole sample. Though magnetic ordering usually creates a shift or splitting of the NMR spectrum, neither was observed for the ^{51}V signal for the $\text{Li}_{0.1}\text{VO}_x\text{-NT}$ sample in a sufficiently wide field range. The absence of

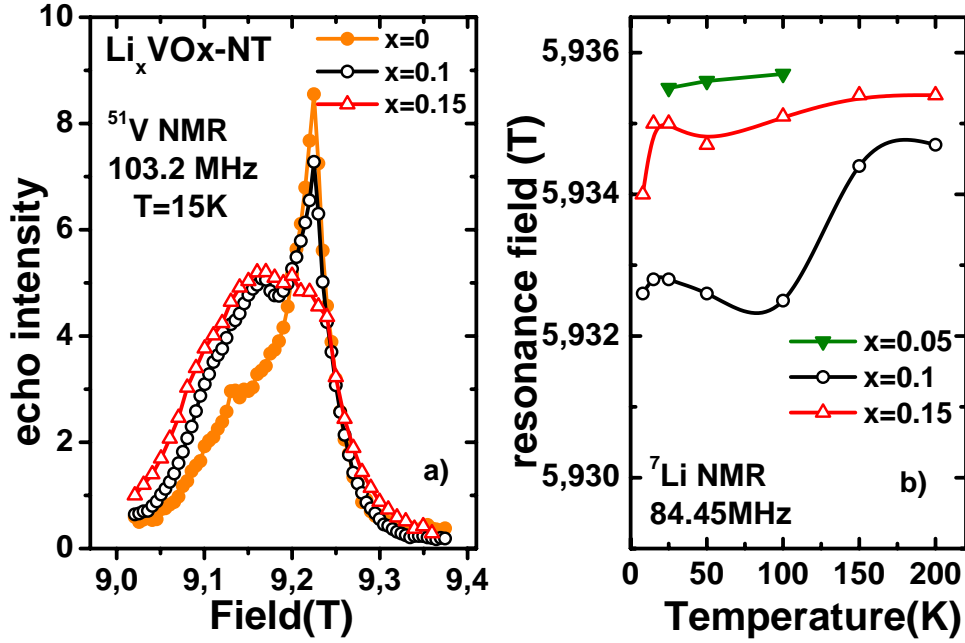


Figure 4.38: a) Low temperature ^{51}V NMR spectra and b) Temperature dependencies of the resonance field of ^{7}Li NMR for $\text{Li}_x\text{VO}_x\text{-NT}$: $x = 0$ (orange), 0.05 (green), 0.1 (black) and 0.15 (red). Lines are guides to the eye.

the significant loss of its intensity suggests that the large part of V ions does sense the charge doping but not the internal field.

The situation with ^{7}Li NMR is different: The resonance field of the signal steadily changes with doping. However, the line shift for $x = 0.1$ is much larger compared to $x = 0.05$ and $x = 0.15$ (Fig. 4.38 b)). This suggests the presence of an internal field at the Li sites only for the strongly magnetic $\text{Li}_{0.1}\text{VO}_x\text{-NT}$. The absence of a second unshifted ^{7}Li line at the expected place between the line positions of $\text{Li}_{0.05}$ and $\text{Li}_{0.15}$ samples indicates that practically *all* Li nuclei experience internal magnetic fields.

The ESR study of undoped $\text{VO}_x\text{-NTs}$ at a frequency $\nu = 9.5\text{GHz}$ reveal similar data to results in [141], i.e. a spectrum comprising two overlapping resonance lines with slightly different g -factors of ~ 2.0 and ~ 1.97 . The first line can be assigned to quasi-free spins associated with V^{4+} ($S = 1/2$) ions in the tetrahedral position. The second line is due to V^{4+} ions in the distorted octahedral coordination which are coupled magnetically into dimers and trimers [136]. In $\text{Li}_x\text{VO}_x\text{-NTs}$ with $x = 0.05$, 0.1, 0.15 and 0.6 a systematic evolution of the lines in the ESR spectrum with increasing the Li doping gives evidence for the increasing number of magnetic V^{4+} ions, and a reduction of the contribution related to spin dimers and trimers, in agreement with the magnetization data (see above). We note that the carbon black used

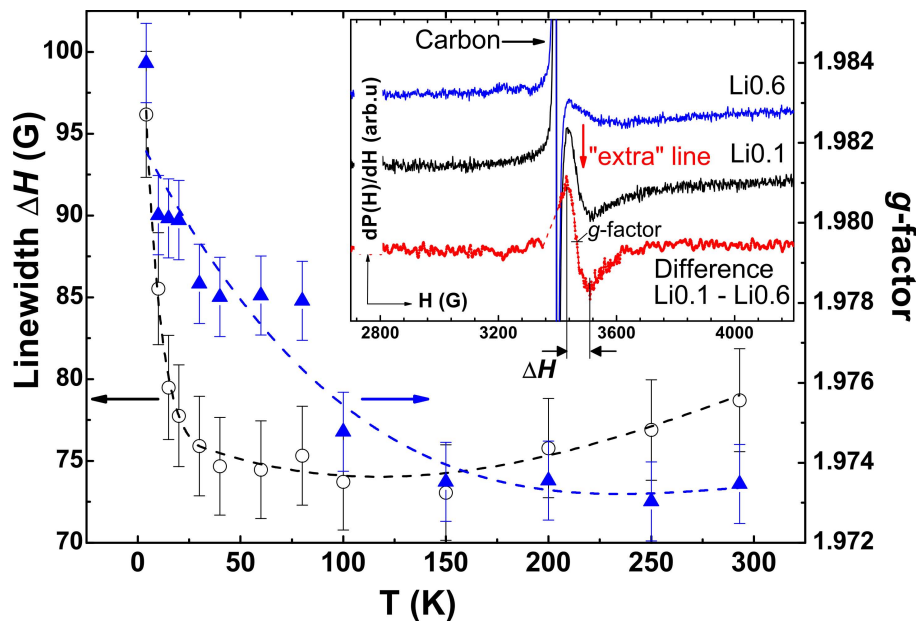


Figure 4.39: Inset: ESR spectra (field derivative of absorption) of $\text{Li}_x\text{VO}_x\text{-NT}$ for $x = 0.6$ (top) and 0.1 (middle) at $T = 300$ K. The "extra" narrow line which is specific for the strongly magnetic sample with $x = 0.1$ (marked by the arrow in the middle spectrum) is singled out by subtracting the top from the middle spectrum (bottom curve). The central sharp line is due to the carbon additive. Main panel: T -dependence of the width ΔH and the g -factor of the "extra" line in the ESR spectrum of $x = 0.1$. Dash lines are guides for the eye.

as a conductive additive for the preparation of Li-doped samples partially screens the penetration of microwaves into the interior of the sample thereby reducing the signal-to-noise ratio and superimposes an additional ESR line (Fig. 4.39, inset). The latter can be identified by measuring the carbon additive separately and accurately subtracted from the spectra. The central result of the ESR study is the observation of an 'extra' narrow resonance line in the strongly magnetic $x = 0.1$ sample. Despite the disturbing effect of the carbon line, the 'extra' line is clearly visible in the raw data (Fig. 4.39, inset, middle curve) and can be accurately singled out, e.g., by subtracting from the $x = 0.1$ spectrum the spectrum of a weaker magnetic sample with a different Li content (Fig. 4.39, inset, bottom curve). The width of this 'extra' line $\Delta H \sim 70$ G is significantly smaller compared to the signals from paramagnetic V^{4+} ions whereas the g -factor of ~ 1.98 is similar. Both ΔH and g change little in a broad T -region above ~ 40 K-70 K and become temperature dependent at lower T (Fig. 4.39). As will be discussed below, this narrow signal is directly related with the ferromagnetic-like behavior of the $x = 0.1$ sample.

Uniform long-range magnetic order in the low-spin ($S = 1/2$) vanadium oxides is not competitive at high temperatures with thermal fluctuations and/or insulator-to-

metal transitions (see, e.g., [142]). A ferromagnetic-like magnetization up to room and even higher temperatures is in particular unexpected. However, in the case of VO_x-NTs an alternative cluster scenario of ferromagnetism is clearly corroborated by μ SR and NMR results presented above. μ SR data yield about 2/3 of the magnetic volume fraction and a broad distribution of static magnetic fields within the sample. The absence of an appreciable shift of the ⁵¹V NMR signal in the ferromagnetic sample suggests that it originates from the regions outside the ferromagnetic clusters. The ⁵¹V-NMR line shift from the nuclei inside the clusters is expected to be as big as in magnetically ordered compounds, hence displacing the signal out of the observation range (see e.g. Ref. [143]). Furthermore, owing to a possible distribution of the clusters' size, as also suggested by the μ SR data, this signal could be very broad and thus practically undetectable. On the other hand, the ⁷Li-NMR data give clear evidence that ferromagnetism is confined to regions around the lithium site which yields a shift of the ⁷Li-NMR line by the internal magnetic field inside the cluster.

Thus one can argue that the Li which is intercalated between the vanadium oxide layers in the walls of VO_x-NTs [138] may play a role of nucleating centers for spin clusters of different size. In fact, the magnetization data (Fig. 4.36) bear features characteristic of a magnetic response of superparamagnetic particles with a broad size distribution, such as, e.g., samples of ultra-fine γ -Fe₂O₃ particles studied in Ref. [144]. Specifically, the small hysteresis in $M(H)$ at room temperature suggests the presence of large clusters with a blocking temperature $T_B > 300$ K. At higher external fields they are already saturated and the observed finite slope of $M(H)$ in this field regime is mainly determined by smaller unblocked superparamagnetic clusters ($T_B \ll 300$ K) [144]. The sharp ESR line with the spin-only paramagnetic resonance field $H_{res}^{par} = h\nu/g\mu_B$ observed in the strongly magnetic Li_{0.1}VO_x-NTs sample (Fig. 4.39) can be straightforwardly assigned to a resonance response of those small unblocked clusters. Above T_B the anisotropy field, that otherwise produces a shift and broadens the signal, is averaged due to thermal fluctuations yielding a narrow line at H_{res}^{par} (see, e.g. Ref. [145]). At low temperatures one can consider the shift of the effective g -factor from the spin-only value and the increase of the width of this signal (Fig. 4.39) as an indication of approaching the T_B of the resonating superparamagnetic clusters. According to the study of the effect of the particle size on the ESR response in Ref. [146], for small particle size (≈ 5 nm) the spectrum is defined by an isotropic and unshifted narrow line. In contrast, for a large particle size (≈ 10 nm) the associated anisotropy field is much stronger, therefore, thermal fluctuations even on a room temperature scale cannot overcome the anisotropic orientation of the magnetic moments. As a result, the spectrum is broad and shifted

towards lower fields due to the influence of the remaining orientational anisotropy. Thus, in the case of a broad size distribution, the ESR response of the blocked clusters in $\text{Li}_{0.1}\text{VOx-NTs}$ could be smeared out and become unobservable, in particular, also due to the limited sensitivity caused by the carbon additive as mentioned above.

Obviously, local charge and structural distortions around an intercalated Li^+ ion as well as nanostructurization of VOx may be crucial for the nucleation of ferromagnetic clusters in VOx-NTs . In this respect one can find a striking similarity with high temperature ferromagnetism (HTFM) with $T_c > 300\text{ K}$ recently observed in nanostructured diluted magnetic semiconductors (DMS) (see, e.g. [147, 148]). Adding a small percentage of magnetic TM ions to nanocrystals [147] or nanowires [148] of nonmagnetic ZnO yields a robust HTFM that was not achieved by doping the bulk ZnO . The occurrence of structural inhomogeneities on the nanometer scale concomitant with the charge localization are the key prerequisites for this remarkable effect. For example, in Ni:ZnO nanocrystals, just by tuning the aggregation of nanocrystals, one obtains HTFM with a T -independent saturation value and a small coercivity, very similar to our findings [147]. The stabilization of HTFM in DMS has been discussed theoretically in terms of collective polaronic effects [149, 150], namely that bound interacting ferromagnetic polarons may be formed due to exchange interaction of localized charges with magnetic impurities, in particular in the presence of defects. One can conjecture a possible relevance of this scenario to VOx-NTs in view of some apparent similarities with DMS: (i) - the current-voltage characteristics of individual tubes reveals a semiconducting behavior with conductivity decreasing upon Li doping [39]; (ii) - electron doping due to the Li intercalation creates additional spin centers and (iii) - locally distorts the structure. A delicate balance between these factors controlled by the Li intercalation may be the reason for a strong sensitivity of the observed effect to the Li content. At small doping levels the amount of nonmagnetic V^{5+} ions (which are the 'holes' in the magnetic subsystem) is big enough to prevent the formation of spin clusters. On the other hand at large Li dopings VOx-NTs turn to a uniform rolled up spin-1/2 plane with predominantly antiferromagnetic interactions which could be much less sensitive to a perturbing influence of Li-caused defects.

Doping dependence of the magnetic response at room temperature (VOx-NT#13) Magnetization experiments were performed also on different batches of vanadium oxide nanotubes. All the results above were performed on batch #5, which, as also shown by the electrochemical experiments behaves different than the

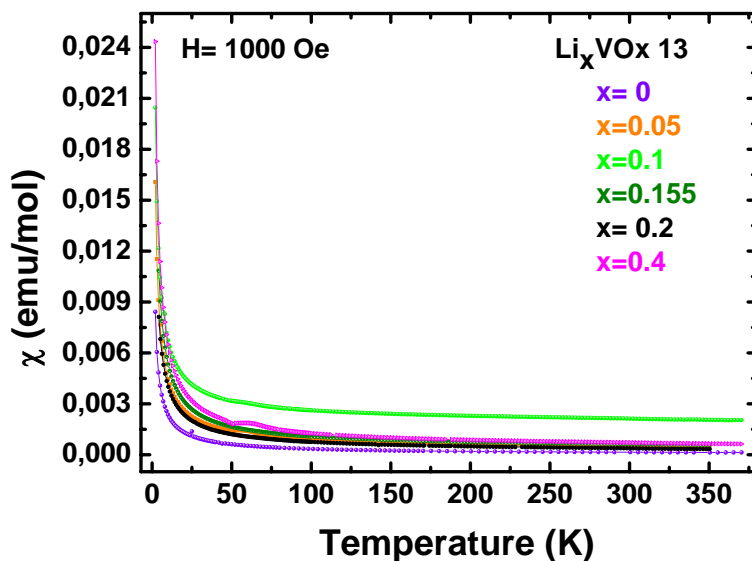


Figure 4.40: Temperature dependence of the $\text{Li}_x\text{VO}_x\text{-NT}$ (batch #13) magnetic susceptibility measured in 1000 Oe applied field. The studied doping level were $x = 0, 0.05, 0.1, 0.2,$ and 0.4 .

other studied batches. The results described in this paragraph have been obtained on $\text{VO}_x\text{-NT}$ batch #13. Using the electrochemical synthesis, five doping levels of $\text{Li}_x\text{VO}_x\text{-NT}$ were obtained: $x = 0.05, 0.1, 0.155, 0.2$ and 0.4 . For the undoped and doped material, temperature dependence of the magnetic susceptibility and field dependence of the magnetization have been measured.

The results from the temperature dependence of the magnetic susceptibility measured in an applied field of 1000 Oe are shown in Fig. 4.40. As visible also from the figure, the $\text{Li}_{0.1}\text{VO}_x\text{-NT}$ again exhibits an extra magnetic moment compared with the other doping levels. The undoped $\text{VO}_x\text{-NT}$ batch #13 however has already different magnetic behavior than the results presented earlier in this chapter. That might be due to possible water intercalation into the compound, or aging of the material, that could influence the oxidation state in the $\text{VO}_x\text{-NTs}$. No indication of AFM dimers is found in the data and the Curie-Weiss fit works pretty well for the whole temperature range. Although not shown, the results are similar with the other studied batches of vanadium oxide nanotubes. The effective moment is the only parameter that really changes with doping, indicating the increasing of the number of the magnetic sites by doping with electrons. The effective moment for $x = 0$ is $0.44\mu_B$ while for the highest doping level it is $0.71\mu_B$. χ_0 is higher for $\text{Li}_{0.1}\text{VO}_x\text{-NT}$ than for the other doping levels

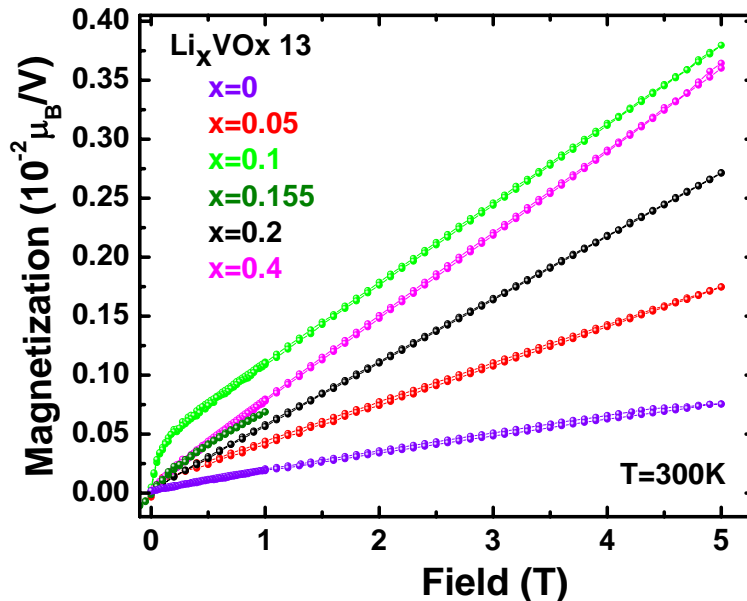


Figure 4.41: Field dependence of the $\text{Li}_x\text{VO}_x\text{-NT}$ (batch#13) magnetization measured at 300 K for $x = 0, 0.05, 0.1, 0.2,$ and 0.4 , measured between 0 T-5 T.

From the Curie constants obtained from the Curie-Weiss fit one can calculate the number of the spins contributing to the Curie-Weiss behavior of the compound ($C = N_{CW} N_A \mu_B^2 / k_B$, where C is the Curie constant, N_{CW} the number of Curie spins, N_A Avogadro's number, μ_B the Bohr magneton and k_B the Boltzmann constant). For undoped $\text{VO}_x\text{-NT}$ batch#13, the N_{CW} is approximately 6.6% and it increases gradually with doping until approximately 17% for the highest doping level. Although not shown, for the field dependence of the magnetization at low temperatures, Brillouin fit were performed, as for the other $\text{VO}_x\text{-NT}$ -see page 77. The linear contribution and the number of spins were not increasing as much as in the previous similarly described results (from $\text{VO}_x\text{-NT}\#5$). The number of the quasifree spins extracted from these fit results in a lower number than the weakly interacting Curie-like 1/2 spins. This is shown in Table. 4.2 For the undoped $\text{VO}_x\text{-NT}$, 4% resulted, and for the highest doping level 5.4%. This difference between the N_{CW} and the quasifree spins deduced from the Brillouin fit support the idea of existing longer chain fragments, i.e. trimers in the magnetic response of the vanadium oxide nanotubes. The magnetic response at low temperatures is therefore given by both the quasifree spins and trimers correlations.

Finally, in Fig. 4.41 the field dependence of the magnetization at room temperature for both the undoped and doped $\text{VO}_x\text{-NT}$ is illustrated. In all cases, the measure-

4 Electrochemically doped Vanadium Oxide Nanotubes

| $\text{Li}_x\text{VO}_x\text{-NT}$ | N_{CW} (%) | N_B (%) | χ_{lin} (10^{-3}emu/mole) |
|------------------------------------|--------------|-----------|---|
| $x = 0$ | 6.6 | 4 | 2.1 |
| $x = 0.05$ | 11.4 | 6.73 | 0.32 |
| $x = 0.1$ | 13.8 | 5.1 | 3.4 |
| $x = 0.2$ | 12.4 | 5 | 3.2 |
| $x = 0.4$ | 17 | 5.4 | 4.3 |

Table 4.2: $\text{Li}_x\text{VO}_x\text{-NT}$ with $x = 0, 0.05, 0.1, 0.2$ and 0.4 - results extracted from fits using the Curie-Weiss and Brillouin function- see text for details.

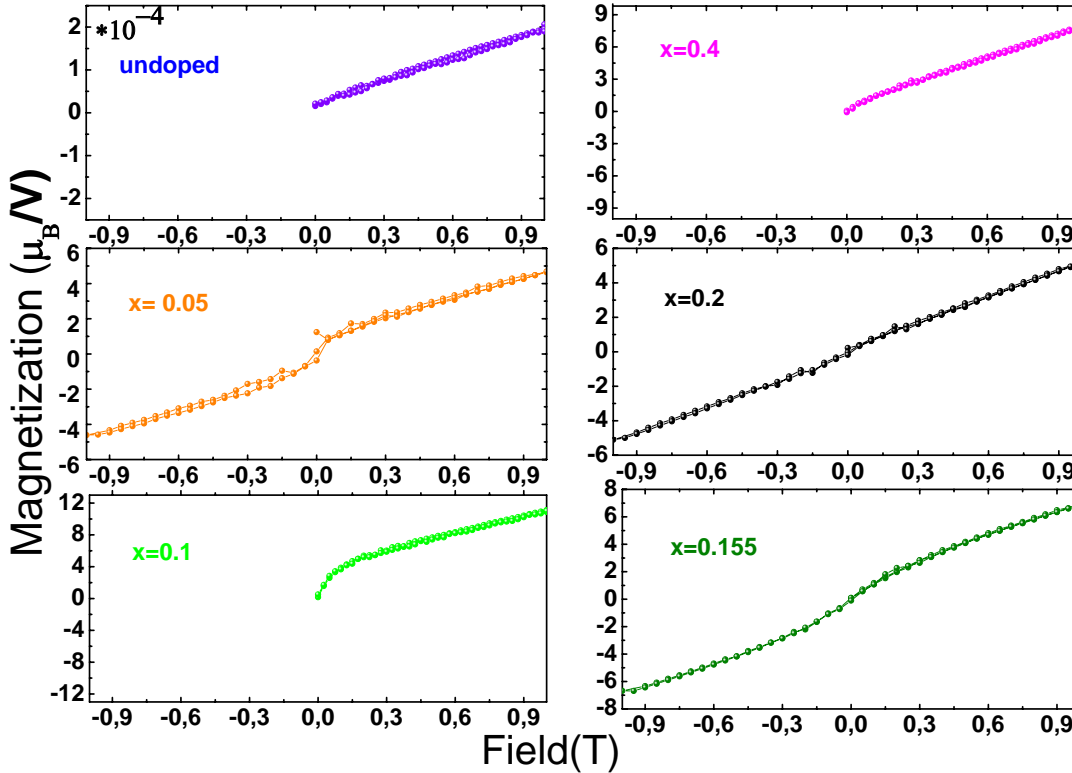


Figure 4.42: Field dependence of the $\text{Li}_x\text{VO}_x\text{-NT}$ (batch#13) magnetization measured at 300 K for $x = 0, 0.05, 0.1, 0.2,$ and 0.4 , measured between 0 T-1 T.

ment was performed between 0 T and 5 T and back to 0 T, in order to observe a possible hysteresis. The highest magnetic value, for all doping levels, is lower than in the previously described results. This might be due to the water intercalation, or other impurities effects that can modify the mixed oxidation state of the compound. In the case of $\text{VO}_x\text{-NT}$ batch#5 the $\text{Li}_{0.1}\text{VO}_x\text{-NT}$ had the maximum magnetization value approximately 10 times higher than the other doping levels. In the case of batch#13, for $x = 0.1$ this is slightly higher than twice the value of $x = 0.05$, at 1 T field. This extra magnetic response in $\text{Li}_{0.1}\text{VO}_x\text{-NT}$, from both $\text{VO}_x\text{-NT}$ batch#5 and batch#13 underlines the possibility that an optimum doping level is needed

to achieve the modification of magnetic properties of VO_x-NTs. Fig. 4.42 shows the same field dependence but in smaller applied fields. A clear non-linear field dependence is observed for the $x = 0.1$ doping level in fields up to 0.2 T. Interestingly, this curvature is not present in the undoped VO_x-NT, then it is slightly present in the $x = 0.05$, it has the maximum signature at $x = 0.1$ and it vanishes at higher doping levels as shown in Fig. 4.42. The observable hysteresis in this field dependencies is very small, or not present. This data suggest again that approximately 10 % lithium doping represents the doping level where the paramagnetic behavior of the undoped VO_x-NT is modified.

4.3 Conclusion

Mixed valency VO_x-NT with structure similar to BaV₇O₁₆nH₂O ($n = 4.4$) have been studied by means of electrochemical and magnetic investigations. Different batches of these vanadium oxide nanotubes have been studied using electrochemical techniques: cyclic voltammograms and/or potentiostatic or galvanostatic experiments. All of them show similar results, with one electron transfer during discharging and charging of the material in a two-electrode like setup. This electron transfer is attributed to the reduction of the non-magnetic V⁵⁺ ion to the magnetic V⁴⁺. The performances obtained from electrochemical experiments are comparable with results on similar nanostructures from literature. The specific discharge capacity of VO_x-NT studied in this work have values around 150 mAh/g. In literature, approximately 160 mAh/g have been found for template free VO_x-NT [22] and values around 80 mAh/g, 120 mAh/g or 150 mAh/g for cations exchanged VO_x-NT, depending on the cations nature (Na, K or Ca). The theoretical capacity is 370 mAh/g, for the unlikely total reduction of V⁵⁺ to V³⁺. Slight differences are encountered between the electrochemical properties of these vanadium oxides batches. These differences might arise from small deviations from the 4.4⁺ mixed valency or due to different water content in the vanadium oxide nanotubes. Therefore, the properties of VO_x-NT as a cathode material in lithium batteries are satisfactory, although they still need to be improved.

Lithium doped vanadium oxide nanotubes have been obtained through electrochemical synthesis. In this way, precise lithium concentration has been obtained for Li_{*x*}VO_x-NT, where $0 \leq x \leq 0.6$. Initially Li_{*x*}VO_x-NT batch#5 with $x=0, 0.05, 0.1, 0.15$ and 0.6 have been studied. Using three different local spin probe techniques like ESR, NMR and μ SR, together with static magnetic susceptibility, an interesting and unexpected result for a low-spin vanadium oxide has been proved.

Optimal lithium concentration of 10 % drastically changes the magnetic properties of the compound. The undoped VO_x-NT show paramagnetic response at 300 K. By doping, the number of magnetic sites has been increased. Moreover, the 10 % lithium doping turns the compound into a strongly magnetic material exhibiting high temperature ferromagnetism, due to formation of nanosize interacting ferromagnetic spin clusters around the intercalated Li ions. Such clusters behave as an ensemble of superparamagnetic particles with a broad size distribution whose big magnetic moments can be easily aligned by a moderate magnetic field even at room temperature. The robustness of the ferromagnetic spin structure may be suggestive of its collective polaronic nature as it has been discussed in [151]. In the undoped VO_x-NT Vavilova and coworkers [136] described the high temperature magnetization as being governed by strongly AFM dimers interactions with a spin gap of 700 K. In the Li_{*x*}VO_x-NT with *x*=0, 0.05, 0.1, 0.15 and 0.6 these strong interactions seem not to be present. If the Curie-Weiss fit is applied for these doped samples, the only parameter that gradually changes with the doping level, is the effective magnetic moment (except χ_0 for *x* = 0.1 doping level). By doping, more magnetic sites are created, resulting in a higher effective magnetic moment for higher doping levels.

Li_{*x*}VO_x-NT batch#13 with *x*=0, 0.05, 0.1, 0.155, 0.2 and 0.4 has been studied as well by means of static magnetic susceptibility. Differences between the two different batches of undoped VO_x-NT appear, probably due to different oxidation state of the V ions and water content. Presence of strong AFM has not been found in neither undoped nor doped VO_x-NT in the second case. By doping with lithium, the same result of increasing the effective magnetic moment has been achieved. A clear non-linear field dependence of the magnetization has been observed for Li_{0.1}VO_x-NT in fields up to 2 T, at room temperature (300 K). This non-linearity is not present in the undoped VO_x-NT but it is visible in Li_{0.05}VO_x-NT and it has the maximum signature at Li_{0.1}VO_x-NT. It can still be observed in Li_{0.155}VO_x-NT. These results show a clear dependence upon doping of a big magnetic moment which can be easily aligned by a relatively small magnetic field, even at room temperature.

5 Electrochemically doped $\text{Sr}_2\text{CuO}_2\text{Br}_2$

5.1 Cuprate Superconductors

In 1986, Bednorz and co-workers discovered the High Temperature Superconductivity (high T_c SC) in the $\text{Ba}_x\text{La}_{5-x}\text{Cu}_5\text{O}_{5(3-y)}$ system with $x = 1$ or 0.75 and $y > 0$ [152]. The appearance of superconductivity in this kind of material was unexpected. Many layered compounds have been synthesized in order to elucidate details of the magnetic properties of this kind of materials.

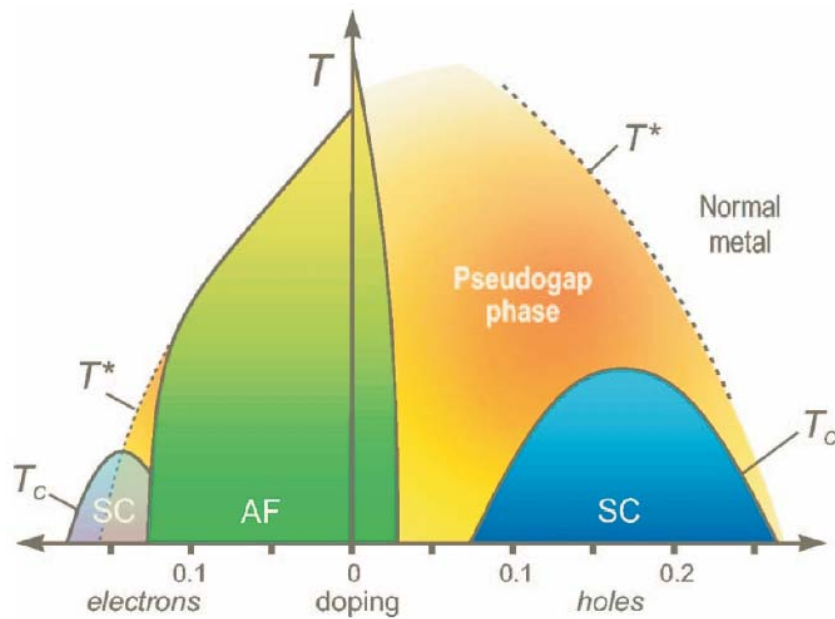


Figure 5.1: Schematic doping phase diagram of electron and hole-doped high- T_c . Adapted from Ref. [153].

The common feature in all high T_c superconductors is the set of n number of CuO_2 planes, separated by the nonmetallic charge reservoir layers [154]. High T_c SC can contain one CuO_2 plane per unit cell (single-layer compounds, for example

$\text{La}_{2-x}\text{Sr}_x\text{CuO}_4$ or $\text{Nd}_{2-x}\text{Sr}_x\text{CuO}_4$), or two layers of CuO_2 planes (double-layered compounds, for example $\text{BiSr}_2\text{CaCu}_2\text{O}_8$ or $\text{YBa}_2\text{Cu}_3\text{O}_y$), and even a larger number of n planes [155]. High T_c superconductivity is achieved when a sufficient density of electrons (yielding to electron doping) or holes (yielding to hole doping) is inserted into cuprate compounds with special physical properties, by chemical substitution or deviations from O stoichiometry. The transition temperature T_c is influenced by the number n of CuO_2 planes. It increases with increasing the number of CuO_2 planes per unit cell.

Fig. 5.1 illustrates the phase diagram of both electron and hole doped superconductors. $\text{La}_{2-x}\text{Sr}_x\text{CuO}_4$ represents one example for a hole doped superconductor. The undoped compound La_2CuO_4 is a Mott insulator. In La_2CuO_4 , La has the oxidation state +3, O has -2, and therefore the resulting oxidation state for Cu is +2, with $3d^9$ electronic configuration. Having one hole in the d shell, band theory for a half field band would imply a metallic behavior. In fact, due to strong electron-electron repulsion effects the compound is an AFM insulator. La_2CuO_4 has a Néel temperature T_N of approximately 300 K, and shows strong AFM correlation above this temperature [154]. When La^{3+} is replaced by Sr^{2+} resulting in a hole-doping process, the Cu^{2+} AFM ordering is drastically suppressed as visible in Fig. 5.1, in the low hole-doping region. Above $x \approx 0.02$ the AFM ordering is completely suppressed, but according to Kastner et al. two-dimensional short range correlations are present [156]. An optimal doping level, $x = 0.15$ is established for the highest $T_c = 40$ K in $\text{La}_{2-x}\text{Sr}_x\text{CuO}_4$. The SC dome in Fig. 5.1, the hole-doped side, can be divided in an under doped and an over doped region. When the number of introduced holes x is lower than the doping level for which the maximum T_c was obtained it represents the under doped region. In this region the T_c increases with increasing the doping level. After the doping level where T_c is maximum, it follows the over doped region, where T_c decreases with increasing the doping level. When $T > T_c$ the pseudo gap region is present with an onset T^* which decreases with increasing the doping level. This pseudo gap was related to superconducting pairing at $T > T_c$ [155]. The region in the phase diagram, outside this pseudo gap region it is represented by the so-called *strange – metal* region, possibly characterized by a quantum critical point lying under the SC dome [154]. Transport experiments suggested that the high-field non superconducting state is described by an insulator for x lower than the optimal doping level, and by an metal when x is higher than the doping level at which T_c is maximum [157].

A candidate for an electron doped superconductor is represented by $\text{Nd}_{2-x}\text{Ce}_x\text{CuO}_4$. It contains single CuO_2 planes, separated by oxygen layers. For $x = 0$ the Cu valency is +2. $\text{Nd}_{2-x}\text{Ce}_x\text{CuO}_4$ has no apical oxygen, as in the case of

$\text{La}_{2-x}\text{Sr}_x\text{CuO}_4$. When x electrons are added to the CuO_2 planes, the AFM transition is persistent until higher doping levels than for hole-doped electrons ($x \approx 0.14$). Right after this, the superconductivity appears until $x < 0.2$. As shown in Fig. 5.1, the SC dome in the case of electron-doped superconductors is more narrow than the one for hole-doped superconductors.

Doping with either holes or electrons a 2D Mott insulator still remains a challenge of discovering all possible contributions and the interplay of different magnetic states. Nevertheless, the magnetic properties of copper oxides compounds are clearly influenced by strong electron-electron correlations, like for example the Coulomb repulsion [158].

When searching for new methods to modify the electronic structure of crystals, the one where an alkaline-metal would be intercalated in order to obtain electron doped superconductors seemed a promising method. By doping, electrons are transferred from the alkaline-metal ions to the host compound. The electronic structure is then altered by the intercalation between the layers of the guest species that act as electron donors or acceptors. One example in this direction is given by $\beta\text{-ZrNCl}$, which when doped with 16% of lithium becomes superconducting with T_c of 12.5 K [159]. The compound contains ZrN double layers as shown in Fig. 5.2, each of which sandwiched between two close-packed Cl layers. When doping with Li, electron transfer occurs to the ZrN layers, and semiconducting $\beta\text{-ZrNCl}$ is changed into a metallic superconductor.

This compound is part of the $\beta\text{-M}'\text{NX}$ family with $M' = \text{Zr}$, Hf and $X = \text{Cl}$, Br, I. All these compounds can be intercalated with lithium, resulting in superconducting materials with T_c of about 12.5 K [159] for $\text{Li}_{0.16}\beta\text{-ZrNCl}$ and 25.5 K for $\text{Li}_{0.48}(\text{THF})_y\text{HfNCl}$ [161]. $\text{Li}_x\text{ASr}_2\text{Nb}_3\text{O}_{10}$ [162] with $A = \text{Rb}, \text{Cs}$ as well as $\text{Li}_x\text{Sr}_2\text{CuO}_2\text{X}_2$ with $X = \text{Br}, \text{I}$ [163] are examples of the perovskite structures which become superconducting by doping with lithium using electrochemical techniques. Layered niobates $\text{Li}_x\text{ACA}_2\text{Nb}_3\text{O}_{10}$ ($A = \text{K}, \text{Rb}, \text{Cs}$) with triple layered perovskite structure NbO_6 , show superconductivity below 5 K [162]. Li-intercalation by a chemical technique using n-butyl lithium leads a T_c of approximately 1 K [164]. In contrast, an electrochemical technique used for Li intercalation increases in some cases the superconducting transition temperature to 5-6 K [162, 163]. Interestingly, the value of T_c is independent on the amount of Li intercalated into the structure. However T_c in these compounds is much lower than for high T_c superconductors although the structures are similar.

$\text{Sr}_2\text{CuO}_2\text{X}_2$ is a member of the Ruddlesden-Popper phases, a layered perovskite with a K_2NiF_4 structure. Its structure is similar to that of $(\text{La}, \text{Sr})_2\text{CuO}_4$, and shown in

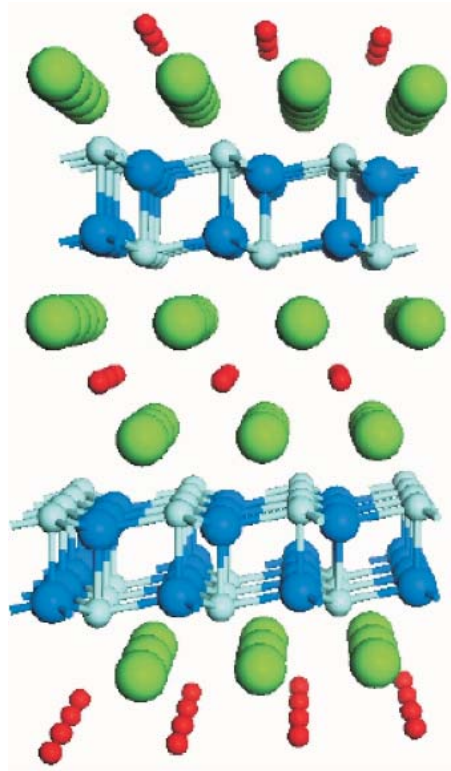


Figure 5.2: Crystal structure of Li_xZrNCl : red represents Li, light blue Zr, blue N, and green spheres represents Cl ions [160].

Fig. 5.3. $(\text{La,Sr})_2\text{CuO}_4$ consists of single CuO_2 planes separated by two rock salt layers, forming CuO_6 elongated octahedra exclusively sharing corners. Out-of-plane oxygen ions (apical oxygen) at the apices of the CuO_6 octahedra in this compound are replaced by X^- ions in $\text{Sr}_2\text{CuO}_2\text{X}_2$, therefore the similarity between the two compounds. The (La,Sr) are replaced by Sr. In the rock-salt layer of Sr and X, Sr^{2+} ions shift slightly towards the nearest CuO_2 plane. In contrast, the X^- ions shift away from the CuO_2 plane. This effect appears due to the larger radius of X^- compared to O^{2-} and the smaller Coulomb attraction between Cu^{2+} and X^- . In this way, X^- - X^- double layers are formed. The electro positive Li^+ ions can be intercalated between these electronegative layers, which are weakly bound through the van der Waals force.

In $\text{A}_2\text{CuO}_2\text{X}_2$ systems with A= alkaline earth metal and X= halogen, with apical halogen ions X, both $\text{Sr}_2\text{CuO}_2\text{F}_{2+x}$ with T_c of 46 K [168] and $(\text{Ca,Na})_2\text{CuO}_2\text{Cl}_2$ with T_c of 26 K [169] are hole doped superconductors. Hole doped carriers were attempted to be introduced into $\text{Sr}_2\text{CuO}_2\text{Cl}_2$ by substitution of Sr sites with Na without any success. The Cu-O bond length of $\text{Sr}_2\text{CuO}_2\text{Cl}_2$ may be too long for hole-doping [170].

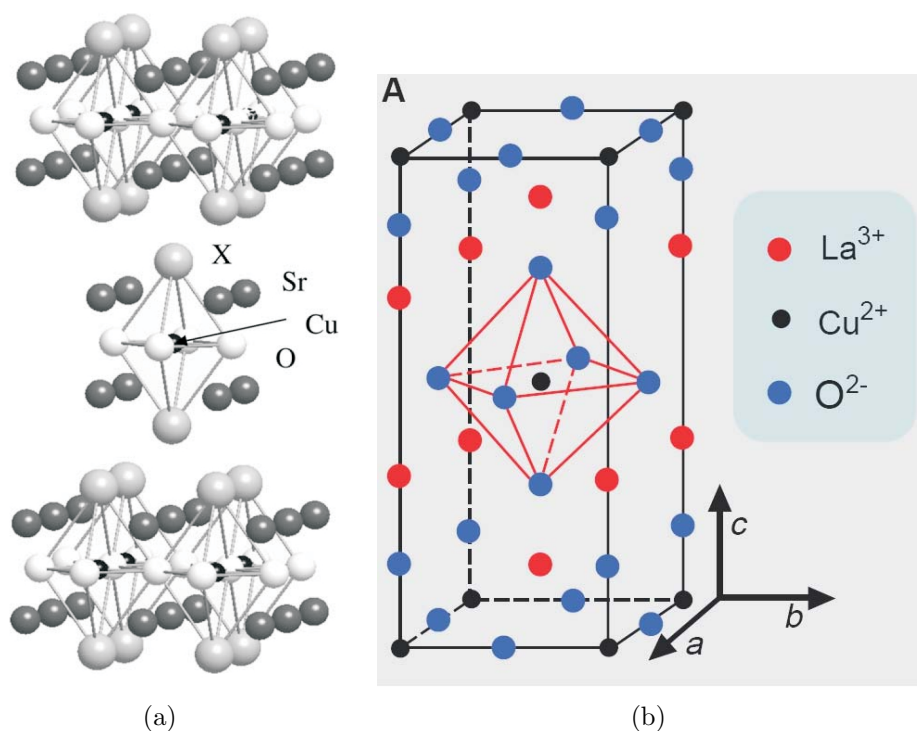


Figure 5.3: Crystal structure of a) $\text{Sr}_2\text{CuO}_2\text{X}_2$ with X= Br, Cl, I [163] and b) $(\text{La,Sr})\text{CuO}_4$, adapted from Ref. [165].

The type of carriers that can be doped into the CuO_2 planes changes from hole-like in $(\text{La,Sr})_2\text{CuO}_4$ to electron-like in $\text{Li}_x\text{Sr}_2\text{CuO}_2\text{X}_2$ due to the increase of the a -axis length from 3.78 Å in $(\text{La,Sr})_2\text{CuO}_4$ to 3.97-3.98 Å in $\text{Sr}_2\text{CuO}_2\text{X}_2$. This indicates that a longer a axis is important for the appearance of electron-doped superconductivity [170–172].

In this chapter, the electrochemical testing of $\text{Sr}_2\text{CuO}_2\text{Br}_2$ will be shown. Using electrochemical techniques, $\text{Li}_x\text{Sr}_2\text{CuO}_2\text{Br}_2$ with different doping level x have been synthesized. The effect of doping on the magnetic properties of the compounds will be analyzed in terms of static magnetic susceptibility.

5.2 Properties of electrochemically doped $\text{Li}_x\text{Sr}_2\text{CuO}_2\text{Br}_2$

5.2.1 Electrochemical characterization and synthesis

The $\text{Sr}_2\text{CuO}_2\text{Br}_2$ polycrystalline host compound used in this work was synthesized as in [173]. SrCuO_2 was prepared by reacting stoichiometric amounts of SrCO_3 and

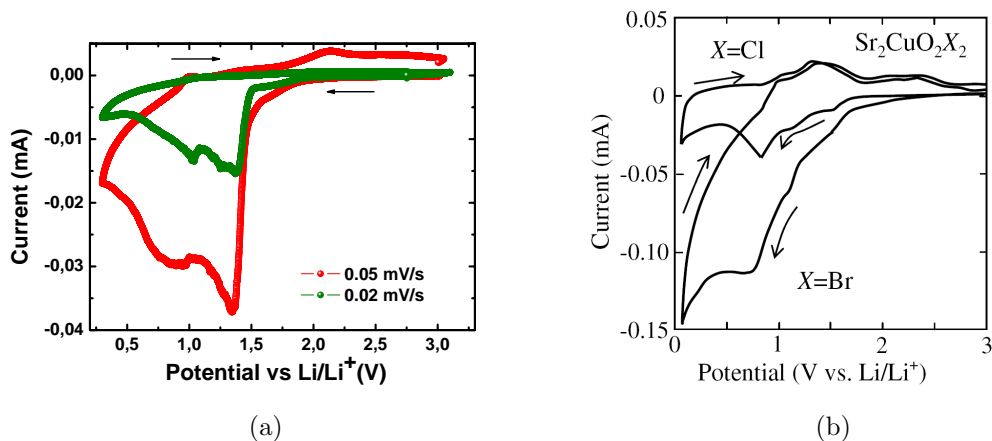


Figure 5.4: Cyclic voltammograms for: a) this work, on $\text{Sr}_2\text{CuO}_2\text{Br}_2$ with 0.05 mV/s and 0.02 mV/s sweeping rate; b) $\text{Sr}_2\text{CuO}_2\text{X}_2$, X= Br, Cl with 0.1 mV/s [163].

CuO powders. These were mixed, ground and heated in air at 925°C for 10h. The powder was then pulverized, pressed into pellets and sintered at 950°C for 20 h. After the single phase SrCuO_2 was obtained, it was mixed with a stoichiometric amount of SrBr_2 , pressed into pellets and then sintered at 825°C for 24 h. The $\text{Sr}_2\text{CuO}_2\text{Br}_2$ was then mixed with naphthalene of 30 wt%, pelletized and then sintered again at 600°C for 6 h to obtain porous $\text{Sr}_2\text{CuO}_2\text{Br}_2$ suitable for lithium intercalation. However, because the pellets would have been too thick for the electrochemical experiments, in this work they were grinded and powder was placed in the Swagelok cell used for the experiments.

Cyclic voltammetry

In order to investigate the electrochemical behavior of $\text{Sr}_2\text{CuO}_2\text{Br}_2$, cyclic voltammetry and potentiostatic experiments were performed. All the experiments were performed in the two-electrode Swagelok-like cell. After testing the material, galvanostatic experiments were performed in order to obtain the final lithium intercalated $\text{Li}_x\text{Sr}_2\text{CuO}_2\text{Br}_2$ used for magnetization measurements.

Fig. 5.4 shows a comparison of CV of $\text{Sr}_2\text{CuO}_2\text{Br}_2$ cycled in a two electrode type cell using LiPF_6 in DMC/EC, and data from literature, where a three electrode type set up and LiClO_4 dissolved in Propylene carbonate (PC) as electrolyte, were used. Kato and coworkers have used pelletized material while in this work the material used, without any additional carbon, was ≈ 20 mg of powder placed onto the positive current collector. The result of CV experiments of the work at hand are shown in Fig. 5.4(a). The starting potential was 3.02 V in the case of the experiment done with

0.05 mV/s, and 2.4 V in the case of 0.02 mV/s sweeping rate. In both experiments, the potential was linearly scanned between 0.3 V and 3.05 V, starting with discharge, i.e. lithium insertion. The two experiments were performed on two different cells. Once the discharging of the cell is started, both experiments show a steep increase of the reduction current at approximately 1.6 V. The current peak reaches a maximum at ≈ 1.35 V, showing clearly that here the electron transfer has its maximum, and therefore the lithium intercalation into the structure takes place. The peak position remains nearly at the same potential for the two performed experiments. In the case of 0.05 mV/s this peak has a pronounced shoulder around 0.9 V. For the second case, with 0.02 mV/s sweeping rate a peak around 1 V is found. This might be due to side reactions and secondary reactions in the experiment, like electrolyte decomposition or weak short circuits. Upon charging, no matching oxidation peak is found. That implies that the intercalated Li during the discharging process remains there when the material is charged. Therefore, no significant lithium extraction takes place during oxidation of the compound, i.e. the Li intercalation is not reversible below 3 V.

The main reduction peak present in Fig. 5.4 takes place at different potential, for the experiments performed in this work, and for those from the literature. In Fig. 5.4(a) the electron transfer is positioned at ≈ 1.35 V, whilst in the literature it is at much lower potential, i.e. 0.8 V. This difference can be well explained by considering the different setup used for the two experiments, the electrolyte with lower ionic conductivity and viscosity used for results from the literature, as well as the sample size that can decrease the electronic conductivity of the positive electrode. Moreover, Kato et al. have used a setup that causes higher polarization which in turn shifts reactions to lower potentials. The shoulder that is present around 1 V in Fig. 5.4(a) is not seen in the data from literature. The rapid increase of the reduction current in Fig. 5.4(b) was assigned to Li deposition on the electrode surface which usually occurs close to 0 V.

Electrochemical synthesis

Using information from the CV experiments, one can conclude that the Li intercalation reaction takes place at voltages where the pronounced reduction peak is found i.e. between 1.6 V and 1.1 V.

Fig. 5.5 shows the result of galvanostatic experiments performed for synthesizing $\text{Li}_x\text{Sr}_2\text{CuO}_2\text{Br}_2$. The electrode material contained pure $\text{Sr}_2\text{CuO}_2\text{Br}_2$. The starting potential for the four different cells are slightly different, ranging from 2.2 V to

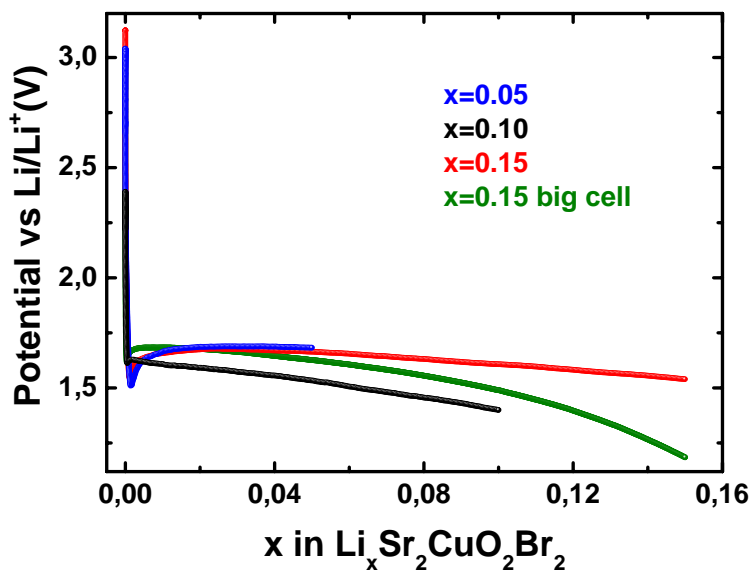


Figure 5.5: Galvanostatic synthesis of $\text{Li}_x\text{Sr}_2\text{CuO}_2\text{Br}_2$.

3.13 V, possibly due to small short circuits or similar side effects that might appear while handling the cell. In all experiments, the constant current was applied until the desired amount x of Li per formula unit was intercalated. Therefore, $x = 0.05$, 0.1 and 0.15 doping level in $\text{Li}_x\text{Sr}_2\text{CuO}_2\text{Br}_2$ were obtained. Different experimental conditions, i.e. usage of the 1/2 inch (red curve) and 1 inch (green curve) diameter swagelok cell lead to different Potential- Composition curves as can be seen in Fig. 5.5. Clearly, all the curves show the same general behavior, with a slight minimum at approximately 1.6 V. They do not coincide due to slight variations of the construction of the electrochemical cell indicated also by different values of the starting potentials, but in all cases the lithium intercalation process takes place in the same potential range.

The galvanostatic mode used in the synthesis of material in Fig. 5.5, was performed with a small constant current applied (≈ 0.03 mA), and it resulted in a slow Li intercalation process (one Li per formula unit intercalated in 100 hours). This route has been chosen to allow a homogeneous lithium intercalation. Contrary, for similar experiment in the literature, a constant potential was applied (potentiostatic mode) matching the potential of the reduction peak found in the CV experiment (see Fig. 5.4(b)), i.e. 0.5 V. This method takes the system away from the equilibrium potential of ≈ 3 V and causes a very fast Li intercalation, which for this system might affect the properties of the intercalated material.

5.2.2 Magnetic properties of $\text{Li}_x\text{Sr}_2\text{CuO}_2\text{Br}_2$

Type I superconductors exhibit zero dc electrical resistance and perfect diamagnetism. They are perfect diamagnets for applied fields lower than the critical temperature T_c and critical field B_c , and become normal in higher temperature and fields. Many of the pure metals are Type I superconductors. Type II superconductors are usually made of metal alloys or complex oxide ceramics. Type II superconductors are also perfect conductors of electric current, with zero resistance, but their magnetic properties are more complex. A type II superconductor totally excludes magnetic flux in the Meissner state when the applied magnetic field is below the lower critical field B_{c1} . Flux is only partially excluded when the applied field has a value in between B_{c1} and B_{c2} . When the applied field is higher than the upper critical field B_{c2} the material is in its normal state [174].

Undoped $\text{Sr}_2\text{CuO}_2\text{Br}_2$

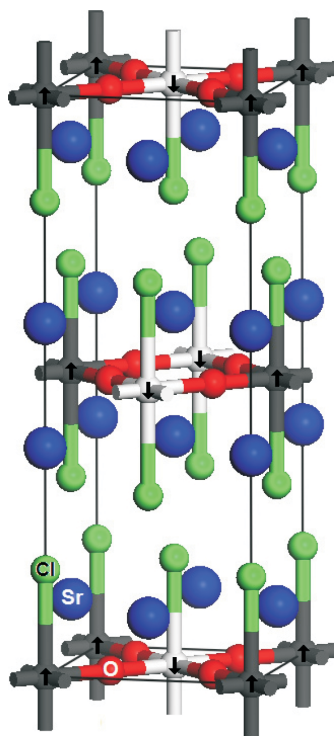


Figure 5.6: The magnetic unit cell of $\text{Sr}_2\text{CuO}_2\text{Cl}_2$. Black, white, red, green and blue spheres represent $\text{Cu}(\uparrow)$, $\text{Cu}(\downarrow)$, O, Cl and Sr atoms. The spins of the Cu atoms are shown as arrows [175].

A good example of a spin-1/2 square lattice Heisenberg antiferromagnet (AFM) model system is given by the body-centered tetragonal K_2NiF_4 -type compound

$\text{Sr}_2\text{CuO}_2\text{Cl}_2$ [173, 176, 177]. This material is isostructural with the one studied in this chapter, $\text{Sr}_2\text{CuO}_2\text{Br}_2$, containing flat CuO_2 sheets where adjacent CuO_2 sheets are separated by two nonmagnetic SrCl layers [178]. The $\text{Sr}_2\text{CuO}_2\text{Cl}_2$ compound undergoes a 3D AFM phase transition below $T_N = 25.1 \pm 5$ K [175] with a magnetic structure (see Fig. 5.6) similar to that of La_2CuO_4 . AFM long-range order of the Cu^{2+} spins is a well known property common to a variety of insulating members of the cuprate family of superconductors. Above the Néel temperature T_N , the temperature dependent magnetic susceptibility $\chi(T)$ of these compounds is very similar to each other and is dominated by strong superexchange interactions between the Cu^{2+} spins in the CuO_2 planes [179–181].

Different attempts to measure the magnetization of the undoped $\text{Sr}_2\text{CuO}_2\text{Br}_2$ used in this work were performed. The compound is relatively sensitive to air. Therefore, its magnetization for both the undoped and the doped material was measured using the sealed quartz tube as described in section 3.2. Using the SQUID no reasonable magnetic signal arising from the investigated material was found. In order to get information about the undoped compound, zero field (ZF) Muon Spin Relaxation (μ^+ SR) measurements were performed by H.-H. Klauss and coworkers in the Paul Scherrer Institut in Villigen, Switzerland.

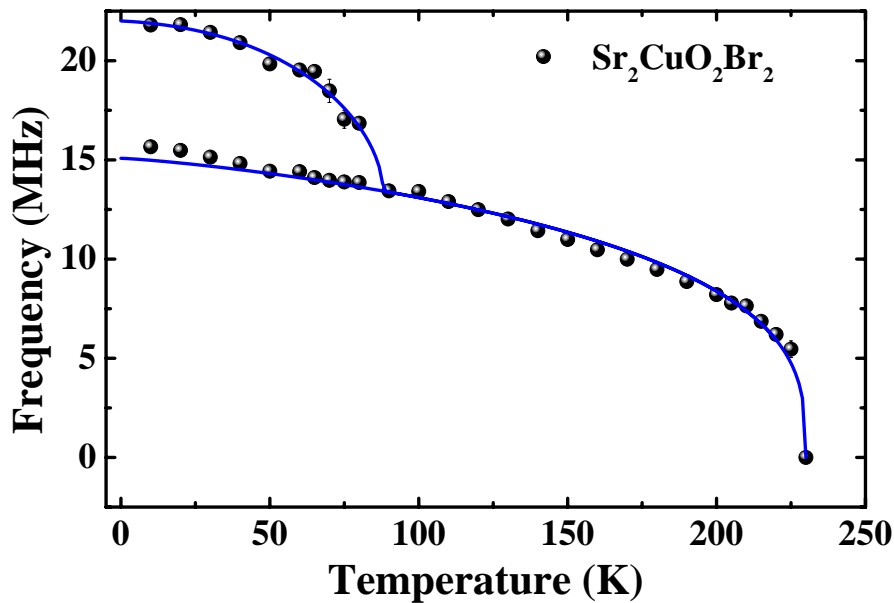


Figure 5.7: Muon spin precession frequency versus temperature for $\text{Sr}_2\text{CuO}_2\text{Br}_2$. Note that the lines are guides to the eye. Courtesy of H.-H. Klauss and coworkers [182].

In Fig. 5.7, the muon study, namely the muon spin precession frequency versus temperature, measured for $\text{Sr}_2\text{CuO}_2\text{Br}_2$ is illustrated. In ZF μ^+ SR, if the muon site is

localized below T_N , i.e. no muon diffusion occurs, the temperature dependence of the muon precession frequency reflects the sublattice magnetization [183]. ZF μ^+ SR on $\text{Sr}_2\text{CuO}_2\text{Br}_2$ shows a spontaneous muon spin precession frequency of ≈ 15 MHz indicating magnetically long range ordered phase below 230 K. Below this temperature, long-living oscillations in the muon polarization are characteristic of long range static magnetic order. This frequency totally disappears above 230 K, indicating the disappearance of the long range magnetic order above the Néel temperature $T_N \approx 230$ K. Below 80 K a second frequency of 22 MHz with a signal fraction of 20% of the total signal amplitude is found, indicating a spin reorientation transition at this temperature. This can be explained by either an intrinsic effect of possible spin reorientation in the material or, by an effect of a possible change of the muon sites at low temperatures. The internal field at the muon sites can be affected by either a dipolar field from the Cu-spins or by the hyperfine field due to the finite electron spin density at the μ^+ site (fermi contact interaction). In this kind of material the contribution of the hyperfine field is likely to be small, therefore, the contributions to the local field are most probably mainly from the Cu moments in several nearest cells.

Similar studies of temperature dependence of the muon spin precession frequency have been performed on $\text{Sr}_2\text{CuO}_2\text{Cl}_2$ having the same crystallographic structure as the compound studied in the present work. Here, the frequency is sharply reduced above 250 K and totally disappears at approximately 270 K, in agreement with neutron experiments from which $T_N \approx 250$ K was found [176]. The muon spin precession frequency observed above 60 K splits into two lines below this temperature. A peak around 50 K in the magnetization versus temperature measured in $H=3$ T suggested that the splitting mentioned above is caused by some intrinsic changes of the magnetic structure of $\text{Sr}_2\text{CuO}_2\text{Cl}_2$, probably a Cu-spin reorientation. The second frequency line in $\text{Sr}_2\text{CuO}_2\text{Br}_2$ and $\text{Sr}_2\text{CuO}_2\text{Cl}_2$ differs, being larger for the first one. This might be due to either a different muon site or a different magnetic structure 80 K.

In conclusion, the temperature dependence of the muon spin precession frequency of $\text{Sr}_2\text{CuO}_2\text{Br}_2$ exhibits properties similar to the 2-d spin-1/2 Heisenberg antiferromagnet $\text{Sr}_2\text{CuO}_2\text{Cl}_2$. The substitution of Br or Cl for the apex oxygens leads to different properties compared to La_2CuO_4 , e.g. larger c-axis parameter (20% larger than in other cuprate compounds) and smaller Madelung potential at Cu site for introducing an electron [177, 183]. The Néel temperature for $\text{Sr}_2\text{CuO}_2\text{Br}_2$ used in this work has been established to 230 K using ZF μ^+ SR studies.

Doped $\text{Li}_x\text{Sr}_2\text{CuO}_2\text{Br}_2$

Although $\text{Sr}_2\text{CuO}_2\text{Cl}_2$ was one of the first candidate for an electron doped superconductor, this material was not successfully doped by now [163, 184, 185]. In this work, $\text{Sr}_2\text{CuO}_2\text{Br}_2$ was successfully intercalated with lithium, i.e. electron doped, using the electrochemical techniques described earlier in this thesis. Galvanostatic experiments were performed and different doping levels were achieved: $x = 0.05$, 0.1 and 0.15 in $\text{Li}_x\text{Sr}_2\text{CuO}_2\text{Br}_2$.

The magnetic properties of $\text{Li}_x\text{Sr}_2\text{CuO}_2\text{Br}_2$ were investigated with a SQUID magnetometer. The samples were inserted into the SQUID at 120 K. The temperature was then decreased to 2 K with no applied field. At this temperature a very small field H was applied and the first zero field cooled (ZFC) magnetization M was measured up to 50 K. After the last point was measured at this temperature, the field was maintained and the temperature was decreased again to 2 K, and here the field cooled (FC) measurement started up to 50 K. The field dependence of the magnetization for different temperatures was measured at low fields, between -200 Oe and 200 Oe. For 2 K, the field dependence was measured up to 1 T.

Temperature dependence of the magnetic susceptibility

The temperature dependence of the magnetic susceptibility ($\chi = M/H$) in ZFC and FC conditions for $\text{Li}_x\text{Sr}_2\text{CuO}_2\text{Br}_2$ has been measured in 2 Oe and 20 Oe applied field. In ZFC conditions, when such a small field is applied, it is reasonable to assume that the superconductor (SC) exhibits diamagnetic shielding or flux exclusion. This means that the magnetic field fails to penetrate the material. Ideally $\chi = -1/4\pi$ (in CGS units or -1 in SI units) for complete flux exclusion. Under FC conditions, the field is applied when the material is still in the normal state, at a temperature above T_c . After cooling below T_c in this conditions, and then starting to record the susceptibility χ as a function of the applied field, the SC exhibits the Meissner effect or flux expulsion.

For the same applied field and the same temperature, $T < T_c$ a type II SC expels less flux when it is FC than it excludes when it is ZFC. The difference between the amount of excluded flux and the amount of expelled flux is the trapped flux sometimes called the pinned flux. Therefore, the magnitude of χ is smaller for the Meissner effect (FC) than for the diamagnetic shielding (ZFC) [186].

The diamagnetic susceptibility resulting from the superconducting shielding currents for $\text{Li}_{0.15}\text{Sr}_2\text{CuO}_2\text{Br}_2$ is illustrated in Fig. 5.8. Values of the susceptibility χ

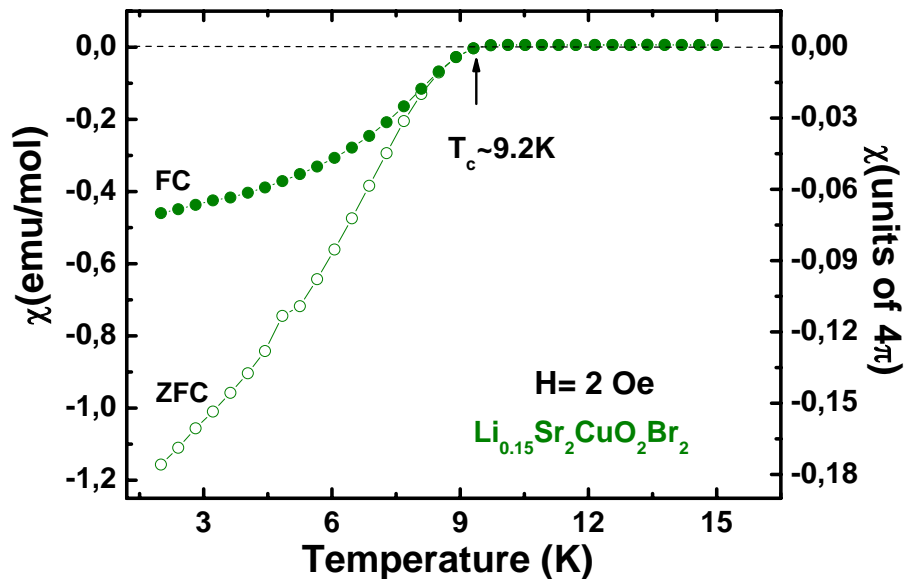


Figure 5.8: Temperature dependence of the magnetic susceptibility for $\text{Li}_{0.15}\text{Sr}_2\text{CuO}_2\text{Br}_2$ in 2 Oe applied field measured on warming for ZFC (open circles) and FC (closed circles). The transition temperature $T_c \approx 9.2$ K is evidenced by the arrow. The T_c has been chosen as the first point situated on the dashed line.

taken from the ZFC experiment measured in 2 Oe applied field are higher than those measured in 20 Oe (not shown in the figure). This might be a sign of superconducting grains weakly coupled by Josephson contacts. This was established also for high T_c superconductors such as $\text{La}_{1.85}\text{Sr}_{0.15}\text{CuO}_4$ [187]. In units of 4π the magnetic susceptibility is -0.18 at 2 K for $x = 0.15$, as shown in Fig. 5.8 in the scale on the right hand side of the graph. This indicates that the susceptibility in this case represents 18% of a perfect diamagnet susceptibility.

Similar results, illustrated in Fig. 5.9, on $\text{Li}_{0.15}\text{Sr}_2\text{CuO}_2\text{Br}_2$ have been performed by Kajita et al. They established a superconducting behavior below $T_c = 8$ K [163, 171, 172]. The superconducting transition temperature T_c shows almost no dependence on the lithium doping level in this material.

The value of the susceptibility at 2 K performed in the work at hand, illustrated in Fig. 5.8 is roughly twice than that in Fig. 5.9, indicating a stronger superconductivity in the $\text{Li}_{0.15}\text{Sr}_2\text{CuO}_2\text{Br}_2$ studied in this work. In addition, the T_c obtained in this work slightly increases compared with results from literature.

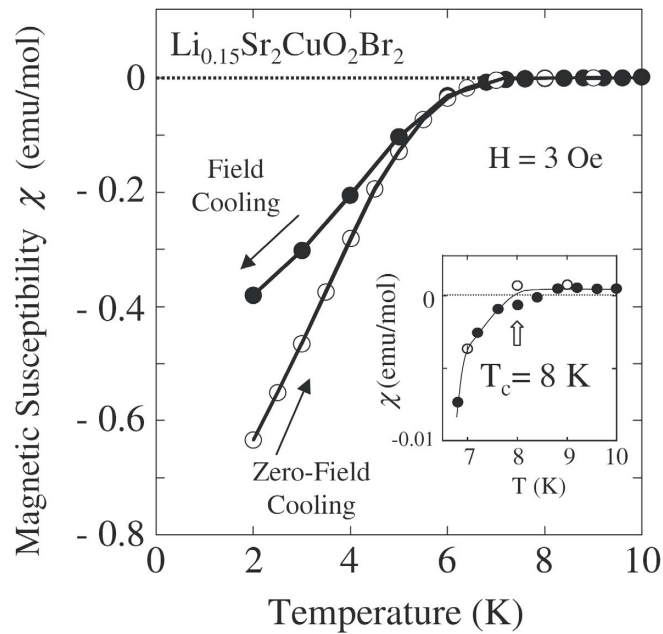


Figure 5.9: Temperature dependence of the magnetic susceptibility for $\text{Li}_{0.15}\text{Sr}_2\text{CuO}_2\text{Br}_2$ in 3 Oe applied field measured on warming for ZFC (open circles) and FC (closed circles). The inset indicates the transition temperature $T_c=8$ K. Adapted from [171].

Field dependence of the magnetization

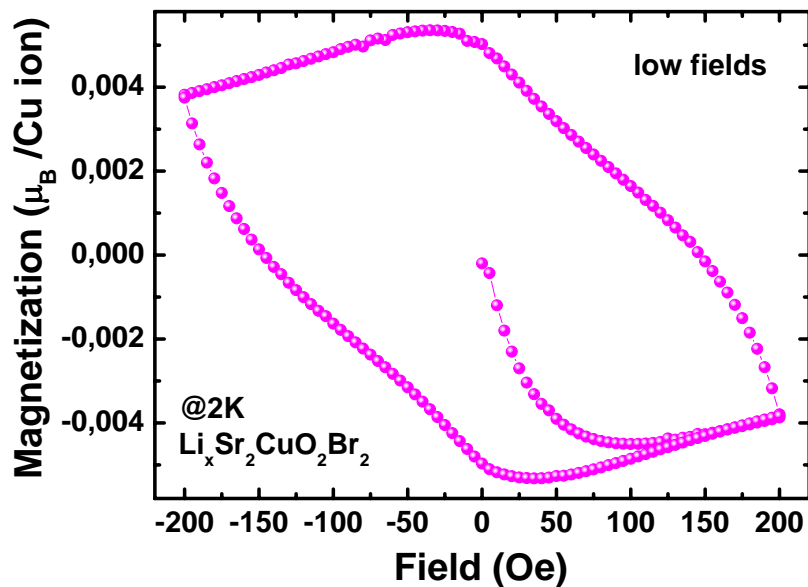


Figure 5.10: Hysteresis loops obtained in low applied fields for $\text{Li}_{0.15}\text{Sr}_2\text{CuO}_2\text{Br}_2$ at $T=2$ K.

The superconductivity of the $\text{Li}_x\text{Sr}_2\text{CuO}_2\text{Br}_2$ was also analyzed by means of the field dependence of the magnetization. The studied compound is the same that gave the diamagnetic response in Fig. 5.8. Fig. 5.10 illustrates the hysteresis loop measured at $T=2\text{ K}$ between -200 Oe and 200 Oe . At low fields $M(H)$ is linear and diamagnetic, i.e. smaller than zero. Then $M(H)$ turns upwards, changes the slope and reaches a minimum at approximately 80 Oe . In the field dependence of the magnetization when the field limit is reached, i.e. 200 Oe and then decreased, a strongly irreversible behavior is seen. This can be understood by the presence of superconducting grains coupled weakly by a network of Josephson contacts. At low fields, the shielding is governed by Josephson currents. When the shielding currents are higher than the critical Josephson currents, the flux can penetrate the region between the superconducting grains. At higher fields each grain is screened individually and therefore, the shielded volume is reduced as it is shown in Fig. 5.11 in fields higher than approximately 0.18 T . Upon reducing the field the flux is trapped between the grains, giving rise to hysteresis effects as can be seen in Fig. 5.10. From these measurements the lower critical field B_{c1} can be determined [167, 188]. B_{c1} is reached at fields for which the magnetization versus the field deviates from the initial linearity [189]. From Fig. 5.10, B_{c1} of approximately 40 Oe is derived. Usually, careful field dependences of the magnetization have to be completed in order to estimate B_{c1} . Hence, the result above is a rough determination.

Fig. 5.12 illustrates the field dependence of the magnetization for temperatures ranging from 2 K , starting on top, in the left hand side down to 10 K . As the temperature is increased towards the critical temperature $T_c \approx 9\text{ K}$, the magnetization versus the applied field decreases and it becomes almost linear and paramagnetic in field, for temperatures $T > T_c$. This can be seen in the measurement at $T=10\text{ K}$. This behavior suggests that the magnetic phase of the normal state is antiferromagnetic. As it has been shown from $\mu^+\text{SR}$ experiments one can actually expect this behavior. However, the data imply the presence of a small ferromagnetic signal with a remnant magnetization of $1.45 \cdot 10^{-5} \mu_B$. One possible explanation for this might be represented by spin canting, due to a non-collinearity of AFM alignment of Cu neighboring spins in the undoped compound. This contribution to $M(H)$ is also visible at higher fields for $T=2\text{ K}$ as visible in Fig. 5.11. Therefore, one can say that the compound is not completely superconducting but also contains antiferromagnetic, normal conducting regions. Over the measured temperature range it is clear that the behavior is that of a typical type II superconductor, modified by a constant background slope resulting from the antiferromagnetism, plus possibly weak ferromagnetism arising from spin canting. This kind of behavior has been observed also for other high T_c superconductors, e.g. $(\text{Y}_{0.8}\text{Ba}_{0.2})_2\text{CuO}_4$ [190].

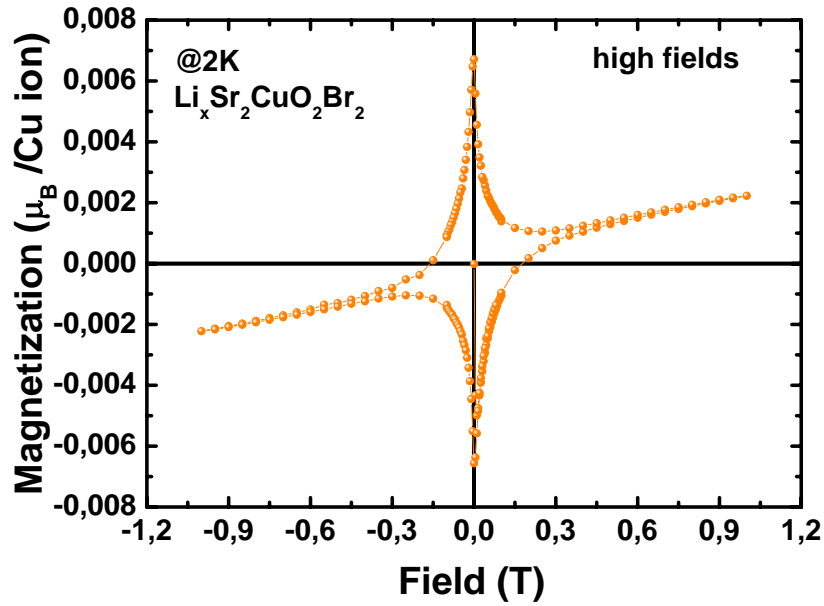


Figure 5.11: Hysteresis loop obtained in high applied fields for $\text{Li}_{0.15}\text{Sr}_2\text{CuO}_2\text{Br}_2$ at $T=2\text{ K}$. The inset is a guide for an estimation of the upper critical field B_{c2} .

Material Instability

Different attempts to obtain superconducting materials by lithium doping of $\text{Sr}_2\text{CuO}_2\text{Br}_2$ were undertaken. The magnetization showed a clear dependence on the time between the electrochemical synthesis and the measurements. The SC behavior for the sample with $x = 0.15$ shown earlier in this chapter has been measured right after the electrochemical synthesis was performed.

In Fig. 5.13 the temperature dependence of the magnetic susceptibility for the sample with $x = 0.05$ and $x = 0.15$ measured in a field of 7 Oe, 3 days after the synthesis is shown. In the inset of the figure the susceptibility of the sample with $x = 0.15$ measured right after the synthesis (green curve) is compared to the sample that was stored 3 days (blue curve) in a Ar-dry box before the measurement was performed. As a result $\chi(T=2\text{ K})$ of the aged sample is approximately 17 times smaller than the fresh sample, with a superconducting volume fraction of 0.09% compared to 18%. When synthesising the $\text{Li}_x\text{Sr}_2\text{CuO}_2\text{Br}_2$, it might be that the lithium intercalation is not homogeneously in the sample. Therefore, part of the sample might have enough intercalated Li in order to show superconducting behavior. Over time and thermal equilibrium, the superconducting fraction in the sample might be affected, and the SC will not be found anymore. It is possible also that the SC appears for a restricted doping level, which might be affected by lithium diffusion.

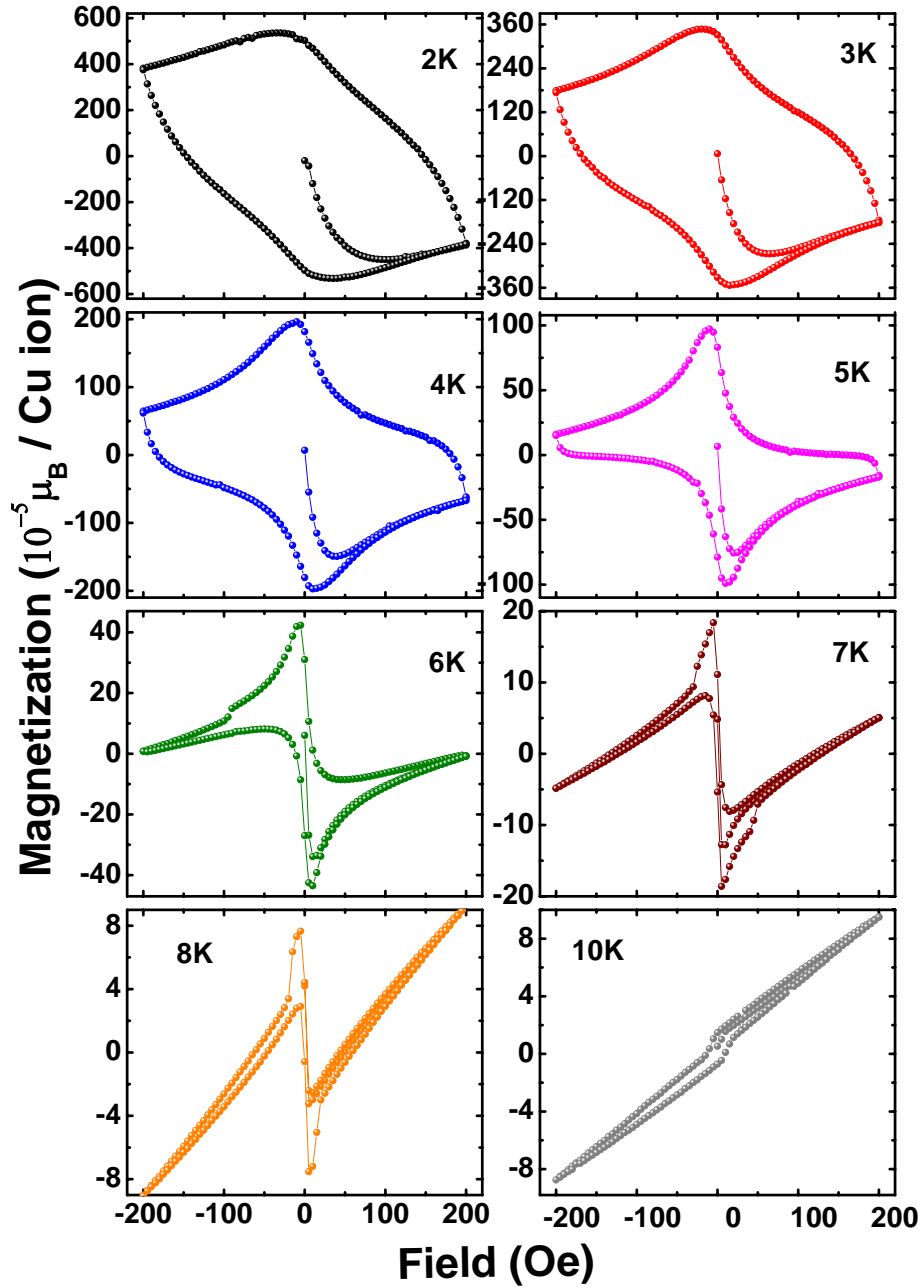


Figure 5.12: Hysteresis loops obtained in low applied fields for $\text{Li}_{0.15}\text{Sr}_2\text{CuO}_2\text{Br}_2$ at $2\text{K} \leq T \leq 10\text{K}$.

5.3 Conclusion

$\text{Sr}_2\text{CuO}_2\text{Br}_2$ has a similar structure with $(\text{La,Sr})_2\text{CuO}_4$, the mother compound of hole doped superconductors $\text{La}_{2-x}\text{Sr}_x\text{CuO}_4$. Electrochemical experiments performed on $\text{Sr}_2\text{CuO}_2\text{Br}_2$ in this work present superior results than similar achieve-

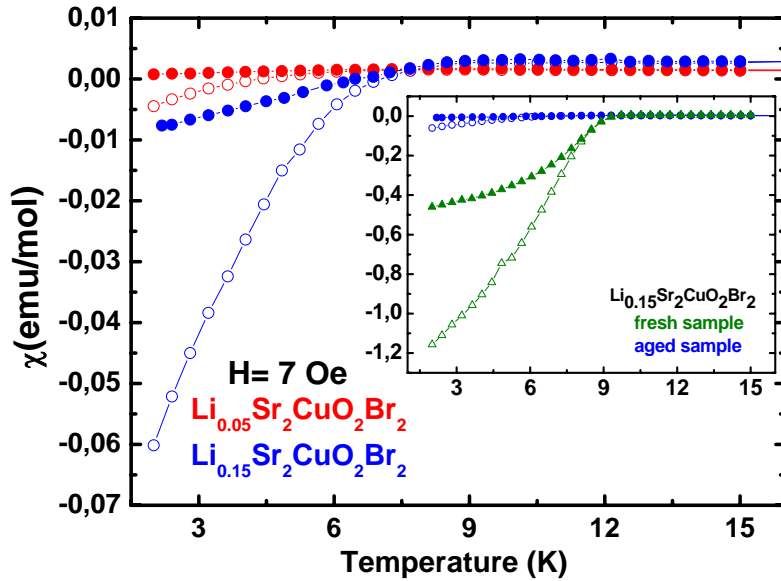


Figure 5.13: Temperature dependence of the magnetic susceptibility in 7 Oe applied field for $\text{Li}_x\text{Sr}_2\text{CuO}_2\text{Br}_2$ for $x = 0.05$ and 0.15 . ZFC measurement is represented by the open circles while the FC by the closed circles. The inset shows $\chi(T)$ for the fresh (green curve) and aged (blue curve) 0.15 doping level.

ments in the literature. Using muon spin relaxation measurements, long range magnetic order in the undoped $\text{Sr}_2\text{CuO}_2\text{Br}_2$ has been established below $T_N \approx 230$ K.

$\text{Li}_x\text{Sr}_2\text{CuO}_2\text{Br}_2$ was synthesized by electrochemical techniques and showed clearly type II superconductivity for $x = 0.15$. The superconductivity was studied by means of temperature dependence of the susceptibility measured in low fields and field dependence of the magnetization measured at temperatures ranging from 2 K to 10 K. The superconducting transition temperature was established at approximately 9 K. From these measurements one can see that the material consists of superconducting grains weakly coupled by Josephson contacts. The lower critical field was approximated to 40 Oe. A coexistence between superconductivity, antiferromagnetism and weak ferromagnetism due to spin canting was deduced from magnetization versus field experiments at various temperatures and low fields.

Using electrochemistry as the method to synthesize lithium doped $\text{Sr}_2\text{CuO}_2\text{Br}_2$, superconductivity with 18% superconducting volume fraction has been successfully obtained. The data presented here, represent the beginning of a future work on this compound, by means of magnetization studies, as well as possibly other methods, such as $\mu^+\text{SR}$ among others.

6 Electrochemically doped MnO₂ nanostructures

6.1 Manganese oxide compounds

One dimensional objects such as nanowires and nanorods represent a big challenge for synthesis due to their peculiar properties and potential applications. The advantages of nanomaterials were described in detail at the beginning of this work. Special attention was attributed to manganese oxide, along with its various derivative compounds. These materials have stimulated notable interest due to their outstanding flexibility associated with novel chemical and physical properties for possible applications, such as molecular sieves, catalysts, magnetoresistance devices, lithium-insertion solid state batteries, cathodes and anodes in aqueous electrochemical capacitors [191–196]. The low cost and the abundance of this material represents a big advantage for its usage as cathode material, as well as its safety to over-charge conditions compared to intensively used LiCoO₂ or LiNiO₂ [197]. This advantage comes from having the thermodynamically stable nature of Mn(IV) in the MnO₂, whilst Co(IV) in LiCoO₂ or Ni(IV) in LiNiO₂ are thermally unstable [198]. The common material MnO₂ is known to be non-toxic and versatile. Compared with vanadium compounds, these materials have higher electrode potentials, around 3.9 V versus Li/Li⁺ for MnO₂ compared with 3.2 V for VO_x-NT.

A short review of structural forms of manganese compounds, together with possible synthesis routes is given in the first part of this chapter. The electrochemical properties of α -MnO₂ nanostructures will be analyzed, and similarities with experiments from the literature will be checked. Using electrochemical techniques, different doping levels in Li_{*x*} α -MnO₂ will be synthesized. The effect of lithium doping in Li_{*x*} α -MnO₂ will be characterized by means of static magnetic susceptibility.

Apart from well known nanostructured layered materials that intercalate guest species between the interlayers, there are other inorganic compounds with high lithium storage capacity after electrochemical lithium doping. Manganese dioxide

compounds are currently under study as positive electrodes for lithium batteries. They became very interesting after being used in natural form MnO₂ from different sources as a depolarizing agent in the Zinc/Ammonium Chloride/Carbon battery by Leclanché in 1866. Later on, synthetic, chemically prepared MnO₂ in the Leclanché batteries improved their performance. A major step was done by using electrochemically prepared material using alkaline electrolytes in commercial batteries [199]. Manganese oxide materials can provide up to 5 V versus metallic lithium [200]. The voltage of the cell depends on the formal valence state of the Mn ions, as well as on the relative energy of the lithium sites in the various derivatives of this compound.

Structural forms of MnO₂

Among the large class of hexagonal close-packed (hcp) structure ^{IV}MX₂ compounds, MnO₂ is the one that presents a complex series of structures, summarized in Table. 6.1. This could be possible due to small ionic radius of Mn⁴⁺ (r=0.53Å) which places the MnO₂ to the lower limit of rutile structure stability. The 3d³ electronic configuration of Mn⁴⁺ stabilizes octahedral coordination. Bi₁₂MnO₂₀ represents one of the rarely examples of Mn⁴⁺ tetrahedrally coordinated by oxygen of [201]. All MnO₂ structures consists of a distribution of Mn⁴⁺ cations in the interstices of relatively close-packed networks of oxygen atoms. The structural complexity of these materials is also given by their redox chemistry which permits closely related compositions with variable amounts of Mn⁴⁺, Mn³⁺ and even Mn²⁺.

The manganese oxides can be divided into several groups such as chemically pure and structurally well characterized ones with close-packed structures (pyrolusite β-MnO₂, ramsdellite MnO₂, spinel λ-MnO₂), tunnel and layer structures (hollandite α-MnO₂, psilomelane, todorokite, phyllosulfates), the “nsutite family” (nsutite γ-MnO₂, ε-MnO₂) and reduced forms (groutite α-MnOOH, groutellite, feitknechtite β-MnOOH, manganite γ-MnOOH, δ-MnOOH, pyrochroite Mn(OH)₂). All these possible forms of manganese oxide differ one from each other by the space group symmetry, valence of the manganese ion and way of linkage of the MnO₆ octahedra. Some of MnO have tunneled structure, with different possible dimension for the tunnel.

The tunnel and layered structures are more important for this work since the compound studied here is supposedly hollandite α-MnO₂ (but actually a slight mixture of this structure and γ-MnO₂). These minerals species have compositions close to MnO₂, but they are not chemically pure manganese dioxide, usually containing

| Mineral | Space Group | Z | a(Å) | b(Å) | c(Å) | $\beta, \gamma(^{\circ})$ |
|------------------------------|-----------------------------------|----|--------|--------|-------|---------------------------|
| Pyrolusite(β) | P4 ₂ /mnm | 2 | 4.3983 | - | 2.873 | 90 |
| Ramsdelite | Pbnm | 4 | 4.533 | 9.27 | 2.866 | 90 |
| Nsutite(γ) | [intergrowth] | 4 | 4.45 | 9.305 | 2.85 | 90 |
| Birnessite | P $\bar{3}$ m1 | 1 | 2.84 | - | 7.27 | 120 |
| ϵ -MnO ₂ | P6 ₃ /mmc ² | 1 | 2.80 | - | 4.45 | 120 |
| Spinel(λ) | Fd $\bar{3}$ m | 16 | 8.029 | - | - | 90 |
| Hollandite(α) | I2/m ⁴ | 2 | 10.026 | 2.8782 | 9.729 | 91.03 |
| Psilomelane | C2/m | 2 | 13.929 | 2.8459 | 9.678 | 92.39 |
| Todorokite | P2/m | 8 | 9.764 | 2.8416 | 9.551 | 94.06 |
| Manganite(γ) | B2 ₁ /d ⁷ | 8 | 8.88 | 5.25 | 5.71 | 90 |
| Groutite(α) | Pnbnm | 4 | 4.560 | 10.700 | 2.870 | 90 |
| Groutellite | [Pnbnm] | 4 | 4.700 | 9.531 | 2.864 | 90 |
| Feitkneichtite(β) | P $\bar{3}$ m1 | 1 | 3.32 | - | 4.71 | 120 |
| Pyrochroite | P $\bar{3}$ m1 | 1 | 3.322 | - | 4.734 | 120 |

Table 6.1: Crystallographic characteristics of Manganese Oxides, oxyhydroxides and hydroxide polymorphs - adapted from [199].

different amounts of intercalated species such as M⁺ or M²⁺ cations or water molecules. The water content of the tunnel structure MnO₂ is related to the tunnel size and to the nature of the interstitial cation. α -MnO₂ exists in nature in forms such as hollandite (BaMn₈O₁₆) and cryptomelane (KMn₈O₁₆). The structure shown in Fig. 6.1 consists of interlinking double chains of MnO₆ octahedra and an interstitial space comprised of one dimensional channels of relative dimension (2x2) and (1x1) that extend in a direction parallel to the c axis of a tetragonal unit cell.

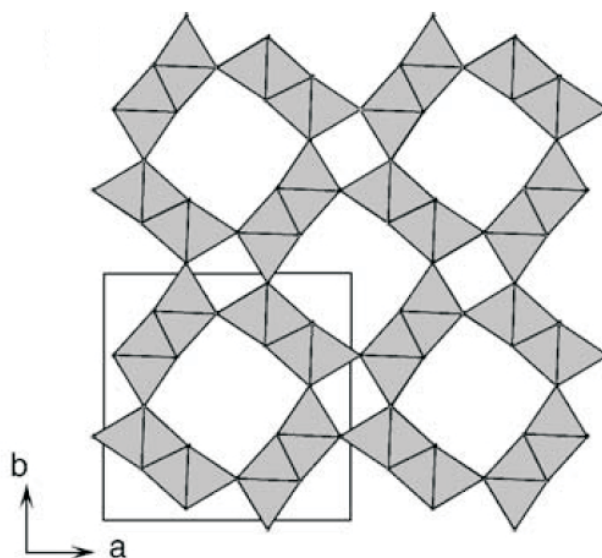


Figure 6.1: Crystal structure of α -MnO₂ [19].

The intercalated cations, Ba²⁺ and K⁺ reside in the center of the (2x2) channels and improve the stability of the material. The presence of these cations obstruct lithium diffusion within this structure, prohibiting the application of α -MnO₂ as electrode material [202]. In the absence of these large cations the structure can be stabilized by water molecules located in the same (2x2) channels. The water can be removed, without the structure collapsing. This would still give to the material a strong tendency of reabsorbing the water if exposed to air.

γ -MnO₂ is part of the “nsutie family”, and it represents a series of synthetic phases, applicable in lithium batteries technologies: natural MnO₂, electrochemical MnO₂ or chemical MnO₂. The structural model for γ -MnO₂ was given by De Wolff, based on observation that rutile and ramsdellite structures have similar arrangements along *a* and *c* axis and differ only by the width of the infinite chain of MnO₆ octahedra along *b* axis. Therefore, γ -MnO₂ can be described by irregular inter growth of elements of ramsdellite MnO₂ domains of size (2x1) and pyrolusite β -MnO₂ domains of size (1x1) [203] as it is shown in the crystal structure illustrated in Fig. 6.2 [19]. This information resulted from diffraction patterns were confirmed by high resolution transmission electron microscopy as well [204]. Due to the mixture of the two structures, the long range ordering along *b* direction is missing, therefore this makes it difficult to study this material with conventional powder diffraction techniques.

Among MnO₂ structures, γ -MnO₂ is the most used as electrode material in lithium batteries. Predominantly, it is used in aqueous Zn/MnO₂ cells, and in primary Li/MnO₂ cells [199]. During discharging, the Li ions are inserted mainly in the (2x1) channels of the ramsdellite domains. The system might deliver a high discharge capacity of 250 mAh/g in the first cycle, which decreases in time [205].

The most popular manganese oxide compound used in lithium battery technologies is LiMn₂O₄ [25, 48, 49]. Its structure contains cubic close packed arrays of oxygen anions. The Mn cations occupy half of the octahedral interstitial sites, and Li cations occupy one eighth of the tetrahedral sites. The interstitial space in the [Mn₂]O₄ framework represents a diamond type network of tetrahedral and surrounding octahedral sites, sharing edges and faces in order to form 3D diffusion pathways for Li⁺ ions diffusion [206]. The electrochemical Li⁺ deinsertion from the tetrahedral sites of LiMn₂O₄ is reversible and takes place at 4 V vs Li/Li⁺. The cubic symmetry of the structure does not change during cycling, and the structure experiences a minimal contraction of the unit cell over a wide ranges of compositions [207].

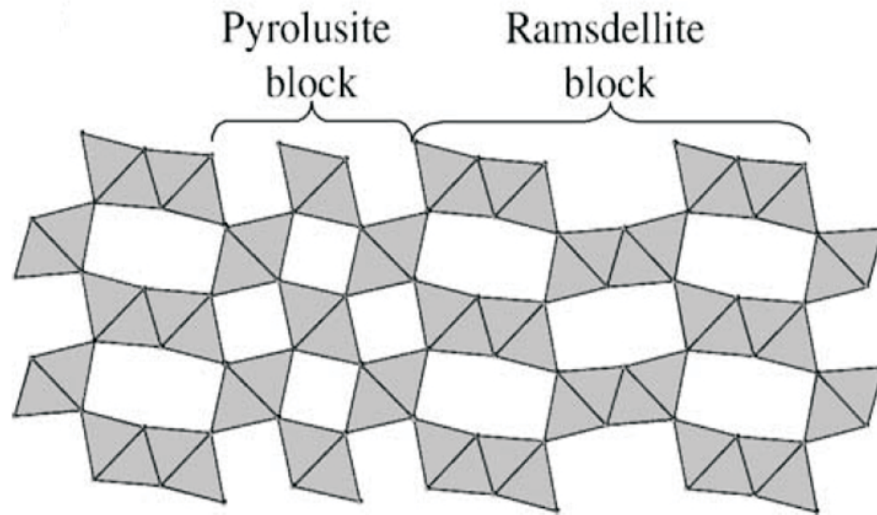


Figure 6.2: Crystal structure of γ -MnO₂ showing the mixture between the ramsdellite and pyrolusite structures [19].

Synthesis routes

Many synthesis routes have been developed to prepare this large variety of manganese oxides, such as thermal [208], refluxing [194, 209, 210], hydrothermal [211], sol-gel [212, 213], electrochemical [19] or solid-state reaction [214]. In most of these synthesis techniques the formation of different tunneled structures has been controlled by adjusting the pH with H₂SO₄ or NaOH solution [210]. More precisely, a hydrothermal preparation of α -MnO₂ nanowires has been achieved by oxidizing MnSO₄ in KMnO₄ [215] and (NH₄)₂S₂O₈ [216], in which cation concentrations were very important for the formation of the tunnel structures. Muraoka et al synthesized single phase α -MnO₂ from hollantide-type (NH₄)_xMn₈O₁₆ and quenching from 440 °C during heating in flowing Ar [208]. Needle like α -MnO₂ crystals have been prepared by ozone-oxidation of Mn²⁺ in high concentrations of H₂SO₄ [194]. γ -MnO₂ nanowires can be synthesized through a coordination-polymer-precursor route [217]. Another method to obtain this material is through a hydrothermal treatment of commercial granular γ -MnO₂ crystals [218]. Pure δ -MnO₂ nanorods were prepared by the sol-gel method [219]. α -, γ -, δ -MnO₂ have small molecules or ions as integral parts of the structure, whilst, β -MnO₂ is relatively pure MnO₂ [220]. β -MnO₂ nanorods can be synthesized by calcinating λ -MnOOH nanorod precursors by carefully controlling the temperature, time, and heating speed of the process [221]. Liu et al. developed an easier synthesis of β -MnO₂ by a simple refluxing route using MnSO₄ · H₂O, Na₂S₂O₈ and NaOH as the raw materials [222]. MnO₂ has also been

prepared by Co and Al substitution through an electrochemical synthesis under hydrothermal conditions [223].

6.2 Properties of electrochemically doped MnO₂ nanostructures

Batteries made of MnO₂ compounds can reach a potential of 5 V, depending on the Mn valence and available Li sites in the structure. Higher voltages arise from a difficult removal of the Li ion from a particular site while charging. During discharging the sites with the deepest energy storage will be occupied first. Most of the MnO₂ structures can retain one Li per formula unit until the rock salt LiMnO₂ is reached. This reaction would involve the complete reduction of Mn⁴⁺ to Mn³⁺ and that would deliver a theoretical capacity of 308 mAh/g [200]. The α -MnO₂ framework can accommodate a significant amount of lithium while initially discharging to 2 V, with a discharge capacity of 210 mAh/g, corresponding to nearly 0.7 Li per Mn. The capacity decreases upon cycling, and this might be related to an instability of the (2x2) channels during electrochemical cycling. Mn and O ions are relocated from the framework into the channels to stabilize the structure [200]. This diffusion of Mn would result in stabilized Li_xMnO₂ structure with defect rock salt character, similar to those created when cycling thin films of LiMn₂O₄.

6.2.1 Electrochemical characterization and synthesis

The material studied in this work was α -MnO₂ without any large cations stabilizing the structure. Different synthesis routes for obtaining this structure were described earlier. The material used in this work was prepared after the synthesis route described by Wang et al. [216]. The goal was to obtain a 1D nanostructure without the presence of catalysts or templates, by a low temperature hydrothermal method through the oxidation of Mn²⁺ by S₂O₈²⁻. Equal amounts of MnSO₄·H₂O and NH₄S₂O₈ (0.008 mol) were placed in distilled water at room temperature in order to obtain a homogeneous solution. Then the mixture was transferred into a Teflon-lined stainless steel autoclave, sealed and kept at 120 °C for 12 h. The result of the reaction was a black solid product that was filtered, washed with distilled water to remove residual parts, and then dried for another 12 h in air. This process can also be used to obtain β -MnO₂ nanorods. For α -MnO₂, 0.015 mol of ((NH₄)₂)SO₄,

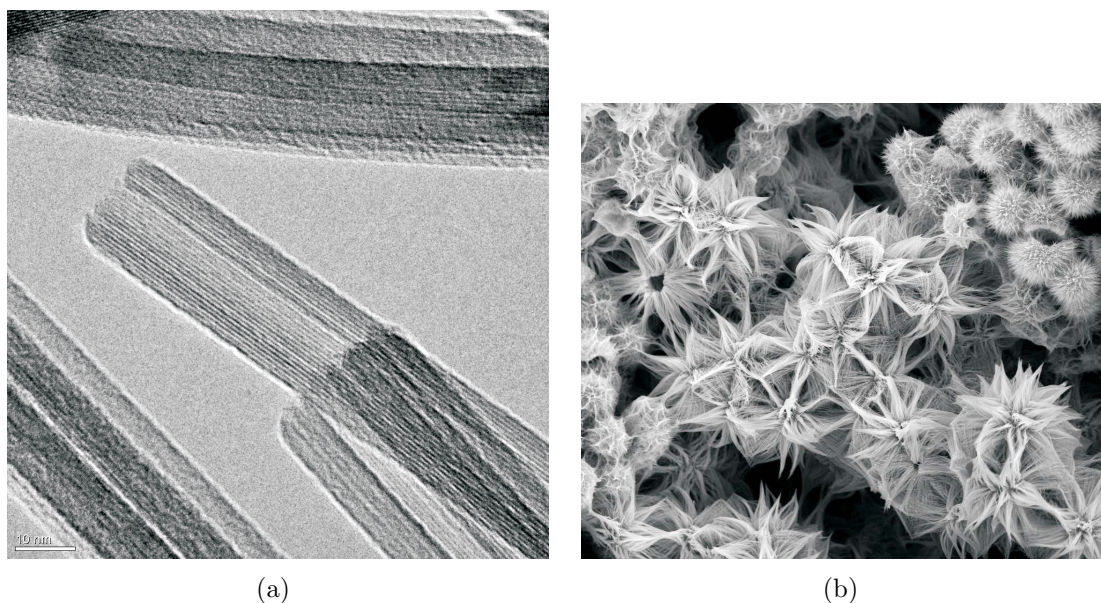


Figure 6.3: Nanostructure morphology of αMnO_2 checked with TEM and SEM techniques.

is included in the reaction. The nanostructured product was observed with Scanning Electron Microscopy (SEM) and Transmission Electron Microscopy (TEM), see Fig. 6.3.

The material contains thin fibers of several micrometers in length and several nanometers in diameter. The SEM image shows that both microspheres [224] and orchid-like [225] nanostructures are present in the structure, formed by multiple nanorods radiating from the center of each structure. As it will be discussed below, the (2x2) tunneled structure $\alpha\text{-MnO}_2$ might contain some $\gamma\text{-MnO}_2$ impurities.

Cyclic Voltammetry

In order to investigate the electrochemical behavior of $\alpha\text{-MnO}_2$, cyclic voltammograms were performed, followed by potentiostatic or galvanostatic experiments. All the experiments were performed in the two-electrode Swagelok-like cell. 5-10wt% of Carbon SP were added for better electronic conductivity of the material. Approximately 20 mg to 30 mg of this mixture was used for each experiment. After testing the material, galvanostatic or potentiostatic experiments were performed in order to obtain the final lithium intercalated Li_xMnO_2 used for magnetic investigations. The first experiment on this material was performed without any additional Carbon. The result is placed in Fig. 6.4. The gray curve from the figure does not show reasonable oxidation/reduction peaks which are expected from the literature. Therefore, the

6 Electrochemically doped MnO₂ nanostructures

material was mixed with 10% Carbon and a new experiment was performed. First, the material is discharged. As the discharge starts a process of electron transfer is visible, with a maximum around 2.8 V. This is attributed to reduction of Mn⁴⁺ to Mn³⁺. During lithium intercalation a small feature can also be seen at potentials of 3.4 V. As it will be discussed later, this is a sign of γ -MnO₂ impurity. While charging the material, the electron peak transfer indicating the oxidation of Mn³⁺ back to Mn⁴⁺ is found at higher potentials, with a reached maximum around 4 V.

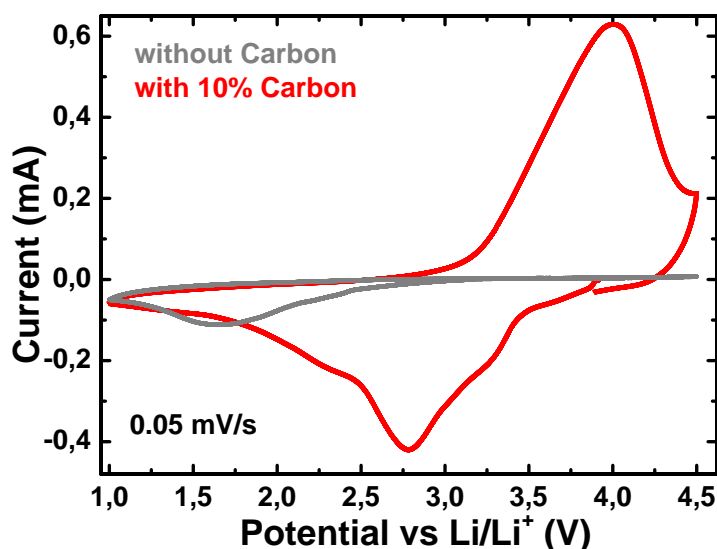


Figure 6.4: Cyclic voltammogram of the first cycle for MnO₂ without (gray curve) and with (red curve) additional Carbon. In both cases a scan rate of 0.05 mV/s was used.

When studying the electrochemical behavior of the MnO₂ nanostructures using different scan rates, Fig. 6.5 is obtained. On the same cell two experiments with scan rates of 0.01 mV/s (green curve) and 0.02 mV/s (red curve) were performed. The other experiments shown in Fig. 6.5 were performed using a fresh cell each time. If in the case of VOx-NT this kind of experiments differ mainly in current intensities, the MnO₂ differ more. It seems that the electrochemical behavior is either sensitive to the rate used for cycling or also to the way the cells are handled during mounting. The starting potentials for these 4 examples are around 3.9 V, the exception is for the blue curve with a scan rate of 0.03 mV/s where this values lies around 3.7 V. From this variation in the initial potential values, one can say that the material is very sensitive to small short circuits or other effects than can influence its electrochemical behavior. The cut off potentials for these experiments were either 1 V-4.8 V for the scan rates of 0.01 mV/s and 0.02 mV/s, 1.8 V-4.8 V for

scan rate of 0.03 mV/s or 1.5 V-4.8 V for scan rate of 0.05 mV/s. While discharging the material a couple of peaks appear starting with the one at 3.38 V, indicating that first electron transfer process evolves here. It is most obvious in the green curve performed with a scan rate 0.01 mV/s. In the next fastest scan rate is not a peak anymore but a pronounced shoulder which vanishes after increasing the cycling speed to 0.05 mV/s. This indicates that some features present here during discharging of the MnO₂ electrode material depend on the speed taken for the experiment.

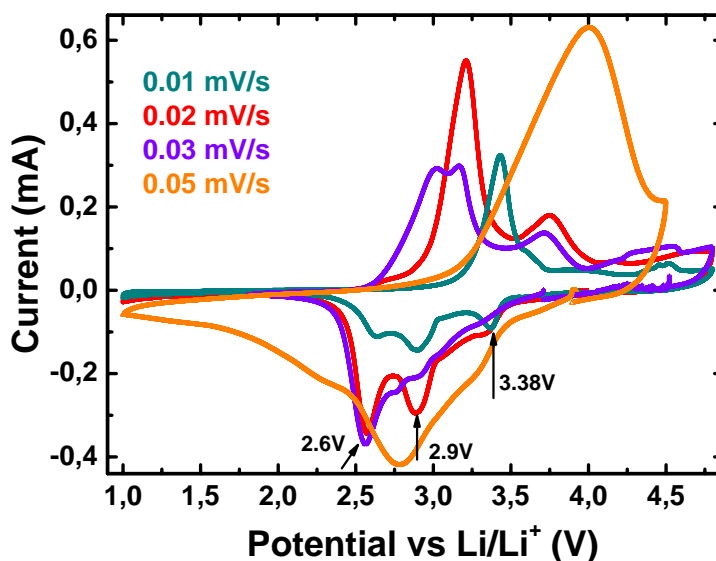


Figure 6.5: Cyclic voltammograms for MnO₂ mixed with Carbon, using different scan rates.

The next possible electron transfer can be described by the peak around 2.9 V, visible in the first two experiments (green and red curve). For the 0.03 mV/s curve this is present as a shoulder and in the last curve it is not visible anymore. A peak around 2.6 V it is visible in the first three experiments, and it differs only in the current intensity. The reduction peak in the case of the orange curve performed with a scan rate of 0.05 mV/s is a broad one with a maximum around 2.8 V. The potential sweeping when 0.05 mV/s scan rate is used might be too fast. That might explain why different features present in CVs obtained with scan rates smaller than 0.05 mV/s, are visible in the CV performed with 0.05 mV/s in a shape of a broad peak. For the oxidation part of the experiment the peaks for the scan rates used are positioned at slightly different values. For the first three scan rates used, it looks like the main electron transfer process shifts towards lower values with increasing

6 Electrochemically doped MnO₂ nanostructures

scan rates. For the experiment performed with a scan rate of 0.03 mV/s the main oxidation peak shows two peaks, possibly due to influence of γ -MnO₂.

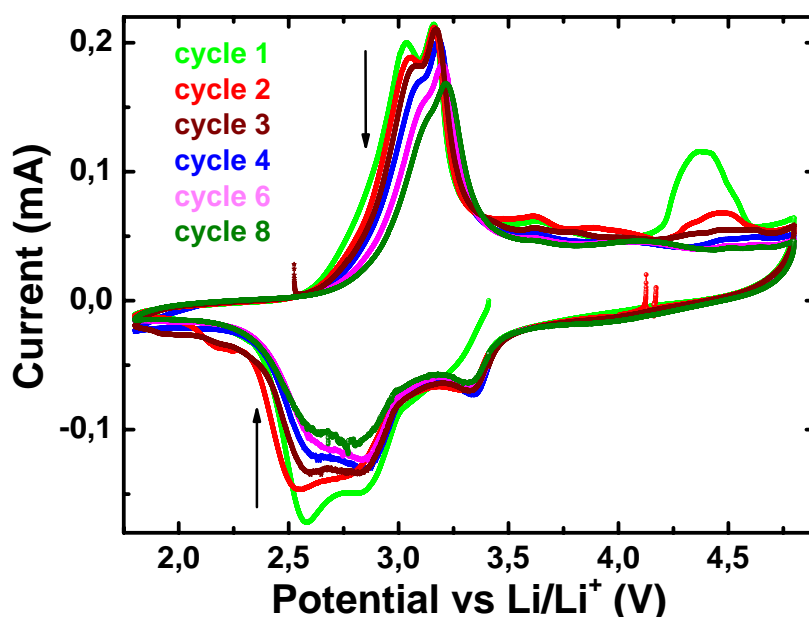


Figure 6.6: Cyclic voltammograms for MnO₂ mixed with Carbon, using a scan rate of 0.02 mV/s. Results shown for cycle 1, 2, 3, 4, 6 and 8.

For a better understanding of the electrochemical behavior of these nanostructures, a set of 9 cycles were performed between 1.8 V- 4.8 V using a scan rate of 0.02 mV/s. For clarity, only cycles 1, 2, 3, 4, 6 and 8 are illustrated in Fig. 6.6.

The electrochemical behavior described by the Fig. 6.6 is different from an α -MnO₂ cyclic voltammogram found in literature [19, 20]. The first cycle in Fig. 6.6 has several peaks while discharging. A very stable electron transfer process is indicated by the feature present at 3.3 V. A reduction peak of α -MnO₂ at this voltage is not known. Over cycling it does not change its position. Around 2.8 V and 2.58 V another two reduction peak are present indicating that the electron transfer takes place in two steps. Over the nine performed cycles these two peaks loose intensity and tend to transform into a broad peak as evidenced by the eighth cycle in Fig. 6.6. The electron transfer during charging the material seems to take place in two steps, indicated by the two peaks found in the first charging cycle, at 3.04 V and 3.16 V. The peak at 3.04 V transforms during cycling, becoming a faint shoulder in the eighth cycle of the experiment. The peak at 3.16 V does not significantly change: in the first three cycles it has almost the same position and in the following cycles it slightly shifts to 3.2 V. A broad peak is found at 4.3 V and it vanishes upon cycling.

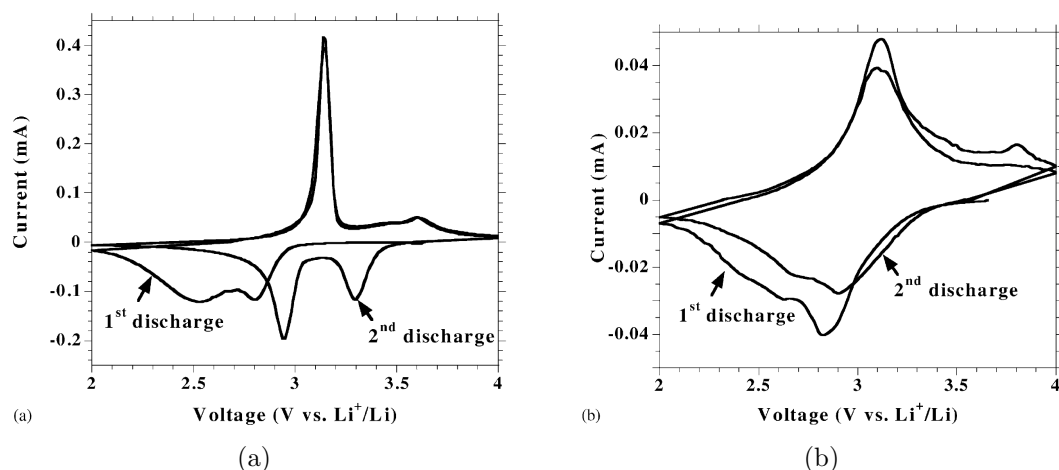


Figure 6.7: Cyclic voltammograms of the first two cycles with a scan rate of 0.005 mV/s: a) γ -MnO₂; b) α -MnO₂ (taken from [19]).

The multiple peaks in both reduction and oxidation of the material, different than results from similar experiments in literature, suggest the idea of a impure α -MnO₂.

The peaks present in the electrochemical testing of the α -MnO₂ have been compared with results on the same material described by Hill et al, illustrated in Fig. 6.7. Hill et al. used for their work a very low scan rate for the experiment. The electrolyte used was the same as the one described for this work, therefore no differences between the two experiments can be assigned to influences of different electrolytes. Their electrode material was mixed with 20 wt.% Carbon and 10 wt.% PVDF binder. In Fig. 6.6 the feature present at 3.3 V is not known to appear in CV of α -MnO₂. This suggest that this might be due to the presence of γ -MnO₂ in α -MnO₂ nanostructures studied in this thesis. A prove for this lies in results of γ -MnO₂ studied by Hill et al., which has a pronounced peak at 3.3 V in the first discharging cycle. In the following cycle it disappears. The authors attributed the difference in the CV shape between the first and second cycle, to irreversible transformation during Li intercalation in the first discharging cycle of γ -MnO₂.

Most probable, the two reduction peaks found at 2.8 V and 2.58 V in Fig. 6.6 are the effect of a mixture of α -MnO₂ and γ -MnO₂. For α -MnO₂ described in Fig. 6.7 by Hill and coworkers, a broad peak and a shoulder are found around the same voltage values, and they do not significantly change during cycling. Interestingly, a peak around 2.8 V is also described in Fig. 6.7 for the second cycle of γ -MnO₂. The presence of γ -MnO₂ (with (1x1) and (2x2) tunnels) impurity in the α -MnO₂ studied in this work might give rise to different lithium sites available for the electrochemical reactions. That might explain the sign of electron transfer in Fig. 6.6, evidenced by peaks found in CV of both mentioned structural forms of MnO₂. The reduction

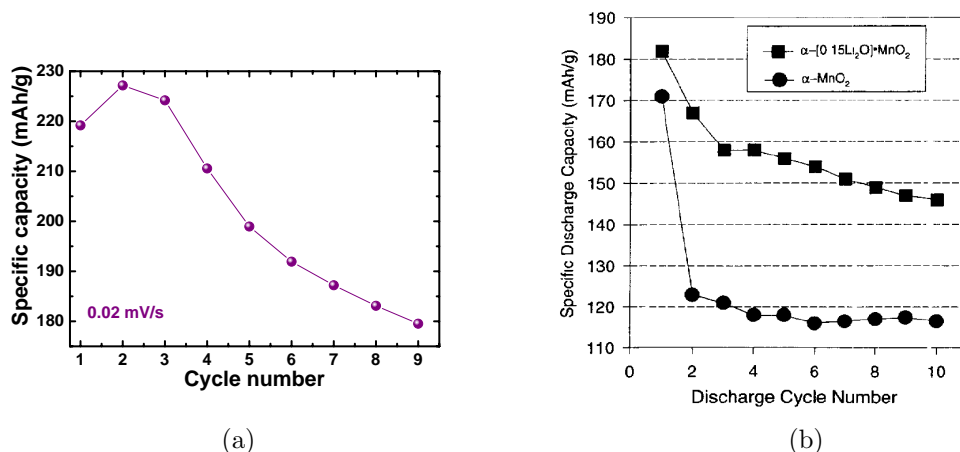


Figure 6.8: Discharge capacity as a function of cycle number for a) this work, values taken from Fig. 6.6; b) heat treated $\alpha\text{-MnO}_2$ and $0.15\text{Li}_2\text{O}\cdot\text{MnO}_2$ [20].

peaks at 2.8 V and 2.58 V are significantly changing during the cycles shown in Fig. 6.6. During cycling, the effect of the $\gamma\text{-MnO}_2$ seems to decrease. The reduction of $\alpha\text{-MnO}_2$ nanostructure in the eighth cycle includes only one peak, as found for other $\alpha\text{-MnO}_2$. Different transformations over cycling in the electrochemical behavior of a structural form of manganese oxide has been established also for $0.15\text{Li}_2\text{O}\cdot\text{MnO}_2$ [20]. These transformations indicate a structural change from the $\alpha\text{-MnO}_2$ framework structure to a defect rock salt structure [200]. Such a structural modification upon lithium intercalation can not be excluded in the case of $\alpha\text{-MnO}_2$ nanostructures studied in this work.

The oxidation peak from both $\gamma\text{-MnO}_2$ and $\alpha\text{-MnO}_2$ in Fig. 6.7 are around 3.1 V. The difference between them is that for the first kind of structure the peak is narrow and has a much higher current intensity than the reduction peak, whilst for the $\alpha\text{-MnO}_2$ the peak is broad and its current intensity is rather symmetric with the one from the reduction peak. For the material described in Fig. 6.6, the oxidation peak is not much higher in current intensity than its reduction pair. Perhaps the transformation from the two oxidation peaks into a broad one is the sign of less influence of $\gamma\text{-MnO}_2$ upon cycling, as suggested also by the reduction part of the CV described in Fig. 6.6.

The capacity loss over cycling for $\alpha\text{-MnO}_2$ nanostructures studied in this work is shown in Fig. 6.8(a). The initial discharge capacity is 219 mAh/g (the theoretical capacity of this compound is 308 mAh/g). This value increases in the second cycle to 227 mAh/g and in the following cycles it continuously decreases until it reaches 179 mAh/g in the ninth cycle. These values are slightly higher than those of heat treated (in order to remove water from the structure) $\alpha\text{-MnO}_2$ and lithia stabilized

0.15Li₂O·MnO₂ illustrated in Fig. 6.8(b) [20]. Galvanostatic studies of α -MnO₂ and γ -MnO₂ studied by Hill et al. have initial discharge capacities of 130 mAh/g, and 180 mAh/g, respectively which stabilizes to 145 mAh/g and 150 mAh/g after 20 cycles. Slightly higher values for these materials were presented elsewhere [226]. α -MnO₂ studied in this work shows good rechargeability, yielding 180 mAh/g after nine cycles. These values are higher than others found in literature as described above. This might be due to the larger surface area of the nanosized structured electrode material. The capacity loss suggests that a small part of the inserted Li helps the structural stability of the α -MnO₂, and therefore this amount is difficult to be extracted once it was inserted into the structure.

Electrochemical synthesis

In order to electrochemically synthesize Li_{*x*} α -MnO₂, 20-30 mg of powder were cycled in potentiostatic or galvanostatic mode. Four different doping levels were achieved: Li_{*x*}MnO₂ with $x = 0.05$, $x = 0.1$, $x = 0.3$ and $x = 0.8$. The result of this synthesis is illustrated in Fig. 6.9. For the potentiostatically synthesized Li_{*x*}MnO₂ the electrode material was discharged with a speed of $C/100$, starting from the initial potential value towards lower potentials until the desired doping level was achieved. For the galvanostatic synthesis of Li_{0.8}MnO₂ a slower speed was used ($C/200$), while a constant current was maintained until 1.6 V.

The arrows on the graph mark two slight changes (plateaus) in the voltage profile of this compound, which might indicate a structural change during cycling as it was also suggested elsewhere [200, 227]. As shown by the figure, the material can accommodate a significant amount of Li, Li_{0.8}MnO₂ yielding a high capacity of 235 mAh/g representing three quarters of the theoretical capacity expected for this material.

6.2.2 Magnetic properties of Li_{*x*}MnO₂ nanostructures

Magnetic properties of manganese oxide

Manganese oxides have been considered to be an interesting material that might present innovative properties rising from the electronic states of the transition metal atom: Mn²⁺ ($3d^5$), Mn³⁺ ($3d^4$), Mn⁴⁺ ($3d^3$) etc, based on large electron correlations. One interesting aspect of these materials is given by the coexistence of two types of d electrons, in the t_{2g} and in the e_g orbitals. Ferromagnetism in these materials

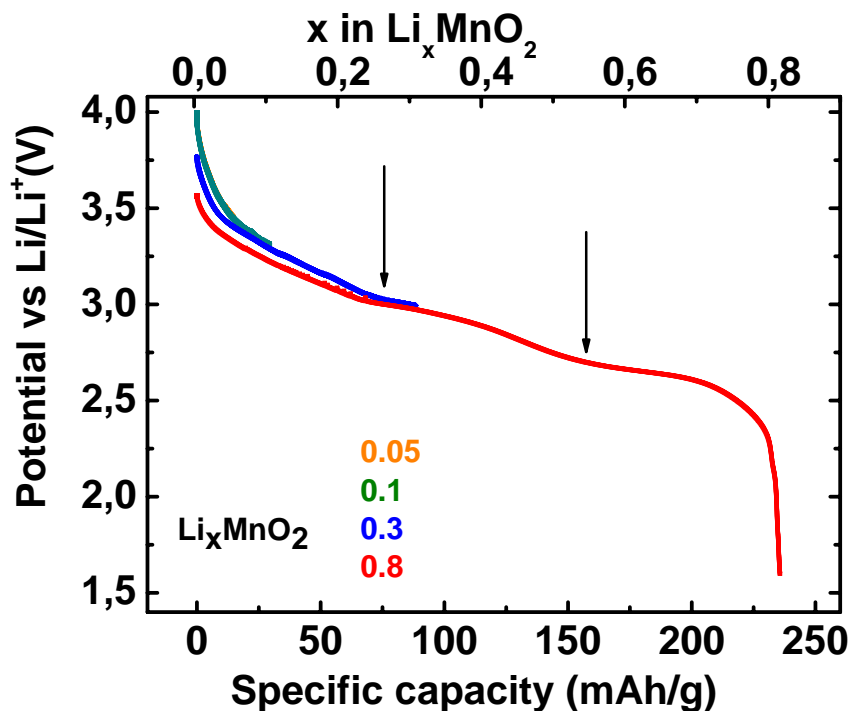


Figure 6.9: Potentiostatic ($x = 0.05, 0.1, 0.3$) and Galvanostatic ($x = 0.8$) synthesis of Li_xMnO_2 .

is known to appear due to coupling between the localized magnetic moments (t_{2g}) with the e_g states interacting by double-exchange.

LiMn_2O_4 represents one of the manganese compounds intensively studied from the magnetization point of view. $\lambda\text{-MnO}_2$ can be obtained if lithium is extracted from this material. If lithium is inserted into LiMn_2O_4 then $\text{Li}_2\text{Mn}_2\text{O}_4$ is created. The magnetic properties of this family of compounds are governed by the interactions between the Mn ions, depending on the Mn valence in the $[\text{Mn}_2]\text{O}_4$ network [228]. For example, $\text{Li}_2\text{Mn}_2\text{O}_4$ has a distorted tetragonal symmetry resulting from collective Jahn-Teller distortion of the high-spin Mn^{3+} ($S = 2$). The magnetic susceptibility of $\text{Li}_2\text{Mn}_2\text{O}_4$ shows no evidence of Curie-Weiss behavior up to 600 K, suggesting short range AFM correlations ascribed to the geometrical frustration in the tetragonal Mn sublattice [229]. In $\text{Li}_x\text{Mn}_2\text{O}_4$, it was proven that the $90^\circ \text{Mn}^{4+} - \text{O}^{2-} - \text{Mn}^{4+}$ interaction results in FM coupling, according to the Goodenough-Kanamori-Anderson rules. That is explained by an empty e_g orbital of Mn^{4+} ($t_{2g}^3 e_g^0$) overlapping with a half filled t_{2g} orbital (both Mn^{4+} and Mn^{3+} have half filled t_{2g} orbitals). This interaction takes place through an O $2p$ orbital that σ bonds with an e_g orbital on one Mn atom, and π bonds with a t_{2g} orbital on the neighboring Mn atom. On the other hand, $\text{Mn}^{3+} - \text{O} - \text{Mn}^{3+}$ and $\text{Mn}^{4+} - \text{O} - \text{Mn}^{3+}$ (in 180° geometry) interaction results in AFM coupling, required by the Pauli exclusion principle [228]. In contrast,

LiMn₂O₄ spinel formally contains a mixture of Mn³⁺ and Mn⁴⁺. Its magnetic properties show paramagnetic behavior down to 4.2 K. Above 140 K a large AFM Θ of -260 K is present (Θ is obtained by fitting the data in the high temperature range with the well-known Curie-Weiss law $\chi = \frac{C}{T-\Theta}$ [139]). After partial Li extraction from this compound, the spinel structure is maintained, and the Mn has an oxidation state of 4⁺. The Curie temperature Θ lowers in delithiated form to -70 K [230]. Spin-glass-like behavior was observed in LiMn₂O₄ and its delithiated form λ -MnO₂, indicating the presence of frozen spins [231]. This behavior was explained by the AFM tetrahedral network in Mn₂O₄ sublattice combined with magnetic disorder given by mixed valence of Mn³⁺ and Mn⁴⁺ that induces competing AFM and FM interactions. Discharging Li_{*x*}Mn₂O₄ resulted in cubic phase of λ -Li_{0.07}Mn₂O₄ with Θ of -74 K and Li_{0.94}Mn₂O₄ with $\Theta = -250$ K. Charging the same compound, the tetragonal Li_{1.82}Mn₂O₄ with $\Theta = -770$ K was obtained. One can see from these results that the Curie temperature increases with increasing the *x* in Li_{*x*}Mn₂O₄ suggesting that the AFM interactions are stronger as the concentration of Mn⁴⁺ decreases (FM interaction between 90° Mn⁴⁺-O-Mn⁴⁺ decreases). Greedan and coworkers established the magnetic properties of orthorhombic LiMnO₂ for the first time [232]. By measuring the temperature dependence of the magnetic susceptibility until 800 K, they found a Θ value suggesting that the Curie-Weiss fit is not valid in this case ($\Theta = -1056$ K and much higher than the highest measured temperature). They also reported long range AFM ordering below 261 K and short range magnetic correlations noticeable in the susceptibility broad peak at 350 K [232]. In contrast to this variety of different properties, all these forms of manganese dioxide exhibit common features in the magnetic susceptibility studies. They all show a thermal hysteresis of the susceptibility as shown in Fig. 6.10, i.e. ZFC and FC measurements diverge below 100 K in the case of LiMnO₂ [232] or 65 K for LiMn₂O₄ [229]. This splitting of ZFC and FC data was attributed to a FM component of the magnetization in the studied systems. Another common characteristic of these systems is a peak in the ZFC magnetization at T_N , indicating AFM ordering in the low temperature regime. This peak can be found at 16 K in λ -Li_{0.07}Mn₂O₄ [231] or at 30 K-32 K in different forms of LiMn₂O₄ [233]. The irreversibility of the ZFC and FC experiments, together with the maximum in the ZFC are characteristics of spin glasses [234]. In most of the cases below the temperature were ZFC and FC split, the FC magnetization detains an abrupt increase and sometimes even a saturation. This behavior was attributed to ferromagnetic component of the magnetization in these compounds.

Magnetic properties of β -MnO₂ (pyrolusite) were studied as well. Liu et al. studied β -MnO₂ nanorods (50 nm- 80 nm in diameter), which in their case showed ferromag-

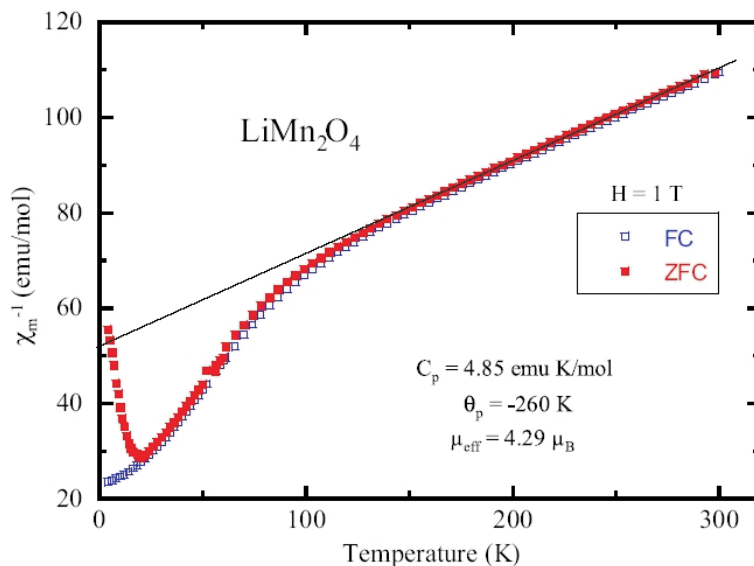


Figure 6.10: Reciprocal magnetic susceptibility of Li₂Mn₂O₄ measured in 1 T applied field [230].

netic behavior at low applied fields with a coercivity of 144 Oe [222]. The system did not reach a saturation magnetization up to an applied field of 3000 Oe. The FM response was again attributed to Mn⁴⁺-O²⁻-Mn⁴⁺ FM interactions. β -MnO₂ (Mn⁴⁺) nanorods covered with a thin layer of α -Mn₂O₃ (Mn³⁺) show a superposition of bulk magnetic properties of β -MnO₂ and α -Mn₂O₃, and FM influences of the interface layer between these two phases. A splitting of the ZFC and FC magnetization is present here as well as in previously described manganese oxides. The splitting is significantly affected by the external applied field indicating a thermally unstable magnetic system. The field dependence of the magnetization at low temperature shows FM behavior, described by a small hysteresis found at 5 K. The FM component that induces this behavior is not present at 55 K or higher temperatures [235]. Jana and coworkers synthesized β -MnO₂ in nanosphere and nanorod shape. Field dependent magnetization studies indicate the superparamagnetic nature of these materials, with a blocking temperature T_B of 4 K in the case of nanorods and 40 K for nanospheres. This shows that the magnetic properties of β -MnO₂ are sensitive to size and shape [236, 237]. Transport and magnetic properties of single crystals of the magnetic conductor β -MnO₂ (with rutile structure) showed metallic behavior due to n -type carriers resulting from an off-stoichiometry β -MnO_{2- δ . The system has a helical magnetic long-range order below T_N of approximately 92 K. The Curie temperature in this material was -783 K [238]. A slightly higher T_N =100 K was found in the dandelion-like β -MnO₂ three-dimensional nanostructure [239].}

Only few magnetic studies were performed in the case of $\alpha\text{-MnO}_2$. Single crystals of the hollandite $\alpha\text{-MnO}_2$ with K^+ as a foreign cation, i.e. $\text{K}_{\geq 0.07}\alpha\text{-Mn}_{>0.93}\text{O}_2$ shows AFM behavior with a Néel temperature $T_N=24.5$ K. The mole ratio between the K and Mn was less than 7% [240]. Another example of studied $\alpha\text{-MnO}_2$ is represented by the $\text{K}_{0.087}$ $\alpha\text{-MnO}_2$ nanotubes, studied by Luo et al.. Field dependence of the magnetic susceptibility together with hysteresis effect, thermoremanent magnetization and memory effect were studied for this compound. The ZFC and FC measurement diverge, as seen in other manganese oxides, below 50 K. An AFM Curie temperature of -303 K was established by fitting the magnetic susceptibility above 150 K. The geometrical frustration arising from the triangular lattice and the mixed $\text{Mn}^{3+}/\text{Mn}^{4+}$ oxidation state [241], together with informations given by the measurements mentioned above suggested that this compound has a spin-glass behavior below 33.1 K. The spin glass behavior for manganese oxide compound has been also established for the hexagonal $\text{Na}_{0.7}\text{MnO}_2$ [242]. Although not identical with the $\text{K}_{0.087}\alpha\text{-MnO}_2$ nanotubes, this has the same environment for the Mn ion. In both cases the Mn is located in the center of an oxygen octahedron, and Mn ions show geometrical frustration due to the triangular arrangement. In both compounds, the intercalation of large cations, i.e. Na and K, induces a mixed valency of Mn^{3+} and Mn^{4+} .

Another hollandite structure, $\text{Ba}_{1.2}\text{Mn}_8\text{O}_{16}$ shows a magnetic transition at 40 K [243]. Presence of a small ferromagnetic component is suggested by magnetic hysteresis loop at 5 K, presumably arising from the ordered spins tilting within the low symmetry structure. The paramagnetic behavior between 150 K and 300 K resulted in $\Theta = -385$ K. The magnetic transition is far below the Curie temperature, therefore magnetic frustration due to the triangular structure of Mn ions and competing AFM and FM interactions was suggested in this compound.

Manganese oxides have interesting magnetic properties, in which the Mn sublattice plays a important role, as well as the mixed valency of the Mn ions. Frustration, as well as AFM and FM competing interactions are present in most of these manganese oxides.

Magnetic properties of undoped and doped $\alpha\text{-MnO}_2$ nanostructures

Undoped $\alpha\text{-MnO}_2$ nanostructures

$\alpha\text{-MnO}_2$ has a tunnel structure (size 2×2) formed by MnO_6 octahedra sharing their corners. The Mn^{4+} atoms situated in the center of the MnO_6 octahedra are triangularly arranged. This spin arrangement often leads to geometrical frustration due to

6 Electrochemically doped MnO₂ nanostructures

the fact that in a equilateral triangle, the situation when only two of the three spins constraints can be satisfied simultaneously, may appear. This geometrical frustration can be defined by a factor equal to Θ/T_N [244]. If this factor is higher than 10 the system is strongly geometrically frustrated. In the case of α -MnO₂ studied in this work this factor is approximately 15 indicating the geometrical frustration, known in other manganese oxides as well.

The magnetic properties of the α -MnO₂ nanostructures used for this work were established elsewhere [137].

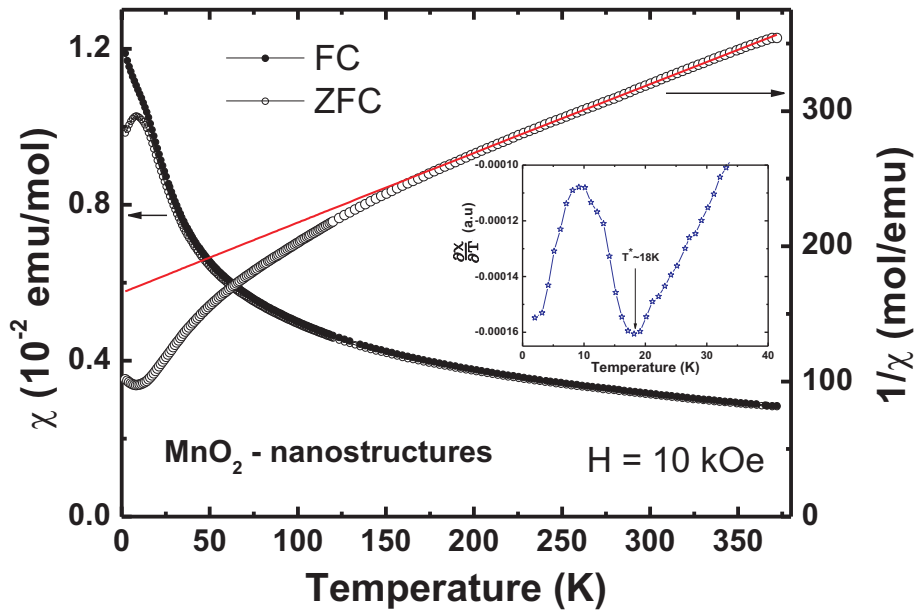


Figure 6.11: Temperature dependence of the FC and ZFC magnetic susceptibility, in the left hand side, and ZFC inverse susceptibility, in the right hand side of the graph. The measurement was performed in 10 kOe applied magnetic field. The red line represents the Curie-Weiss fit in high temperature regime. Adapted from Ref. [137]. The inset represents the $\partial\chi/\partial T$ of the FC susceptibility. The $T^* \approx 18$ K is estimated from the minimum of this derivative, as indicated by the arrow in the inset.

Fig. 6.11 shows the FC and ZFC magnetic susceptibility measured in 10 kOe applied magnetic field. First, the system was cooled down to 2 K, then the magnetic field was applied and the measurement has been performed while warming up to 370 K, resulting the ZFC measurement. At 370 K the field was maintained, the system cooled again to low temperature and FC measurement was performed while warming. In the right hand ordinate of Fig. 6.11, the inverse susceptibility is plotted together with the Curie-Weiss fit ($\chi = \frac{C}{T-\Theta}$) performed in the temperature range

constant taken from this fit is 1.90 emuK/mol, and it implies an effective moment of the Mn ions $\mu_{\text{eff}}=3.9\mu_B$, which is close to the theoretical value of the effective moment $3.87\mu_B$, for Mn⁴⁺ (3d³, S=3/2). The negative sign of the Curie-temperature $\Theta=-300$ K implies that a strong AFM coupling between the Mn spins is present, as expected from the Goodenough-Kanamori-Anderson rules. In the left hand ordinate of Fig. 6.11, the ZFC and FC magnetic susceptibilities of α -MnO₂ are illustrated. In the inset of Fig. 6.11 the derivative of the FC measurement is shown, in order to extract information about the AFM transition temperature. The AFM ordering temperature is attributed to domain formation, and it is established as the minimum of the $\partial\chi/\partial T$, as shown in the inset of Fig. 6.11. This criteria of establishing the transition temperature will be used here in the future. For α -MnO₂ nanostructures studied in this work, $T^*\approx 18$ K, compared to 24.5 K for single crystal, needle-like α -MnO₂ [240]. The difference in the T^* between single crystal and nanostructured α -MnO₂ might come from smaller grain size of the material in the nanostructured material. The triangular geometry of the Mn atoms in α -MnO₂ is expected to result in a geometrical frustrated system. Indeed, taking into account the high value of the Curie temperature, -300 K and the transition temperature $T^*\approx 18$ K, one can obtain the frustration factor for α -MnO₂ $f\approx 15$.

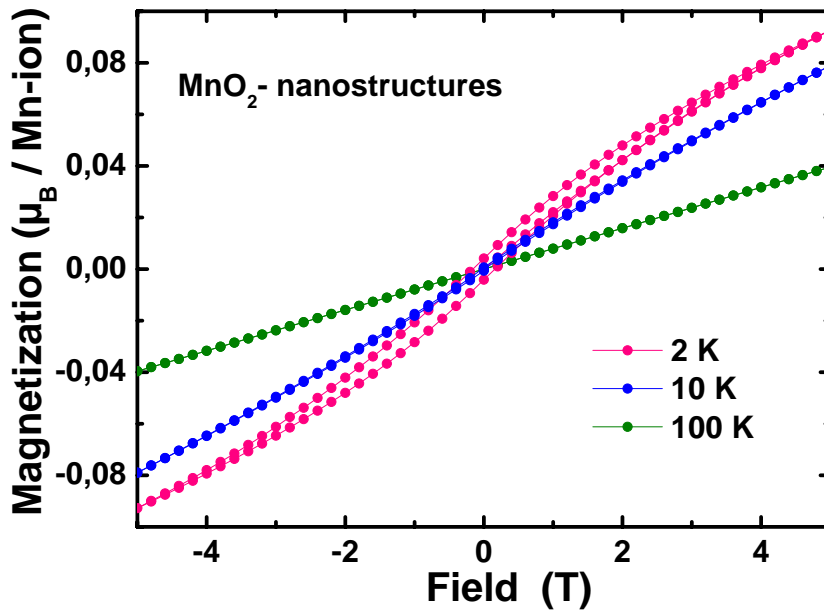


Figure 6.12: Field dependence of the magnetic susceptibility measured at different temperatures. Adapted from Ref. [137].

The field dependence of the magnetization for α -MnO₂ nanostructures, illustrate a small hysteresis present at very low temperatures (2 K) without saturation of the magnetic moments up to the highest magnetic field of 50 kOe, as shown in Fig. 6.12. This is consistent with the temperature hysteresis below T^* in Fig. 6.11. At higher temperatures (300 K) the hysteresis is not present. The small hysteresis at low temperature indicates the presence of a FM component in the system. Frustration together with competition between AFM (between Mn⁴⁺- Mn⁴⁺) and FM (between 90° Mn⁴⁺- O- Mn⁴⁺) interactions are known characteristics of materials with spin glass behavior.

Doped Li_xMnO₂

Using electrochemical techniques, four doping levels for α -MnO₂ nanostructures were obtained, namely 0.05, 0.1, 0.3 and finally 0.8. For each doping level, temperature dependence of the magnetic susceptibility and field dependence of the magnetization were studied. All the samples were measured in the quartz tubes described in the Chapter 3.2.

Fig. 6.13 shows the temperature dependence of the magnetic susceptibility measured in ZFC and FC conditions in applied magnetic field of 10 kOe, for Li_x α -MnO₂ nanostructures. From top to bottom, the results for $x = 0, 0.05, 0.1, 0.3$ and 0.8 are shown. The result of the electrochemical doping showed that for the maximum doping level $x = 0.8$, relatively three quarters of the theoretical capacity of Mn⁴⁺ reduction to Mn³⁺ has been achieved. For $x = 0.3$, approximately 30% of the theoretical capacity was obtained. These informations confirm the amount of lithium intercalation into the α -MnO₂. The result of doping the system with electrons is formation of a mixed valency, Mn⁴⁺/Mn³⁺, due to reduction of the Mn⁴⁺ (S=3/2) to Mn³⁺ (S=2). At a first glance, the temperature dependence of the magnetic susceptibility looks similar for all Li_x α -MnO₂ nanostructures. The cusp in the ZFC measurements might be attributed to domain wall movement. The separation of the ZFC and FC measurements at low temperatures is a sign of weak FM in the system. The lines in Fig. 6.13 represents the Curie-Weiss fit in high temperature range.

Using the position of the minimum in the derivative of the FC susceptibility, as illustrated in Fig. 6.13, the transition temperature T^* has been established for all doping levels. The doping dependence of the transition temperature is shown in Fig. 6.14(a). For the undoped α -MnO₂, the data show $T^* \approx 20$ K. T^* reaches 40 K for Li_{0.8}MnO₂. The frustration factor can be calculated for all doping level, except the sample with $x = 0.8$. It slightly decreases with doping since T^* is increasing

6.2 Properties of electrochemically doped MnO₂ nanostructures

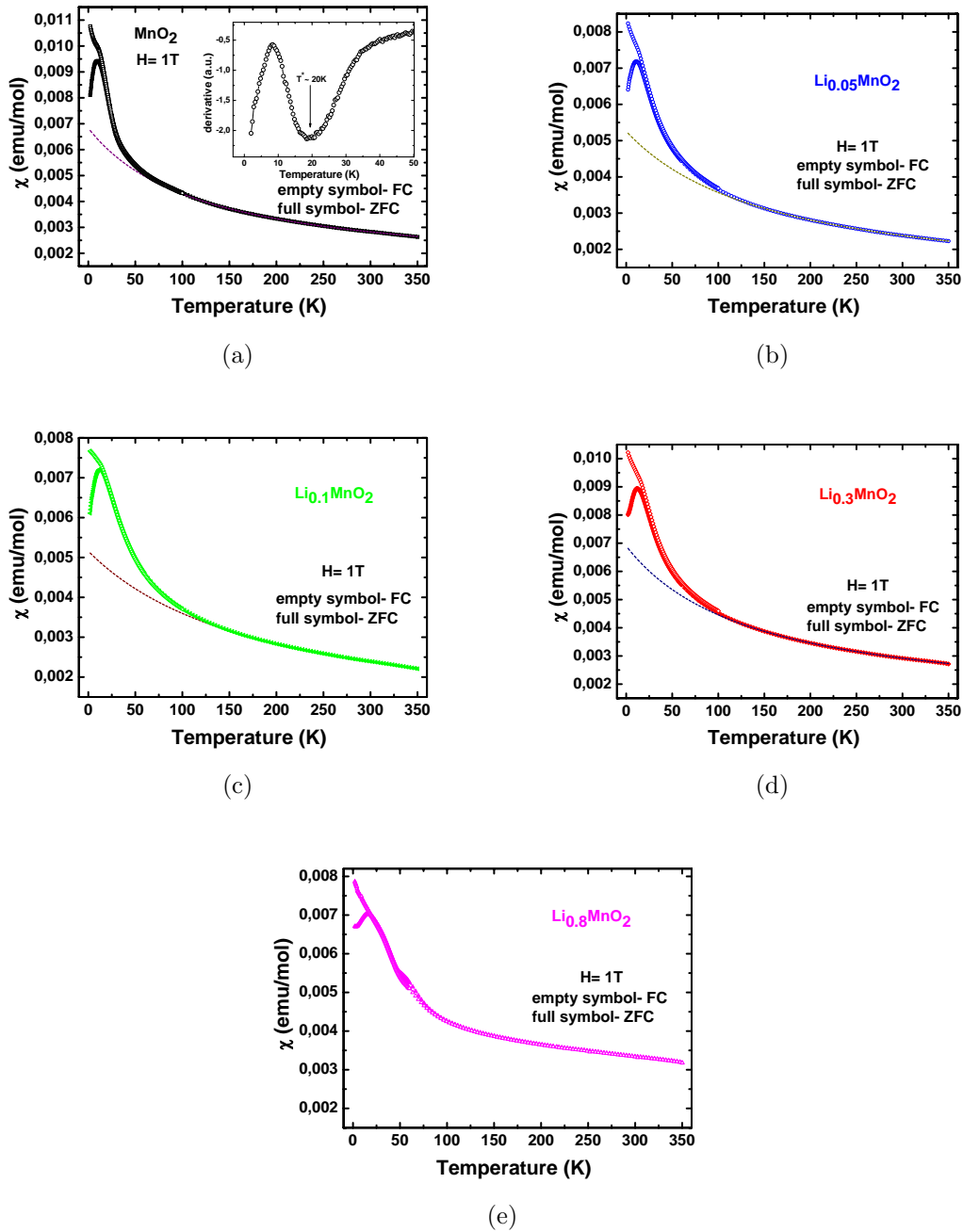


Figure 6.13: $\text{Li}_x\text{-MnO}_2$ nanostructures. Temperature dependence of both ZFC (full symbol) and FC (empty symbol) magnetic susceptibilities measured in 10 kOe applied magnetic field for $x = 0, 0.05, 0.1, 0.3$ and 0.8 . The inset in (a) illustrates the transition temperature T^* . The same criterion was used to establish this transition for all the other doping levels.

6 Electrochemically doped MnO₂ nanostructures

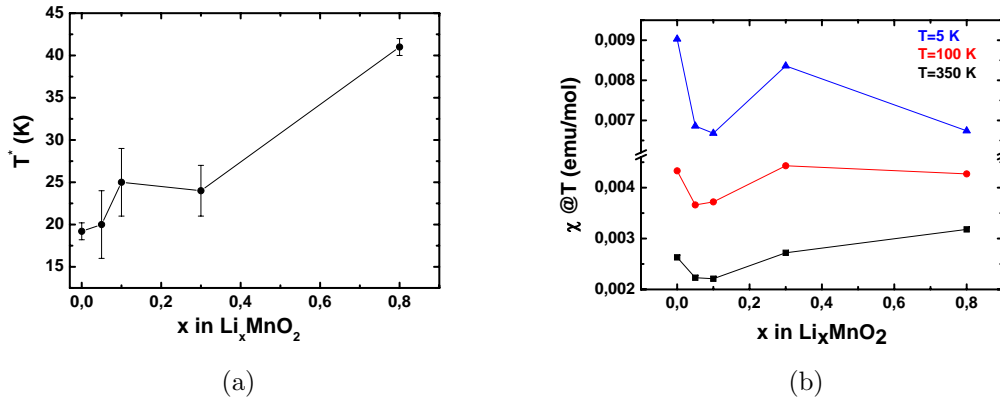


Figure 6.14: a) Transition temperature for Li_xMnO_2 with $x = 0, 0.05, 0.1, 0.3$ and 0.8 , obtained from derivative of FC magnetic susceptibility measured in 10 kOe; b) The ZFC magnetic susceptibility measured at 5 K, 100 K and 350 K in applied field of 10 kOe.

while θ is rather not affected by doping. With introducing more electrons in the structure, T^* increases and becomes broader. This can be observed also in Fig. 6.13 where the FC susceptibility for $\text{Li}_{0.8}\text{MnO}_2$ is almost straight at low temperatures, while the undoped MnO_2 has a visible shoulder.

Fig. 6.14(b) is a resume of Fig. 6.13. The doping dependence of the ZFC magnetic susceptibility measured in 10 kOe, at three different temperatures (5 K, 100 K and 350 K) are presented. At low temperatures, after 5 and 10% lithium doping, the susceptibility decreases, and it increases back for 30% lithium doping, close to the value of the undoped compound. For the highest doping level it decreases again. Interestingly, at high temperatures, for low doping levels, the susceptibility decreases, and then increases with doping. Moreover, at high temperature of 350 K, for the highest lithium concentration, the magnetic susceptibility is 0.003 emu/mol compared to 0.002 emu/mol in the case of the undoped $\alpha\text{-MnO}_2$. This extra magnetic moment might arise from a FM contribution on top of the paramagnetic behavior expected at this high temperatures, or signature of Pauli susceptibility as it will be discussed later.

Table. 6.2 summarizes the fit results of temperature dependences of the magnetic susceptibility, using the Curie-Weiss function ($\chi = \frac{C}{T-\Theta}$). The values of the undoped MnO_2 are slightly different than those mentioned earlier from [137], possibly due to slight differences in the composition or homogeneity of the samples, as well as different sample holder. (For example, residual water can be easily trapped in the tunnel structure and therefore might affect the composition of the material, due to Mn^{3+} formation [245].). Using the value of the Curie constant from Table. 6.2 the

effective moment for $x = 0$ can be estimated to $p_{\text{eff}}=3.67\mu_B$, indicating a valency for the Mn atom higher than 4. This might be influenced by the presence of Mn ions in a higher state, e.g. Mn⁵⁺ ($p_{\text{eff}}=2.83\mu_B$). Considering this, the valency in the undoped MnO₂ is approximately 4.2. If one considers that in Li_{0.05}MnO₂, 5% of the Mn⁴⁺ become Mn³⁺, and 95% remain Mn⁴⁺, this should give an effective moment of 3.73 (taking p_{eff} for Mn⁴⁺ equal to $3.67\mu_B$, as obtained from the experiment). If in this way, the expected effective moments are calculated for all doping levels, obtaining 3.79 for Li_{0.1}MnO₂ and 4.03 for Li_{0.3}MnO₂. As shown by Table.6.2, the measured effective moments are lower than those expected. These differences might arise from either unknown impurities, residual components of the starting materials used for synthesis (MnSO₄. H⁺-H⁺ interactions) or water intercalation that modifies the oxidation state of the Mn. The “impurification” of the α -MnO₂ with γ -MnO₂ does not modify the valency of the Mn in α -MnO₂, but it can provide additional magnetic sites, that can interact in a non trivial way. For Li_{0.8}MnO₂ the Curie fit would result in a value of the Curie temperature much higher than the maximum measured temperature, therefore in this case the Curie fit can not be applied. From the results of the Curie fit one can see that the Curie temperature, indicating strong AFM correlations does not variate upon doping.

| Li _x MnO ₂ | C (emuK/mol · Oe) | θ (K ($\pm \approx 2$)) | $p_{\text{eff}}^{\text{exp}}$ ($\mu_B/\text{f.u.}$) | $p_{\text{eff}}^{\text{th}}$ ($\mu_B/\text{f.u.}$) |
|----------------------------------|--------------------|-----------------------------------|---|--|
| $x = 0$ | 1.69 | -303 | 3.67 | 3.87 |
| $x = 0.05$ | 1.41 | -297 | 3.35 | 3.91 |
| $x = 0.1$ | 1.42 | -297 | 3.37 | 3.96 |
| $x = 0.3$ | 1.73 | -298 | 3.71 | 4 |

Table 6.2: Fitting results in high temperature regime using the Curie-Weiss function for ZFC magnetic susceptibility for Li_xMnO₂ with $x = 0, 0.05, 0.1$ and 0.3 . The last column in the table indicates the theoretical values for p_{eff} for the different doping levels.

Fig. 6.15 illustrates the field dependence of the magnetization measured at a temperature of 2 K between -5 T and 5 T. For the undoped α -MnO₂ a small hysteresis is visible, as mentioned earlier, indicating a very weak FM-like behavior of the measured magnetization presumably due to a non-collinearity of AFM alignment of neighboring spins, which results in spin canting. Upon doping, the hysteresis effect is clearly diminishing. Interestingly, for 0.05, 0.1 and 0.3, the hysteresis seems to be independent on the lithium concentration into the compound. For the highest doping level, compared with the others, the hysteresis is almost not visible. The not too small values of the magnetization as well as the missing hysteresis and the clear linearity of the $M(H)$ curve for Li_{0.8}MnO₂ indicates the absence of strong FM moments,

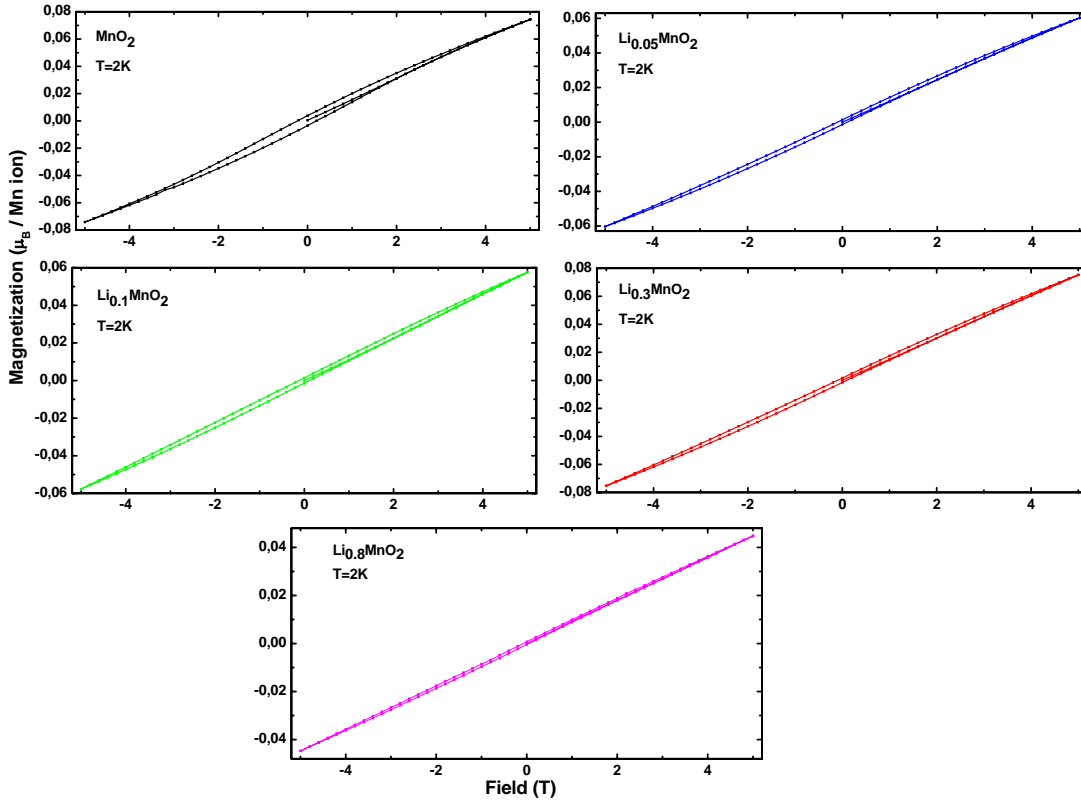


Figure 6.15: Field dependence of the magnetization for Li_xMnO_2 with $x = 0, 0.05, 0.1, 0.3$ and 0.8 measured at $T=2$ K.

Upon doping, the starting valency Mn^{4+} in $\alpha\text{-MnO}_2$ would reduce to Mn^{n+} where $3 \leq n \leq 4$. As the result of the Curie fit revealed, in the $\alpha\text{-MnO}_2$ the actual valency is $\text{Mn}^{3.73+}$. For the low doping levels, this valency decreases to ≈ 3.4 , and for $x = 0.3$ it increases again around the same value of the starting compound.

$\text{Li}_{0.8}\text{MnO}_2$ Fig. 6.16 shows the FC magnetic susceptibility for both the undoped $\alpha\text{-MnO}_2$ nanostructures and $\text{Li}_{0.8}\text{MnO}_2$ measured at different magnetic fields. Following the results of the derivative for both samples, with $x = 0$ and $x = 0.8$, one can estimate that the transition temperature T^* slightly changes. For the undoped $\alpha\text{-MnO}_2$, at 100 Oe applied field, $T^* = 13$ K, and it shifts to 18 K in 10 kOe magnetic field. $\frac{dT^*}{dB}$ is larger than zero, indicating the presence of FM-like behavior. This is in agreement with the increase of the magnetic susceptibility at low temperatures in the undoped $\alpha\text{-MnO}_2$ illustrate in Fig. 6.11. For $\text{Li}_{0.8}\text{MnO}_2$, at 100 Oe applied field T^* is at much higher temperature, of 35 K, and much broader. It reaches 40 K when 10 kOe magnetic field is applied. The applied field influence on $\chi(T)$ for $\text{Li}_{0.8}\text{MnO}_2$ seems to be less than for the undoped compound. Perhaps the AFM transition T^*

is affected by the creation of Mn³⁺ magnetic sites, and therefore maybe by the presence of direct exchange FM interactions. The formation of Mn³⁺ may influence the frustration in Li_{0.8}MnO₂.

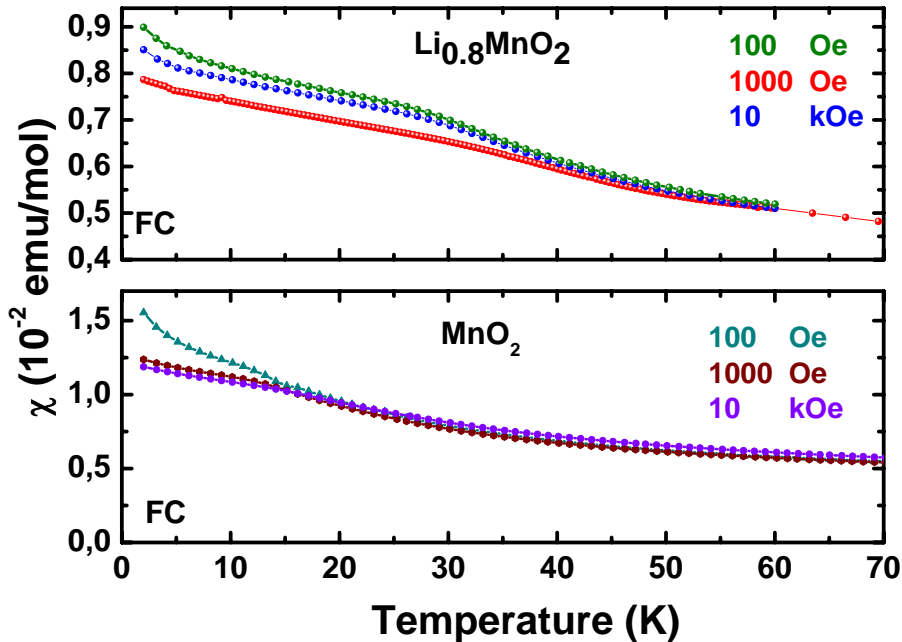


Figure 6.16: Temperature dependence of the magnetic susceptibility (FC) for MnO₂ and Li_{0.8}MnO₂ in different applied magnetic fields.

Fig. 6.17 illustrates the ZFC and FC magnetic susceptibility measured in 100 Oe, 1000 Oe, and 10 kOe for Li_{0.8}MnO₂. For each field, first the ZFC and then the FC measurement was performed, both on warming. The first measurement was done with 100 Oe, then 1000 Oe and finally with 10 kOe. The splitting of the ZFC and FC measurement is present, as it was also seen in the undoped MnO₂, shown in Fig. 6.11. Below roughly 50 K the ZFC and FC in Li_{0.8}MnO₂ diverge, for all three applied fields. The abrupt increase of the FC susceptibility from the point where it does not coincide with the ZFC anymore, is attributed to a FM component in the system, as also described for other manganese oxides.

In Fig. 6.14(b) is shown that at high temperatures, the magnetic susceptibility for Li_{0.8}MnO₂ is higher than the in the undoped compound. The Curie fit could not be applied in the case of Li_{0.8}MnO₂. An extra magnetic moment in high temperatures of $\chi(T)$ for Li_{0.8}MnO₂ might arise from delocalized electrons (conduction electrons from the e_g orbitals) that turn over when a magnetic field is applied. Such a contribution from conducting electrons, i.e. Pauli susceptibility, would imply a temperature-independent additional contribution to the susceptibility.

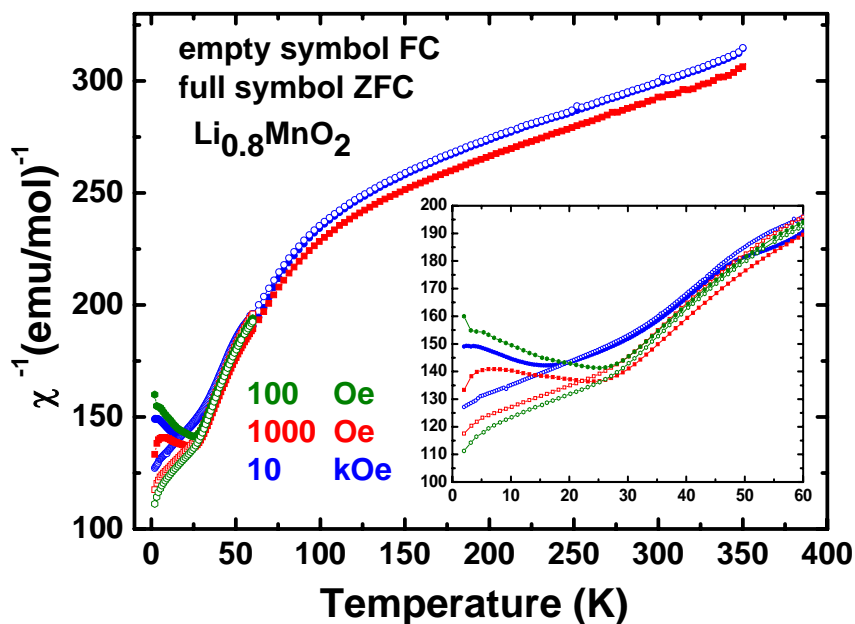


Figure 6.17: Temperature dependence of the magnetic susceptibility, both ZFC and FC for $\text{Li}_{0.8}\text{MnO}_2$ in different applied magnetic fields.

Finally, the field dependence of the magnetization at different temperatures for $\text{Li}_{0.8}\text{MnO}_2$ is shown in Fig. 6.18. A very small hysteresis is found at a low temperature of 2 K, which completely disappears already at 25 K, and a totally linear behavior is seen at 300 K, indicating the antiferromagnetism in the system.

In the beginning of this section, while describing general properties of manganese oxides the type of correlations between combinations of Mn^{4+} and Mn^{3+} were mentioned. In $\alpha\text{-MnO}_2$, AFM (between Mn^{4+} - Mn^{4+}) and FM (between 90° Mn^{4+} - O- Mn^{4+}) interactions are known to govern the magnetic behavior of the compound. When Mn is in a mixed oxidation state, possible interactions between the magnetic spins are more complicated. The AFM superexchange interaction between Mn^{3+} - O- Mn^{4+} is a well known interaction in manganese oxide with mixed valency of the Mn atom [246]. When two Mn ions, Mn^{3+} and Mn^{4+} are separated by one O^{2-} , a exchange interaction between these two Mn ions, mediated by the oxygen, appears. The electron from the e_g orbital of Mn^{3+} can hop back and forth between its initial position and the empty site of the e_g orbital of Mn^{4+} . The induced exchange Mn^{3+} - O- Mn^{4+} leads to a parallel spin alignment, and therefore results in FM coupling of Mn spins [247]. Therefore, in the compound studied here, by doping, more possible FM interactions between Mn^{3+} and Mn^{4+} might be expected from super-exchange interactions.

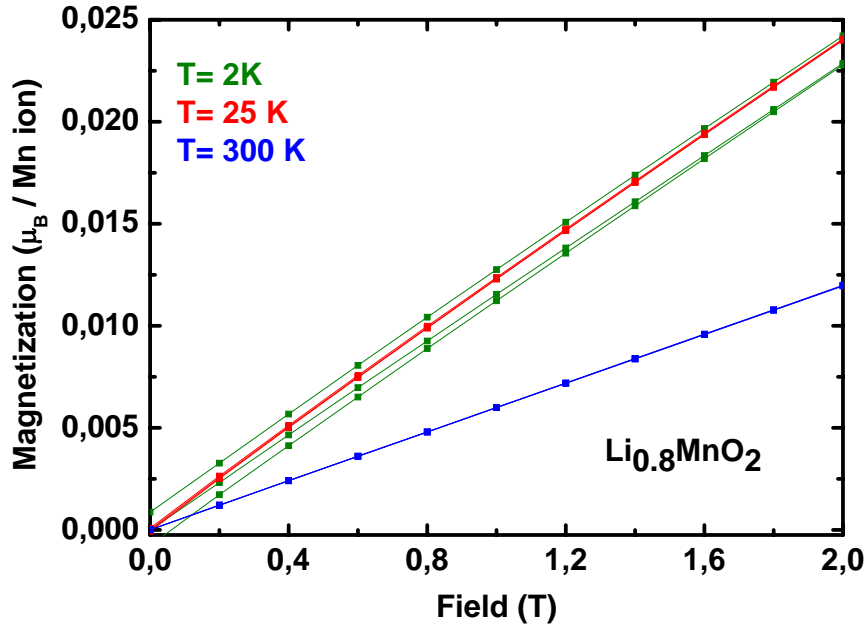


Figure 6.18: Field dependence of the magnetization for $\text{Li}_{0.8}\text{MnO}_2$ measured at 2 K, 25 K and 300 K.

From the field dependence of the magnetization, the reduction of the FM component which induces a hysteresis in the undoped $\alpha\text{-MnO}_2$ is seen. This might be influenced by spin-canting of two neighbours which are AFM coupled. For $\text{Li}_{0.8}\text{MnO}_2$ most of the Mn^{4+} are reduced to Mn^{3+} . One can assume that the 90° FM interactions $\text{Mn}^{4+} - \text{O}^{2-} - \text{Mn}^{4+}$ in the $\alpha\text{-MnO}_2$ nanostructures are less present when doping. As a result, the AFM interactions are more favorable. For the highest doping level, the impossibility of fitting the results with the Curie-Weiss fit, induces the idea of Pauli paramagnetism contribution at high temperatures. Clearly, the magnetic properties of the doped $\alpha\text{-MnO}_2$ are very complex, due to many possible interactions and other kind of contributions.

The complexity of manganese oxide compounds is very well known. For example, in Fig. 6.19 the electronic phase diagram for $\text{La}_{1-x}\text{Sr}_x\text{MnO}_3$, $\text{Nd}_{1-x}\text{Sr}_x\text{MnO}_3$ and $\text{Pr}_{1-x}\text{Ca}_x\text{MnO}_3$ is shown. As the hole concentration x changes in these compounds, depending on the measured temperature the systems can change from AFM to FM, or from paramagnetic insulating (PI) state they can change to paramagnetic metallic (PM), or spin-canted insulating states (CI) etc. All these variations in physical properties are influenced by the doping level.

The static magnetic studies shown in this chapter, are not enough to clearly elucidate the effect of doping on the $\text{Li}_x\alpha\text{-MnO}_2$. A good establishment of the crys-

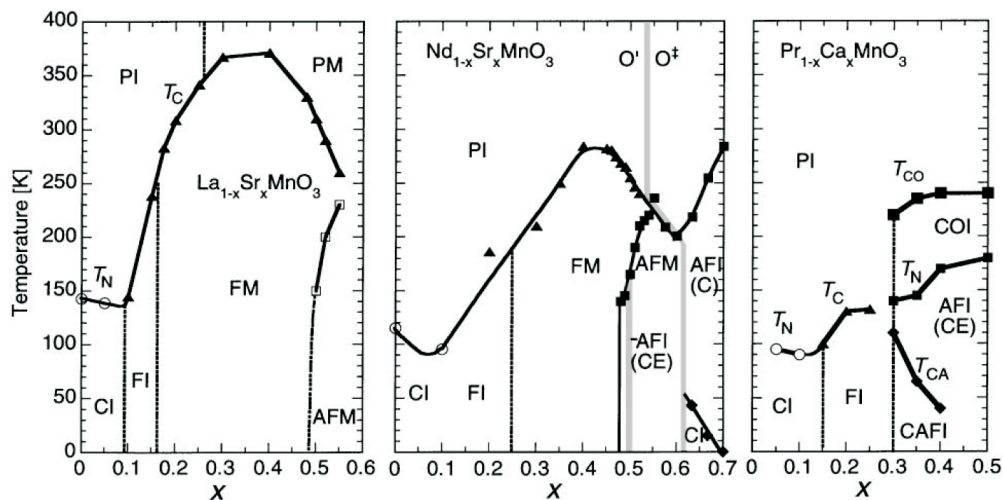


Figure 6.19: The magnetic and electronic phase diagram of different manganese oxides, which reveal, the complexity of this kind of compound. Adapted from Ref. [248].

tallographic structure, before and after the lithium doping, impurity effects as well as a theoretical model of possible interactions between the Mn spins in the doped $\alpha\text{-MnO}_2$ nanostructures might give in the future deeper interpretation of the doping effect in this material.

6.3 Conclusion

The tunneled structure $\alpha\text{-MnO}_2$ nanostructures (with (2×2) tunnel dimension) have been studied in this chapter. The structure is formed by MnO_6 octahedra which share their corners in order to form the (2×2) tunnel. The Mn^{4+} atoms are situated in the center of the MnO_6 octahedra and they have triangular arrangement. The electrochemical studies performed on this compound displayed a mixture between the $\alpha\text{-}$ and $\gamma\text{-MnO}_2$. This was revealed from cyclic voltammograms performed over nearly ten cycles, which showed features arising from both structural forms of the manganese oxides. The system is clearly sensitive to the scan rate used for electrochemical experiments. The specific discharge capacities are approximately 200 mAh/g, lower than the theoretical capacity for $\alpha\text{-MnO}_2$, 308 mAh/g, but higher than similar experiments from the literature.

Using electrochemical techniques, four doping levels have been achieved in Li_xMnO_2 with $x = 0.05, 0.1, 0.3$ and 0.8 . The temperature dependence of the magnetic susceptibility as well as the field dependence of the magnetization were measured. The low doping levels seem not to change drastically the magnetic properties of the

undoped α -MnO₂. The frustration factor calculated for $x = 0, 0.05, 0.1, 0.3$ does not change significantly. For the highest doping level, spin canting of AFM spins and Pauli susceptibility of delocalized spins might influence the magnetic properties. It is clear that by doping, different interactions might appear, due to formation of the Mn³⁺, by reducing the Mn⁴⁺ upon electrons intercalation. The mixed valency in the studied compound, and different possible interactions arising between magnetic spins give a complexity to the magnetic properties of doped α -MnO₂.

This page intentionally contains only this sentence.

7 Conclusions

In this work electrochemical techniques were used to dope conventionally prepared transition metal oxide compounds. The oxidation state of the transition metal ion was tuned by intercalation of lithium into the crystal structure, i.e. by electrochemical doping, and the result of this approach was studied. Electrochemical doping made it possible to reach unusual high and mixed valence states of the transition metal not accessible by standard solid state chemistry. The effect of lithium doping on the magnetic properties of the studied materials was investigated by bulk and local probe techniques. Although the investigation of magnetic properties of transition metal oxides was the main focus of this work, also the potential of these materials as cathodes in lithium batteries was explored.

Electrochemistry is a powerful tool that offers the possibility to vary the oxidation state of transition metal ions and therefore induce among other effects, structural deformations which may change the physical properties as shown in the second chapter of this work. These structural changes influence the lithium's insertion/extraction processes in the studied electrode materials. The interplay between electrochemistry as a synthesis method of novel materials and the study of the physical properties of these materials may result in a better understanding of the process of lithium ion diffusion. This, in turn can improve the functionality of alkali-ion batteries made of transition metal oxides.

Chapter 4 addressed the electrochemical properties as well as the effect of Li-insertion on the magnetic properties of nanoscale Vanadium oxides, i.e. Vanadium oxide nanotubes (VOx-NT). Electrochemical Li intercalation was applied to modify the electronic and magnetic properties of the VOx-NT. Cyclic voltammetry, potentiostatic, and galvanostatic experiments were performed using a two-electrode Swagelok-type cell. With these techniques, the possibility of using this nanotube form of vanadium oxide as a cathode material in lithium batteries was investigated. The specific discharge capacity of VOx-NT studied in this work exhibits values of approximately 150 mAh/g. This capacity is almost half of the capacity expected for total reduction of V^{5+} to V^{3+} (370 mAh/g), but among the highest described in the

7 Conclusions

literature. Using cyclic voltammetry, an electron transfer process that reduces V^{5+} to V^{4+} was found at potentials between 2.5 V and 2.8 V for all studied VOx-NT, with one exception (VOx-NT#5). However, the detailed study of the electrochemical performance of VOx-NT was not the main topic of this work.

The pristine VOx-NT is already a mixed valent oxide with 60 % of nonmagnetic V^{5+} and 40 % of magnetic V^{4+} that shows complex magnetic properties. Electrochemical methods were used to obtain different levels of charge doping, i.e. a variable lithium amount x was intercalated into pristine VOx-NT to obtain $Li_xVOx-NT$ with $x \leq 0.6$. The effect of lithium doping on the magnetic properties was studied with static magnetic susceptibility and three different local probe techniques, i.e. ESR, NMR, and μ SR. Several series of lithium doped VOx-NT were synthesized. In the first series $Li_xVOx-NT$ with $x=0, 0.05, 0.1, 0.15$ and 0.6 was successfully prepared. This elaborate study lead to the important conclusion that an optimal lithium concentration drastically changes the magnetic properties of the VOx-NT. Lithium doping of the pristine VOx-NT increases the number of the magnetic sites, i.e. $V^{4+}(S=1/2)$. This was indicated by the increase of the effective magnetic moment of the vanadium ion with doping. Moreover, lithium doping also drastically changed the magnetic interaction between the vanadium magnetic moments. This transformed the pristine VOx-NT into a high temperature ferromagnet at an optimal lithium doping of 10 % lithium per formula unit of VOx-NT.

The detailed magnetic studies revealed that the charge doping of the VOx-NT and the structural distortion created around the intercalated lithium cause the formation of self-assembled nanoscale ferromagnets in VOx-NT. These small ferromagnetic clusters around the intercalated lithium sites are responsible for the high temperature ferromagnetism of $Li_{0.1}VOx-NT$. The ferromagnetic clusters behave as an ensemble of superparamagnetic particles with a broad size distribution and a large magnetic moment that can be easily aligned by a moderate magnetic field, even at room temperature. This behavior of the ferromagnetic clusters may suggest their collective polaronic nature, similar to the scenario proposed for high temperature ferromagnets in nanoscale diluted magnetic semiconductors. This suggests that an appropriate tuning of the electronic, structural and magnetic properties of transition metal oxide nanostructures may result in high temperature ferromagnetism.

Another series of electrochemically lithium doped VOx-NT, with $x=0, 0.05, 0.1, 0.155, 0.2$ and 0.4 in $Li_xVOx-NT$ were studied as well by means of static magnetic susceptibility. Besides the expected increase of the vanadium's magnetic moment, a non-linear field dependence of the magnetization was observed for $Li_{0.1}VOx-NT$ in an applied field of up to 2 T at room temperature. This non-linearity is not present

in the undoped VO_x-NT, but visible also in Li_{0.05}VO_x-NT and Li_{0.155}VO_x-NT. These results once more show a clear dependence of the magnetic properties on doping. Also in this series lithium doping induced a large magnetic moment which could be easily aligned by a relatively small magnetic field at room temperature. The results presented here show that nanoscaled transition metal oxides have unique tunable magnetic properties not found in their bulk counterparts.

Another material which was electrochemically modified was Sr₂CuO₂Br₂ (see chapter 5). Its crystallographic structure consists of CuO₄ layers and is isostructural to the hole-doped high- T_c superconductor La_{2- x} Sr₂CuO₄. Electron doping by electrochemical lithium intercalation caused the emergence of superconductivity in this system. Studies of static magnetic susceptibility revealed that the superconducting transition in Li_{0.15}Sr₂CuO₂Br₂ occurs at approximately $T_c = 9$ K, with a superconducting volume fraction of approximately 18% at 2 K. The field dependence of the magnetization for temperatures ranging from 2 K to 10 K suggests the coexistence of superconductivity, antiferromagnetism and weak ferromagnetism that could be due to spin canting. Here, electrochemical doping offers a route to study the electronic phase diagram of the new electron doped superconductor Li _{x} Sr₂CuO₂Br₂.

The third material investigated in this thesis is nanoscaled α -MnO₂ (see chapter 6). Its structure consists of tunnels formed by square rings of eight MnO₆ octahedra (2 by 2 octahedra). Oxidation and reduction potentials obtained from cyclic voltammograms however imply a mixture of α - and γ -MnO₂ in the pristine material. Upon cycling, the material shows evidence of features from both structural forms of the manganese oxides. Investigation of the electrochemical performance yields a specific discharge capacity of approximately 200 mAh/g. Although this value is significantly smaller than the theoretical 308 mAh/g, it clearly exceeds literature data. The main focus, however, was again put on the electrochemical doping of this material. By lithium intercalation Li _{x} α -MnO₂ with $x = 0.05, 0.1, 0.3$ and 0.8 was obtained. For $0 \leq x \leq 0.3$, the antiferromagnetic order which evolves in α -MnO₂ at $T^* \approx 18$ K was nearly unaffected. In addition, a Curie-Weiss analysis of the magnetization data revealed a doping independent frustration parameter $\Theta/T^* \approx 15$. For $x = 0.8$, the susceptibility could not be described in terms of a Curie-Weiss law. In contrast, the data imply an increased manganese magnetic moment up to high temperatures. The origin of this enhanced manganese magnetic moment, however, remains unclear. Possibly it is due to the interplay of mixed valent manganese in Li _{x} α -MnO₂ and the many possible magnetic exchange interactions between manganese magnetic moments which can lead to very complex

7 Conclusions

magnetic properties.

To all three compounds studied in this work, electrochemical doping was successfully applied to control and modify the oxidation state of the transition metal ion. In this way, new materials with complex electronic and magnetic properties unavailable through standard solid state chemistry were prepared.

Bibliography

- [1] K. Nakamura, H. Hirano, D. Nishioka, S. Endou, K. Itsuki, Y. Michihiro, T. Moriga, N. Kuwata, and J. Kawamura, *Solid State Ionics* **180**, 621-625 (2009).
- [2] J. Xie, N. Imanishi, T. Zhang, A. Hirano, Y. Takeda, and O. Yamamoto, *J. Power Sources* **189**, 365-370 (2009).
- [3] T. Okumura, T. Fukutsuka, Y. Uchimoto, N. Sakai, K. Yamaji, and H. Yakokawa, *J. Power Sources* **189**, 643-645 (2009).
- [4] J. Xie, T. Tanaka, N. Imanishi, T. Matsumura, A. Hirano, Y. Takeda, and O. Yamamoto, *J. Power Sources* **180**, 576-581 (2008).
- [5] G. Rouse, C. Wurm, M. Morcrette, J. Rodriguez-Carvajal, J. Gaubicher and C. Masquelier, *Int. J. Inorganic Materials* **3**, 881-887 (2001).
- [6] G. Ceder and A. Van der Ven, *Electrochem. Acta* **45**, 131-150 (1999).
- [7] C. Delmas, J.P. Péres, A. Rougier, A. Demourgues, F. Weill, A. Chadwick, M. Broussely, F. Perton, Ph. Biensan and P. Willmann, *J. Power Sources* **68**, 120-125 (1997).
- [8] J.R. Dahn and R.R. Haering, *Solid State Communications*, **40**, 245-248 (1981).
- [9] H. Abiko, M. Hibino, and T. Kudo, *Electrochem. Solid-State Lett.* **1(3)**, 114-116 (1998).
- [10] K. Takada, H. Sakurai, E. Takayama-Muromachi, F. Izumi, R.A. Dilanian and T. Sasaki, *Nature* **422**, 53-55 (2003).
- [11] A. Salvatore Arico, P. Bruce, B. Scrosati, J-M. Tarascon and W. Van Schalkwijk, *Nature Materials* **4**, 366-377 (2005).
- [12] P.G. Bruce, B. Scrosati and J-M. Tarascon, *Angew. Chem. Int. Ed.* **47**, 2930-2946 (2008).
- [13] P. Poizot, S. Laruelle, S. Grugeon, L. Dupont and J-M. Tarascon, *Nature* **407**, 496-499,(2000).

- [14] P. Gibot, M. Casas-Cabanas, L. Lafont, S. Levasseur, P. Carlach, St. Ephane Hamelet, J-M. Tarascon and C. Masquelier, *Nature Materials* **7**, 741-747 (2008).
- [15] C. Delmas, M. Maccario, L. Croguennec, F. Le Cras, and F. Weill, *Nature Materials* **7**, 665-671 (2008).
- [16] T. Drezen, N-H. Kwon, P. Bowen, I. Teerlinck, M. Isono, and I. Exnar, *J. Power Sources* **174**, 949-953 (2007).
- [17] J. Ma and Q-Z. Qin, *J. Power Sources* **148**, 66-71 (2005).
- [18] Z. Liu, W. Wang, X. Liu, M. Wu, D. Li, and Z. Zeng, *J. Solid State Chem.* **177**, 1585-1591 (2004).
- [19] L.I. Hill, A. Verbaere and D. Guyomard, *J. of Power Sources* **119-121**, 226-231 (2003).
- [20] C.S. Johnson, D.W. Dees, M.F. Mansuetto, M.M. Thackeray, D.R. Vissers, D. Argriou, C.-K. Loong, and L. Christensen, *J. Power Sources*, **68**, 570-577 (1997).
- [21] C. O'Dwyer, V. Lavayen, D.A. Tanner, S.B. Newcomb, E. Benavente, G. Gonzáles, and C.M. Sotomayor Torres, *Adv. Funct. Mat.* **19**, 1736-1745 (2009).
- [22] M.E. Spahr, P Stoschitzki-Bitterli, R. Nesper, O. Haas and P. Novák, *J. Electrochem. Soc.* **146(8)**, 2780-2783 (1999).
- [23] S. Nordlinder, L. Nyholm, T. Gustafsson and K. Edström, *Chem. Mater.* **18**, 495-503 (2006).
- [24] R.M. Dell and D.A.J. Rand, *Understanding Batteries*, RSC 2001, Chapter 1.
- [25] J-M. Tarascon and M. Armand, *Nature* **414**, 359-366 (2001).
- [26] Y. Wang and G. Cao, *Adv. Mater.* **20**, 2251-2269 (2008).
- [27] N. Pinna, U. Wild, J. Urban and R. Schlögl, *Adv. Mater.* **15**, 329 (2003).
- [28] X. Liu, C. Täschner, A. Leonhardt, M. H. Rümmeli, T. Pichler, T. Gemming, B. Büchner, and M. Knupfer, *Phys. Rev. B* **72**, 115407 (2005).
- [29] J.C. Hulteen and C.R. Martin, *J. Mater. Chem.* **7**, 1075 (1997).
- [30] Robert Scott Morris, US Patent, US 2007/0190422A1 (2007).

- [31] C.K. Chan, H. Peng, G. Liu, K. McIlwrath, X.F. Zhang, Robert A. Huggins and Y. Cui, *Nature Nanotechnology* **3**, 31-35 (2008).
- [32] V. Cimalla, C.-C. Röhlig, J. Pezoldt, M. Niebelschütz, O. Ambacher, K. Brückner, M. Hein, J. Weber, S. Milenkovic, A.J. Smith, and A.W. Hassel, *J. Nanomaterials* **2008**, 638947 (2008).
- [33] S. Brittman, A.J. Smith, S. Milenkovic, and A.W. Hassel, *Electrochim. Acta.* **53**, 324-329 (2007).
- [34] M. Zhang, Y. Bando and K. Wada, *J. Mater. Sci. Lett.* **20**, 167 (2001).
- [35] X. Shi, S.H. Raymond, J. Sanedrin, C. Galvez, D.G. Ho, B. Hernandez, F. Zhou and M. Selke, *Nano Lett.* **2**, 289 (2002).
- [36] S. Nordlinder, K. Edström and T. Gustafsson, *Electrochemical and Solid-State Letters* **4(8)**, A129-A131 (2001).
- [37] J. Curiale, R.D. Sanchez, H.E. Troiani, A.G. Leyva and P. Levy, *Appl. Phys. Lett.* **87**, 043113 (2005).
- [38] arXiv:0710.3767v1.
- [39] L. Krusin-Elbaum, D. M. Newns, H. Zeng, V. Derycke, J. Z. Sun and R. Sandstrom, *Nature* **431**, 672 (2004).
- [40] N. Imanishi, M. Fujiyoshi, Y. Takeda, O. Yamamoto and M. Tabuchi, *Solid State Ionics* **118**, 121-128 (1999).
- [41] D. Linden, *Handbook of batteries- second edition*, McGraw- Hill, Inc (1994), Chapter 35.
- [42] K. Mitzushima, P.C. Jones, P.J. Wiseman, J.B. Goodenough, *Mater. Res. Bull.* **15**, 783 (1980).
- [43] J.B. Goodenough, *J. Power Sources*, doi:10.1016/j.jpowsour.2007.06.217 (2007).
- [44] S. Levasseur, M. Ménétrier, E. Suard and C. Delmas, *Solid State Ionics* **128**, 11 (2000).
- [45] P.S. Herle, B. Eliis, N. Coombs and L.F. Nazar, *Nat. Mater.* **1**, 123 (2002).
- [46] J.B. Goodenough, K. Mitzushima, U.S. Patent 4, 302, 518 (1980).
- [47] M. Stanley Whittingham, *Chem. Rev.* **104**, 4271- 4301 (2004).

- [48] J. M. Tarascon, W. R. McKinnon, F. Coowar, T. N. Bowmer, G. Amatucci, and D. Guyomard, *J. Electrochem. Soc.* **141**, No. 6, 1421-1431 (1994).
- [49] D. Guyomard and J.M. Tarascon, *Solid State Ionics* **69**, 222-237 (1994).
- [50] J. Jamnik and J. Maier, *Phys. Chem. Chem. Phys.* **5**, 5215-5220 (2003).
- [51] Y. F. Zhukovskii, P. Balaya, E. A. Kotomin, and J. Maier, *Phys. Rev. Lett.* **96**, 058302 (2006).
- [52] C. Kim, M. Noh, M. Choi, J. Cho and B. Park, *Chem. Mater.* **17**, 3297-3301 (2005).
- [53] T. Ohzuku, Z. Takehara and S. Yoshizawa, *Electrochimica Acta* **24**, 219-222 (1979).
- [54] L. Kavan, D. Fattakhova and P. Krtil, *J. Electrochem. Soc.* **146** (4), 1375-1379 (1999).
- [55] Y.-S. Hu, L. Kienle, Y-G. Guo, and J. Maier, *Adv. Mater.* **18**, 1421-1426 (2006).
- [56] M. Anji Reddy, M. Satya Kishore, V. Pralong, V. Caignaert, U.V. Varadaraju and B. Raveau, *Electrochemistry Communications* **8**, 1299-1303 (2006).
- [57] H. Zhou, D. Li, M. Hibino, and I. Honma, *Angew. Chem. Int. Ed.* **44** 5, 797-802 (2004).
- [58] C. Jiang, E. Hosono and H. Zhou, *Nanotoday* **14**, 28-33 (2006).
- [59] T. Kudo, Y. Ikeda, T. Watanabe, M. Hibino, M. Miyayama, H. Abe and K. Kajita, *Solid State Ionics* **152-153**, 833-841(2002).
- [60] M.Hibino, K. Abeb, M. Mochizuki and M. Miyayamac, *Journal of Power Sources* **126**, 139-143 (2004).
- [61] H. Kawaoka, M. Hibino, H. Zhou and I. Honma, *Journal of Power Sources* **125**, 85-89 (2004).
- [62] C.J. Wen and R.A. Huggins, *J. Solid State Chem.* **37** 271-278 (1981).
- [63] A. Durif, *Crystal chemsitry of condensed phosphates*, New York, London: Plenum, 1995.
- [64] A.K. Padhi, K.S. Nanjundaswamy, C. MAsquelier and J.B. Goodenough, *J. Electrochem. Soc.* **144**, 2581-2586 (1997).

- [65] D. Riou, N. Nguyen, R. Benloucif and B. Raveau, *Mater. Res. Bull.* **25**, 1363-1369 (1990).
- [66] K.H. Lii, Y.P. Wang, Y.B. Chen and S.L. Wang, *J. Solid State Chem.* **86**, 143-148 (1990).
- [67] G. G. Amatucci, J. M. Tarascon, and C. Klein, *J. Electrochem. Soc.* **143**, 1114-1123 (1996).
- [68] M. Shibuya, T. Nishina, T. Matsue and I. Uchida, *J. Electrochem. Soc.* **143**, 3157-3160 (1996).
- [69] M. Nishizawa, S. Yamamura, T. Itoh and I. Uchida, *Chem. Commun.* 1631-1632 (1998).
- [70] J. Molenda, A. Stoklosa and T. Bak, *Solid State Ionics* **36**, 53-58 (1989).
- [71] M. Ménétrier, I. Saadoune, S. Levasseur, and C. Delmas, *J. Mater. Chem.* **9**, 1135-1140 (1999).
- [72] F.C. Chou, J.H. Cho, P.A. Lee, E.T. Abel, K. Matan and Y.S. Lee, *Phys. Rev. Lett.* **92**, 157004 (2004).
- [73] C. Delacourt, PhD Thesis, Université de Picardie Jules Verne, Amiens-France (2006).
- [74] C.H. Hamann, A. Hamnett and W. Vielstich, *Electrochemistry*, Wiley-VCH 2007, Chapter 5.
- [75] H. Girault, *Analytical and physical electrochemistry*, Chapter 7, EPFL Press (2004).
- [76] W. Weppner and R. Huggins, *J. Electrochem. Soc.* **124(10)**, 1569-1578 (1977).
- [77] Biologic Science Instruments, <http://www.bio-logic.info/>, Application note 1.
- [78] A. S. Prakash, D. Larcher, M. Morcrette, M. S. Hegde, J-B. Leriche and C. Masquelier, *Chem. Mater.* **17**, 4406-4415 (2005).
- [79] A.H. Thomson, *J. Electrochem. Soc.* **126(4)**, 608-616 (1979).
- [80] H. Maeter, Diploma thesis, Technische Universität Braunschweig-Germany, 2007.
- [81] M. D. Levi and D. Aurbach, *J. Phys. Chem. B* **101(23)**, 4641-4647 (1997).
- [82] J-S Bae and S. Pyun, *Solid State Ionics* **90**, 251-260 (1996).

- [83] H-C Shin and S. Pyun, *Electrochim. Acta* **44**, 2235-2244 (1999).
- [84] C. Delmas, H. Cognac-Auradou, J.M. Cocciantelli, M. Ménétrier, J.P. Doumerc, *Solid State Ionics* **69**, 257-264 (1994).
- [85] M. D. Levi, G. Salitra, B. Markovsky, H. Teller, D. Aurbach, U. Heider and L. Heider, *J. Electrochem. Soc.* **146(4)**, 1279-1289 (1999).
- [86] Z. Lu, M.D. Levi, G. Salitra, Y. Gofer, E. Levi and D. Aurbach, *J. Electroanalytical Chemistry* **491**, 211-221 (2000).
- [87] E. Markevich, M.D. Levi and D. Aurbach, *J. Electroanal. Chem.* **580(2)**, 231-237 (2005).
- [88] D.O. Raleigh and H.R. Crowe, *J. Electrochem. Soc* **116(1)**, 40-48 (1969).
- [89] J. Wang, *Analytical electrochemistry*, Wiley-VCH 2006, chapter 1.
- [90] J. Wang, *Analytical electrochemistry*, Wiley-VCH 2006, chapter 2.
- [91] R.S. Nicholson and I. Shain, *Anal. Chem.* **36**, 706-723 (1964).
- [92] F. J. Himpsel, J. E. Ortega, G. J. Mankey, R. F. Willis, *Adv. Phys.* **47(4)**, 511-597 (1998).
- [93] J. A. Brug, L. Tran, M. Bhattacharyya, J. H. Nickel, T. C. Anthony, and A. Jander, *J. Appl. Phys.* **79(8)**, 4491-4495 (1996).
- [94] D. N. Lambeth, E. M. T. Velu, G. H. Bellesis, L. L. Lee, and D. E. Laughlin, *J. Appl. Phys.* **79(8)**, 4496-4501 (1996).
- [95] S. Iijima, *Nature* **354**, 56-58 (1991).
- [96] W. Tremel, *Angew. Chem. Int. Ed.* **38(15)**, 2175-2179 (1999).
- [97] G. R. Patzke, F. Krumeich, and R. Nesper, *Angew. Chem. Int. Ed.* **41**, 2446-2461 (2002).
- [98] J.W. Mintmire, B.I. Dunlap, and C.T. White, *Physical Review Letters* **68(5)**, 631-634 (1992).
- [99] N. Hamada, S. Savada, and A. Oshiyama, *Physical Review Letters* **68(10)**, 1579-1581 (1992).
- [100] R. Saito, M. Fujita, G. Dresselhaus, and M. S. Dresselhaus, *Appl. Phys. Lett.* **60 (18)**, 2204-2206 (1992).
- [101] B. Cheng and E. T. Samulski, *J. Mater. Chem.* **11**, 2901-2902 (2001).

- [102] D. Vollath and D. V. Szabo, *Acta Mater.* **48**, 953-967 (2000).
- [103] H.-J. Muhr, F. Krumeich, U. P. Schönholzer, F. Bieri, M. Niederberger, L. J. Gauckler, and R. Nesper, *Adv. Mater.* **12 (3)**, 231-234 (2000).
- [104] P.M. Ajayan, O. Stephan, Ph. Redlich and C. Colliex, *Nature* **375**, 564-567 (1995).
- [105] R. Nesper, M. Spahr, M. Niederberger and P. Bitterli, US patent US6.605.266 B2 (2003).
- [106] G. Gao, *Nanostructures and Nanomaterials: Synthesis, Properties and Applications*, Imperial College Press 2004, Chapter 6.
- [107] F. Krumeich, H.-J. Muhr, M. Niederberger, F. Bieri, B. Schnyder and R. Nesper, *J. Am. Chem. Soc.* **121**, 8324-8331 (1999).
- [108] F. Bieri, F. Krumeich, H.-J. Muhr and R. Nesper, *Helv. Chim. Acta.* **84**, 3015-3022 (2001).
- [109] F. Krumeich, H.-J. Muhr, M. Niederberger, F. Bieri and R. Nesper, *Z. Anorg. Allg. Chem.* **626**, 2208-2216 (2000).
- [110] X. Wang, L. Liu, R. Bontchev and A. J. Jacobson, *Chem. Commun.*, 1009-1010 (1998).
- [111] J.M. Reinoso, H.-J. Muhr, F. Krumeich, F. Bieri and R. Nesper, *Helv. Chim. Acta.* **83**, 1724-1733 (2000).
- [112] A. Doble, K. Ngala, S. Yang, P. Y. Zavalij and M. S. Whittingham, *Chem. Mater.* **13(11)**, 4382-4386 (2001).
- [113] K. S. Pillai, F. Krumeich, H.-J. Muhr, M. Niederberger, and R. Nesper, *Solid State Ionics* **141-142**, 185-190 (2001).
- [114] S. Nordlinder, J. Lindgren, T. Gustafsson and K. Edström, *J. Electrochem. Soc.* **150(5)**, E280-E284 (2003).
- [115] D. Sun, C.W. Kwon, G. Baure, E. Richman, J. MacLean, B. Dunn and S.H. Tolbert, *Adv. Funct. Mater.* **14(12)**, 1197-1204 (2004).
- [116] W. Dong, D.R. Rolison and B. Dunn, *Electrochem. Solid-State Lett.* **3(10)**, 457-459 (2000).
- [117] A.F. Gross, V. H. Le, B.L. Kirsch, and S.H. Tolbert, *J. Am. Chem. Soc.* **124(14)**, 3713-3724 (2002).

- [118] S. Nordlinder, A. Augustsson, T. Schmitt, J. Guo, L.C. Duda, J. Nordgren, T. Gustafsson and K. Edström, *Chem. Mater.* **15**, 3227-3232 (2003).
- [119] L-Q. Mai, W. Chen, Q. Xu, J-F. Peng and Q-Y. Zhu, *Chem. Phys. Lett.* **382**, 307-312 (2003).
- [120] C. Leger, S. Bach, P. Soudan, and J.-P. Pereira-Ramos, *J. Electrochem. Soc.* **152(1)**, A236-A241 (2005).
- [121] J.M. Cocciantelli, M. Ménétrier, C. Delmas, J.P. Doumerc, M. Pouchard, and P. Hagemuller, *Solid State Ionics* **50**, 99-105 (1992).
- [122] S. Nordlinder, PhD Thesis, Uppsala University, Sweden 2005.
- [123] C.J. Patrissi and C.R. Martin, *J. Electrochem. Soc.* **146(9)**, 3176-3180 (1999).
- [124] B.Li, Y. Xu, G. Rong, M. Jing and Y. Xie, *Nanotechnology* **17**, 2560-2566 (2006).
- [125] S. Lu, L. Hou, and F. Gan, *Adv. Mater.* **9(3)**, 244-246 (1997).
- [126] A.C. Santulli, W. Xu, J.B. Parise, L. Wu, M.C. Aronson, F. Zhang, C-Y. Nam, C.T. Black, A.L. Tiano, and S.S. Wong, *Phys. Chem. Chem. Phys.* **11**, 3718-3726 (2009).
- [127] P.D. Dernier and M. Marezio, *Phys. Rev. B* **2(9)**, 3771-3776 (1970).
- [128] A. Zylbersztein and N.F. Mott, *Phys. Rev. B* **11**, 4383-4395 (1975).
- [129] J.P. Pouget, H. Launois, J.P.D'Haeneus, P. Merenda, and T.M. Rice, *Phys. Rev. Lett.* **35(13)**, 873-875 (1975).
- [130] T.M. Rice, H. Launois, and J.P. Pouget, *Phys. Rev. Lett.* **73(22)**, 3042 (1994).
- [131] J. Park, In Hwan Oh, E. Lee, K. Won Lee, C. Eui Lee, K. Song, and Y.-J. Kim, *Appl. Phys. Lett.* **91**, 153112 (2007).
- [132] M. Itoh, N. Akimoto, H. Yamada, M. Isobe, and Y. Ueda, *J. Phys. Chem. Solids*, **62**, 351-354 (2001).
- [133] S. Kondo, D.C. Johnston, C.A. Swenson, F. Borsa, A. V. Mahajan, L.L. Miller, T. Gu, A. I. Goldman, M.B. Maple, D.A. Gajewski, E.J. Freeman, N.R. Dilley, R.P. Dickey, J. Merin, K. Kojima, G.M. Luke, Y.J. Uemura, O. Chmaissem, And J.D. Jorgensen, *Phys. Rev. Lett.* **79(19)**, 3729-3732 (1997).
- [134] H-A. Krug von Nidda, R. Bulla, N. Büttgen, M. Heinrich, and A. Loidl, *Eur. Phys. J. B* **34**, 399-407 (2003).

- [135] M. Kanada, H. Harashina, S. Tanaka, T. Fukamachi, Y. Kobayashi, and M. Sato, *J. Phys. Soc. Jpn.* **67**(8), 2904-2909 (1998).
- [136] E. Vavilova, I. Hellmann, V. Kataev, C. Täschner, B. Büchner, and R. Klingeler, *Phys. Rev. B* **73**, 144417 (2006).
- [137] I. Hellmann, Phd Thesis, TU-Dresden, Germany 2009.
- [138] I. Hellmann, C. Täschner, R. Klingeler, A. Leonhardt, B. Büchner, and M. Knupfer, *J. Chem. Phys.* **128**, 224701 (2008).
- [139] J.H. Van Vleck, *Physica* **69**, 177-192 (1973).
- [140] S.J. Blundell, *Contemp. Phys.* **40**, 175 (1999).
- [141] H. Kweon, K.W. Lee, E.M. Lee, J. Park, I-M. Kim, C.E. Lee, G. Jung, A. Gedanken, and Y. Kolytyn, *Phys. Rev. B* **76**, 045434 (2007).
- [142] J. B. Goodenough, *Annu. Rev. Mater. Sci.* **1**, 101-138 (1971).
- [143] T. Kiyama, T. Shiraoka, M. Toh, L. Kano, H. Ichikawa, and J. Akimitsu, *Phys. Rev. B* **73**, 184422 (2006).
- [144] J.M.D. Coey and D. Khalafalla, *Phys. Stat. Sol.(a)* **11**, 229-241 (1972).
- [145] R. Berger, J-C. Bissey, J. Kliava, H. Daubric, and C. Estournès, *J. Magn. Magn. Mat.* **234**, 535-544 (2001).
- [146] F. Gazeau, V. Shilov, J.C. Bacri, E. Dubois, F. Gendron, R. Perzynski, Yu.L. Raikher, and V.I. Stepanov, *J. Magn. Magn. Mat.* **202**, 535-546 (1999).
- [147] P.V. Radovanovic and D. R. Gamelin, *Phys. Rev. Lett.* **91**(15), 157202 (2003).
- [148] G.Z. Xing, J.B. Yi, J.G. Tao, T. Liu, L.M. Wong, Z. Zhang, G.P. Li, S.J. Wang, J. Ding, T. C. Sum, C.H.A. Huan, and T. Wu, *Adv. Mater.* **20**, 3521-3527 (2008).
- [149] A. Kaminski and S. Das Sarma, *Phys. Rev. Lett.* **88**(24), 247202 (2002).
- [150] A.C. Durst, R.N. Bhatt, and P.A. Wolff, *Phys. Rev. B* **65**, 235205 (2002).
- [151] A. Popa, E. Vavilova, Y. Arango, I. Hellmann, V. Kataev, C. Täschner, H.-H. Klauss, H. Maeter, H. Luetkens, B. Büchner, and R. Klingeler, *Eur. Phys. Lett.* **88**, 57002 (2009).
- [152] J.G. Bednorz and K.A. Müller, *Z. Phys. B - Condensed Matter* **64**, 189-193 (1986).

- [153] O. Fischer, M. Kugler, I. Maggio-Aprile, C. Berthod, and C. Renner, *Rev. Mod. Phys.* **79(1)**, 353-419 (2007).
- [154] P.A. Lee, N. Nagaosa, and X.-G. Weng, *Rev. Mod. Phys.* **78(1)**, 17-85 (2006).
- [155] D.N. Basov and T. Timusk, *Rev. Mod. Phys.* **77(2)**, 721-779 (2005).
- [156] M.A. Kastner, R. Birgeneau, G. Shirane, Y. Endoh, *Rev. Mod. Phys.* **70(3)**, 897-927 (1998).
- [157] G.S. Boebinger, Y. Ando, A. Passner, T. Kimura, M. Okuya, J. Shimoyama, K. Kishio, K. Tamasaku, N. Ichikawa, and S. Uchida, *Phys. Rev. Lett.* **77(27)**, 5417-5420 (1996).
- [158] A. Damascelli, Z. Hussain, and Z.-X. Shen, *Rev. Mod. Phys.* **75(2)**, 473-541 (2003).
- [159] B. Yamanaka, H. Kawaji, K. Hotehama, and M. Oshashi, *Adv. Mater.* **8(9)**, 771-774 (1996).
- [160] Y. Taguchi, A. Kitora, and Y. Iwasa, *Phys. Rev. Lett.* **97**, 107001 (2006).
- [161] B. Yamanaka, K. Hotehama, and H. Kawaji, *Nature* **392**, 580-582 (1998).
- [162] M. Kato, A. Inoue, I. Nagai, M. Kakihana, A.W. Sleight, and Y. Koike, *Physica C* **388-389**, 445-446 (2003).
- [163] M. Kato, T. Kajita, R. Hanakago, and Y. Koike, *Physica C* **445-448**, 26-30 (2006).
- [164] Y. Takano, S. Takayanagi, S. Ogawa, T. Yamadaya, and N. Môri, *Sol. Stat. Comm.* **104(3)**, 215-217 (1997).
- [165] J. Orenstein and A.J. Millis, *Science* **288**, 468-474 (2000).
- [166] R.J. Cava, R.B. van Dover, B. Batlogg, and E.A. Rietman, *Phys. Rev. Lett.* **58(4)**, 408-410 (1987).
- [167] H. Takagi, S. Uchida, H. Obara, K. Kishio, K. Kitazawa, K. Fueki, and S. Tanaka, *Jpn. J. Appl. Phys. Lett.* **26(4)**, L434-L436 (1987).
- [168] M. Al-Mamouri, P.P. Edwards, C. Greaves, and M. Slaski, *Nature* **369**, 382-384 (1994).
- [169] Z. Hiroi, N. Kobayashi, and M. Takano, *Nature* **371**, 139-141 (1994).
- [170] Y. Tokura, *Physica C* **185-189**, 174-179 (1991).

- [171] T. Kajita, M. Kato, T. Suzuki, T. Itoh, T. Noji, and Y. Koike, *Jpn. J. Appl. Phys. Lett.* **43(11B)**, L1480-L1481 (2004).
- [172] T. Kajita, M. Kato, T. Noji, and Y. Koike, *AIP Conf. Proc.* **850(1)**, 535-536 (2006).
- [173] L.L. Miller, X.L. Wang, C. Stassis, and D.C. Johnston, *Phys. Rev. B* **41(4)**, 1921-1925 (1990).
- [174] C.P. Poole Jr., *Handbook of Superconductivity*, Academic Press, Chapter 1 and 3 (2000).
- [175] D.S. Middlemiss and W.C. Mackrodt, *J. Phys. Condens. Matter* **20**, 015207, 1-8 (2008).
- [176] D. Vaknin, S.K. Sinha, C. Stassis, L.L. Miller, and D.C. Johnston, *Phys. Rev. B* **41(4)**, 1926-1933 (1990).
- [177] L.P. Le, G.M. Luke, B.J. Sternlieb, Y.J. Uemura, J.H. Brewer, T.M. Riseman, D.C. Johnston, and L.L. Miller, *Phys. Rev. B* **42(4)**, 2182-2187 (1990).
- [178] H. Müller- Buchbaum, *Angew. Chem. Int. Ed. Engl.* **16**, 674-687 (1977).
- [179] D.C. Johnston, *PRB* **62(8)**, 957-960 (1989).
- [180] J.M. Tranquada, A.H. Moudden, A.I. Goldman, P. Zolliker, D.E. Cox, G. Shirane, S.K. Sinha, D. Vaknin, D.C. Johnston, M.S. Alvarez, A.J. Jacobson, *Phys. Rev. B* **38(4)**, 2477- 2485 (1988).
- [181] D. Vaknin, E. Caignol, P.K. Davies, J.E. Fischer, D.C. Johnston, D.P. Goshorn, *Phys. Rev. B* **39(13)**, 9122-9125 (1989).
- [182] H. Luetkens, H. Maeter, H-H. Klauss, unpublished.
- [183] L.P. Le, G.M. Luke, B.J. Sternlieb, Y.J. Uemura, J.H. Brewer, T.M. Riseman, D.C. Johnston, L.L. Miller, Y. Hidaka, and H. Murakami, *Hyp. Int.* **63**, 279-286 (1990).
- [184] T. Kajita, M. Kato, T. Suzuki, T. Itoh, T. Noji, and Y. Koike, *Physica C* **426-431**, 500-504 (2005).
- [185] M. Kato, Y. Imai, T. Kajita, Y. Takarabe, T. Minakawa, K. Nemoto, H. Tezuka, T. Noji and Y. Koike, *Materials Science and Engineering B* **148**, 53-57 (2008).
- [186] C.P. Poole Jr, T. Data, and H.A. Farach, *Copper Oxide Superconductors*, John Wiley Sons, Inc., Chapter 8 (1988).

- [187] B. Renker, I. Apfelstedt, H. K pfer, C. Politis, H. Rietschel, W. Schauer, H. W hl, U. Gottwick, H. Kneissel, U. Rauchschalbe, H. Spille, and F. Teglich, *Z. Phys. B- Condensed Matter* **67**, 1-7 (1987).
- [188] S. Hikami, S. Kagoshuma, S. Komiyama, T. Hirai, H. Minami, and T. Masumi, *Jpn. J. Appl. Phys.* **26(4)**, L347-L348 (1987).
- [189] S. Senoussi, M. Oussena, and S. Hadjoudj, *J. Appl. Phys.* **63(8)**, 4176-4178 (1988).
- [190] J.Z. Sun, D.J. Webb, M. Maito, K. Char, M.R. Hahn, J.W.P. Hsu, A.D. Kent, D.B. Mitzi, B. Oh, R. Beasley, T.H. Geballe, R.H. Hammond, and A. Kapitulnik, *Phys. Rev. Lett.* **58(15)**, 1574-1576 (1987).
- [191] R. von Helmolt, J. Wecker, B. Holzapfel, L. Schultz and K. Samwer, *Phys. Rev. Lett.* **71(14)**, 2331-2333 (1993).
- [192] A.R. Armstrong and P.G. Bruce, *Nature* **381**, 499-500 (1996).
- [193] B. Ammundsen and J. Paulsen, *Adv. Mater.* **13(12-13)**, 943-956 (2001).
- [194] N. Kijima, H. Yasuda, T. Sato and Yosimura, *J. Solid State Chem.* **159**, 94-102 (2001).
- [195] F.Y. Cheng, J. Chen, X.L. Gou and P.W. Shen, *Adv. Mater.* **17**, 2753-2756 (2005).
- [196] M. Toupin, T. Brousse and D. Belanger, *Chem. Mater.* **16(16)**, 3184-3190 (2004).
- [197] C.S. Johnson, *J. Power Sources* **165**, 559-565 (2007).
- [198] D.D. MacNeil, Z. Lu, Z. Chen, J.R. Dahn, *J. Power Sources* **108**, 8-14 (2002).
- [199] Y. Chabre, and J. Pannetier, *Prog. Solid. St. Chem.* **23**, 1-130 (1995).
- [200] M.M. Thackeray, *Prog. Solid St. Chem* **25**, 1-71 (1997).
- [201] U. Delicat, S.F. Radaev, M. Tr mel, P. Behrens, Y.F. Kargin, and A.A. Mar'in, *J. Solid State Chem.* **110**, 66-69 (1994).
- [202] T. Ohzuku, M. Kitagawa, K. Sawai, and T. Hirai, *J. Electrochem. Soc.* **138**, 360-365 (1991).
- [203] P.M. DeWolff, *Acta Cryst.* **12**, 341-345 (1959).
- [204] S. Turner and P.R. Buseck, *Nature* **304**, 143-146 (1983).

- [205] T. Ohzuku, M. Kitagawa, K. Sawai, and T. Hirai, *J. Electrochem. Soc.* **136**, 3169-3174 (1989).
- [206] M. Winter, J.O. Besenhard, M.E. Spahr, and P. Novák, *Adv. Mater.* **10(10)**, 725-763 (1998).
- [207] W.I.F. David, M.M. Thackery, L.A. De Picciotto, and J.B. Goodenough, *J. Solid State Chem.* **67(2)**, 316-323 (1987).
- [208] Y. Muraoka, H. Chiba, T. Atou, M. Kikuchi, K. Hiraga, Y. Syono, S. Sugiyama, S. Yamamoto, J-C. Grenier, *J. Solid State Chem.* **144**, 136-142 (1999).
- [209] R.N. DeGuzman, Y.F. Shen, E.J. Neth, S.L. Suib, C-L. O'Young, S. Levine, and J.M. Newsam, *Chem. Mater.* **6**, 815-821 (1994).
- [210] T.D. Xiao, P.R. Strutt, M. Benaissa, H. Chen, and B.H. Kear, *Nanostruct. Mater.* **10(6)**, 1051-1061 (1998).
- [211] Y.F. Shen, R.P. Zerger, and S.L. Suib, *Science* **260**, 511-515 (1993).
- [212] S. Ching, J.L. Roark, N. Duan, and S.L. Suib, *Chem. Mater.* **9(3)**, 750-754 (1997).
- [213] S. Ching, D.J. Petrovay, M.L. Jorgense, and S.L. Suib, *Inorg. Chem.* **36**, 883-890 (1997).
- [214] Q. Lia, G. Luoa, J. Lib, and X. Xia, *J. Mater, Process. Technol.* **137**, 25-29 (2003).
- [215] X. Wang and Y. Li, *Chem. Commun.*, 764-765 (2002).
- [216] X. Wang and Y. Li, *J. Am. Chem. Soc.* **124(12)**, 2880-2881 (2002).
- [217] Y. Xiong, Y. Xie, Z. Li, and C. Wu, *Chem. Eur. J.* **9**, 1645-1651 (2002).
- [218] Z.-Y. Yuan, Z. Zhang, G. Du, T.-Z. Ren, B.-L. Su, *Chem. Phys. Lett.* **378**, 349-353 (2003).
- [219] F.A. Al-Sagheer, and M.I. Zaki, *Colloids Surf. A. Physicochem. Eng. Asp.* **173**, 193-204 (2000).
- [220] S.A. Chambers, and Y. Liang, *Surf. Sci.* **420**, 123-133 (1999).
- [221] G. Xi, Y. Peng, Y. Zhu, L. Xu, W. Zhang, W. Yu, and Y. Qian, *Mater. Res. Bull.* **39**, 1641-1648 (2004).
- [222] X.-M. Liu, S.-Y. Fu, C.-J. Huang, *Powder Technol.* **154**, 120-124 (2005).

- [223] E. Macheaux, A. Verbaere, and D. Guyomard, *J. Power Sources* **157**, 443-447 (2006).
- [224] H.-E. Wang and D. Qian, *Mat. Chem. Phys.* **109**, 399-403 (2008).
- [225] X. Li, W. Li, X. Chen, and C. Shi, *J. Crys. Growth* **297**, 387-389 (2006).
- [226] C.S. Johnson, M.F. Mansuetto, M.M. Thackeray, Y. Shao-Horn, and S.A. Hackney, *J. Electrochem. Soc.* **144(7)**, 2279-2283 (1997).
- [227] C.S. Johnson, and M.M. Thackeray, *J. Power Sources* **97-98**, 437-442 (2001).
- [228] A. Masquelier, M. Tabuchi, K. Ado, R. Kanno, Y. Kobayashi, Y. MAki, O. Nakamura, and J.B. Goodenough, *J. Solid State Chem.* **123**, 255-266 (1996).
- [229] A.S. Wills, N.P. Raju, C. Morin, and J.E. Greedan, *Chem. Mater.* **11**, 1936-1941 (1999).
- [230] C.M. Julien, A. Ait-SAlah, A. Mauger, F. Gendron, *Ionics* **12**, 21-32 (2006).
- [231] Y-II Jang, B. Huang, F.C. Chou, D. R. Sadoway, and Y-M. Chiang, *J. Appl. Phys.* **87(10)**, 7382-7388 (2000).
- [232] J.E. Greedan, N.P. Raju, and I.J. Davidson, *J. Solid State Chem.* **128**, 209-214 (1997).
- [233] J.E. Greedan, N.P. Raju, A.S. Wills, C. Morin, and S.M. Shaw, *Chem. Mater.* **10**, 3058-3067 (1998).
- [234] K. Binder and A.P. Young, *Rev. Mod. Phys.* **58**, 801-976 (1986).
- [235] H. J. Kim, J.B. Lee, Y-M. Kim, M-H. Jung, Z. Jaglicic, P. Umek, J. Dolinsek, *Nanoscale Res. Lett.* **2**, 81-86 (2007).
- [236] S. Jana, S. Basu, S. Pande, S. Kumar Ghosh, and T. Pal, *J. Phys. Chem.* **111**, 16272-16277 (2007).
- [237] S. Jana, S. Pande, A. Kumar Sinha, and T. Pal, *Inorg. Chem.* **47**, 5558-5560 (2008).
- [238] H. Sato, T. Enoki, M. Isobe, and Y. Ueda, *Phys. Rev. B* **61(5)**, 3563-3569 (2000).
- [239] B. Tang, G. Wang, L. Zhuo, and J. Ge, *Nanotechnology* **17**, 947-951 (2006).
- [240] N. Yamamoto, T. Endo, M. Shimada, and T. Takada, *Japan. J. Appl. Phys.* **13(4)**, 723-724 (1974).

- [241] J. Luo, H.T. Zhu, F. Zhang, J.K. Liang, G.H. Rao, J.B. Li, and Z.M. Du, *J. Appl. Phys.* **105**, 093925 (2009).
- [242] J.B. Luo, Y.G. Zhao, G.M. Zhang, S.M. Guo, Z. Li, and J.L. Luo, *Phys. Rev. B* **75**, 125115 (2007).
- [243] S. Ishiwata, J.W.G. Bos, Q. Huang, and R.J. Cava, *J. Phys: Condes. Mater.* **18**, 3745-3752 (2006).
- [244] A.P. Ramirez, *Annu. Rev. Mater. Sci.* **24**, 453-481 (1994).
- [245] L. Li, Y. Pan, L. Chen, G. Li, *J. Solid State Chem.* **180**, 2896-2904 (2007).
- [246] J.B. Goodenough, A.L. Loeb, *Phys. Rev.* **98(2)**, 391-408 (1955).
- [247] C. Zener, *Phys. Rev.* **82**, 403-405 (1951).
- [248] Y. Tokura and Y. Tomioka, *J. Magn. Magn. Mater.* **200**, 1-23 (1999).

This page intentionally contains only this sentence.

List of Figures

| | | |
|------|--|----|
| 2.1 | Different shapes and design of lithium batteries | 6 |
| 2.2 | Classical electrochemical cell | 7 |
| 2.3 | Current and possible materials in lithium batteries | 8 |
| 2.4 | Operation of a electrochemical cell- discharge mode | 9 |
| 2.5 | Operation of a electrochemical cell- charge mode | 10 |
| 2.6 | Volumetric and gravimetric energy density for main types of batteries | 12 |
| 2.7 | LiMO ₂ structure with M=Co or Ni | 13 |
| 2.8 | TEM of Vanadium Oxide Nanotubes | 14 |
| 2.9 | LiVP ₂ O ₇ structure | 20 |
| 2.10 | Tunnels in LiVP ₂ O ₇ and VP ₂ O ₇ | 21 |
| 2.11 | Electrical conductivity for Li _x CoO ₂ | 23 |
| | | |
| 3.1 | Swagelok cell | 26 |
| 3.2 | Setup of the electrochemical experiment | 27 |
| 3.3 | Monophasic and biphasic domains | 29 |
| 3.4 | GITT experiment | 30 |
| 3.5 | PITT experiment | 31 |
| 3.6 | The incremental capacity from a potentiostatic experiment | 32 |
| 3.7 | Sketch of a Cyclic Voltammogram experiment | 33 |
| 3.8 | I-V curve obtained from a CV experiment | 34 |
| 3.9 | Quartz tube for magnetic measurements | 37 |
| | | |
| 4.1 | TEM image of one VO _x -NT | 41 |
| 4.2 | Morphology of VO _x -NT | 42 |
| 4.3 | BaV ₇ O ₁₆ structure | 44 |
| 4.4 | BaV ₇ O ₁₆ structure, side and plan view | 45 |
| 4.5 | Electronic diffraction pattern of VO _x -NT upon doping with lithium | 47 |
| 4.6 | Nanotube morphology of Vanadium Oxide Nanotubes | 49 |
| 4.7 | CV for VO _x -NT#5 | 50 |
| 4.8 | CV for VO _x -NT#12- first cycle, no carbon | 51 |
| 4.9 | CV for VO _x -NT#12, first cycle, with carbon | 51 |

| | |
|---|----|
| 4.10 CV for VO _x -NT#12 with 0.05 mV/s | 52 |
| 4.11 CV for VO _x -NT#12 with 0.02 mV/s | 53 |
| 4.12 CV for VO _x -NT#13, first cycle | 54 |
| 4.13 CV for VO _x -NT#13 with 0.05 mV/s | 55 |
| 4.14 CV for VO _x -NT#13 with 0.05 mV/s | 55 |
| 4.15 Discharge capacities (CV) for VO _x -NT#13 | 57 |
| 4.16 CV for VO _x -NT#14 with 0.02 mV/s | 58 |
| 4.17 CV for VO _x -NT#18 | 58 |
| 4.18 CV for VO _x -NT#18 with 0.02 mV/s | 59 |
| 4.19 CV for VO _x -NT#18 with 0.05 mV/s | 59 |
| 4.20 Discharge capacities (CV) for VO _x -NT#18 | 60 |
| 4.21 CV with 0.05 mV/s for different kinds of VO _x -NTs | 61 |
| 4.22 CV for all VO _x -NTs with 0.05 mV/s | 62 |
| 4.23 CV for Na ⁺ -exchanged VO _x -nanorolls | 63 |
| 4.24 Specific discharge capacities for VO _x -NTs (this work) and VO _x nanorolls | 65 |
| 4.25 Potentiostatic experiment for VO _x -NT#13 | 67 |
| 4.26 Incremental capacity for VO _x -NT#13 (potentiostatic experiment) . | 67 |
| 4.27 discharge/charge curves for VO _x -NT#13 | 68 |
| 4.28 discharge/charge curves for Ca-exchanged VO _x -NT | 68 |
| 4.29 Discharge capacities for VO _x -NT#13 and template free VO _x -NT . . | 69 |
| 4.30 Discharge capacities for the ion-exchanged VO _x -NT | 70 |
| 4.31 Potentiostatic experiment for VO _x -NT#12 | 71 |
| 4.32 Temperature dependence of the magnetic susceptibility for Li _{<i>x</i>} VO _x -NT | 76 |
| 4.33 Field dependence of the magnetization in Li _{<i>x</i>} VO _x -NT at 4.2 K . . . | 77 |
| 4.34 Li _{<i>x</i>} VO _x -NT, Brillouin fit results | 78 |
| 4.35 Field dependence of the magnetization of Li _{<i>x</i>} VO _x -NT at 300 K . . . | 79 |
| 4.36 Field dependence of the magnetization of Li _{0.1} VO _x -NT at different temperatures | 80 |
| 4.37 ZF- μ SR spectra for Li _{<i>x</i>} VO _x -NT | 81 |
| 4.38 ⁵¹ V NMR spectra for Li _{<i>x</i>} VO _x -NT | 82 |
| 4.39 ESR spectra for Li _{<i>x</i>} VO _x -NT | 83 |
| 4.40 Li _{<i>x</i>} VO _x -NT(batch#13), temperature dependence of the magnetic susceptibility | 86 |
| 4.41 Li _{<i>x</i>} VO _x -NT(batch#13), field dependence of the magnetic suscepti- bility at 300 K, 0 T-5 T | 87 |
| 4.42 Li _{<i>x</i>} VO _x -NT(batch#13), field dependence of the magnetic suscepti- bility at 300 K, 0 T-1 T | 88 |

| | | |
|------|---|-----|
| 5.1 | Phase diagram high- T_c | 91 |
| 5.2 | Li_xZrNCl crystal structure | 94 |
| 5.3 | $\text{Sr}_2\text{CuO}_2\text{X}_2$ and $(\text{La},\text{Sr})\text{CuO}_4$ crystal structures | 95 |
| 5.4 | CV on $\text{Sr}_2\text{CuO}_2\text{Br}_2$ | 96 |
| 5.5 | Galvanostatic synthesis of $\text{Li}_x\text{Sr}_2\text{CuO}_2\text{Br}_2$ | 98 |
| 5.6 | $\text{Sr}_2\text{CuO}_2\text{Cl}_2$ magnetic unit cell | 99 |
| 5.7 | $\text{Sr}_2\text{CuO}_2\text{Br}_2$, μ^+ SR study | 100 |
| 5.8 | $\text{Li}_{0.15}\text{Sr}_2\text{CuO}_2\text{Br}_2$, temperature dependence of the magnetic susceptibility, $H=2$ Oe | 103 |
| 5.9 | $\text{Li}_{0.15}\text{Sr}_2\text{CuO}_2\text{Br}_2$ in $H=3$ Oe | 104 |
| 5.10 | $\text{Li}_{0.15}\text{Sr}_2\text{CuO}_2\text{Br}_2$, field dependence of the magnetization at $T=2$ K (low fields) | 104 |
| 5.11 | $\text{Li}_{0.15}\text{Sr}_2\text{CuO}_2\text{Br}_2$, field dependence of the magnetization at $T=2$ K (high fields) | 106 |
| 5.12 | $\text{Li}_{0.15}\text{Sr}_2\text{CuO}_2\text{Br}_2$, field dependence of the magnetization at $T=2$ K-10 K (low fields) | 107 |
| 5.13 | $\text{Li}_x\text{Sr}_2\text{CuO}_2\text{Br}_2$, temperature dependence of the magnetic susceptibility | 108 |
| 6.1 | Crystal structure of $\alpha\text{-MnO}_2$ [19]. | 111 |
| 6.2 | Crystal structure of $\gamma\text{-MnO}_2$ | 113 |
| 6.3 | αMnO_2 morphology | 115 |
| 6.4 | CV of αMnO_2 , with and without Carbon | 116 |
| 6.5 | CV of αMnO_2 , different scan rates | 117 |
| 6.6 | CV of αMnO_2 with 0.02 mV/s | 118 |
| 6.7 | CV on $\alpha\text{-MnO}_2$ and $\gamma\text{-MnO}_2$ | 119 |
| 6.8 | Discharge capacity for $\alpha\text{-MnO}_2$ | 120 |
| 6.9 | Electrochemical synthesis of Li_xMnO_2 | 122 |
| 6.10 | magnetic susceptibility of $\text{Li}_2\text{Mn}_2\text{O}_4$ | 124 |
| 6.11 | Temperature dependence of the FC and ZFC magnetic susceptibility of the undoped $\alpha\text{-MnO}_2$ | 126 |
| 6.12 | Field dependence of the magnetic susceptibility measured at different temperatures. Adapted from Ref. [137]. | 127 |
| 6.13 | Temperature dependence of the magnetic susceptibility for $\text{Li}_x\alpha\text{-MnO}_2$ nanostructures | 129 |
| 6.14 | Transition temperature for Li_xMnO_2 | 130 |
| 6.15 | Field dependence of the magnetization for Li_xMnO_2 | 132 |
| 6.16 | Temperature dependence of the magnetic susceptibility for MnO_2 and $\text{Li}_{0.8}\text{MnO}_2$ | 133 |

| | | |
|------|--|-----|
| 6.17 | Temperature dependence of the magnetic susceptibility for MnO_2 and $\text{Li}_{0.8}\text{MnO}_2$ | 134 |
| 6.18 | Field dependence of the magnetization for $\text{Li}_{0.8}\text{MnO}_2$ measured at 2 K, 25 K and 300 K. | 135 |
| 6.19 | The magnetic and electronic phase diagram of different manganese oxides | 136 |

Some of the results from this work were reported in published papers or during scientific meetings:

Publications

A. Popa, E. Vavilova, Y. Arango, I. Hellmann, V. Kataev, C. Täschner, H.-H. Klauss, H. Maeter, H. Luetkens, B. Büchner, and R. Klingeler, *Eur. Phys. Lett* **88**, 57002 (2009)

R. Klingeler, N. Leps, I. Hellmann, A. Popa, C. Hess, A. Kondrat, J. Hamann-Borrero, G. Behr, V. Kataev, B. Büchner, arXiv:0808.0708

B. Antonioli, B. Büchner, J. K. Clegg, K. Gloe, K. Gloe, L. Götzke, A. Heine, A. Jäger, K. A. Jolliffe, O. Kataeva, V. Kataev, Rüdiger Klingeler, T. Krause, L. F. Lindoy, A. Popa, W. Seichter and M. Wenzel, *Dalton Transaction* **24**, 4795-4805 (2009)

Abstract

The physics of transition metal oxides is controlled by the combination and competition of several degrees of freedom, in particular the charge, the spin and the orbital state of the electrons. One important parameter responsible for the physical properties is the density of charge carriers which determines the oxidization state of the transition metal ions. The central objective in this work is the study of transition metal oxides in which the charge carrier density is adjusted and controlled via lithium intercalation/deintercalation using electrochemical methods. Lithium exchange can be achieved with a high degree of accuracy by electrochemical methods. The magnetic properties of various intermediate compounds are studied.

Among the materials under study the mixed valent vanadium-oxide multiwall nanotubes represent a potentially technologically relevant material for lithium-ion batteries. Upon electron doping of VOx-NTs, the data confirm a higher number of magnetic V⁴⁺ sites. Interestingly, room temperature ferromagnetism evolves after electrochemical intercalation of Li, making VOx-NTs a novel type of self-assembled nanoscaled ferromagnets. The high temperature ferromagnetism was attributed to formation of nanosize interacting ferromagnetic spin clusters around the intercalated Li ions. This behavior was established by a complex experimental study with three different local spin probe techniques, namely, electron spin resonance (ESR), nuclear magnetic resonance (NMR) and muon spin relaxation (μ SR) spectroscopies.

Sr₂CuO₂Br₂ was another compound studied in this work. The material exhibits CuO₄ layers isostructural to the hole-doped high-T_c superconductor La_{2-x}Sr₂CuO₄. Electron doping is realized by Li-intercalation and superconductivity was found below 9 K. Electrochemical treatment hence allows the possibility of studying the electronic phase diagram of Li_xSr₂CuO₂Br₂, a new electron doped superconductor. The effect of electrochemical lithium doping on the magnetic properties was also studied in tunnel-like α -MnO₂ nanostructures. Upon lithium intercalation, Mn⁴⁺ present in α -MnO₂ will be reduced to Mn³⁺, resulting in a Mn mixed valency in this compound. The mixed valency and different possible interactions arising between magnetic spins give a complexity to the magnetic properties of doped α -MnO₂.

Acknowledgments

Herewith I would like to thank those many people who have helped so this work will be accomplished. Firstly, I would like to thank Prof. Bernd Büchner who gave me the possibility of starting my PhD in his group in IFW Dresden. His door was always open for whatever problems there were, and I always left from him having the feeling that it might be a light at the end of the tunnel.

I am much indebted to my supervisor, Dr. Rüdiger Klingeler, for trusting me whenever I did not. Without his careful supervision I could not be in the point of finishing my thesis. I thank him for giving me the freedom of making the electrochemistry story work, and therefore gaining a lot of experience in solving a lot of problems. I am sure it was not always easy to keep reading my thesis, and I appreciate his patience and way of taking the best out of the story.

I appreciate the effort of Prof. Alexander Revcolevschi from Université Paris Sud-France, for reading this manuscript as a Referee of my thesis. I am grateful to Prof. Hans-Henning Klauss from TU-Dresden for supervising the μ SR measurements and interpretation of the results.

For the first three years of my PhD the financial support came from the International Max Planck Research School for “Dynamical Processes in Atoms, Molecules and Solids” coordinated by Ulf Saalman. This gave me the opportunity to meet nice people and have a lot of fun during the annual retreats.

I am grateful to Dr. Christine Täschner for synthesizing the Vanadium oxide nanotubes and manganese oxides nanostructures. I appreciate her support in solving issues related to these compounds. I thank Nadja Winzent for preparing the $\text{Sr}_2\text{CuO}_2\text{Br}_2$, and for the fact that she was always friendly whenever I had of course, a lot of questions. I thank Margitta Deutschmann, Falk Herold, and Andrea Voß for technical support.

Special thanks to Dr. Vladik Kataev, for his clear answers and help throughout my PhD work. I thank Yullieth Arango and Jenia Vavilova for measuring ESR and NMR, respectively. I thank to all three for so many discussions about vanadium oxides.

I appreciate the opportunity that Prof. Christian Masquelier gave me by initiating me in the battery business. Although it was not easy, the time I spent in his group

at the Laboratoire de Réactivité Chimie des Solides in Amiens- France was very helpful for my future work. I thank Mathieu Morcrette, Gérard Quoirin, Charles Delacourt, Frederic Sauvage and Pierre Gibot for the great help.

My life in Dresden would have never been easy without the help of so many people. Firstly, I will never thank enough to Ingo Hellmann. He spent a lot of time helping me with all the things I had to solve right after I came to Dresden. He was always there for any question, complain or said mood I had, and he always knew how to bring a smile on my face. I thank him for trying to teach me German, and for all the help he gave me with the measurements and the results during our very long and fruitful discussions.

I had the luck to share the office for the first year of my PhD with Anja Waske, Olga Shuleshova, and Christian Kramberger. Thank you for the nice atmosphere you all created. A really large help I got from Dr. Natalia Tristan, Norman Leps, Florian Kretzschmar, Dr. Ulrike Köhler and Sebastian Gaß for all the problems I had during measurements. Special thanks to Norman Leps for his patience of answering all kind of crazy questions. Sharing the office with Liran Wang, Anupama Parameswaran, Carsten Jähne and Wolfram Lorenz is a great pleasure. Special thanks to Liran and Anupama for all the nice discussions we always have.

I received a lot of support from the group of Dr. Helmut Ehrenberg, and especially from Dr. Kristian Nikolowski when I start building the electrochemistry equipment. Thank you!

I am thankful to Kerstin Höllerer and Manja Maluck for their effort and patience whenever I needed help for solving administrative issues.

I am very lucky having Andrew Smith as my friend in the last years. Thank you for everything you said and done. I appreciate your help and guidance for teaching me \LaTeX , and I know it was not always easy. Thank you for all the critics and over reading this manuscript.

My Romanian group helped me having a small home in Dresden. A big THANKS to all of them. Firstly, I am very lucky for meeting Tania Mirela Pletea. She has always only special words and attitude towards me. I thank her for trusting me to be a part of Sebastian's life. I appreciate her friendship and unlimited help whenever it was the case. I appreciate the wonderful moments I shared with Cristina Bran, Mihaela Buschbeck, Flaviu Gostin, Ruxandra Costescu, Andreea Budea and Andrea Kellenberger. A special thanks to Claudia Apetrii, for eventually being my friend and for sharing nice and bad moments with me. Your friendship is very important to me.

My old friends in Romania helped me to keep remembering where I am coming from. I appreciate the joy that Oana Tomescu, Catalina Scoarță, and Cristina Farcaș show each time I go back home. I always spend very nice time with my cousins Alina Tomoioagă and George Busuioc. I thank both of you for your friendship and for having the patience of listening to me. I appreciate the friendship over the last 10 years of Silvia Ocheșanu. Thank you for being my very good friend, for showing me things I never saw and for always being there for me.

I appreciate the support of my colleagues from the National Institute for Materials Physics in Bucharest- Romania before I came to Dresden. Special thanks to Dr. Ioana Pintilie, Dr. Lucian Pintilie, Dr. Manuela Budea, Prof. Dr. Toni Boțilă, Dr. Viorica Stancu, Marian Niță and Marian Lișcă. I appreciate the effort of Carmen Mantoma, Irina Dumitriu and especially Răzvan Roescu for supporting me in taking the decision of starting a PhD outside of Romania.

I would not be here without the love and guidance of my grandmother, Elena Busuioc. If all of us would be like her, the world would be a better place. I appreciate the support I had from my parents during my long years of study. My brother, Florin Popa helped me a lot during this work, both for personal and scientific issues. I am very happy for spending holidays together with his wife Lili and their wonderful kids.

Last, but definitely not the least I am grateful to Hemke Maeter, for his love and patience especially during writing this manuscript. Thank you for taking care about me and for being my worst critic when correcting this thesis. Thank you for sharing great moments with me.

Nu aș fi aici fără dragostea și lungile așteptări ale bunicii mele, Elena Busuioc. Îți mulțumesc pentru tot ceea ce ai făcut întodeauna pentru mine și pentru dragostea ta nemărginită. Mulțumesc părinților mei, Mariana și Dan Popa pentru sprijinul lor de-a lungul timpului și pentru că au crezut întodeauna că pot voi fi mai bună.

Die Arbeit “ Electrochemistry and magnetism of lithium doped transition metal oxides”, vorgelegt von Andreia Ioana Popa, wurde unter Betreuung von Prof. Dr. B. Büchner am Institut für Festkörperforschung (IFF) des Instituts für Festkörper- und Werkstoffforschung Dresden e.V. (IFW Dresden) angefertigt.

Versicherung

Hiermit versichere ich, dass ich die vorliegende Arbeit ohne die unzulässige Hilfe Dritter und ohne Benutzung anderer als der angegebenen Hilfsmittel angefertigt habe, die aus fremden Quellen direkt oder indirekt übernommenen Gedanken sind als solche kenntlich gemacht. Die Arbeit wurde bisher weder im Inland noch im Ausland in gleicher oder ähnlicher Form einer anderen Prüfungsbehörde vorgelegt.

Ich erkenne hiermit die Promotionsordnung der TU Dresden an.

Dresden, den 31.07.2009

(Andreia Ioana Popa)

Curriculum Vitae

Personal Records

| | |
|-----------------------|---|
| Name | Andreia Ioana Popa |
| Address | Königsbrückerstr. 58, 01099, Dresden, Germany |
| Contact | e-mail: A.Popa@ifw-dresden.de |
| Date of birth | 20.12.1979 |
| Place of birth | Bacau, Romania |
| Nationality | Romanian |
| Languages | Romanian, English, French |
| Marital Status | Single |

Education

| | |
|----------------------------|--|
| 10. 2005 – present | PhD student at Leibniz Institute for Solid State Research, IFW-Dresden |
| 10. 2005 | Admission to International Max Planck Research School- “Dynamical Processes in Atoms, Molecules, and Solids”, Dresden, Germany |
| 08. 2005 – 09. 2005 | Guest Scientist at Leibniz Institute for Solid State Research, IFW-Dresden |
| 12. 2003 – 10. 2005 | Assistant researcher at National Institute of Materials Physics, Bucharest- Magurele, Romania |
| 09. 2003 – 06. 2005 | Master of Science, University of Bucharest, Romania |
| 09. 1999 – 07. 2003 | Bachelor of Science, University of Bucharest, Romania |
| 09. 1994 – 07. 1998 | High School in Bacau, Romania |
| 09. 1986 – 06. 1994 | Gymnasium in Bacau, Romania |